DISS. ETH N^{O} 24919

Characterization and Polymer Electrolyte Fuel Cell Application of Bimetallic Aerogels

A thesis submitted to attain the degree of

DOCTOR OF SCIENCES of ETH ZURICH

(Dr. sc. ETH Zurich)

presented by

SEBASTIAN MICHAEL HENNING

M.Sc., Technical University of Munich

born on *June 4th, 1988*

citizen of Germany

accepted on the recommendation of

Prof. Dr. Thomas Schmidt, examiner
Prof. Dr. Maksym Kovalenko, co-examiner
Dr. Juan Herranz, co-examiner

2018

Summary

The commercial breakthrough of hydrogen-powered fuel cell electric vehicles (FCEVs) is among others deferred by the substantial costs of the central polymer electrolyte fuel cells (PEFCs) that provide electric energy to the powertrain system. In order to meet the automotive power density and durability requirements, state-of-the art PEFCs contain high amounts of the noble metal platinum (Pt) to catalyze the electrochemical reactions. Thus, this thesis commences by pointing out different strategies to reduce the utilization of expensive Pt and concomitantly PEFC costs while maintaining performance. The main research direction combines two approaches by focusing on unsupported and Pt-alloy oxygen reduction reaction (ORR) catalysts simultaneously. First, the synthesis of a novel Pt-Ni aerogel material is presented, followed by extensive structural characterization to explain the high ORR activity of this catalyst. It was found that the applied aqueous synthesis under ambient conditions leads to the formation of homogeneous alloys with catalytic activity comparable to state-of-the-art carbon-supported Pt-alloy catalysts. Next, another aerogel derivative (Pt-Cu) was produced and the stability vs. non-noble metal dissolution was tested. The results pointed at moderate Cu dissolution and an almost linear relationship between alloy phase Cu-content and ORR activity was discovered. The second part comprises the PEFC implementation of Pt-Ni aerogel to demonstrate the catalyst's applicability and relevance of the pursued strategy. It could be shown that the addition of a filler material to the catalyst layers of Pt-Ni aerogel is pivotal to obtain the desired porosity and pore size distribution for efficient reactant mass transport. Ultimately, a performance in H_2/air polarization curves commensurate to that of catalyst layers from a commercial Pt on carbon benchmark catalyst (Pt/C) was achieved. When tested for degradation under start-up/shut-down condition of PEFCs, Pt-Ni aerogel demonstrated strongly superior durability to Pt/C as expressed by preservation of the cell's power density and the catalyst's surface area. This was related to the integrity of the catalyst layers and the catalyst after the test due to the absence of a corrodible carbon support. Additionally, PEFC durability tests simulating a typical FCEV driving cycle indicated substantial Ni dissolution from the Pt-Ni aerogel catalyst pointing at the suppression of the latter phenomena as the next important development step. Overall, this work demonstrates the great potential of PEFCs with Pt-alloy aerogel catalysts since power density and durability match or exceed the one of Pt/C PEFCs. Through application of a further optimized aerogel catalyst, a reduction in Pt utilization and PEFC costs can be envisioned.

Zusammenfassung

Der kommerzielle Erfolg von Brennstoffzellenfahrzeugen, die mit Wasserstoff betrieben werden, wird unter anderem durch die hohen Kosten der zentralen Polymerelektrolytbrennstoffzellen gehemmt. Dabei stellen letztere Polymerelektrolyt-brennstoffzellen die notwendige Energie für den Antriebsstrang bereit. Um die Anforderungen der Automobilindustrie an Leistungsdichte und Widerstandsfähigkeit zu erfüllen, enthalten modernste Brennstoffzellen erhebliche Mengen des Edelmetalls Platin (Pt) um die elektrochemischen Reaktionen zu katalysieren. Folglich beginnt diese Arbeit mit einem Überblick über verschiedene Strategien, wie der Pt-Einsatz und gleichzeitig die Brennstoffzellenkosten ohne Leistungseinbußen gesenkt werden können. Im zentralen Forschungsansatz werden zwei Strategien kombiniert und der Fokus auf Pt-Legierung-Katalysatoren ohne Trägermaterial für die Sauerstoffreduktionsreaktion gelegt. Zunächst wird die Syntheseroute eines neuartigen Pt-Ni Aerogels vorgestellt und dessen Struktur intensiv charakterisiert, um die hohe katalytische Aktivität für die Sauerstoffreduktion zu erklären. Dabei wurde herausgefunden, dass unter Umgebungsbedingungen eine homogene Legierung mit der eingesetzten Synthese erhalten wird, dessen katalytische Aktivität vergleichbar ist mit modernsten Pt-Legierung-Katalysatoren auf Kohlenstoffträger-material. Anschließend wurde ein weiteres Aerogel (Pt-Cu) synthetisiert und die Stabilität hinsichtlich Auflösung des Nichtedelmetalls untersucht. Die Ergebnisse deuteten auf moderate Kupferauflösung hin und es konnte ein direkter Zusammenhang zwischen Kupfergehalt in der Legierung und der katalytischen Aktivität festgestellt werden. Im zweiten Teil wird die Implementierung des Pt-Ni Aerogels in der Polymerelektrolyt-brennstoffzelle beschrieben, um die Anwendbarkeit des Katalysators und die Relevanz des verfolgten Ansatzes zu unterstreichen. Hierbei konnte gezeigt werden, dass der Zusatz eines Füllmaterials zu den Katalysatorschichten des Pt-Ni Aerogels entscheidend ist, um die gewünschte Porosität und Porengrößenverteilung für effizienten Stofftransport der reaktiven Gase zu erhalten. Letztendlich wurden Strom-Spannungs-Kennlinien in Wasserstoff/Luft Atmosphäre aufgezeichnet, die denen von Katalysatorschichten aus kommerziellen Pt-Katalysatoren auf Kohlenstoffträgermaterial (Pt/C) entsprachen. Bei Belastungstests, die das Starten/Abschalten von Brennstoffzellenfahrzeugen simulieren, wies das Pt-Ni Aerogel deutlich höhere Stabilität als Pt/C auf, was sich an dem Erhalt der Brennstoffzellen-Leistungsdichte und der Katalysatoroberfläche zeigte. Dieses Verhalten konnte mit der Unversehrtheit der Katalysatorschicht und des Katalysators nach dem Test

aufgrund der Abwesenheit des korrodierbaren Kohlenstoffträgermaterials erklärt werden. Zusätzlich wurde in Belastungstests, die das Brennstoffzellenverhalten während des normalen Fahrzyklus nachahmen, signifikante Nickelauflösung aus dem Pt-Ni Aerogel beobachtet. Dies bedeutet, dass sich der nächste wichtigste Entwicklungsschritt mit der Verminderung dieses Phänomens beschaffen muss. Insgesamt unterstreicht diese Arbeit das große Potential von Polymerelektrolytbrennstoffzellen mit Pt-Legierung Aerogel Katalysatoren, denn es wurden Leistungsdichten und Widerstandsfähigkeiten gemessen, die denen von Pt/C Brennstoffzellen entsprechen bzw. diese sogar übertreffen. Weitere Optimierung vorausgesetzt, ist durch die Anwendung von Aerogel Katalysatoren eine Reduktion des Pt-Einsatzes und der Brennstoffzellenkosten vorstellbar.

Acknowledgements

I would first like to thank Prof. Thomas Schmidt and Dr. Juan Herranz for their great guidance and support over the course of my PhD research and Prof. Maksym Kovalenko for being co-examiner of this work. What is more, I am grateful to Dr. Laura Kühn for the synthesis of the aerogel catalyst samples discussed in this work. Next, I would like to acknowledge the support of Hiroshi Ishikawa and Ryo Shimizu in assisting with the experimental work. Moreover, I highly appreciate Dr. Elisabeth Müller's effort to teach me how use the focused ion beam/secondary electron microscope and her help with the electron microscopy experiments. Additionally, I am indebted to Dr. Pierre Boillat and his group for providing the differential fuel cell that was used in this work and to Dr. Alexandra Pătru for developing the spray coating system. Further, I am thankful for Christian Marmy's help in designing, making and repairing various devices in the laboratory and for Cordelia Gloor's assistance in administrative matters. Last but not least, I thank my family and friends for their continuous support. Funding by the Swiss National Science Foundation (20001E_151122/1), the German Research Foundation (EY 16/18-1) and the European Research Council (ERC AdG 2013 AEROCAT) is greatly acknowledged.

Table of Contents

Declaration of Self-Citations

This PhD thesis is a cumulative doctoral thesis based on 5 peer-reviewed published manuscripts. Moreover, the following individual contributions to this work should be noted.

Individual contributions

S. Henning performed and designed experiments, analyzed, interpreted and illustrated data, wrote the thesis and manuscripts.

L. Kühn performed the catalyst synthesis, catalyst acid washing, and selected X-ray diffraction experiments.

H. Ishikawa and **R. Shimizu** assisted in performing fuel cell experiments.

J. Herranz assisted in experimental design, discussed results, supervised the work, evaluated and edited manuscripts, and performed the X-ray photoelectron spectroscopy measurements.

T. J. Schmidt assisted in experimental design, discussed results, supervised the work, evaluated and edited manuscripts.

M. Nachtegaal contributed to the analysis of X-ray absorption spectroscopy data.

M. Werheid, D. Abbott and **B. Kim** took transmission electron microscopy images.

E. Müller assisted in performing focused ion beam - scanning electron microscopy experiments.

R. Hübner performed the scanning transmission electron microscopy - energy dispersive X-ray spectroscopy experiments and data analysis.

M. Adam performed the nitrogen physisorption experiments.

Chapter 2

This chapter contains excerpts from B. Cai, S. Henning, J. Herranz, T. J. Schmidt and A. Eychmüller, Nanostructuring Noble Metals as Unsupported Electrocatalysts for Polymer Electrolyte Fuel Cells, *Adv. Energy Mater.*, 1700548 (2017).

Chapter 4

Includes the formatted version of S. Henning, L. Kühn, J. Herranz, J. Durst, T. Binninger, M. Nachtegaal, M. Werheid, W. Liu, M. Adam, S. Kaskel, A. Eychmüller and T. J. Schmidt, Pt-Ni Aerogels as Unsupported Electrocatalysts for the Oxygen Reduction Reaction, *J. Electrochem. Soc.*, **163**, F998 (2016).

Chapter 5

Includes the formatted version of S. Henning, L. Kühn, J. Herranz, M. Nachtegaal, R. Hübner, M. Werheid, A. Eychmüller and T. J. Schmidt, Effect of Acid Washing on the Oxygen Reduction Reaction Activity of Pt-Cu Aerogel Catalysts, *Electrochim. Acta*, **233**, 210 (2017).

Chapter 6

Includes the formatted version of S. Henning, H. Ishikawa, L. Kühn, J. Herranz, E. Müller, A. Eychmüller and T. J. Schmidt, Unsupported Pt-Ni Aerogels with Enhanced High Current Performance and Durability in Fuel Cell Cathodes, *Angew. Chem. Int. Ed.*, **56**, 10707 (2017).

Chapter 7

Includes the formatted version of S. Henning, J. Herranz, H. Ishikawa, B. Kim, D. Abbott, L. Kühn, A. Eychmüller and T. J. Schmidt, Durability of Unsupported Pt-Ni Aerogels in PEFC Cathodes, *J. Electrochem. Soc.*, **164**, F1136 (2017).

Chapter 8

This chapter contains excerpts from B. Cai, S. Henning, J. Herranz, T. J. Schmidt and A. Eychmüller, Nanostructuring Noble Metals as Unsupported Electrocatalysts for Polymer Electrolyte Fuel Cells, *Adv. Energy Mater.*, 1700548 (2017).

1 Introduction

1.1 Motivation

Low temperature polymer electrolyte fuel cells (PEFCs) are energy conversion devices that transform chemical energy to electrical energy at high efficiency (typically ≥ 50 %). Numerous fuels have been tested for such application, the most popular being CH_3OH, C_2H_5OH, and H_2.[1] The latter hydrogen-powered PEFCs in conjunction with electric engines have been predicted and promoted as next generation local-emission free and quiet powertrains for vehicles since decades. Yet, the first commercial fuel cell electric vehicle (FCEV) was only introduced in 2015 by Toyota and sales numbers have been low due to the high price (57500 USD[2]) and the sparse hydrogen refueling infrastructure.[3] Although the development of FCEVs is also pursued by other car manufacturers and future car releases have been announced, further cost reductions remain the key to being able to serve the mobility mass market in the future. In the meantime, recent progress of Li-ion battery technology has fostered the advent of battery electric vehicles (BEVs) with promising driving ranges. While the success of either technology depends among others on further research progress, fuel prices, customer preferences and policy decisions, it is worthwhile to briefly highlight advantages and disadvantages of both concepts. FCEVs feature short fueling times and long driving ranges per tank, comparable to those for combustion engine powered vehicles. Additionally, the modularity of the system, i.e. energy conversion device and tank, allows for decoupling of power output and energy. While these features offer a clear advantage vs. BEVs, the latter exhibit higher energy efficiency (≈ 90 % vs. ≈ 55 %[1, 3]) and require less investment to build the complementing refueling infrastructure. All things considered, the future will most likely see co-existence of BEVs and FCEVs since one or the other constitutes the better business case for the myriad different applications of vehicles.

To foster the development and cost reduction necessary to commercialize FCEVs, the U.S. Department of Energy (DOE) periodically releases cost and performance targets for PEFCs. For 2020, an overall cost target for the fuel cell power system (i.e. FC stack and balance-of-plant components) of 40 $/kW has been set and a price guideline for the fuel cell stack of 20 $/kW has been released.[3, 4] In that respect, the detailed cost breakdown in Figure 1.1 points to the catalyst material as the major cost block of the fuel cell stack. This is caused by the great amount of carbon-supported platinum nanoparticle (Pt/C) catalyst

(up to 0.4 mg_{Pt}/cm^2_{geom}) that is required to account for the large overpotential of the electrochemical reduction of oxygen on the cathode side in state-of-the art PEFCs.[5] To reduce these excessive Pt loadings and thus PEFC costs, a lot of research effort is dedicated to enhancing the catalysts' activity and stability, e.g. by alloying platinum with other metals like Ni, Cu, Co[6] and by replacing or completely removing the carbon support that suffers from significant corrosion during the normal operation of PEFCs.[3, 7, 8]

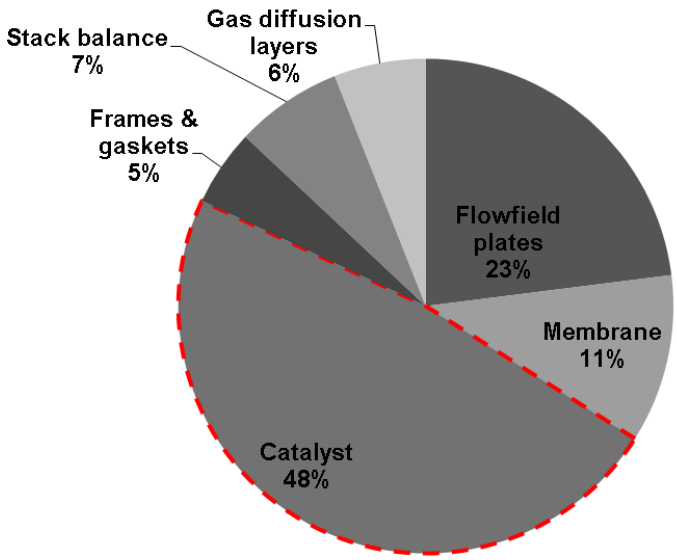

Figure 1.1 Estimated fuel cell stack cost breakdown from reference 9 based on an annual global production volume of half a million FCEVs.

1.2 Objectives and Outline

Keeping the requirement to reduce Pt loadings in mind, the aim of this thesis is to investigate a novel type of unsupported Pt-alloy catalyst for application in PEFCs, thereby combining both improvement strategies (i.e. activity and stability) mentioned above. This work will first cover synthesis, characterization and activity measurements of unsupported Pt-Ni and Pt-Cu catalysts with extended 3D structures and high surface areas (aerogels) in liquid electrolyte half cells. Following the implementation of the most promising aerogel as cathode catalyst in PEFCs, the relationship between electrode structure and performance is investigated by focused ion beam - scanning electron microscopy (FIB-SEM) tomography and electrochemical tests in a differential fuel cell. This work concludes by demonstrating the superior durability of the novel material vs. a commercial Pt/C catalyst, when subjected to an accelerated stress test (AST) at high potential conditions. The comprehensive approach outlined above that comprises material synthesis,

characterization, model and real application performance tests is of particular importance since it aspires to bridge the gap between a fundamental research approach and development towards application.

2 PEFC Fundamentals

2.1 Thermodynamics and Voltage Losses

The electrochemical reactions at the anode and cathode of PEFCs are as follows.

Anode (hydrogen oxidation reaction, HOR):	$2H_2$	$\rightarrow 4H^+ + 4e^-$
Cathode (oxygen reduction reaction, ORR):	$O_2 + 4e^- + 4H^+$	$\rightarrow 2H_2O$
Total:	$2H_2 + O_2$	$\rightarrow 2H_2O$

The maximum useful work associated with this last chemical reaction is given by the Gibbs free energy of reaction for water formation (ΔG^R) that is a function of enthalpy (ΔH^R) and entropy (ΔS^R) changes.[1]

$$\Delta G^R = \Delta H^R - T\Delta S^R \tag{2.1}$$

At a given temperature T (in K), this allows for the calculation of the reversible fuel cell voltage E_{rev} (in V).

$$E_{rev} = -\frac{\Delta G^R}{zF} \tag{2.2}$$

where z is the number of transferred electrons per formed H_2O molecule (here: 2) and F is the Faraday constant (96485 C/mol). Under standard conditions, i.e. T = 298 K and gas pressure of 1013 hPa, E_{rev} amounts to 1.23 V ($\Delta G^R = \Delta G^0$). In a first approximation, both ΔH^R and ΔS^R are independent of the temperature in the operating regime of PEFCs (i.e. $\Delta H^R \approx \Delta H^0$ and $\Delta S^R \approx \Delta S^0$) and the temperature dependent reversible potential $E_{rev(T)}$ can be calculated as follows.[10, 11]

$$E_{rev(T)} = \frac{-\Delta G^0 + (T - 298\ K)\Delta S^0}{2F} = 1.23 - 0.9 \times 10^{-3}\ (T - 298\ K) \tag{2.3}$$

If additionally, the potential dependence on reactant activities according to the Nernst equation is considered, one obtains the following.

$$E_{rev(T,p_{O_2},p_{H_2})} = 1.23 - 0.9 \times 10^{-3}\ (T - 298\ K) + \frac{RT}{2F} \ln\left(\frac{{p_{O_2}}^{0.5}\ p_{H_2}}{p_{H_2O}}\right) \tag{2.4}$$

where p_{O_2}, p_{H_2}, and p_{H_2O} are the dimensionless reactant pressures, derived from dividing the actual pressure by a reference pressure of 1013 hPa. Under the assumption that the cell is operating with a water activity of unity, i.e. relative humidity (RH) ≥ 100 %, equation (2.4) simplifies to

$$E_{rev(T,p_{O_2},p_{H_2})} = 1.23 - 0.9 \times 10^{-3}\ (T - 298\ K) + \frac{RT}{2F} \ln\left({p_{O_2}}^{0.5}\ p_{H_2}\right) \tag{2.5}$$

The reversible potential as introduced above can only be obtained if the Gibbs free energy of formation is converted to electrical work without any losses. In a real PEFC, however, three irreversibilities occur, which are best illustrated by a polarization or I/E curve that shows the cell potential E_{cell} as a function of the current density i (see Figure 2.1).

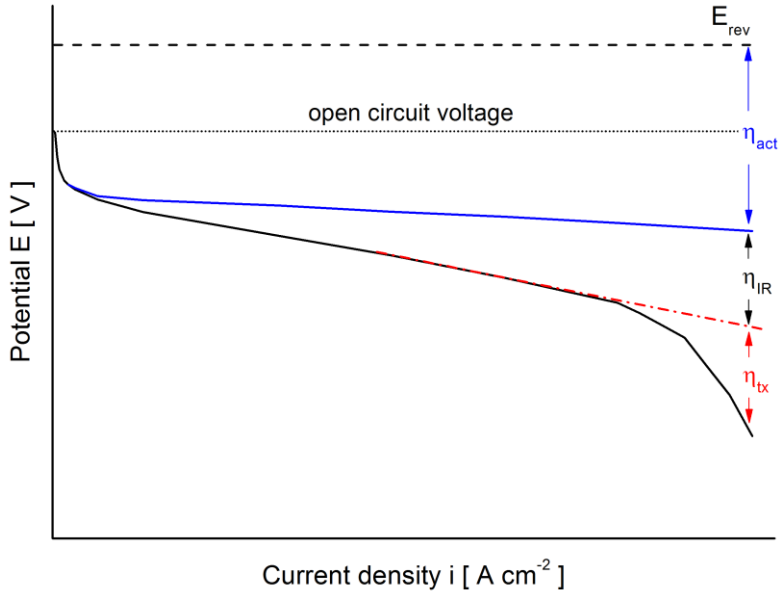

Figure 2.1 Schematic PEFC polarization curve featuring the reversible potential (dashed line) and different voltage loss contributions.

The following different voltage loss contributions (overpotentials) cause the reduction of the cell potential with respect to the reversible potential: the activation overpotential η_{act}, the ohmic overpotential η_{IR} and the mass transport overpotential η_{tx}.[1]

$$E_{cell} = E_{rev} - \eta_{act} - \eta_{IR} - \eta_{tx} \tag{2.6}$$

The activation potential η_{act} occurs once current is drawn from the cell and is associated with the reaction kinetics for HOR and ORR. It can be expressed as the sum of HOR and ORR overpotentials (η_{HOR} , η_{ORR}).

$$\eta_{act} = |\eta_{HOR}| + |\eta_{ORR}| \tag{2.7}$$

Due to the extremely fast kinetics for the HOR (large exchange current density),[12] the activation overpotential is almost exclusively caused by η_{ORR} and η_{act} can be approximated by only considering the Butler Volmer equation for the latter term.[13]

$$i = i_0 \left[\exp\left(\frac{\alpha_a F}{RT}\eta_{ORR}\right) - \exp\left(-\frac{\alpha_c F}{RT}\eta_{ORR}\right)\right] \tag{2.8}$$

In this equation, i_0 is the ORR exchange current density, α_a and α_c the anodic and cathodic transfer coefficients (here equal to 1; containing the symmetry factor β and the number of transferred electrons in an assumed reaction mechanism[11]) and R the universal gas constant (8.314 J K^{-1} mol^{-1}). For large overpotentials, i.e. negative $\eta_{ORR} << \frac{RT}{F}$, the first term in equation (2.8) becomes negligible and the current can be written as.

$$i = -i_0 \exp\left(-\frac{\alpha_c F}{RT}\eta_{ORR}\right) \tag{2.9}$$

Taking the logarithm, this can be converted to the Tafel equation (2.10) with a Tafel slope of $b = -\left(\frac{2.303\ RT}{\alpha_c\ F}\right)$:

$$\eta_{ORR} = \left(\frac{2.303\ RT}{\alpha_c\ F}\right)\log(i_0) - \left(\frac{2.303\ RT}{\alpha_c\ F}\right)\log|i| = a + b\ \log|i| \tag{2.10}$$

The ohmic voltage losses η_{IR} can be expressed as the sum of bulk electronic resistance R_{elec}, contact resistance R_{con}, RH-dependent membrane proton resistance R_{ion} and effective proton resistance in the catalyst layers R_{H+} that increase linearly with the current density according to Ohm's law.

$$\eta_{IR} = i(R_{elec} + R_{con} + R_{ion} + R_{H+}) \tag{2.11}$$

Finally, the mass transport or gas diffusion overpotential η_{tx} becomes relevant at high current densities as discernable from Figure 2.1 and is caused by H_2/O_2 concentration gradients, i.e. reduced reactant availability at the reactive sites. Reasons for the reactant depletion are limited diffusion rates, poor fuel and oxygen/air supply as well as diffusive barriers due to electrode flooding by the generated water.[1]

It must be noted that even in the absence of the loss terms described above, the cell's open circuit voltage (OCV) is typically lower than the theoretical reversible fuel cell voltage E_{rev} of 1.23 V at 25°C. This originates from the diffusion of hydrogen fuel through the membrane to the cathode side (crossover) where it directly reacts with oxygen and the formation of a mixed potential through the oxidation of the Pt catalyst surface.

2.2 Basic Components

2.2.1 From Stack to Membrane Electrode Assembly

At the heart of the fuel cell system in FCEVs is the fuel cell stack that consists of several single cells connected in series (cf. Figure 2.2) to increase the output voltage. Each single cell is composed of a membrane electrode assembly (MEA) sandwiched between two flow

field plates that provide an electrical pathway and access to the reactive gases (H_2 and O_2/air) through a gas channel network.[14]

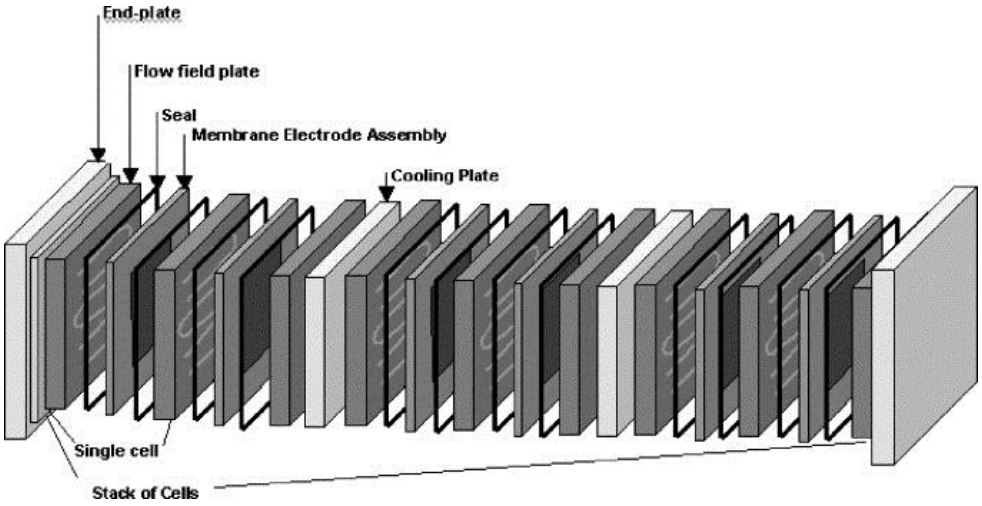

Figure 2.2 Main components in a fuel cell stack. Reproduced with permission.[15] Copyright 2003, Elsevier.

The MEA (see Figure 2.3), sort of the heart of the fuel cell, is composed of anodic gas diffusion layer (GDL), anodic catalyst layer (CL), membrane, cathodic CL and cathode GDL. Each of these components has complementary roles and research to further improve them individually is necessary and ongoing. The outer GDLs transport reactants from the gas channels to the CLs, manage the water content in the cell and transfer electrons plus heat.[16, 17] The central membrane transports protons and water from anode to cathode, whilst acting as an electronic insulator to prevent cell short circuits. State-of-the art materials mainly consist of cast perfluorosulfonic acid (PFSA) ionomer (e.g. Nafion) or composites of the former and microporous supports.[18, 19] Lastly, the CLs convert the reactants electrochemically and control the circulation of electrons, protons, reactants and product water, thus playing a key role for overall fuel cell performance.[20]

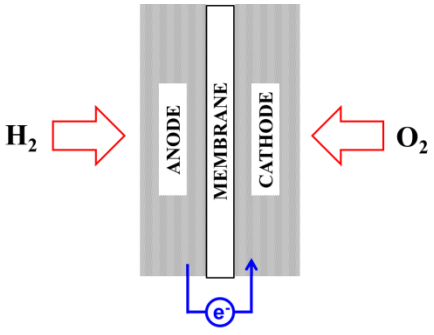

Figure 2.3 Schematic drawing of the membrane electrode assembly.

2.2.2 Catalyst Layers

In order to better understand the above mentioned processes occurring in the catalyst layer, they will be discussed in detail considering a state-of-the-art Pt-M/C catalyst (carbon supported alloy of platinum and non-noble metal (M)) and exclusively regarding the cathodic CLs.[3, 21] This choice is motivated by the higher voltage losses at the cathode vs. anode, caused by the extremely fast hydrogen oxidation reaction kinetics on Pt discussed above and negligible gas diffusion resistances for H_2.[13]

To begin with, typical Pt-M/C CLs consist of the catalyst nanoparticles, carbon support, ionomer and pores,[3, 20, 22, 23] and can be described at three different scales, as illustrated in Figure 2.4.[22] At the microscale (< 10 nm), the electrochemical conversion of O_2 to H_2O takes place at the surface of Pt-M nanoparticles, whereby the number of active sites and reactivity is determined by shape, size and composition of the particles.[20, 24] In the absence of mass transport limitations, the reactivity of nanoparticles, expressed as a current density, can be described by the Butler Volmer equation that relates current density and potential (cf. equation (2.8) in section 2.1).[10, 20] Looking at the mesoscale (tens of nm), the Pt-M nanoparticles are either located on the surface of carbon agglomerates (diameter of 50 - 300 nm)[22, 25] or inside of primary pores (2 - 20 nm)[22, 25] that are present in between the primary carbon particles (≈ 20 nm).[25] Naturally, for the electrochemical conversion to occur, Pt-M nanoparticles need access to electrons, O_2 and protons. Whereas the former is provided through the network of conductive carbon agglomerates that extends all the way to the GDL, oxygen and proton transport are more complex.

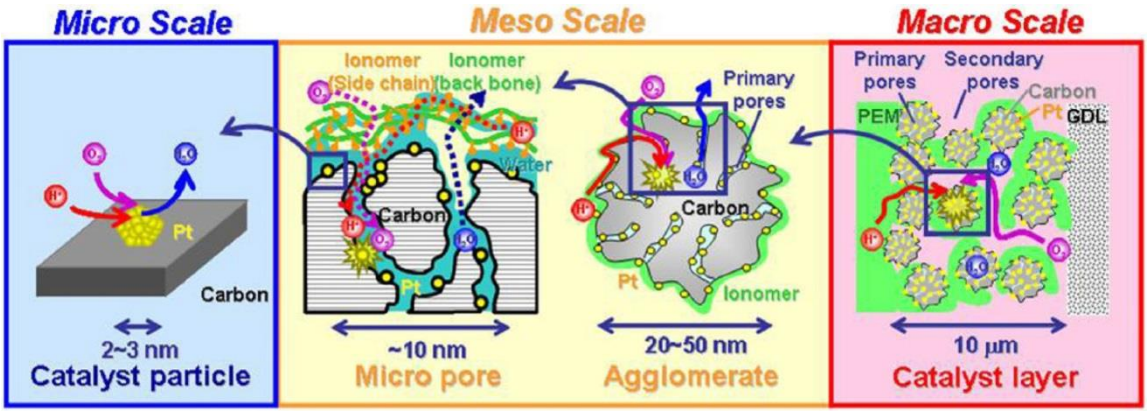

Figure 2.4 Different scales of the catalyst layer, highlighting relevant processes and structural features. The red, purple and blue circles represent protons, oxygen and water, respectively. Reproduced with permission.[22] Copyright 2011, Elsevier.

It has been experimentally observed that the ionomer forms a thin film around the carbon agglomerates,[26] the thickness being a function of the ionomer-to-carbon-ratio (I/C).[22] Nonetheless, there is proof that this thin film is not uniform in thickness and complete coverage is not achieved for all types of carbon supports, even at higher I/C-ratios.[22, 27] State-of-the-art PFSA ionomers transport protons to the active sites through the sulfonic acid groups attached to the polymer chain, whereby the conductivity is linked to acid strength, acid content (ion exchange capacity IEC) and water content.[18] With primary pores being inaccessible to ionomer,[18, 22] proton transport to Pt-M nanoparticles inside the carbon agglomerates is only feasible if these pores are filled with water, making such conditions desirable to reach high performance.[3, 20] To describe the transport process of O_2 gas to the active sites, the secondary pores between carbon agglomerates (≈ 20 - 100 nm[20], or up to 200 nm[28]) on the macroscale of the CL (cf. Figure 2.4) need to be considered. In optimized CLs under the desired PEFC operation conditions, these secondary pores, in contrast to the primary pores discussed earlier, ought to be free of liquid water to allow for effective gas transport from the GDL through molecular and Knudsen diffusion.[20, 29] Naturally, the transport effectiveness is also a function of the CL thickness, that depends on the loading (mg_{Pt}/cm^2_{geom}), Pt concentration (wt. % Pt/C) and I/C-ratio,[30] whereby the application-relevant thicknesses usually are between 5 and 15 µm.[3, 20, 22, 23, 31] Ultimately, O_2 needs to pass, i.e. dissolve and diffuse, through the ionomer film to reach the active site. This step can be described as a local O_2 transport resistance that accounts for up to 50 % of the overpotential associated with O_2 transport losses in PEFC cathodes at low loadings (≈ 0.1 mg_{Pt}/cm^2_{geom}) and high current densities > 1.5 A/cm^2_{MEA}.[29, 32] The resistance scales inversely with the Pt electrochemical surface area (ECSA), i.e. great catalyst dispersion is advantageous, and the latest results indicate that the thin ionomer film's O_2 transport resistance is increased locally by the interaction with the Pt surface, thus pointing at advanced ionomer development as a key strategy to mitigate this issue.[32]

2.3 Catalyst Layers from Supported vs. Unsupported Materials

It goes without saying that the structure and thus performance of the CLs is profoundly influenced by the properties of the catalyst material itself.[22, 33] This renders CL design on an individual material basis necessary, yet provides opportunities to optimize the CL structure through targeted design of the catalyst materials. The fact that the structure of the CL is closely interlinked with the catalyst material used can for instance be illustrated by calculating the thickness of the CL when going from supported to unsupported

catalysts. Considering a state-of-the-art 50 wt. % Pt-M/C catalyst, at an I/C-ratio = 1, with a CL porosity of 60 %,[30, 34] a loading of 0.2 mg_{Pt}/cm^2_{geom}, and assuming ionomer and carbon densities of ≈ 2 g/cm^3,[35] the thickness amounts to ≈ 5 µm (thereby overlooking the negligible thickness contribution from Pt-M nanoparticles). Due to the 10-fold larger density of Pt vs. C, the removal of the carbon support upon transitioning to unsupported materials leads to an expected thickness of only ≈ 0.5 µm, ≈ 90 % lower than that of Pt/C CLs (assuming porosities of 60 % for both materials[36] and an ionomer-to-catalyst ratio of 0.1 for the unsupported catalyst) and that can profoundly affect the optimal CL design.[20]

In principle, transitioning from supported to unsupported catalysts can entail alterations of electron, proton, reactant and product water transport in the CLs. Envisioning unsupported catalysts either as extended Pt-M surfaces or Pt-M nanoparticulate building blocks (i.e. conductive materials), electron transport will occur similarly to Pt-M/C CLs. For the ultrathin CLs expected with unsupported catalysts as illustrated by the calculation above, it is reasonable to assume that the proton concentration is significantly increased and can approach the proton bulk concentration in the membrane.[20] Moreover, it has been found that purely metallic surfaces like the nanostructured thin films (NSTFs) from 3M,[37] which will be introduced in detail later (section 2.5.1.2), rely on proton conduction on the Pt surface and function well in the absence of ionomer.[32] While such proton conduction could be provided either by diffusion of H_2O or hydrogen adsorbed on the Pt-surface (H_{ads}), or by H^+-diffusion within very thin surface water films,[38] the latest results indicate the preponderating importance of the latter.[39, 40] As for reactant and product water transport, it is paramount for CLs derived from unsupported catalysts to exhibit appropriate porosities and pore size distributions to enable diffusion between active sites and the GDL, as it is also the case for conventional CLs prepared with carbon supported catalysts (cf. section 2.2.2). Keeping in mind that, in the latter case, this porosity is provided by the carbon support material exclusively (i.e. through the stacking of 50 - 300 nm large carbon agglomerates which results in free spaces[25]), retaining such property with unsupported catalysts and their potentially smaller agglomerate dimensions constitutes a major challenge for the preparation of the catalyst layer, and should also be considered at the initial stage of catalyst synthesis. At the same time, the expected thinning of the CLs due to the use of unsupported catalysts will certainly alter mass transport properties and water distribution,[31] possibly translating into pore structure requirements different from the ones established for conventional CLs.

2.4 Degradation Phenomena in Catalyst Layers

As mentioned in chapter 1, state-of-the art catalysts and thus catalyst layers suffer from limited stability under the normal operation of PEFCs.[3, 7, 8, 41] In this respect, the automotive application causes dynamic load cycling that can trigger rapid changes between low and high cell voltages (≈ 0.6 - 1.0 V).[41] Under such conditions, Pt particle growth, triggered by Pt dissolution (oxidation) and redeposition (reduction) on the surface of larger particles (Ostwald ripening), as well as by Pt particle migration and coalescence, have been reported as dominant degradation mechanisms.[42, 43] What is more, during start-up or shut-down of the PEFC, a hydrogen/air front can move through the anode channels separating the fuel cell into an active and passive part (see Figure 2.5 below).[44, 45] In the passive part of the anode, the potential is significantly lower than in the active side due to the presence of oxygen gas (≈ - 0.6 V vs. ≈ 0 V)[44] and the high electron conductivity. This increases the cathode potential in the passive part to ≈ 1.5 V vs. the anode causing carbon corrosion and oxygen evolution.[42, 46] A similar effect is observed during local fuel starvation conditions (e.g. due to water accumulation in anode GDL or flow field), when the permeation of oxygen through the membrane to the starved domains creates alike circumstances. Lastly, high potentials of ≈ 1.5 V at the anode can occur if an entire cell in a stack is not supplied by hydrogen and other reactions (carbon corrosion, oxygen evolution) need to produce the electrons and protons required at the cathode.[47]

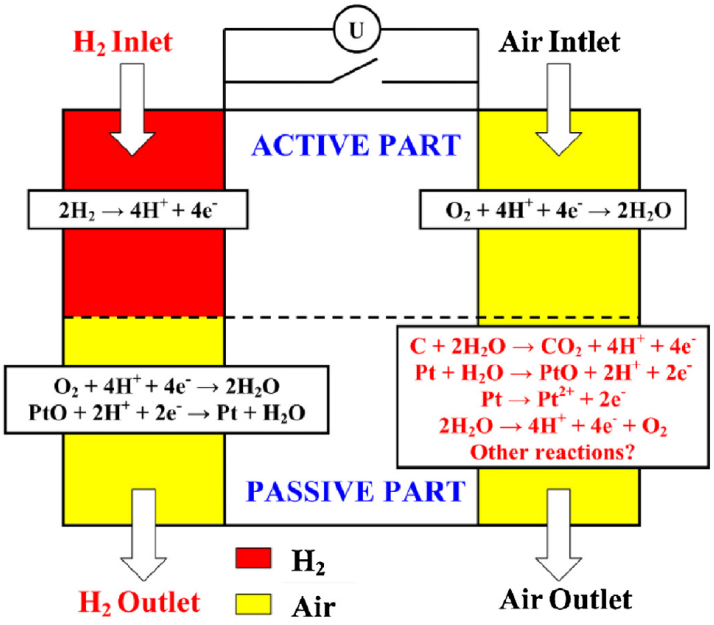

Figure 2.5 Schematic representation of chemical reactions occurring in a PEFC under start-up or shut-down conditions. Reproduced with permission.[45] Copyright 2013, Elsevier.

The carbon corrosion mentioned above, that can lead to Pt nanoparticle detachment[7] and collapse of the catalyst layer structure,[45, 48] is the main reason for development of unsupported catalysts. Provided that the PEFC implementation is successful, these materials promise greater durability under automotive fuel cell relevant conditions. In the following section, synthesis, characterization and PEFC tests of promising unsupported materials shall be discussed.

2.5 Promising Types of Unsupported Catalysts

2.5.1 Synthesis and Characterization

2.5.1.1 Noble-metal Based Aerogels

Synthesis and features

Metallic aerogels assembled from noble metal colloidal nanoparticles (NPs) are of enormous scientific and technological interest owing to their ultralow density, high surface area, and large open interconnected pores.[49] They combine the properties of the noble metal (e.g. catalytic activity, electric conductivity) with large surface area (providing more reactive sites), high porosity (facilitating mass transfer) and self-supportability (eliminating the need for a carbon support), thus rendering these noble metal aerogels promising candidates for electrocatalysis.[49] As a proof-of-concept, e.g. metallic aerogels with compositions of pure Pd and Au, as well as alloyed Pd_xPt_y, Pt_xNi_y (cf. chapter 4) and Pt_xCu_y (cf. chapter 5) have recently been synthesized and evaluated for electrocatalysis.[50-54] Linking aerogel research and nanotechnology, hierarchical aerogels with primary and secondary pore structures built from shape-engineered NPs have also been reported in the form of either hollow shell or dendritic particles.[55-57]

As illustrated in Figure 2.6, the general synthesis of noble metal aerogels via the sol-gel process consists of three steps: i) the synthesis of nano-sized building blocks (NBBs); ii) the gelation of the NBBs into hydrogels (plus shape-control of the hydrogel) and iii) the supercritical drying of the hydrogel to yield an aerogel. These three strategies are outlined in different colors in paths I (B1-H1-A1), II (B1-H1-H2-A2) and III (B1-B2-H3-A3) of Figure 2.6. In strategy I, solid noble metal NPs with controlled compositions are employed as NBBs, thus resulting in a nanowire-based aerogel. Citrate and cyclodextrin are frequently utilized as the stabilizers to narrow the size distribution of the metal NPs.[58] The relatively weak coordination interaction between the stabilizer and metal NPs is critical for the

gelation step (from B1 to H1 in Figure 2.6), which can be realized spontaneously[50, 51, 53] or via controlled destabilization (by heating[59] or adding salt[60] and cross-linkers[61]).

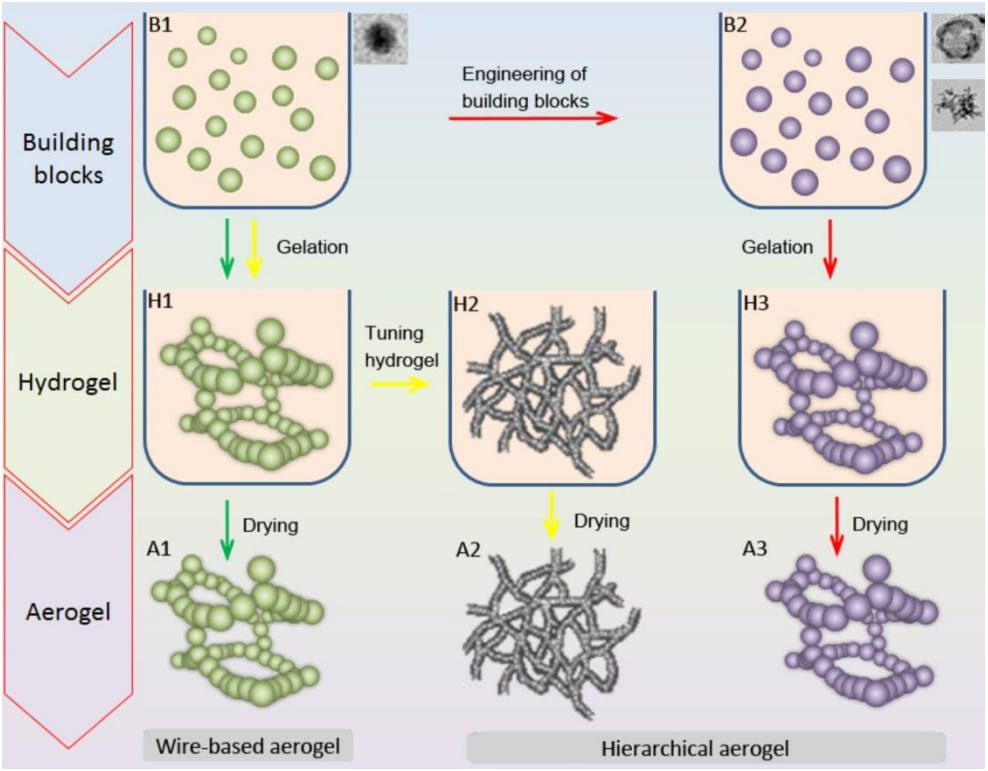

Figure 2.6 Schematic illustration of the synthesis procedures of noble metal-based aerogels via sol-gel processes. In general there are three steps, including preparation of NBBs, gelation to hydrogel and supercritical drying to aerogel. Depending on the engineering of each selected step, the strategies can be divided into three and lead to different structures. Green arrows: Strategy I (B1-H1-A1); Yellow arrows: Strategy II (B1-H1-H2-A2); Red arrows: Strategy III (B1-B2-H3-A3). The spontaneous gelation method which belongs to Strategy I can exempt the B1 step, where hydrogels were formed directly via the reduction of metal precursors. The TEM images next to B1 and B2 are examples of the NBBs. Reproduced with permission.[62] Copyright 2017, Wiley-VCH.

Besides the porous and interconnected 3D network structure, hierarchical aerogels also possess backbones with locally modified morphologies instead of solid nanochains. As shown in Figure 2.6, this sub-structure can be obtained either by tailoring the hydrogel via strategy II (B1-H1-H2-A2)[57] or engineering the NBBs via strategy III (B1-B2-H3-A3).[55] At present, research on metallic hierarchical aerogels prepared by manipulation of the NBBs is still in its infancy and lags far behind the abundance of colloidal metallic nanoarchitectures.[63] This may be ascribed to the frequent requirement of strong stabilizers for the shape-control of the metallic NPs, which is extremely detrimental to the subsequent gelation/destabilization of these colloids.[58] Future research may focus on realizing the

gelation by controlled chemical/physical removal/complexation of the surface ligands, or by adjusting the chemical parameters of the solvent (e.g. ionic strength, dielectric coefficient).

Wire-based aerogels

The synthesis of metallic aerogels following strategy I (Figure 2.6) generally yields wire-based aerogels. The nanowire-like backbones are derived from the fusion and connection of the particulate NBBs (mostly noble metal NPs) during the gelation process. Depending on the elemental composition and distribution, these aerogels can be divided into three types: monometallic aerogels (Pd, Pt, Au, Ag),[50, 52, 60, 61] bimetallic alloy aerogels (Pd_xPt_y, Pt_xNi, Pt_xCu, etc),[51, 53, 64] and mixed multi/bi-metallic aerogels (Au-Pd, Pd-Pt, Au-Ag-Pt, etc.).[59, 65] Figure 2.7 shows representative scanning electron microscopy (SEM) and transmission electron microscopy (TEM) images of the wire-based aerogels. They all exhibit high porosity with numerous open pores and similar 3D network structures with extended nanowires interconnected randomly. The nanowire-like backbones show similar diameters to those of the original NPs, confirming the presumption that the hydrogel formed from the starting NPs without any intermediate agglomeration steps.

Using citrate-stabilized Pd NPs as the NBBs, pure Pd aerogels were obtained by destabilizing the concentrated colloidal sols by either heat treatment[59] or adding calcium ions[61]. Following a similar strategy, Ag and Pt aerogels were fabricated using H_2O_2 and ethanol as the destabilizer.[60] It should be pointed out that the concentration step of as-prepared NPs required for these approaches, however, is usually time-consuming, thereby limiting scale-up of the synthesis. To address this, spontaneous gelation of the in situ generated NPs with[50] or without[51] the modification of cyclodextrins was developed to synthesize Pd (Figure 2.7A-C) and Pt aerogels. In a similar way, Au aerogels (Figure 2.7D-F) were synthesized by a dopamine-induced gelation of the as-prepared Au NPs based on the complexation between dopamine and Au.[52] To endow aerogels with additional properties, bimetallic Pd_xPt_y aerogels with tunable composition were prepared based on the spontaneous gelation method (Figure 2.7G-I).[51] Following the same strategy, Pt-based aerogels with compositions of Pt_3Ni (Figure 2.7J-L), $Pt_{1.5}Ni$, Pt_3Cu and PtCu were also fabricated and investigated as ORR electrocatalysts (see chapters 4 and 5 in this work).[53, 66] To accelerate hydrogel formation, Zhu et al. reported a series of MCu (with M = Pd, Pt, or Au) bimetallic aerogels based on the in situ reduction of metal precursors at elevated temperature, thereby indeed observing an enhancement of the gelation kinetics.[64]

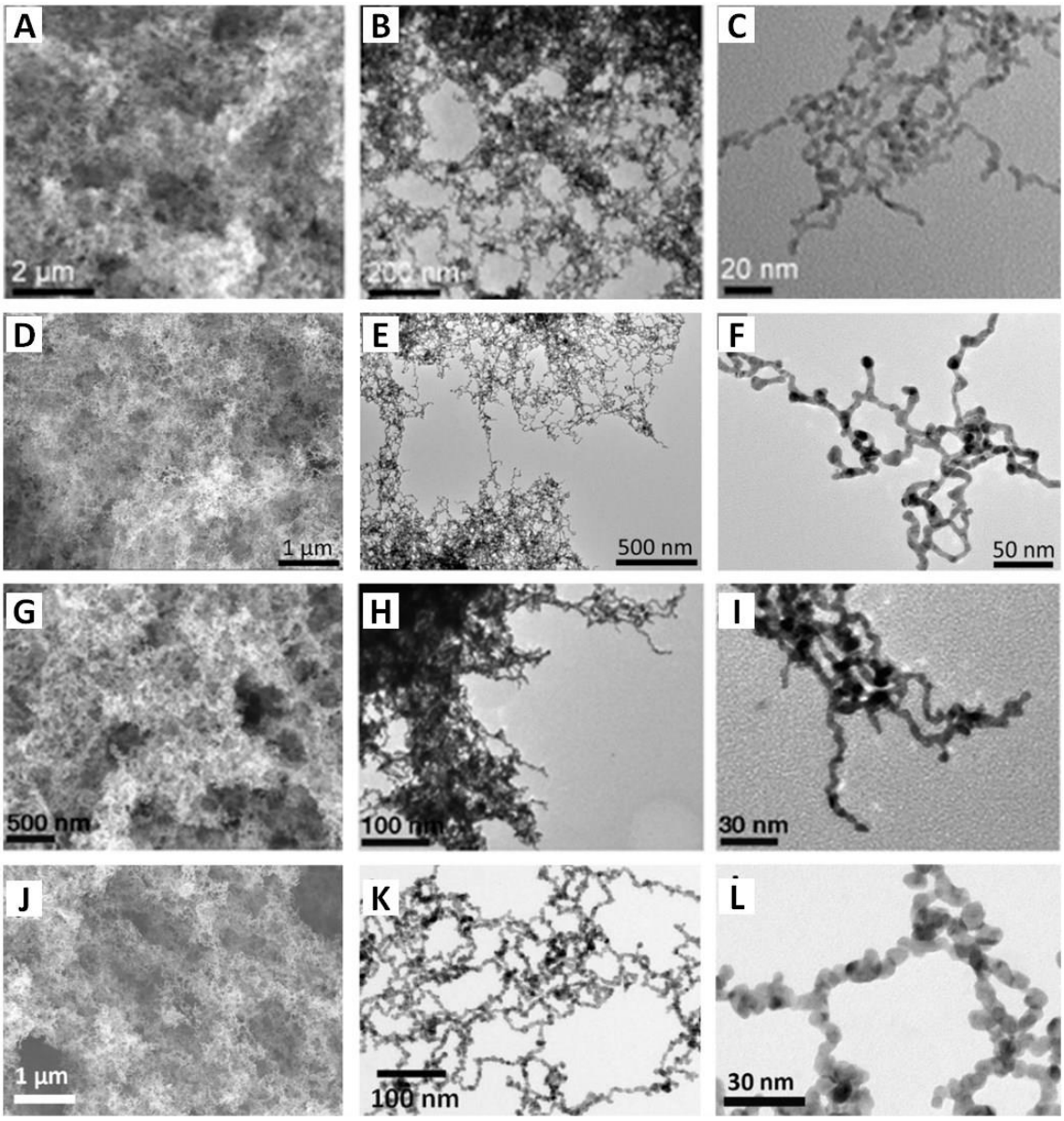

Figure 2.7 SEM and TEM images of some representative wire-based mono/bimetallic aerogels. (A-C) Pd aerogels. Reproduced with permission.[50] Copyright 2012, Wiley-VCH. (D-F) Au aerogels. Reproduced with permission.[52] Copyright 2016, American Chemical Society. (G-H) $Pd_{50}Pt_{50}$ aerogels. Reproduced with permission.[51] Copyright 2013, Wiley-VCH. (J-L) Pt_3Ni aerogels.[53]

The average density of the metallic aerogels was estimated to be 0.016 - 0.050 g/cm^3, which amounts to approximately one thousandth of that of the corresponding bulk materials. Their porosity and surface area were further investigated by N_2-physisorption measurements. The N_2 adsorption-desorption isotherms obtained for all these metallic aerogels show a combination of the characteristics of type II and type IV isotherms (Figure 2.8A-C), indicating the wide-spread presence of both meso- and macropores within the

aerogel structures. The specific surface areas of the aerogels determined based on the Brunauer−Emmett−Teller (BET) method are in the range of 32 - 168 m^2/g. As shown in Figure 2.8D-E, the metallic aerogels revealed a wide pore size distribution in the aerogels ranging from micropores to meso/macropores, which could also be observed in the SEM and TEM images (Figure 2.7 and Figure 2.9). The hierarchical pore systems hold the potential for reducing the diffusion barriers in catalysis applications since the diffusion rates through 10 - 50 nm pores can approach those of molecules in open media.[67]

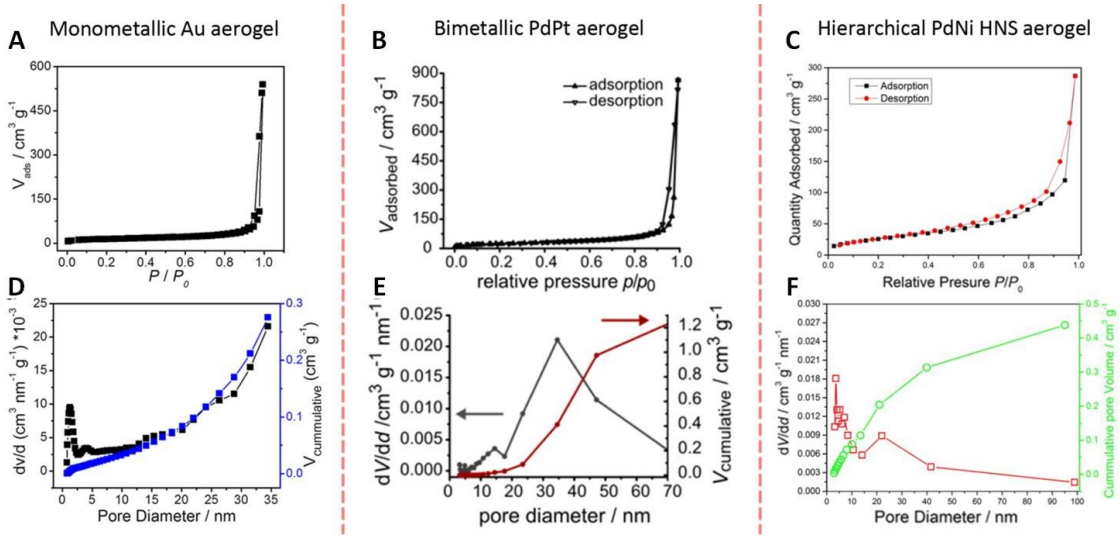

Figure 2.8 Nitrogen physisorption isotherms, pore size distributions, and cumulative pore volumes ($V_{cumulative}$) of different metallic aerogels. (A, D) Monometallic Au aerogels. Reproduced with permission.[52] Copyright 2016, American Chemical Society. (B, E) Bimetallic PdPt aerogels. Reproduced with permission.[49] Copyright 2015, American Chemical Society. (C, F) Hierarchical PdNi HNS aerogels. Reproduced with permission.[55] Copyright 2015, Wiley-VCH.

Hierarchical aerogels

Following strategies II and III in Figure 2.6, hierarchical aerogels that generally combine a 3D interconnected porous structure on the macroscale and a fine-tuned configuration of local backbones at the nanoscale can be obtained (Figure 2.9). This combination usually leads to an integration of several catalysis enhancement factors in hierarchical aerogels. Recently, PdNi hollow nanospheres (HNSs) were employed as NBBs to fabricate a hierarchical aerogel with a well-defined 3D necklace-like network structure (Figure 2.9A-C).[55] The hollow cavity distributed throughout the networks could further be identified by a distinct peak (at ca. 22 nm) in the pore size distribution analysis (Figure 2.8F). This aerogel exhibited an improved electrocatalytic activity for ethanol oxidation when

compared to the isolated HNSs and Pd/C. Subsequently, a series of hierarchical aerogels were synthesized from the gelation of colloidal Ni-Pd_xPt_y NBBs with continuously engineered shape and varied composition.[56] Taking the extreme composition of Ni-Pt as an example (Figure 2.9D-F), low magnification SEM/TEM images reveal that this hierarchical aerogel features a porous structure similar to that of the wire-based aerogel while exhibiting a dendritic morphology at the nanoscale. In addition, Arachchige et al. reported a salt-mediated method to self-assemble AuAg, PdAg and PtAg nanoshells into a gel structure.[68] Thiolate-coated Ag nanoshells with varying size and shell thickness were then assembled into monolithic hydro/aerogels via oxidative removal of the surface thiolates.[69]

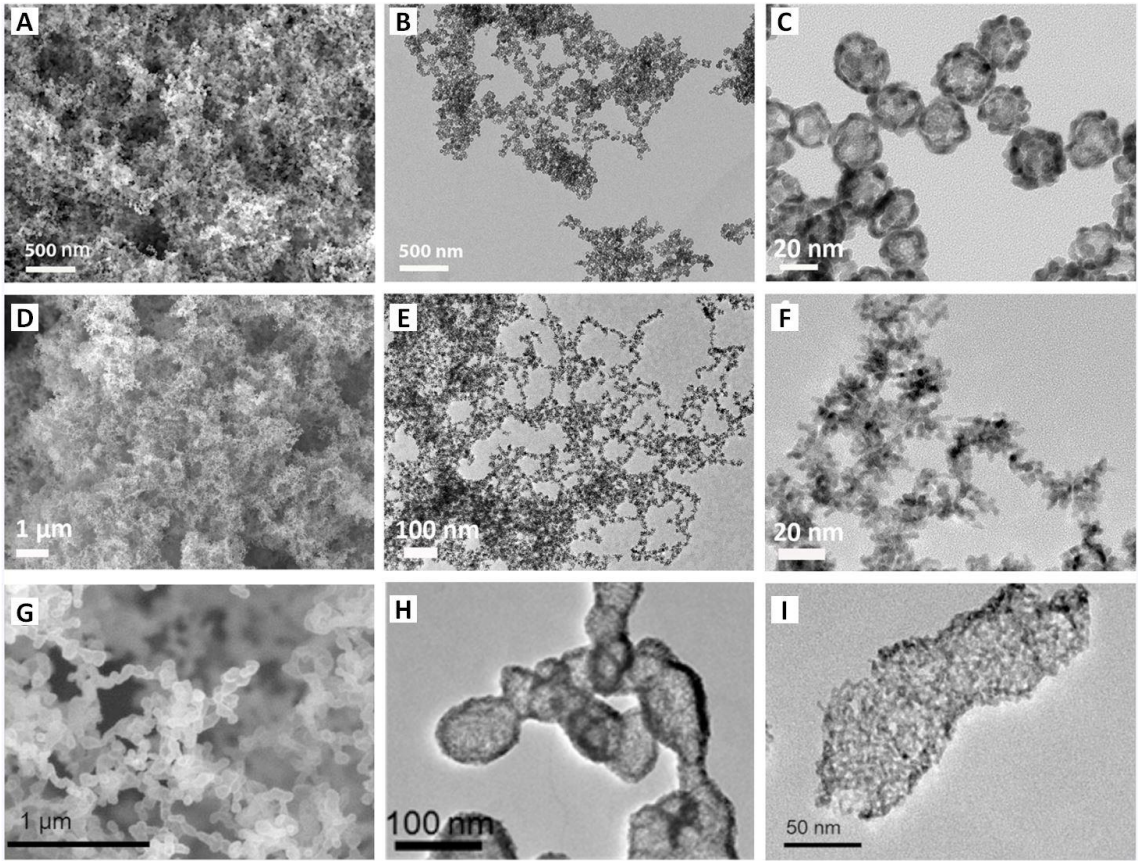

Figure 2.9 SEM and TEM images of the hierarchical aerogels: (A-C) Pd-Ni hollow nanospheres aerogel from Strategy III. Reproduced with permission.[55] Copyright 2015, Wiley-VCH. (D-F) Pt-Ni dendritic aerogel from Strategy III. Reproduced with permission.[56] Copyright 2017, Wiley-VCH. (G-I) PtAg nanotubular aerogel from Strategy II. Reproduced with permission.[57] Copyright 2016, American Chemical Society.

By taking advantage of hydrogel engineering, PtAg nanotubular aerogels were fabricated via a simple galvanic replacement reaction between the in situ, spontaneously gelated Ag hydrogel and the Pt precursor.[57] As shown in Figure 2.9G-I, the resulting PtAg aerogels possess hierarchical porous network features with primary macropores from the aerogel network and secondary micropores from the porous surface of the nanotube-backbones, resulting in high porosities and large specific surface areas. Due to its unique structure, the as-prepared PtAg aerogel exhibits 19-fold enhanced electrocatalytic activity towards formic acid oxidation as compared to Pt black.[57]

2.5.1.2 Nano/meso-structured Thin Films

Another unique category of unsupported electrocatalysts are Pt-based meso- and nano-structured thin films (MSTFs and NSTFs), developed by 3M using magnetron sputter deposition of Pt thin film alloys on crystalline organic whiskers.[70-72] Figure 2.10A illustrates the step-by-step preparation process of the NSTFs as well as their transformation to MSTFs via annealing in a reductive atmosphere. The support is a thin layer of an oriented array of crystalline organic whiskers, namely perylene red, less than 1 μm tall and 30 nm × 55 nm in cross-section at a number density of ≈ 35 whiskers/μm^2.[37] These non-conductive and electrochemically stable organic whiskers eliminate carbon corrosion, and their crystallinity facilitates the subsequent nucleation and thin film growth of the sputtered catalyst materials. To date, a series of Pt-based NSTF catalysts (Pt-Ni, Pt-Co, Pt-Ir, Pt-Co-Ni, Pt-Co-Mn, Pt-Co-Fe, etc.) with well-defined extended and nanoscale surfaces have been developed by sputtering the catalyst layer onto the whisker substrate.[37, 70, 72-74] Their unique thin film structure significantly reduces the population of low-coordination number atoms and hence increases the surface specific activity for ORR about 5-10 times with respect to commercial Pt/C catalysts, which is in line with the activity values of polycrystalline or single crystal bulk surfaces.[37] Since the NSTF catalysts already exhibit large extended metal surfaces, they are less susceptible to the loss of surface area, thus enhancing their durability. In addition, the elimination of carbon corrosion at high voltage makes them particularly useful at the PEFC anode where high tolerance to anode fuel starvation events and cell reversal are required (see also section 2.4).[70]

The highly corrugated surface of as-sputtered NSTFs occupied by pyramid-like pillars with a cross-section of ≈ 6 nm can be gradually smoothed by heating up to 400^{o}C in a reductive atmosphere.[75] As depicted in Figure 2.10B-C, the annealing process triggers the transformation from NSTFs to MSTFs while retaining the whisker's vertically aligned

morphology, even if the organic whisker support is completely removed. In situ high resolution TEM (Figure 2.10C-D) illustrates that the initially corrugated surface morphology is transformed into a more homogeneous, flat and ordered thin film with large crystalline domains (20 - 40 nm). Simultaneously, the fraction of undercoordinated sites is further reduced, since (111) surface facets start to prevail, thereby promising improved activity for ORR. Indeed, as claimed by Stamenkovic et al., NSTF catalysts can successfully mimic the catalytic behavior of polycrystalline bulk materials, whereas Pt alloy MSTF catalysts exceed the activity of the latter.[75] For instance, PtNi MSTFs show a remarkable 20-fold enhancement in the ORR activity over commercial Pt/C (cf. section 8.1). A thin film catalyst composed of vertically aligned Pt-Ni nanorod-arrays has also been fabricated by a glancing angle deposition technique, which leads to more dense arrays.[76] These findings provide a proof-of-concept for designing highly active and durable electrocatalysts by tailoring the composition, morphology and mesoscale structure of the thin-film-based materials.

In another study, Kibsgaard et al. reported a new synthesis for surface-extended Pt MSTF catalysts via electrodeposition of Pt into a mesoporous silica film that serves as a template.[77] As outlined in Figure 2.10F, the silica film with a double gyroid (DG) morphology was prepared by calcination of the surfactant-silica mixture and then removed after electro-filling with Pt. The resulting Pt DG MSTF maintains the interlocked, twisted network structure after removal of the silica, displaying a high porosity with an average pore-to-pore distance of 6.7 nm, and an average pore diameter of 3−4 nm. Similar to the MSTFs discussed above, the continuous nature of the DG-structured MSTFs promises improved stability due to the mitigation of Ostwald ripening and Pt migration/agglomeration and the suppression of carbon corrosion. Following a similar procedure, a Pt_xNi alloy was fabricated into a highly ordered DG-shaped mesoporous thin film.[78] The resulting Pt_xNi MSTF catalysts maintained the DG meso-structure and good activity after intensive accelerated stability testing, which shows the promise of mesoscale structured Pt-based ORR catalysts.

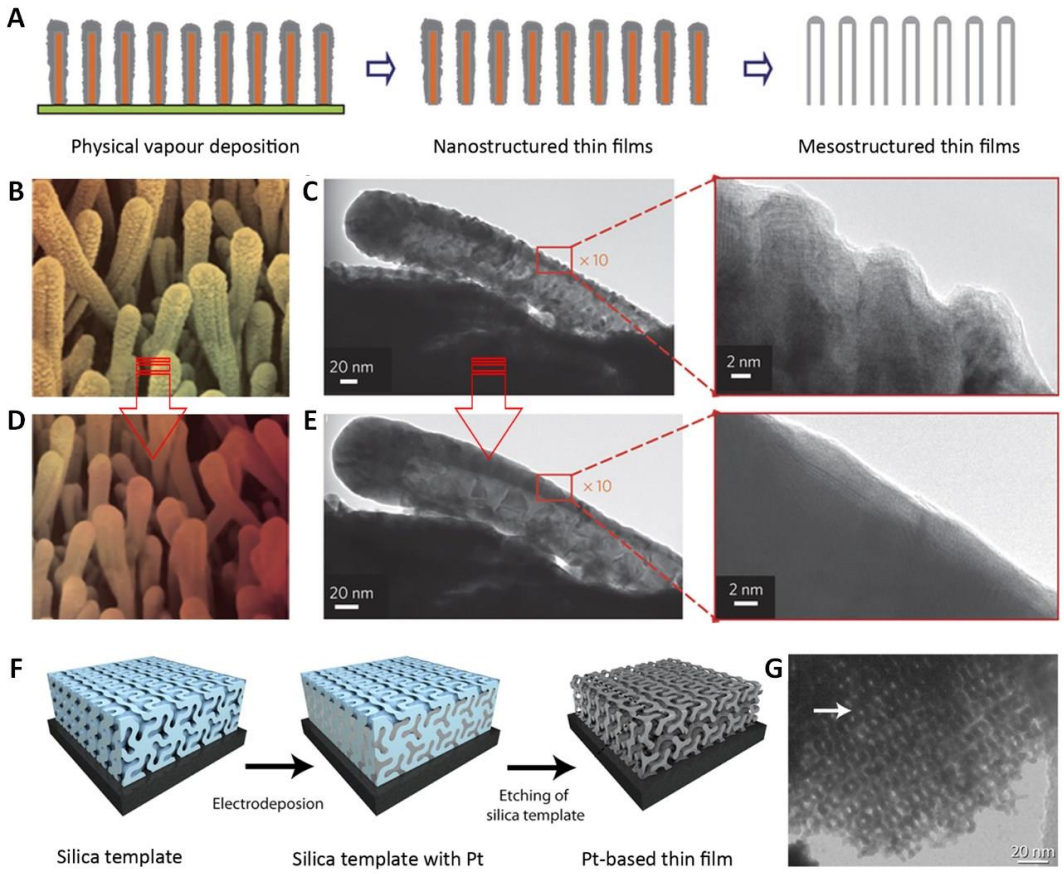

Figure 2.10 (A) Schematic illustration of the preparation of NSTFs and their transformation to MSTFs. High-resolution SEM images of (B) NSTF and (D) MSTF. In situ TEM analysis during the transformation from (C) NSTF to (E) MSTF by annealing at 400°C in reductive atmosphere. Reproduced with permission.[75] Copyright 2012, Nature Publishing Group. (F) Schematic synthesis procedure for Pt or Pt-alloy mesoporous double gyroid thin films by electrodeposition on a silica template. Reproduced with permission.[78] Copyright 2016, Elsevier. (G) TEM image of the Pt mesoporous double gyroid thin film. Reproduced with permission.[77] Copyright 2012, American Chemical Society.

2.5.1.3 Template-derived Pt-based Nanostructures with Controlled Morphology

In addition to the thin film approaches introduced above, other template methods have been applied to prepare nano-sized Pt-based architectures with porous, hollow or core-shell structures.[79, 80] When used as electrocatalysts, these Pt-based nanostructures with relatively large diameters (about 50 nm to 100 nm) and extended surfaces frequently eliminate the need for a carbon support and provide electronic conductivity and porosity by themselves. Well-established examples are the one-dimensional (1D) nanowires and nanotubes developed by the groups of Yan and Pivovar (as shown in Figure 2.11A-C,

taking Pt-Co nanowires as an example).[81] For instance, Pt and PtPd nanotubes were synthesized via galvanic replacement of Ag nanowire templates, exhibiting an outer diameter of 50 nm, a length of 5 - 20 μm and a thickness of 4 - 7 nm.[82] Because of their unique combination of dimensions at multiple length scales, these nanotubes can provide high surface area owing to their nano-sized wall thickness without the need for a carbon support, thus exhibiting an ORR mass activity twice higher than Pt black. Porosity was subsequently added on the wall of the Pt nanotubes, thereby increasing the Pt normalized surface area and mass activity for ORR.[83] By replacing subsurface Pt with Pd, Pd-Pt core-shell nanotubes with size similar to the Pt nanotubes discussed above, were also studied in an effort to improve the Pt utilization for ORR.[84] By optimizing the Pt coating, this core-shelled electrocatalyst exceeded the DOE mass activity target on a Pt-normalized basis. After that, Cu, Ni and Co nanowires have sequentially been explored as templates to prepare Pt-shell nanowire ORR electrocatalysts which incorporate activity enhancements due to their extended Pt surfaces and the transition-metal alloying effect.[85-87] Varying the amount of the Pt precursor during the galvanic replacement step of their synthesis allowed for the investigation of a wide range of compositions. Although these Pt-coated Cu/Ni/Co nanowires showed improved ORR activity and durability, it should be pointed out that the Pt-on-Co nanowire catalysts could feature low mechanical stability, because the Co nanowire 'core' is immediately etched upon exposure to acid, leaving only a Co-containing free-standing 'Pt shell' (nanotube) as the active catalyst material.[86] Recently, a follow-up study by the same group has showed that the Pt-Ni nanowires reached a maximum ORR performance after annealing at 200°C, due to the balancing of the initial activity and durability.[88]

Another example of unsupported 1D electrocatalysts are the PtFe ordered intermetallic nanotubes that are fabricated by coaxial nozzle electrospinning with separate core and shell solutions.[31] The core silica content in the as-spun nanofibers is subsequently removed by calcination in air, resulting in a recrystallization of the shell Fe/Pt contents into an intermetallic phase with an ordered face-centered tetragonal (fct) structure. The resulting fct PtFe nanotubes show an average outer diameter of ≈ 120 nm and 'infinite' length. This combination of multiple length scales allows discarding of the carbon support, and the material's anisotropic morphology is expected to improve mass transport and proton conductivity in the electrode.[31]

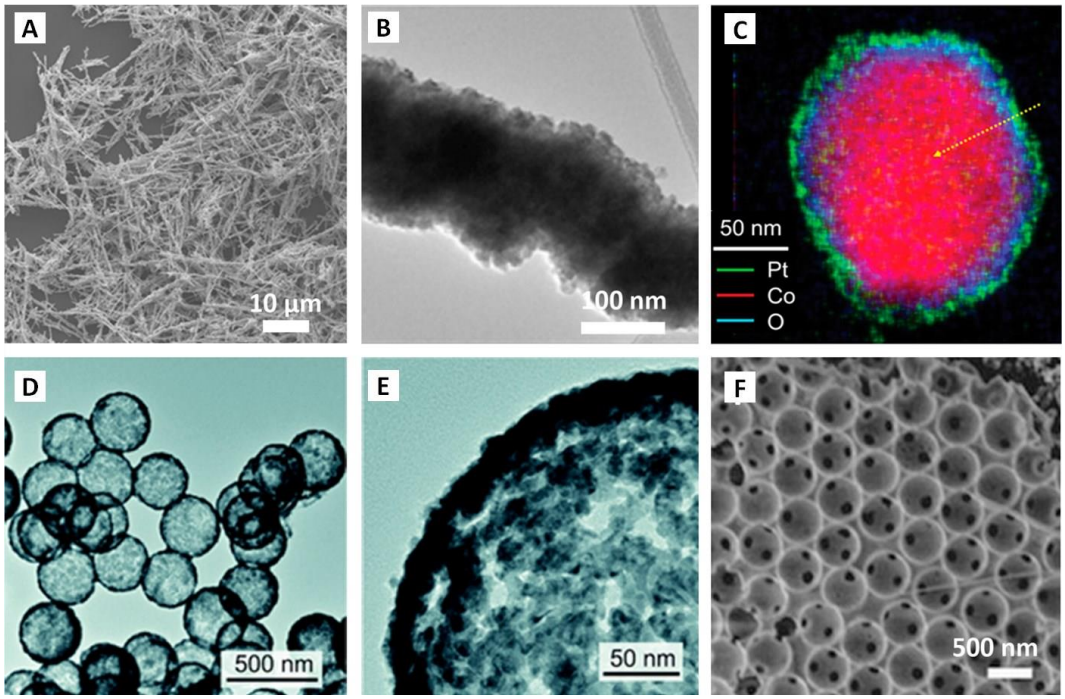

Figure 2.11 (A) SEM, (B) TEM and (C) energy-dispersive X-ray spectrum images of a cross-section of the Pt-coated Co nanowires. Reproduced with permission.[86] Copyright 2014, American Chemical Society. (D, E) TEM images of the connected Pt-Fe catalysts with a porous hollow capsule structure. Reproduced with permission.[89] Copyright 2015, Royal Society of Chemistry. (F) SEM image of an inverse-opal Pt electrode surface prepared by electrodeposition using a self-assembled polystyrene template. Reproduced with permission.[90] Copyright 2013, Nature Publishing Group.

In another report, surface-modified silica particles were employed to assemble Pt-Fe NPs, followed by dissolution of the silica template.[89] The resulting PtFe catalyst with a network structure consisting of porous and hollow capsules from interconnected nanoparticles exhibits a shell thickness and pore size of ≈ 10 nm and an outer diameter of ≈ 400 nm (Figure 2.11D-E). This unsupported catalyst enabled the formation of a thin cathode with a thickness of 1 - 1.5 µm, nearly one-fifth that of a conventional electrode implementing a carbon-supported catalyst (see section 2.5.2 for details).

Finally, ordered macroporous Pt electrodes with inverse opal structures were also applied as cathode catalysts in PEFCs.[90] The Pt inverse opal electrode was fabricated directly on thiol-modified GDLs by electrodeposition of the infiltrated Pt precursor, followed by removal of the self-assembled polystyrene template. The resulting electrode duplicated the hexagonal close-packed structure from the polystyrene beads, resulting in a periodic inverse opal structure with interconnected macropores and a large surface area and volume (Figure 2.11F). As demonstrated in a practical PEFC, the periodic Pt cathode

maintains an inverse opal structure entirely within the membrane electrode assembly and leads to a robust and integrated configuration of catalyst layers. Therefore, the periodic structured electrode minimizes the loss of catalyst materials and maintains an effective porosity, as well as an improved mass transfer and effective water management, owing to its morphological advantages.[90]

2.5.2 PEFC Test

Conventional CLs (see section 2.2.2) based on Pt-M/C catalysts are commonly prepared by processing the catalyst material into inks or pastes through addition of ionomer and water/alcohol, before applying these mixtures to either the membrane or GDL via spraying or coating techniques.[19] Naturally, similar processes were used for preparing CLs with unsupported Pt black catalysts from the 1950s until the 1980s; however the results obtained for this material will be discarded in this section due to the high loadings of ≈ 4 mg_{Pt}/cm^2_{geom} typically used in those studies.[19]

The first promising PEFC experiments with unsupported catalysts, however, were conducted on CLs that were prepared by electrodeposition or sputter deposition of Pt onto the GDL.[23] Yet due to the limited ECSAs of < 10 m^2/g_{Pt}, the fuel cell performance of the resulting gas diffusion electrodes (GDE) could not match that of conventional Pt/C systems; for a detailed summary of PEFC results on CLs prepared by sputtering the reader is referred to reference 23. In the following, examples of how researchers have achieved increased ECSA values and improved gas transport by increasing the CLs meso- and macroporosity will be presented.

Sievers et al. used an alternating sputtering approach of Pt and Co to create a CL matrix consisting of noble and non-noble metal domains.[91] The latter were mostly removed through dissolution during cell conditioning, leaving behind a mesoporous PtCo CL with improved mass-normalized performance at high current densities under H_2/air operation with respect to pure Pt CLs prepared by the same process. The macroporous Pt CLs with inverse opal structure on a GDL exhibit an ECSA amounting to 24 m^2/g_{Pt}, greatly exceeding the values of the first sputtered CLs.[90] The power densities in H_2/air operation surpassed those of conventional Pt/C systems, also owing to the unsupported CLs advantageous morphology, i.e. large void volume and interconnected macropores.

In addition, the NSTF catalysts feature ECSAs of up to 17 m^2/g_{Pt} since the target metal is sputtered on a vertically aligned surface of crystalline organic whiskers (for details on the

synthesis and characterization see section 2.5.1.2).[37] As NSTFs and their corresponding CLs are the most thoroughly investigated unsupported system up to date, they can serve as an instructive case study to highlight the challenges of optimizing CL, MEA and operation conditions. NSTF-based MEAs are prepared by hotpressing the Pt-M sputtered whiskers onto the membrane, decreasing the whisker-whisker spacing and embedding them up to ≈ 20 % of their length (0.5 µm) into the membrane. Under steady-state operation, NSTF catalysts have exceeded the performance of Pt/C electrodes, reaching inverse power densities of 0.16 g_{Pt}/kW and meeting the DOE's initial MA target of 0.44 A/mg_{Pt} at 0.9 vs. the reversible hydrogen electrode (V_{RHE}), as well as showing less than 40% activity loss after 30000 accelerated stress test cycles.[37, 92] Like the other systems mentioned above, NSTF CLs do not contain ionomer and rely on proton conduction via the extended Pt surface. However, since proton conductivity decreases significantly at low relative humidities,[40] implementation in an automotive PEFC stack would require a larger and expensive humidification system, which is an important disadvantage vs. Pt-M/C CLs.[93] Additionally, under wet conditions (RH ≈ 100 %) and temperatures below 60°C (occurring e.g. upon car start-up) NSTF cathode CLs have a propensity to flooding, restricting the access of reactants and leading to cell reversal.[37, 93, 94] These observations prove the need for an efficient water management to improve the operational robustness of such systems. Indeed, efforts to increase the proton conductivity and the water removal capability by coating the whiskers' surface with ionomer were undertaken, yielding only minor improvement in high current density performance,[94] possibly due to the simultaneous increase in O_2 mass transport resistance.[37] Further strategies to mitigate this challenges include a dispersed catalyst/NSTF hybrid electrode, in which a Pt/C interlayer between whiskers and GDL serves as water storage and removal buffer,[94] and water removal through the anode by using differential pressures and thinner membranes.[37]

Owing to the rapid progress in the synthesis of unsupported catalyst materials with well-defined and hierarchical structural motifs, researchers are now working on implementing these materials in PEFCs, also using the classic approach to prepare CLs introduced at the beginning of this section. Thereby, it is of utmost importance that the advantageous structure of the unsupported catalysts is not destroyed during its processing and can be transferred to the catalyst layers. Ultimately, this has to be investigated individually for different materials. However, in the studies cited in the following and the experiments of this thesis no changes of the materials' structures have been observed.

Recently, the group of Yamaguchi reported on the fuel cell performance of hollow PtFe alloy nanocapsule electrocatalysts.[36, 89] CLs (with a thickness of ≈ 1 µm) were prepared by dispersing the catalyst and Nafion ionomer (optimized ionomer-to-catalyst ratio ≈ 0.13) in a water/isopropanol mixture, followed by sonication and pulse spraying onto the membrane. Comparison of TEM images of the catalyst material before and after this processing step in references 36 and 89 indicates that the nanostructure is retained. Moreover, it was found that additional autoclaving of the ink for 24 h at 200°C leads to more uniform coverage and thinner ionomer films around the nanocapsules, correlating with significantly improved performance at high relative humidity (RH = 90 %) conditions. The authors explained this observation by the considerable swelling of the nonuniform, locally thick ionomer layers obtained without autoclaving at high RH conditions, which results in the blockage of the interspaces between the nanocapsules and limits oxygen diffusion. Further experiments indicated the presence of liquid water inside the CL under varying operation conditions, again highlighting the challenges of water removal and effective water management with such materials and thin CLs. Despite these shortcomings, the PtFe nanocapsule MEAs showed neither changes in the H_2/O_2 I/E curves nor ECSA loss after 10000 cycles of start-stop durability test (1.0 - 1.5 V_{RHE}, 500 mVs^{-1}), demonstrating the benefits of working with unsupported systems.[36, 89, 95]

Similar efforts have been undertaken by the group of Pivovar that works on the implementation of Pt-Ni nanowires (cf. section 2.5.1.3) in real PEFCs. First tests showed significantly reduced ORR activities and ECSA values with respect to rotating disk electrode (RDE) data (see section 3.5 for details on RDE),[96] which can be related to significant Ni dissolution from the catalyst during break-in and conditioning, leading to ionomer poisoning effects.[97-99] Such poisoning suppresses the ORR on the Pt surface through a reorientation of the polymer network and causes reduced proton transport that affects high current density performance.[100] Eventually, these shortcomings were mitigated by introducing two acid soaking steps of the MEA (15 hours, 0.01 M H_2SO_4, 20°C) in the multi-step cell activation process.[99, 101] MEAs treated in this way show reduced Ni content, improved high current density performance plus increased ECSA and ORR activities, albeit the latter two are still significantly lower than the respective values from RDE studies.[101] Although further research on proton transport, oxygen transport and the cell activation process is needed to trigger performance improvements, PtNi nanowire CLs have already displayed superior performance to Pt/C in start-stop durability tests.[99]

Another successful demonstration of unsupported electrocatalysts, fct Pt-Fe nanotubes, was incorporated into ionomer free CLs by the spraying technique.[31] Under the PEFC test conditions in H_2/O_2 and H_2/air recommended by the DOE,[95] the fct PtFe nanotubes showed maximum power densities comparable to Pt/C systems and superior durability under accelerated degradation test conditions (potential of 1.4 V for 3 hours).

As this chapter illustrates, the CL is an integral and complex part of the PEFC and optimizing the former is key to high device performance. Regarding the development of unsupported PEFC catalysts, many synthesis strategies and a great variety of materials have been reported in the literature (cf. section 2.5.1). Nonetheless, only few researchers implemented their novel catalysts in the PEFC and focused on the critical issue of catalyst layer optimization. The promising results in these rare studies (see above) demonstrate both the potential of unsupported catalysts and the need of greater research effort in this domain.

3 Methods and Experimental Techniques

3.1 Synthesis

Pt_xM (M = Ni or Cu) aerogels were synthesized according to the generic procedure described in Figure 3.1; details can be found in sections 4.3 and 5.3.1. In brief, Pt and M precursors were dissolved in ultrapure water and stirred until the mixing was complete. Subsequently, $NaBH_4$ solution was added while stirring vigorously to reduce the precursors. The obtained dispersion of Pt_xM nanoparticles was kept for about four days until black Pt_xM hydrogel formed at the bottom of the container. This hydrogel was washed with water multiple times and the solvent was exchanged with acetone afterwards. The resulting anhydrous gels were subjected to critical point drying in CO_2. All synthesis in this work was performed by L. Kühn (cf. declaration of individual contributions on page 10).

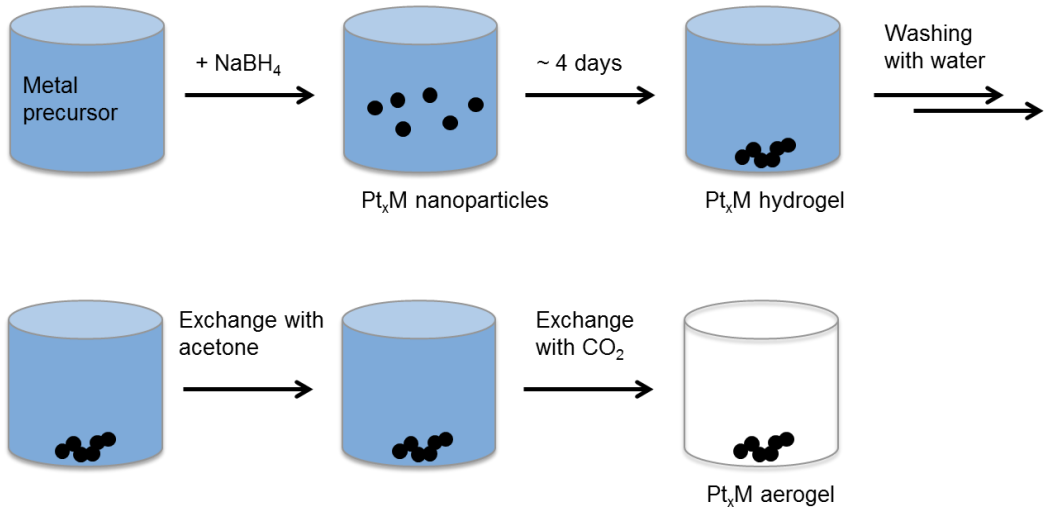

Figure 3.1 Generic synthesis outline for the bimetallic Pt_xM (M = Ni or Cu) aerogels discussed in this work.

3.2 X-ray Diffraction and X-ray Photoelectron Spectroscopy

X-ray diffraction (XRD) is employed to non-destructively characterize crystalline materials. It provides information on crystallinity, phases, preferred crystal orientation and chemical composition of the sample. The X-ray diffraction peaks result from constructive interference of a monochromatic X-ray beam that is scattered at the lattice planes of the investigated material. Interference occurs when the conditions of Bragg's law are met:[102]

$$n\lambda = 2d\sin\theta \quad (3.1)$$

where n is an integer, λ the wavelength of the incident X-ray beam, d the interplanar spacing responsible for the diffraction and θ the diffraction angle. In an XRD experiment, the sample is scanned through a range of 2θ angles in order to cover all potential diffraction directions. Subsequently, diffraction peaks are converted into d-spacings which, upon comparison to standard reference patterns, allows for identification of crystalline faces in the analyzed compound.

X-ray photoelectron spectroscopy (XPS) is a technique used to identify and quantify the elemental composition of the outer 5 - 10 nm of a solid surface and to reveal the chemical environment of the elements.[103, 104] For this purpose, the sample is typically irradiated with monoenergetic X-rays from an aluminum or magnesium Kα source which causes the emission of photoelectrons. Subsequently, the kinetic energy E_{kin} of the emitted photoelectrons is measured which allows for the calculation of the electron binding energy E_b by:

$$E_{kin} = h\nu - E_B - \phi_s \quad (3.2)$$

where hν is the energy of the incident X-ray and ϕ_s is the spectrometer work function that accounts for the minimum energy necessary to remove an electron from the instrument.[103] As each element has a characteristic set of binding energies for the different electron energy levels in the atom, elements can be identified by comparison to known standards or literature values. Additionally, the chemical state of the elements can be deduced from small deviations in the binding energies.

3.3 X-ray Absorption Spectroscopy

3.3.1 Basics

X-ray absorption spectroscopy (XAS) can provide information about the local electronic and geometric structure of the investigated sample. When irradiated with hard X-rays, the atoms in the sample can absorb the X-ray and a core-level electron is emitted as a photo-electron. The absorption process can be analyzed by measuring the transmission of the X-rays through the sample:

$$I = I_0 e^{-\mu(E)t} \quad (3.3)$$

where I_0 and I are the X-rays intensities before and after the sample, μ(E) the X-ray energy dependent absorption coefficient and t the sample thickness, respectively.[105] The absorption coefficient μ(E) increases sharply when the X-ray energy exceeds the absorption energy E_0 of the respective material and core-level electrons are promoted to the continuum. The emitted photo-electron can scatter from the neighboring atoms in the sample and return to the absorbing central atom. This leads to an energy-dependent self-interference effect of the photo-electron, changing the absorption probability at the central atom and causing oscillations of μ(E).

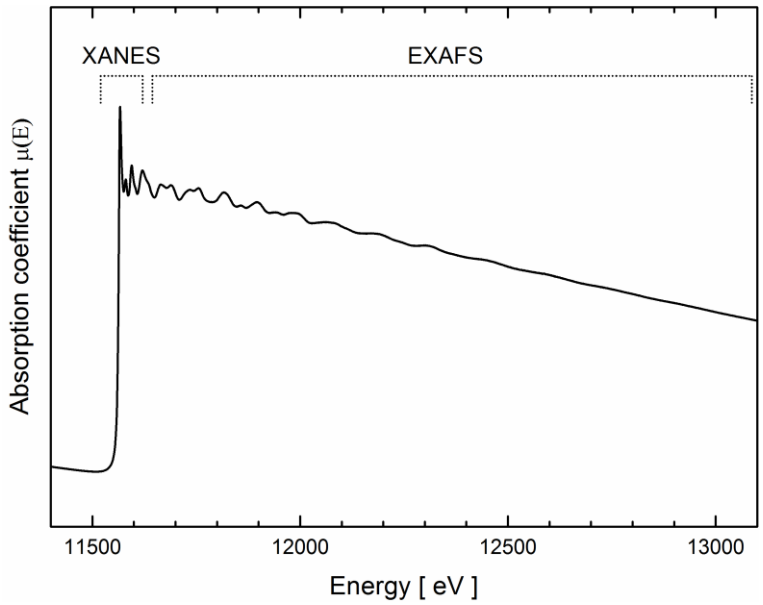

Figure 3.2 X-ray absorption spectrum of a Pt foil at the at the Pt L_3 absorption edge (11564 eV). The dotted brackets indicate the energy range of XANES and EXAFS regions, respectively.

X-ray absorption spectroscopy can be broken down into two regimes, X-ray absorption near-edge spectroscopy (XANES, $E_0 - 50$ eV < E < $E_0 + 50$ eV) and extended X-ray absorption fine structure (EXAFS, E > E_0 + 50 eV) as illustrated in Figure 3.2. Analysis of the former XANES can provide information about oxidation state and coordination chemistry.[106, 107] An increase of the former oxidation state becomes apparent as a shift of the absorption energy E_0 to higher energies concomitant with an increase in the white line intensity i.e. the first main peak above the absorption edge.[108] The latter effect is caused by an increased number of unoccupied electronic states which augments the X-ray absorption probability.[109] From analysis of the EXFAS, the coordination number of the central absorbing atom and interatomic distances to neighboring atoms can be determined as will be shown in the following.

3.3.2 Data Treatment

Following the conversion of the measured intensities into μ(E), a smooth pre-edge function is subtracted to account for instrumental background and absorption form other edges (i.e. other atoms in the sample). Next, a post-edge background function $\mu_0(E)$ that corresponds to the absorption of a free atom is subtracted and μ(E) is normalized to the magnitude of the edge step $\Delta\mu_0(E_0)$. The resulting isolated EXAFS spectrum χ(E) is defined as

$$\chi(E) = \frac{\mu(E) - \mu_0(E)}{\Delta\mu_0(E_0)} \tag{3.4}$$

and typically expressed in terms of the photoelectron wavenumber k rather than energy as χ(k) with

$$k = \sqrt{\frac{2m_e(E - E_0)}{\hbar^2}} \tag{3.5}$$

where m_e is the electron mass and ħ the reduced Planck constant.[105]

The isolated EXAFS spectrum χ(k) is subsequently fitted to the EXAFS equation

$$\chi(k) = \sum_{j=1}^{shells} \frac{N_j S_0^2 f_j(k) e^{-2k^2\sigma_j^2} e^{-2R_j/\lambda(k)}}{kR_j^2} \sin[2kR_j + \delta_j(k)] \tag{3.6}$$

where N_j is the number of atoms of type j at the distance R_j from the central absorbing atoms, S_0^2 the amplitude reduction term due the relaxation process after photoionization, $f_j(k)$ the backscattering amplitude, $\delta_j(k)$ the backscattering phase shift, λ(k) the mean free path of the electron and σ_j^2 the relative mean square disorder of the distance R_j due to thermal and static motions.[105, 110] The terms $e^{-2k^2\sigma_j^2}$ and $e^{-2R_j/\lambda(k)}$ account for the finite lifetime of the excited state and inelastic scattering, respectively.[106] Fitting the data to the EXAFS equation to obtain a structural model (i.e. bond lengths and coordination numbers) requires chemical knowledge of the sample since the backscattering amplitude $f_j(k)$, phase shift $\delta_j(k)$, amplitude reduction term S_0^2 and mean free electron path λ(k) need to be obtained from reference compounds or have to be calculated theoretically.

3.4 Focused Ion Beam - Scanning Electron Microscopy Tomography

To obtain a three dimensional image of the catalyst layer, i.e. the morphology of solid and pores, FIB-SEM tomography was used. In brief, this is a serial sectioning technique, in which a thin layer of e.g. the CL is first removed with a focused ion beam, followed by the

recording of a scanning electron microscopy image. Upon multifold repetition, a stack of 2D images is obtained and used for three dimensional reconstruction.

The samples for FIB-SEM tomography were prepared by spraying the catalyst ink onto either a GDL (Sigracet GDL 25 BC) or a gold foil to have a substrate with high electronic conductivity. Subsequently, they were attached to SEM stubs by conductive carbon tapes and, if needed, silver paint was applied to further increase conductivity. Next, the specimen were transferred to a Zeiss NVision 40 microscope with a Ga^+ beam source and the area of interest on the catalyst layer was covered with a smooth carbon and platinum layer (≈ 200 nm each) to avoid curtain effects.[48] Prior to serial sectioning, a cuboid-shaped structure (see Figure 3.3) was prepared with the focused ion beam to create space for the removal of material.

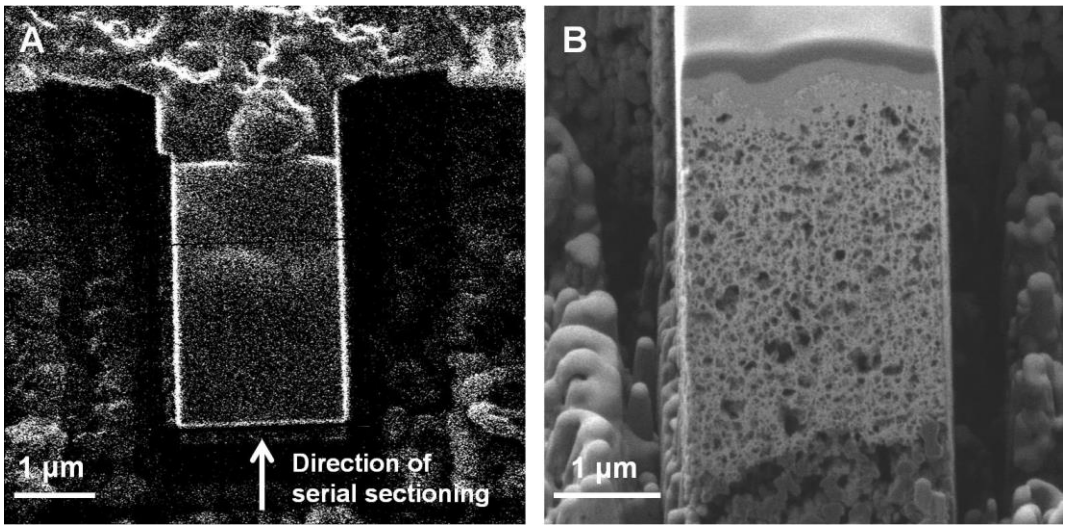

Figure 3.3 Top-view FIB (A) and side-view SEM image (B) of the cuboid shaped structure in the catalyst layer.

The serial sectioning was performed at an acceleration voltage of 30 kV (beam current of 10 pA) for the Ga^+ beam while setting a slice thickness of ≈ 5 nm. The accuracy of the slice thickness was confirmed after the measurement by dividing the cut length by the number of slices. For each section, SEM images at a magnification of ≈ 14000 and an acceleration voltage of 1 kV were recorded with a secondary (SE) and energy selective backscattered electron (ESB) detector. The reconstruction of the three dimensional structure is described in section 6.5.1.

3.5 Electrochemical Characterization in Liquid Electrolyte Half Cells

3.5.1 ORR Activities

The electrochemical activities of ORR catalysts were studied in liquid half cells using the thin-film rotating disk electrode (RDE) technique.[35, 111] To prepare the catalyst for characterization, it was dispersed in a mixture of water and alcohol by ultrasonic treatment and drop-casted atop a glassy carbon disk embedded in polytetrafluoroethylene (PTFE) that serves as the working electrode (WE) in the experiment. The catalyst loadings are generally very low (< 100 µg/cm^2_{disk}) to obtain thin films < 1 µm which avoids reactant concentration gradients within this layer.[35] Optimization of the ink composition and drying process is crucial to obtain smooth thin films that are paramount for reliable results.[112, 113]

Working electrodes obtained in the way described above were subsequently attached to a rotatable shaft and immersed into a glass cell filled with electrolyte (see Figure 3.4) that was saturated with O_2 gas. To complement the electrochemical three electrode setup, a counter and reference electrode were connected to the main electrode compartment. Rotating the working electrode creates a uniform, laminar flow across the surface which allows for precise control of the mass transport to the catalyst thin film. The corresponding limiting current density i_{lim} follows an equation developed by Levich[114]

$$i_{lim} = 0.62nFD^{2/3}\upsilon^{-1/6}\omega^{1/2}c_0 \tag{3.7}$$

where n is the number of transferred electrons (4 per O_2 molecule), F the Faraday constant (96485 C/mol), D the diffusion coefficient of O_2 in the electrolyte, v the kinematic viscosity of the electrolyte, ω the angular frequency and c_0 the bulk concentration of O_2 in the electrolyte.

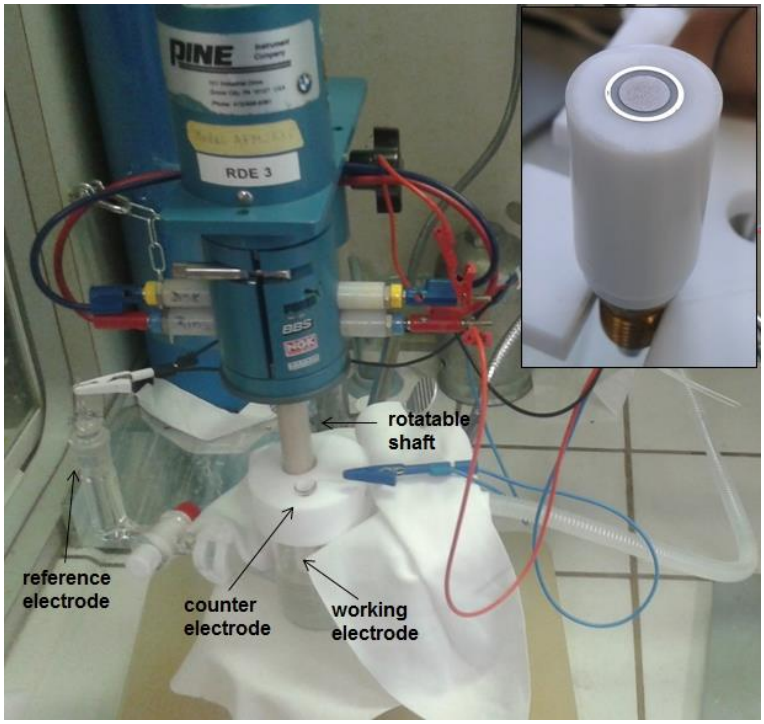

Figure 3.4 Three electrode glass cell setup in rotating disk electrode configuration. The inset shows a working electrode (see text above) from Pine Research Instrumentation Inc.

Figure 3.5 illustrates the dependence of the limiting current density on the rotation speed in rounds per minute (rpm) and highlights three different regions in the voltammogram. At potentials < 0.7 V_{RHE}, the current density is controlled by the mass transport to the electrode surface. Above 0.7 V_{RHE} exists a region of mixed control by mass transport and ORR kinetics (i.e. the rate constant of the electron transfer). The effect of mass transport becomes negligible at minor current densities for which true kinetic currents can be measured. To extend the potential range in which ORR kinetics can be investigated, measured current densities i were converted to kinetic current densities i_{kin} by applying the Koutecky-Levich equation under the assumption of first order reaction kinetics with respect to the O_2 concentration[115]

$$\frac{1}{i} = \frac{1}{i_{kin}} + \frac{1}{i_{lim}} = \frac{1}{i_{kin}} + \frac{1}{0.62nFD^{2/3}\upsilon^{-1/6}\omega^{1/2}c_0} \tag{3.8}$$

Lastly, the measured potential (E_m) was corrected for the high frequency resistance between reference and working electrode (R_Ω) and the kinetic current density at a given potential can be extracted (i.e. $E_{R\text{-}corr.} = E_m - i\,R_\Omega$). It is customary to compare the kinetic currents at 0.9 V_{RHE} (derived from experiments at a rotation speed of 1600 rpm) after normalization to the mass of noble metal on the WE.[35, 113, 116]

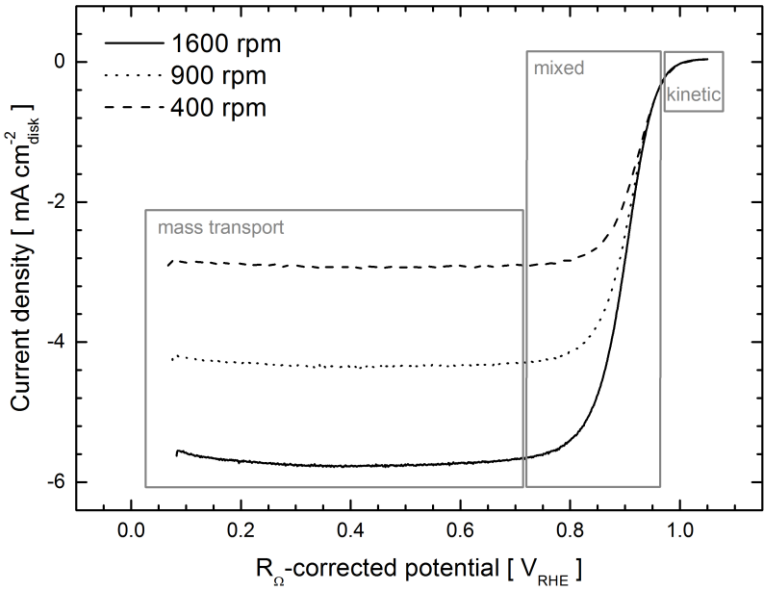

Figure 3.5 Anodic ORR polarization curves at different rotation speeds and at a scan rate of 5 mVs^{-1} for a commercial Pt/C catalyst (30 wt. % Pt, E-TEK) in O_2-saturated 0.1 M $HClO_4$ electrolyte. The polarization curves can be divided into three parts, in which the current density is either controlled by mass transport ('mass transport'), mass transport and ORR kinetics ('mixed'), or ORR kinetics ('kinetic'), respectively.

3.5.2 Electrochemical Surface Area

The setup described above can likewise be used to determine the ECSA (in m^2/g_{Pt}) of catalysts by cyclic voltammetry. For Pt-based catalyst, this is commonly achieved by evaluating the charge associated to the hydrogen underpotential deposition (H_{upd}: $H_{ads} \rightarrow H^+ + e^-$) by integrating the current between 0.05 V_{RHE} and 0.4 V_{RHE} after subtracting the double layer current contribution.[111, 117] Dividing this charge by the conversion factor 210 $\mu C/cm^2_{Pt}$[117] and the catalyst loading L (g_{Pt}/electrode) yields

$$\mathrm{ECSA} = \frac{\mathrm{Q}^{\mathrm{Hupd}}_{\mathrm{DL-corrected}}}{210\ \mu\mathrm{C\ cm}^{-2}_{\mathrm{Pt}}\ L\ 10^4} = \frac{\frac{1}{\upsilon}\int(\mathrm{i} - \mathrm{i}_{\mathrm{DL}})\mathrm{dE}}{210\ \mu\mathrm{C\ cm}^{-2}_{\mathrm{Pt}}\ L\ 10^4} \tag{3.9}$$

where $Q_{DL\text{-}corrected}$ refers to the double layer corrected charge of the H_{upd} peaks (in µC), v to the scan rate of the cyclic voltammetry, i and i_{DL} to the current and current in the double-layer region at 0.4 V_{RHE} respectively. Figure 3.6 displays the cyclic voltammogramm (CV) of a commercial Pt/C catalyst in which the double layer current and H_{upd} charge are highlighted.

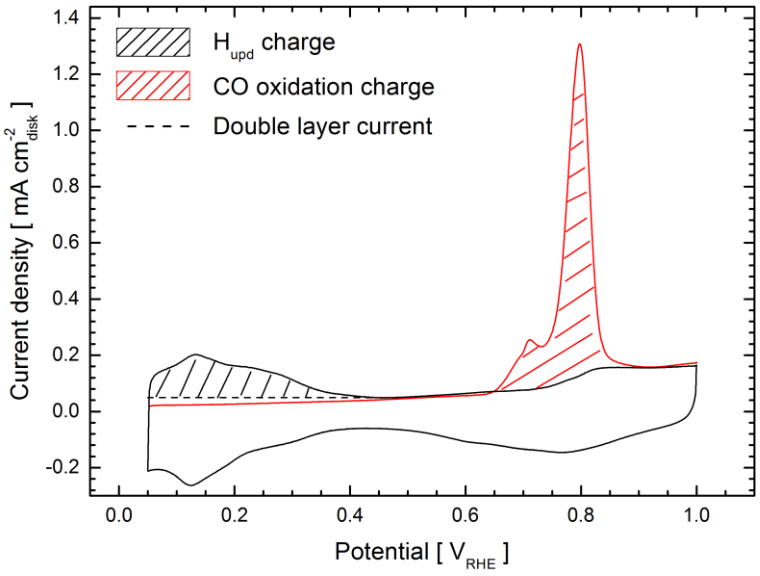

Figure 3.6 CV of a commercial Pt/C catalyst (30 wt. % Pt, E-TEK) in N_2-saturated 0.1 M $HClO_4$ electrolyte at a scan rate of 20 mVs^{-1}. Note that the red curve corresponds to a CV recorded in the course of a CO stripping experiment as described below. Black and red shaded areas highlight H_{upd} and CO oxidation charges, respectively.

Since the H_{upd} method relies on the adsorption/reduction of protons from the electrolyte to form a monolayer of hydrogen on the Pt surface that can be oxidized during the anodic potential sweep, it is very sensitive to changes in the H-adsorption behavior of the catalyst surface.[118] Thus, to avoid errors in ECSA estimation, the catalyst surface is often additionally probed by carbon monoxide (CO) that can adsorb on the Pt surface and be removed by electrochemical oxidation ($CO_{ads} + H_2O \rightarrow CO_2 + 2H^+ + 2e^-$). For this CO stripping experiment, the electrolyte was first purged with CO gas while the electrode was held at a constant potential of 0.1 V_{RHE} at which the Pt surface gets covered by a CO monolayer.[111, 119] Next, the electrolyte was purged with N_2 gas to remove the CO gas, followed by the oxidation of pre-adsorbed CO by a single anodic potential sweep (see red curve in Figure 3.6; current $i_{anodic,1}$ in equation (3.10)). The charge associated to CO oxidation was obtained by subtracting the anodic sweep of a subsequent CV (cf. black curve in Figure 3.6; current $i_{anodic,2}$ in equation (3.10)) to account for double layer and oxide formation currents. As CO oxidation is a 2-electron process, the conversion factor is 420 $\mu C/cm^2_{Pt}$,[119] i.e. twice the one for the H_{upd} method.

$$\mathrm{ECSA} = \frac{\mathrm{Q}_{\mathrm{net}}^{\mathrm{CO\ oxidation}}}{420\ \mu\mathrm{C\ cm}_{\mathrm{Pt}}^{-2}\ L\ 10^4} = \frac{\frac{1}{\upsilon}\int\left(\mathrm{i}_{\mathrm{anodic},1} - \mathrm{i}_{\mathrm{anodic},2}\right)\mathrm{dE}}{420\ \mu\mathrm{C\ cm}_{\mathrm{Pt}}^{-2}\ L\ 10^4} \qquad (3.10)$$

3.6 Experiments in Differential PEFC

3.6.1 Preparation of Catalyst Coated Membranes

In the first step to prepare catalyst coated membranes (CCMs), a Nafion XL-100 membrane (DuPont) was cut into rectangles (2.6 cm x 1.6 cm) with flattened corners using a customized punching tool. Next, the backing film and cover sheet were removed from the cut membrane and the mass of the latter was determined with a microbalance. Subsequently, it was soaked in ultrapure water (18.2 MΩ cm, Elga Purelab Ultra) and fixed taut in a spraying frame with a 1 cm^2 cutout as shown in Figure 3.7A to remove any membrane wrinkling. In the meantime, the catalyst was processed into inks according to the procedures described in sections 6.5.1 and 7.3.

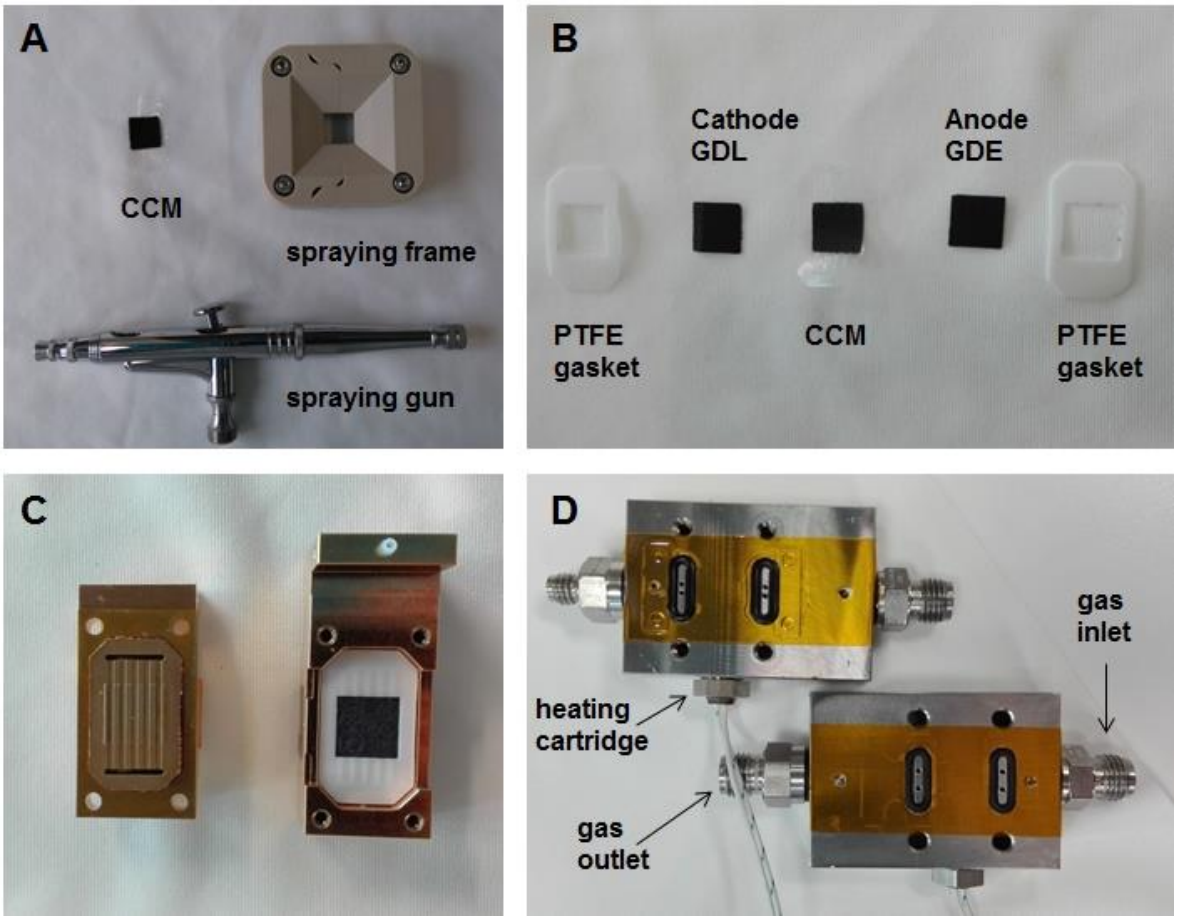

Figure 3.7 (A) Airbrush spraying gun, spraying frame and CCM after the spraying step. (B) Components of the MEA: PTFE gasket, cathode GDL, CCM, anode GDE and PTFE gasket (from left to right). (C) Top and bottom part of differential fuel cell. (D) End plates including gas inlet/outlet and heating cartridges.

Afterwards, the catalyst ink was sprayed onto the membrane with an airbrush spraying gun (HP-410, Conrad Electronics AG, cf. Figure 3.7A) at an air pressure of 1.2 bar_{abs}. During this step, the spraying frame was periodically turned by 90° to achieve a more uniform distribution of the catalyst in the active area of 1 cm^2. After drying the sample for a couple of hours, the mass was again determined on a microbalance and the mass difference was calculated. Due to the significant mass change of Nafion membranes upon the varying relative humidities in the environment (e.g. between first and second weighing), the obtained mass difference can yield inaccurate catalyst loadings. To mitigate this issue, the mass of the Nafion membrane at the second weighing was corrected by the relative weight change of a reference Nafion membrane that was weighted at the same times as the processed membrane. Subsequent steps of MEA preparation are described in sections 6.5.1 and 7.3.

3.6.2 Differential PEFC

The PEFC performance of MEAs is commonly assessed by recording polarization or I/E curves. Naturally, drawing conclusions from such experiments can become challenging when working with complex systems in which multiple effects are superimposed.

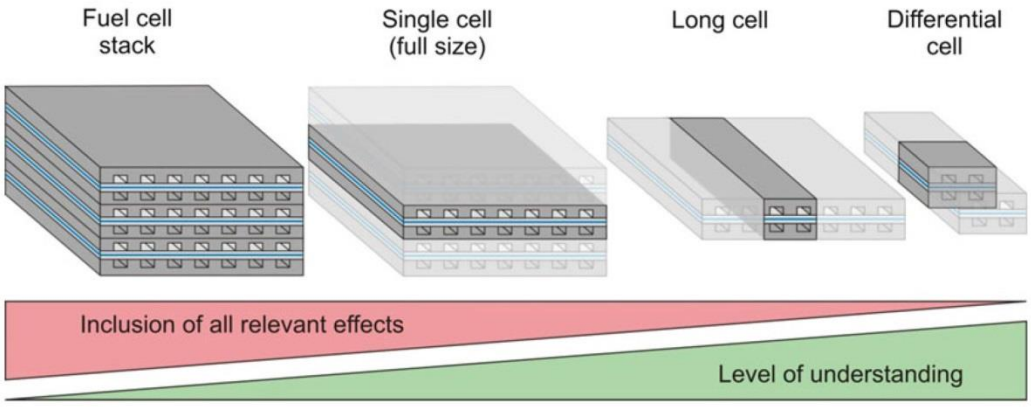

Figure 3.8 Scheme of downscaling possibilities for PEFC experiments to increase the level of understanding. Reproduced with permission.[120] Copyright 2014, Springer.

As illustrated in Figure 3.8, a full-size stack has the greatest relevance for real operation, however the analysis possibilities of the catalyst layers properties (e.g. mass transport) are limited due to cell-to-cell and channel-to-channel distribution of the gas flow.[120] On the other hand, the use of a differential PEFC allows an investigation of CLs under homogeneous, well-defined conditions in the absence of along-the-channel effects such as changing temperature, relative humidity and gas concentration.[121] The cell used in this

study (see Figure 3.7C) was developed by Oberholzer and coworkers[122] and features five channels/ribs of 1 mm width and 0.55 mm depth at an active area of 1 cm^2. The cell is made from aluminum and was coated with a thin gold layer to mitigate corrosion. A defined GDL compression (25 %) was achieved by employing a set of steel spacers between top and bottom part and the cell sealing was provided by two 350 µm thick PTFE gaskets (see Figure 3.7B). The differential fuel cell was placed between two endplates (see Figure 3.7D) that provide gas inlet/outlet and temperature control of the system. Experiments were performed on an in-house built test bench, whereby potential and current were controlled by a Biologic VSP-300 potentiostat with a 10A/5V current booster in combination with the EC-Lab® V11.01 software package.

3.6.3 Quantification of Voltage Loss Contributions

As introduced in section 2.1, three major overpotentials cause the deviation of the cell potential from the thermodynamic potential. In this work, the ohmic voltage losses η_{IR} were obtained from electrochemical impedance spectroscopy measurements as it will be shown later in sections 6.5.1 and 6.5.3. In brief, the high frequency resistance R_Ω in impedance spectra recorded during polarization curves can account for the sum of bulk electronic resistance R_{elec}, contact resistance R_{con}, and membrane proton resistance R_{ion} (i.e. $R_\Omega = R_{elec} + R_{con} + R_{ion}$), while the effective proton resistance in the catalyst layers R_{H+} was derived from electrochemical impedance measurements in H_2/N_2 condition. Next, the activation overpotential η_{act} (equivalent to η_{ORR}) can be computed from the η_{IR}-free potential at low current densities (≤ 0.1 mA/cm^2_{MEA}) at which mass transport contributions are negligible (i.e. $\eta_{tx} \approx 0$). This data range displays the logarithmic relation between potential and current density expected from the Butler Volmer equation ($\eta_{ORR} \propto \log(i)$), and can therefore be used to calculate η_{ORR} at various current densities. Lastly, the mass transport overpotential η_{tx} constitutes the remaining difference between the thermodynamic and cell potential after all other overpotentials have been accounted for.

4 Synthesis and Characterization of Pt-Ni Aerogel Catalysts

4.1 Pt-Ni Aerogels as Unsupported Electrocatalysts for the Oxygen Reduction Reaction

Pursuing the goal outlined in chapter 1 to investigate unsupported Pt-alloy catalysts for the ORR, in this chapter a novel synthesis route for the preparation of Pt-Ni aerogels with different Ni content is presented, followed by a systematic study of the materials' composition, structure and ORR activity. First, it is demonstrated by TEM and N_2-physisorption measurements that the synthesized catalysts indeed exhibit an aerogel structure. Next, the effect of Ni content (Pt_3Ni vs. $Pt_{1.5}Ni$) on the aerogel's properties is explored by XRD, XPS, XANES and EXAFS analyses. Subsequently, these findings are confirmed by in-situ electrochemical experiments in alkaline electrolyte. The study concludes by comparing the ORR activity of Pt-Ni aerogels to a commercial Pt/C benchmark and DOE targets.

Pt-Ni Aerogels as Unsupported Electrocatalysts for the Oxygen Reduction Reaction

Sebastian Henning[a,‡], Laura Kühn[b,‡], Juan Herranz[a], Julien Durst[a], Tobias Binninger[a], Maarten Nachtegaal[c], Matthias Werheid[b], Wei Liu[b], Marion Adam[e], Stefan Kaskel[e], Alexander Eychmüller[b] and Thomas J. Schmidt[a,e]

[a]Electrochemistry Laboratory, Paul Scherrer Institut, 5232 Villigen, Switzerland

[b]Physical Chemistry, Technische Universität Dresden, Bergstr. 66b, 01062 Dresden, Germany

[c]Paul Scherrer Institut, 5232 Villigen, Switzerland

[d]Chair of Inorganic Chemistry I, Technische Universität Dresden, Bergstr. 66, 01062 Dresden, Germany

[e]Laboratory of Physical Chemistry, ETH Zurich, 8093 Zurich, Switzerland

[‡]These authors contributed equally

ABSTRACT

The commercial feasibility of polymer electrolyte fuel cells passes by the development of Pt-based, O_2-reduction catalysts with greater activities and/or lower Pt-contents, as well as an improved stability. In an effort to tackle these requirements, unsupported bimetallic Pt-Ni nanoparticles interconnected in the shape of nanochain networks (aerogels) were synthesized using a simple one-step reduction and gel formation process in aqueous solution. The products of this novel synthetic route were characterized by X-ray absorption spectroscopy to elucidate the materials' structure. Using electrochemical experiments, we probed the surface composition of the as-synthesized aerogels and of equivalent materials exposed to acid, and concluded that a Ni-(hydr)oxide side phase is present in the aerogel with a larger Ni-concentration. Regardless of this initial surface composition, the Pt-Ni aerogels feature a ≈ 3-fold increase of surface-specific ORR activity when compared to a commercial platinum-on-carbon catalyst, reaching the mass-specific requirement for application in automotive PEFCs.

Published in *J. Electrochem. Soc.*, **163**, F998 (2016).

4.2 Introduction

State-of-the-art polymer electrolyte fuel cells require large amounts of carbon supported platinum nanoparticle catalysts (≈ 0.4 mg_{Pt}/cm^2_{geom})[5] to account for the large overpotential of the oxygen reduction reaction. Thus, Pt contributes significantly to the fuel cell system cost, and progress to reduce its loading is crucial to meet the long-term PEFC cost target of 40 $/kW set by the U.S. Department of Energy.[95] One approach to reduce this excessive Pt-loading relies on increasing the catalysts' ORR activity, e.g. by alloying platinum with other metals like Ni, Cu and Co, to form materials which show up to one order of magnitude higher mass-specific activity than commercial Pt/C catalysts.[6] On the other hand, these carbon-supported materials suffer from significant carbon- and Pt-corrosion during the standard operation of PEFCs, gradually compromising their efficiency and reliability.[24] To partially overcome stability issues, research focuses on unsupported materials (e.g. Pt-coated Ni, Co or Cu nanowires[86, 87, 123]) besides extended metal surfaces (e.g. 3M® nanostructured thin film catalysts[71]) or alternative supports (e.g. conductive metal oxides[33, 124-126]). Naturally, those materials should be processable into catalytic layer architectures that provide reactant and product diffusion pathways similar to those in conventional Pt/C electrodes to guarantee high catalyst utilization and PEFC performance.[127]

To meet the requirements mentioned above, unsupported bimetallic electrocatalysts with high surface area (up to ≈ 80 m^2/g_{metal}) and nanochain network structure, referred to as aerogels, have been synthesized.[49, 59, 128] The synthetic routes to prepare such materials vary, but generally involve the use of stabilizing surfactants and/or organic solvents[129-131] that can poison the catalyst's surface and decrease its activity. In contrast to those approaches, our groups have developed a facile one-step synthesis for mono- and bimetallic aerogels based on the reduction of metal salts by $NaBH_4$ in aqueous solution without addition of stabilizing surfactants.[51]

On the basis of previous work on Pt-Pd alloy aerogels prepared with the aforementioned method,[51] we have adapted our synthetic approach to the combination of a noble and a non-noble metal, targeting a reduced noble metal content while maintaining a high ORR activity. As we will demonstrate in this article, the combination of Pt and Ni yielded materials with a mass-specific ORR activity ≈ 2-fold higher than that of a commercial Pt/C catalyst and that reaches the DOE target for automotive PEFC application.[3]

4.3 Experimental

Pt-Ni hydrogels were prepared by a simple co-reduction route in aqueous solution under ambient conditions (room temperature, air). Briefly, Pt and Ni precursors were dissolved in water (18.2 MΩ cm, Millipore) in the Pt^{4+}:Ni^{2+} molar proportions required to reach the targeted Pt:Ni ratio, and reduced by $NaBH_4$. Selecting the synthesis of Pt_3Ni hydrogel as an example, 585 µL of a 0.205 M H_2PtCl_6 solution (8 wt. % in H_2O, Sigma Aldrich) [final reactant concentration 0.15 mM] and 4 ml of a freshly prepared 10 mM $NiCl_2$ solution ($NiCl_2$*$6H_2O$ 99 %, Sigma Aldrich) [final reactant concentration 0.05 mM] were dissolved in 790 ml water and stirred until mixing was complete. Subsequently, 7.0 ml of a freshly prepared 0.1 M $NaBH_4$ solution (granular, 99.99 %, Sigma Aldrich) [c(Pt^{4+} + Ni^{2+}):c($NaBH_4$)=1:1.25] were added under vigorous stirring. Upon addition of $NaBH_4$, the color of the solution turned immediately from light yellow to dark brown. The solution was kept stirring for another 30 min. Afterwards, the reaction solution was divided and transferred to 100 ml vials. After about four days, black Pt_xNi hydrogel was formed at the bottom of the containers. The hydrogel parts obtained from the same synthesis were collected in a small vial and washed with water. For this, half of the supernatant was removed and replaced cautiously with fresh water. This step was repeated six times. Afterwards, the solvent was exchanged stepwise with acetone. Again, half of the supernatant was removed and replaced by acetone. This step was repeated 11 times. The resulting anhydrous gels were transferred to a critical point dryer (Critical Point Dryer 13200J-AB, SPI Supplies) operating with CO_2.

XAS spectra at the Pt L_3 and Ni K edges were recorded at the SuperXAS beamline of the Swiss Light Source (Paul Scherrer Institut, Villigen, Switzerland), whereby the monochromator energy was calibrated using Pt and Ni foils, respectively. Measurements were performed ex-situ in transmission mode on pouch bags made from conductive Kapton® tape that were filled with aerogel powder. The quick-EXAFS (QEXAFS) method was used to increase time resolution;[132] 100 and 600 quick-XAS spectra were recorded at the Pt L_3 and Ni K edges, respectively. These XAS data were first analyzed with the JAQ analyzer software which allows averaging of individual XAS spectra into a single spectrum. Subsequently, Athena of the Demeter software package was used for normalization and background subtraction.[110] The fit of the EXAFS oscillations was performed with Artemis[110] using a face centered cubic Pt-Ni structure for the paths description. Amplitude reduction terms were calculated from EXAFS fits of Pt and Ni reference foils assuming a coordination number of 12 and amounted to $S_{0,Ni}^2$ = 0.97 and $S_{0,Pt}^2$ = 0.85, respectively.

Electrolyte solutions were prepared from $NaOH \cdot H_2O$ pellets (99.995% purity, TraceSELECT, Sigma Aldrich) or 60% $HClO_4$ (Kanto Chemical Co., Inc.) diluted in ultrapure water (18.2 MΩ cm, Elga Purelab Ultra). High purity N_2 (5.0), O_2 (5.0) and CO (4.7) were purchased from Messer AG, Switzerland. The benchmark catalyst for this study is a Pt/Vulcan XC-72 electrocatalyst with a Pt weight fraction of 30 % purchased from E-TEK Inc. (Lot# C0160311). The electrochemical measurements in acid were performed in a house-made three electrode glass cell. A reversible hydrogen electrode was connected to the main cell compartment through a Luggin cappilary, and a gold mesh (99,99 % metals basis, Alfa Aesar) held in a separate tube in contact with the main cell served as counter electrode. The working electrode was a PTFE-made, interchangeable rotating ring-disk electrode (Pine Research Instrumentation) equipped with a Pt-ring and a mirror-polished, glassy carbon disk insert (5 mm diameter, HTW Hochtemperatur-Werkstoffe GmbH). Before the measurements, the WE was mounted to a polyetheretherketone shaft that was attached to a modulated speed rotator (both Pine Research Instrumentation). A Biologic VSP-300 was used as potentiostat, in combination with the EC-Lab® V10.44 software package. The ohmic drop was determined by electrochemical impedance spectroscopy, applying a 5 mV perturbation (100 kHz to 1 Hz) at 0.45 V_{RHE}. The setup for measurements in alkaline electrolyte was described in detail in a previous work.[133] In brief, it consisted of a house-made polytetrafluoroethylene cell with a four-necked glass cover. A calomel reference electrode (ALS Co., Ltd.) was kept in a separated glass holder filled with electrolyte connected to the main compartment through a Luggin capillary consisting of a fluorinated ethylene propylene (FEP) tube closed with a 50 µm thick Nafion membrane (Ion Power, New Castle, DE). The setup was completed by a gas bubbler and a gold mesh counter electrode.

Thin-film electrodes were prepared by dispersing catalyst materials in mixtures of ultrapure water (18.2 MΩ cm, Elga Purelab Ultra) and isopropanol (99.9 %, Chromasolv Plus® for HPLC, Sigma Aldrich), followed by 10 min sonication in an ultrasonic bath (USC100T, 45 kHz, VWR). Fractions of the inks were pipetted onto the glassy carbon inset of the RRDE to obtain catalyst loadings of 30 and 15 $\mu g_{Pt}/cm^2_{electrode}$ for Pt-Ni aerogels and Pt/C, respectively. Subsequently, coatings were dried under a gentle N_2-flux.

4.4 Results and Discussion

Bimetallic aerogels with various Pt:Ni atomic ratios were synthesized by the simple co-reduction process of $NiCl_2 \cdot 6H_2O$ and H_2PtCl_6 with $NaBH_4$ in aqueous solution described in the experimental section 4.3.

The composition of the Pt-Ni aerogels produced in this manner was determined by inductively coupled plasma-optical emission spectrometry (ICP-OES) and compared to the values expected on the basis of the initial precursor ratios. As Figure 4.7 in section 4.6.2 shows, a decrease in the extent of reduction of the Ni-precursor is observed upon preparation of Pt-Ni aerogels with $x(Ni)_{ICP\text{-}OES}$-values above 25 at. %. Motivated by this result, two samples were selected for further characterization and analysis: one with a final Ni content ≤ 25 at. % (Pt_3Ni, $x(Ni)_{expected} \approx x(Ni)_{ICP\text{-}OES} \approx 25$ at. %) and one with > 25 at. % Ni ($Pt_{1.5}Ni$, $x(Ni)_{expected} \approx 50$ at. % vs. $x(Ni)_{ICP\text{-}OES} \approx 40$ at. %).

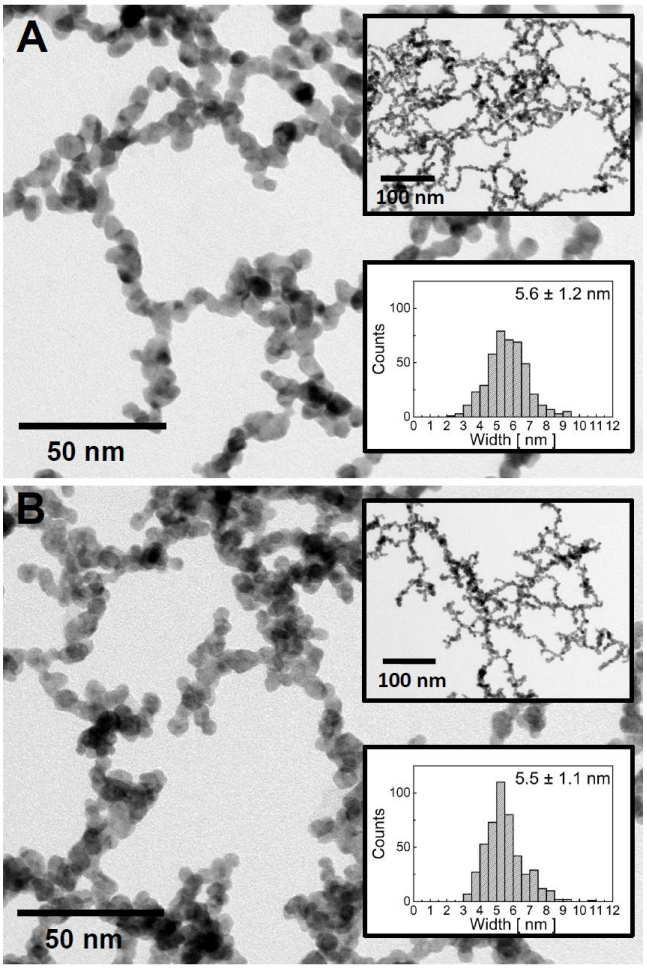

Figure 4.1 TEM images of Pt_3Ni (A) and $Pt_{1.5}Ni$ (B) aerogel; the insets show the corresponding distributions of nanochain diameters and TEM images with lower magnification.

Figure 4.1 shows representative transmission electron microscopy images of the Pt_3Ni and $Pt_{1.5}Ni$ aerogels that look similar to those obtained for aerogels with other Pt-Ni compositions (not shown here). In agreement with previous work,[51] the materials consist of a 3D structure of nanochains that are composed of interconnected/fused nanoparticles. The quality of the nanochain network is supported by the fact that no isolated nanoparticles can be observed. Additionally, nanochain diameters from TEM images based on measurement of the chain's width at different spots are on average ≈ 5 nm for both samples (cf. Table 4.1).

To highlight the reproducibility of our synthesis, the good agreement between nanochain diameter distributions of different batches is illustrated in Figure 4.8 (section 4.6.2). Moreover, the surface areas of the aerogels were analyzed by N_2-physisorption measurements (cf. Figure 4.9, section 4.6.2). Both materials exhibited a type II isotherm and a slight hysteresis indicating the presence of macropores and some mesopores.[134] Surface areas were estimated from Brunauer-Emmett-Teller plots to 55 m^2/g_{Pt} and 58 m^2/g_{Pt} for Pt_3Ni and $Pt_{1.5}Ni$, respectively (cf. Table 4.1).

Table 4.1 Crystallite size, nanochain diameter and surface area values of the Pt_3Ni and $Pt_{1.5}Ni$ aerogels, derived from XRD, TEM, N_2-physisorption, H_{upd} and CO stripping analysis.

Catalyst	**Size [nm]**		**Surface area [m^2/g_{Pt}]**				
	XRD	TEM	XRD_{calc}[1]	TEM_{calc}[1]	H_{upd}[2]	CO strip.[3]	N_2-physis.
Pt_3Ni	6.7 ± 1.3	5.6 ± 1.2	35 ± 7	41 ± 9	32 ± 2	30 ± 2	55
$Pt_{1.5}Ni$	6.0 ± 1.0	5.5 ± 1.1	46 ± 8	51 ± 10	30 ± 1	28 ± 1	58

[1] Surface area values based on the assumption of nanowires with a cylindrical geometry of diameter equal to the one averaged from XRD or TEM measurements, along with alloy density values of 19.0 (Pt_3Ni) and 17.3 g/cm^3 ($Pt_{1.5}Ni$).

[2] Extracted from the integration of H_{upd} desorption peaks (cf. Figure 4.11, section 4.6.2) using the double layer current as an extended baseline and averaged on the basis of 3 independent measurements.

[3] Based on the integration of the charges for the CO oxidation peak using the subsequent CV as a baseline (cf. Figure 4.11, section 4.6.2) and averaged on the basis of 3 independent measurements.

The samples were further characterized by X-ray diffraction (see Figure 4.10, section 4.6.2) in order to investigate alloy formation between Pt and Ni. The (111) reflections at 2θ-values of 40.73° (Pt_3Ni) and 41.04° ($Pt_{1.5}Ni$) present a shift with respect to pure Pt (39.83°).[135] These shifts to larger angles, also observed for the (220) reflections at

≈ 67.71° (pure Pt), confirm alloy formation between Pt and Ni. The greater 2θ shift for $Pt_{1.5}Ni$ compared to Pt_3Ni indicates a larger Ni-concentration in the alloy phase of this aerogel. Analysis of the XRD spectra was concluded by calculating crystallite sizes on basis of the full width at half maximum of the (111) reflections (Scherrer equation); the resulting values tabulated in Table 4.1 coincide well with the average nanochain diameters derived from TEM images.

The crystallite sizes and nanochain diameters from XRD and TEM analyses were used to calculate surface areas assuming cylindrical nanowires and compared to the respective values derived from N_2-physisorption and electrochemical measurements. The latter electrochemical surface areas were determined by integration of the charges corresponding to the underpotential deposition of hydrogen (H_{upd}) on Pt[35] and the oxidation of a monolayer of carbon monoxide potentiostatically adsorbed on the Pt-surface (CO stripping)[119, 136] (see Figure 4.11, section 4.6.2)). As summarized in Table 4.1, the ECSAs of both aerogels are similar (≈ 30 m^2/g_{Pt}) and ≈ 20 - 40 % lower than the surface areas obtained from BET plots or estimated from the XRD- or TEM-derived diameters on the basis of a cylindrical geometry approximation. This difference most likely results from the interconnectivity between the nanowires that form the tridimensional network and from the lack of wettability of micropores in the nanostructures, which are accessible to the N_2-adsorbate used in the physisorption measurements.

To elucidate the aerogels' electronic and local structure, X-ray absorption spectroscopy at the Ni K edge (8333 eV) was used to characterize the Pt_3Ni and $Pt_{1.5}Ni$ aerogels, as well as a $Ni(OH)_2$ (β-phase) reference sample.[137] The X-ray absorption near edge structure region within ± 30 eV of the absorption edge reveals significant differences among the Pt-Ni aerogels (see Figure 4.2A). The position of the absorption edge of the $Pt_{1.5}Ni$ aerogel is shifted to higher energy and the white line intensity is increased compared to that of the Pt_3Ni aerogel, suggesting a partial oxidation of Ni in the $Pt_{1.5}Ni$ aerogel.[108]

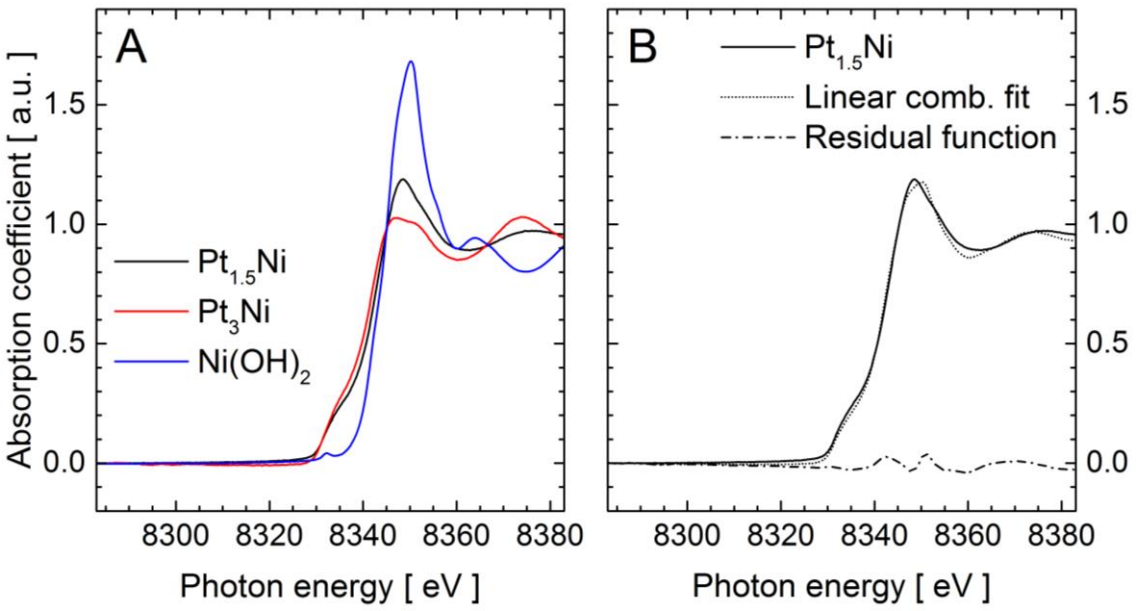

Figure 4.2 (A) X-ray absorption near edge structure at the Ni K edge (8333 eV) for the Pt_3Ni aerogel, the $Pt_{1.5}Ni$ aerogel and a $Ni(OH)_2$ reference. (B) Fit of the $Pt_{1.5}Ni$ aerogel spectrum as a linear combination of the Pt_3Ni aerogel and $Ni(OH)_2$ spectra.

Considering the resembling nanochain diameters of both materials and the 2-fold larger Ni-concentration of the $Pt_{1.5}Ni$ sample, this difference in the Ni-oxidation states cannot be exclusively assigned to the Ni on the aerogels' surfaces (which would get oxidized upon contact with air). Alternatively, this discrepancy could be additionally related to the formation of Ni-(hydr)oxide sidephase(s) in the $Pt_{1.5}Ni$ aerogel, implying that only a fraction of the Ni is involved in the alloying with Pt. This hypothesis is further supported by the good agreement between the XANES recorded for the $Pt_{1.5}Ni$ aerogel and the corresponding fit as a linear combination of the Pt_3Ni aerogel and $Ni(OH)_2$ spectra, displayed in Figure 4.2B. The best fit was obtained for relative weights of 75 % and 25 % for Pt_3Ni and $Ni(OH)_2$ respectively, confirming that a significant amount of the Ni in the $Pt_{1.5}Ni$ aerogel is present in the form of a Ni-(hydr)oxide phase. Surface-sensitive X-ray photoelectron spectroscopy in the Ni $2p_{3/2}$ region (cf. Figure 4.12, section 4.6.2) also corroborates this observation. The sharp peak at ≈ 852.6 eV in the spectrum of Pt_3Ni is associated with Ni^0,[138-140] whereas the $Pt_{1.5}Ni$ spectrum only contains a minor shoulder at the same energy, pointing at a larger content of Ni^0 in Pt_3Ni when compared to $Pt_{1.5}Ni$. Moreover, this finding is in qualitative agreement with previous work by Park et al.[135], who investigated carbon-supported Pt_3Ni and PtNi nanoparticles of 3 - 4 nm diameter prepared by an aqueous-based approach similar to the one used here.

Next, the local structure of both Pt-Ni aerogels was studied by additionally analyzing the extended X-ray absorption fine structure spectra collected at both the Pt L_3 (11564 eV) and the Ni K (8333 eV) edge. The outcome of the simultaneous first shell fit of the Pt L_3 and Ni K EXAFS spectra of Pt_3Ni is summarized in Table 4.2, and the Fourier transformed (FT) EXAFS spectra and corresponding fits are shown in Figure 4.3. The close agreement between the experimental data and the corresponding fits at the Pt L_3 and Ni K edge is discernable from Figure 4.3 and confirmed by the low R-factor value.[2] Additionally, the properties of our Pt_3Ni aerogel and those reported for a Pt_3Ni/C catalyst with a similar particle size in reference 141 are very comparable (cf. Table 4.2), as one would expect from the similarities between the individual building blocks of both materials, i.e. Pt_3Ni nanoparticles.

Table 4.2 Structural parameters derived from the fitting of the EXAFS (Pt L_3 and Ni K edges) of the Pt_3Ni aerogel. Values in brackets are extracted from reference 141 and were determined for a Pt_3Ni/C catalyst of similar particle size. Note that R-factor values below 0.02 are regarded as indicative of a good quality EXAFS fit.[2]

Coord. shell	Coord. number	Bond length [Å]	σ^2 [10^{-3} Å^2]	R-factor
Pt-Pt	7.5 ± 1.0 (8.0)	2.71 ± 0.01 (2.71)	7 ± 1	0.01
Pt-Ni	2.5 ± 0.7 (2.0)	2.66 ± 0.03 (2.65)	13 ± 1	0.01
Ni-Pt	5.0 ± 1.2	2.66 ± 0.03	13 ± 1	0.01
Ni-Ni	2.8 ± 1.1	2.58 ± 0.03	12 ± 4	0.01

Moreover, the Cowley's short range order parameter (α) which quantifies the homogeneity of bimetallic nanoparticles can be derived from the EXAFS analysis as follow,[142, 143]

$$\alpha = 1 - \frac{\mathrm{CN_{Pt-Ni}}/(\mathrm{CN_{Pt-Pt}} + \mathrm{CN_{Pt-Ni}})}{\mathrm{x_{Ni}}} \qquad (4.1)$$

whereby $CN_{Pt\text{-}Ni}$ and $CN_{Pt\text{-}Pt}$ refer to the Pt-to-Ni and Pt-to-Pt coordination numbers, respectively, and x_{Ni} stands for the molar concentration of Ni in the alloy (i.e. 0.25). This calculation yields a value of 0.0 ± 0.3 that is indicative of a homogeneously random alloy.[142] Our attempt at fitting the first shell EXAFS of $Pt_{1.5}Ni$ considering Pt-Pt, Pt-Ni, Ni-Pt and Ni-Ni scattering contributions was unsuccessful (not shown here), possibly due to the sample inhomogeneity caused by the presence of a Ni-(hydr)oxide sidephase inferred above. Again, this finding is endorsed upon comparison of the Ni K edge Fourier

transformed EXAFS for both aerogels (see Figure 4.4), in which $Pt_{1.5}Ni$ displays a first coordination shell between 1.5 - 1.8 Å indicative of Ni-O scattering [108] that is only minor for the Pt_3Ni aerogel.

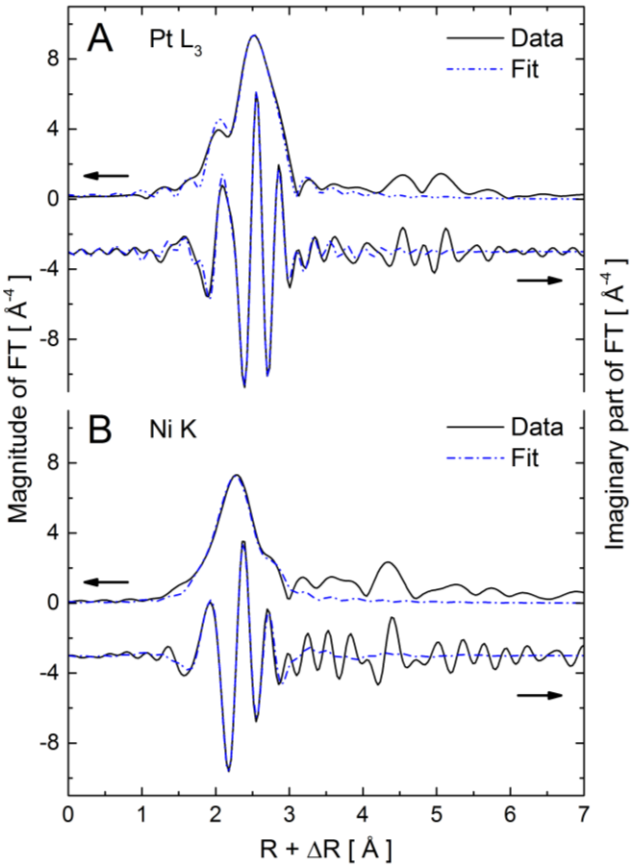

Figure 4.3 EXAFS fit and experimental data (k^3-weighted) in R-space (uncorrected for phase shifts) for Pt_3Ni aerogel at the Pt L_3 (A) and Ni K edge (B).

In a final effort to verify the hypothesized presence of two separate phases in the $Pt_{1.5}Ni$ aerogel, the surface compositions of the as prepared Pt_3Ni and $Pt_{1.5}Ni$ aerogels were investigated electrochemically by cyclic voltammetry. Since Ni is thermodynamically prone to dissolution in acid electrolyte,[144] the measurements were initially carried out in alkaline medium (0.1 M NaOH) to prevent its leaching from the alloy surface.[35] The presence of Pt and Ni on the catalyst surface is indicated by element specific features in the CVs, whereby the peaks between ≈ 0.05 - 0.4 V vs. reversible hydrogen electrode are associated to H_{upd} on polycrystalline Pt.[145] For Ni, the oxidation of $Ni(OH)_2$ to NiOOH at ≈ 1.4 V_{RHE} and its quasi-reversible, subsequent reduction in the negative going scan provides such a characteristic feature.[146]

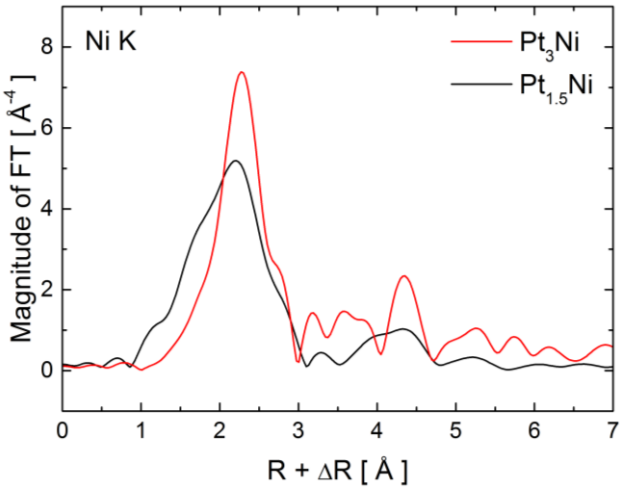

Figure 4.4 Ni K edge EXAFS Fourier transformation (k^3-weighted) in R-space (uncorrected for phase shifts) for Pt_3Ni and $Pt_{1.5}Ni$ aerogel.

According to the solid curves in Figure 4.5 (CVs in alkaline electrolyte between 0.05 and 1.6 V_{RHE}), both aerogels exhibit Pt-related H_{upd} features, but only $Pt_{1.5}Ni$ displays pronounced $Ni(OH)_2$ oxidation/NiOOH reduction peaks as well. Consequently, the Pt_3Ni surface contains but traces of Ni, as one would expect from the nominal composition (Pt:Ni = 3:1) and alloy homogeneity derived from the XAS-analysis, whereas $Pt_{1.5}Ni$ contains a significant amount of surface Ni possibly in the form of a (hydr)oxide phase, further supporting the hypothesis that not all Ni is present as a Pt-Ni alloy phase.

To probe the stability of this surface Ni species in acid, the experiment was continued by immersing each electrode in a separated electrochemical cell filled with 0.1 M $HClO_4$ electrolyte, followed by the recording of 25 potential cycles between 0.05 and 1.0 V_{RHE}. Subsequently, CVs were again recorded in 0.1 M NaOH to identify possible changes in the surface. Interestingly, at this point both materials display very similar voltammetric profiles, with a complete absence of redox transitions at ≈ 1.4 V_{RHE} that indicates the complete dissolution of the Ni-(hydr)oxide sidephase upon conditioning in acid medium.

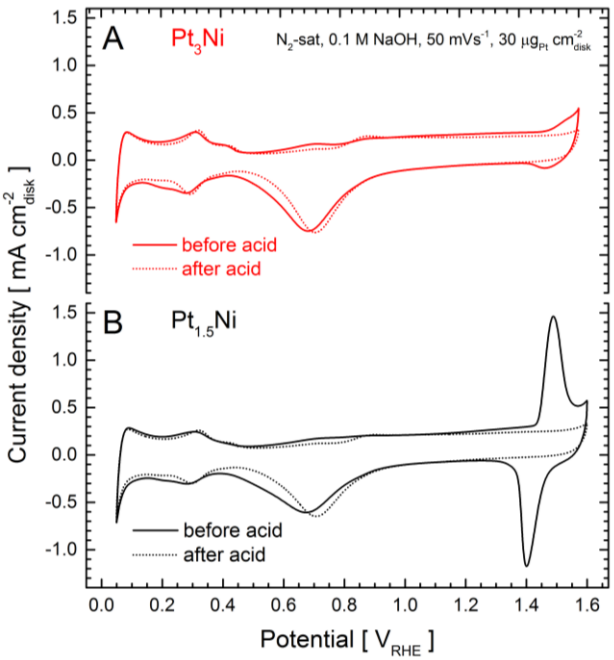

Figure 4.5 Cyclic voltammograms in N_2-saturated 0.1 M NaOH electrolyte at 50 mVs^{-1} of Pt_3Ni (A) and $Pt_{1.5}Ni$ (B) aerogel. CVs before (solid) and after (dotted) 25 conditioning cycles in 0.1 M $HClO_4$ electrolyte between 0.05 and 1.0 V_{RHE} are shown.

After this structural characterization, the ORR activity of both Pt-Ni aerogels in acid medium (0.1 M $HClO_4$) was determined using rotating disk electrode voltammetry, whereby a commercial Pt/C catalyst (30 % Pt/Vulcan XC-72) served as benchmark. The ECSA- and mass-specific ORR activities at 0.95 V_{RHE} are shown in Figure 4.6. The average ECSA values from H_{upd} and CO stripping analysis summarized in Table 4.1 were used for normalization. The potential of 0.95 V_{RHE} was chosen instead of 0.9 V_{RHE} because the latter was too close to the diffusion-limited regime to allow for accurate correction of mass transport losses (cf. polarization curves in Figure 4.13, section 4.6.2).[147] Moreover, mitigating such high currents by reducing the catalyst loading on the electrode was not possible, since minimal loadings of 30 $\mu g_{Pt}/cm^2_{electrode}$ were required for both aerogels to fully cover the glassy carbon disk.

As displayed in Figure 4.6A, both aerogels show a ≈ 3-fold increase of the ECSA-specific activity vs. Pt/C that can be partially assigned to their larger particle size (cf. average aerogel diameters of 5.5 nm listed in Table 4.1, vs. the 3.4 nm of the 30 % Pt/C benchmark estimated in reference 148. However, the limited sensitivity of the ORR-kinetics to the Pt particle size within the corresponding range of ECSA-values (≈ 50 m^2/g_{Pt} for Pt/C vs. ≈ 30 m^2/g_{Pt} for the PtNi-aerogels, see Figure 4.6A) would imply that the

aerogels' larger size can only account for an activity increase of ≈ 20 %.[24, 35] Thus, the great majority of the observed ≈ 3-fold activity enhancement can be explained by a down shift of the d-band center through alloying with Ni.[149] According to literature, this shift decreases the fractional coverage of spectator species at a given potential and increases the number of free sites for O_2 adsorption and subsequent ORR activity.[150]

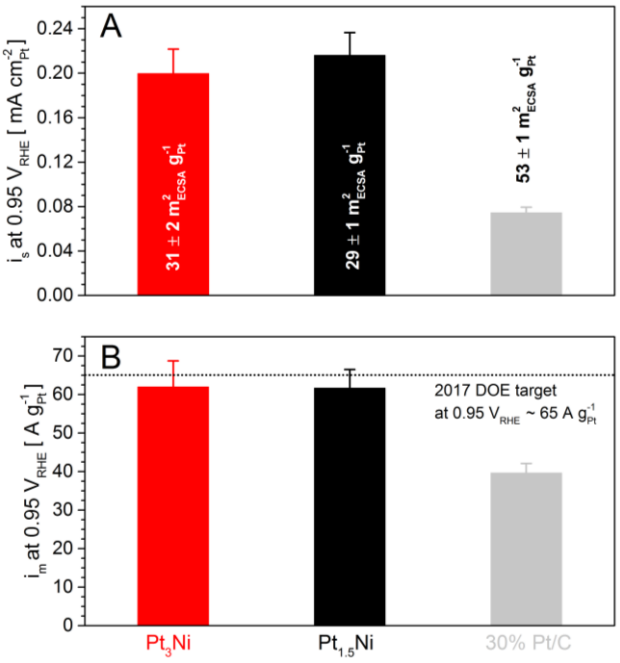

Figure 4.6 Pt-ECSA (A) and mass-specific (B) ORR activity values at 0.95 V_{RHE} for Pt-Ni aerogels and Pt/C (averaged from 3 independent measurements). The dotted line represents the DOE ORR activity target at 0.95 V_{RHE}, extrapolated from the benchmark value of 440 A/g_{Pt} at 0.9 V_{RHE}[3] assuming a Tafel slope of 60 mV dec^{-1}.[151] Activity values were extracted from anodic polarization curves in O_2-saturated 0.1 M $HClO_4$ electrolyte (5 mVs^{-1}), corrected for IR-drop and mass transport losses (Koutecky-Levich equation). Reported ECSA values are averaged from results for H_{upd} and CO stripping analysis (cf. Table 4.1).

Upon conversion of these figures into mass-specific ORR activities (Figure 4.6B), Pt_3Ni and $Pt_{1.5}Ni$ reach the DOE ORR activity target at 0.95 V_{RHE} that was extrapolated from the reported value[3] of 440 A/g_{Pt} at 0.9 V_{RHE} assuming a Tafel slope of 60 mV dec^{-1} consistent with our measurements (cf. Figure 4.13, section 4.6.2).[151] Following the same approach, the ORR activity values at 0.95 V_{RHE} for both Pt-Ni aerogels (≈ 62 ± 5A/g_{Pt}) can be extrapolated to ≈ 422 ± 34 A/g_{Pt} at 0.9 V_{RHE}, in good agreement with recent reports on de-alloyed Pt-Ni/C catalysts based on RDE[152] and fuel cell[153] tests. The almost identical ECSA and ORR activity values for the two aerogels agree with the above conclusion that

their surface compositions become much alike after a few conditioning cycles in 0.1 M $HClO_4$ (see Figure 4.5), in which surface-Ni and $Ni(OH)_2$ sidephases dissolve into the acid electrolyte.

4.5 Conclusion

In summary, we have presented a new facile synthesis for the preparation of Pt-Ni bimetallic aerogels. Extensive sample characterization suggested complete alloy formation in the case of Pt_3Ni, along with limited alloying upon targeting larger Ni contents using this synthetic approach. Electrochemical measurements of the aerogels' catalytic activity towards oxygen reduction revealed a 3-fold ECSA-specific activity increase when compared to commercial Pt/C catalysts that is in agreement with reports in the literature. Additionally, the mass-specific ORR activity of the Pt-Ni aerogels is comparable to that of state-of-the-art, de-alloyed Pt-Ni/C materials, and meets the DOE-target value for automotive FC application. Future work will therefore focus on investigating the stability of these Pt-Ni aerogels under PEFC-relevant working conditions and comparing their behavior to that of commercial Pt/C catalysts, as to verify the stability enhancement expected from the absence of a carbon support in these novel materials.[89]

4.6 Appendix – Supplementary Information

4.6.1 Materials and Methods

Electron microscopy

Transmission electron microscopy was performed using a Tecnai T20 from FEI equipped with a LaB_6 cathode at an accelerating voltage of 200 kV. TEM specimens were prepared by drop casting a dispersion of aerogel in acetone on a copper grid with a thin Formvar-carbon film. For determination of the aerogel nanochain diameter histogramms, the nanochain diameter was measured at least in 200 different spots.

N_2-physisorption

Nitrogen physisorption isotherms were measured at 77 K on a Quantachrome Autosorb 1C instrument. About 50 mg of the aerogel was transferred to the measuring cell and degassed at 323 K under vacuum for at least 24 h. Specific surface areas were calculated using the multipoint BET equation ($0.05<p/p_0<0.2$).

X-ray diffraction measurements

Pt-Ni aerogels were analyzed in capillary tubes for a total acquisition time of 16 h using an X'celerator Phillips expert diffractometer between 2θ = 10° and 100°, with a step of 0.03°, using Cu $K\alpha_1$ monochromatic radiation (λ = 0.15406 nm) .

X-ray photoelectron spectroscopy

X-ray photoelectron spectroscopy measurements were performed using a VG ESCALAB 220iXL spectrometer (Thermo Fischer Scientific) with an Al Kα monochromatic source and a magnetic lens system. Binding energies of the acquired spectra were referenced to the C 1s line at 284.9 eV. Quantification of different Ni species through deconvolution of the XPS spectra remains out of the scope of this study due its complexity[138] and limited additional insight for our purpose.

4.6.2 Supplementary Figures

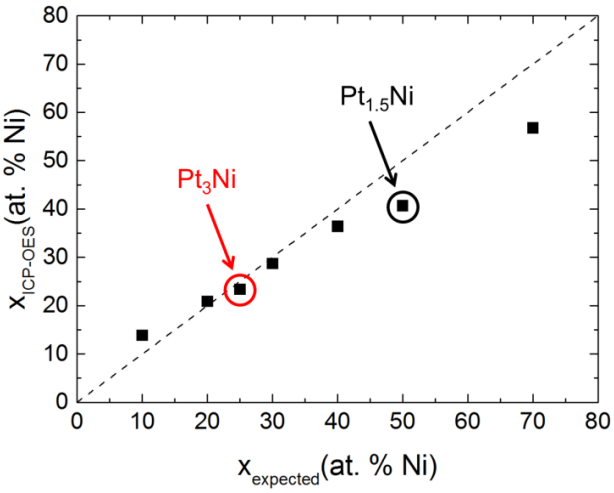

Figure 4.7 Relation between the Ni content of various Pt-Ni aerogels as determined by ICP-OES (squares) and the corresponding, expected Ni concentration based on the Pt-to-Ni precursor ratio (dotted line).

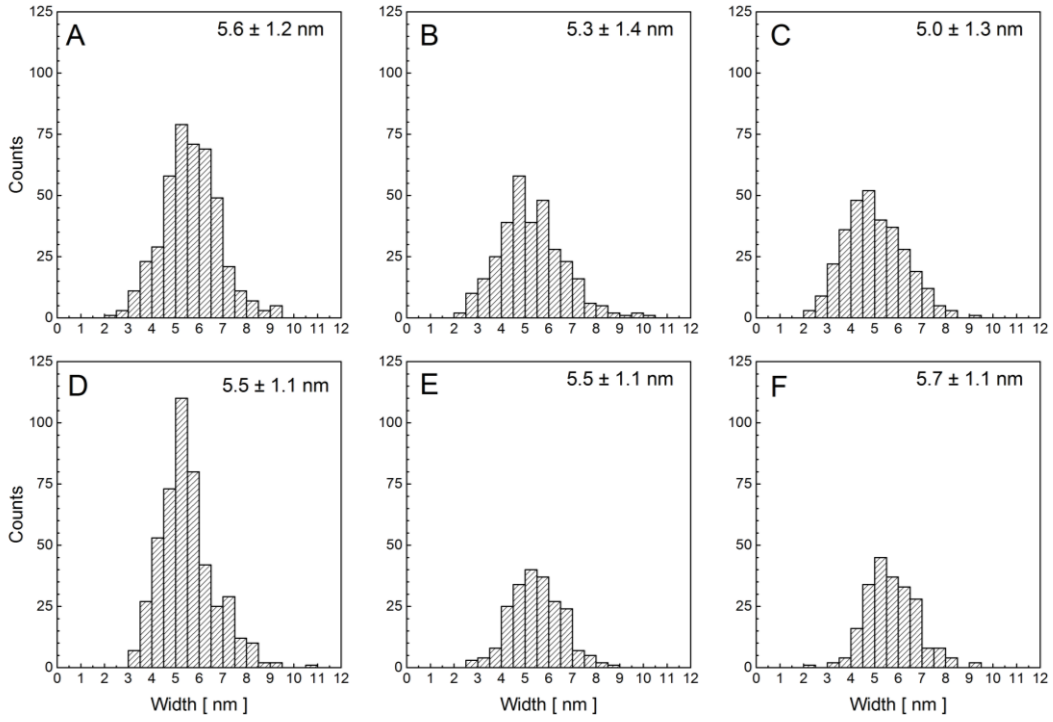

Figure 4.8 Nanochain diameter distributions from TEM images based on measurement of the chain's width at various spots for different samples of Pt_3Ni (A-C) and $Pt_{1.5}Ni$ (D-F) aerogel.

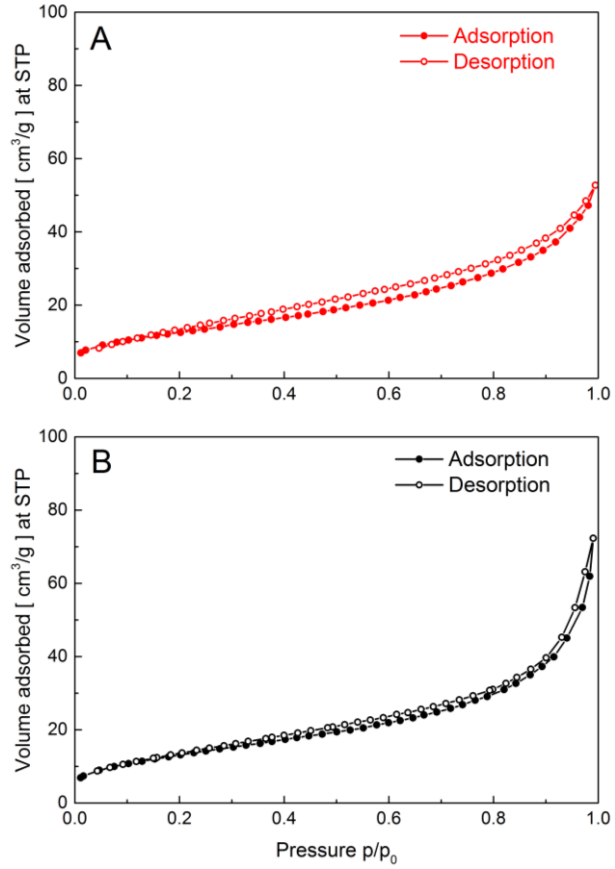

Figure 4.9 N_2-physisorption isotherms for Pt_3Ni (A) and $Pt_{1.5}Ni$ (B).

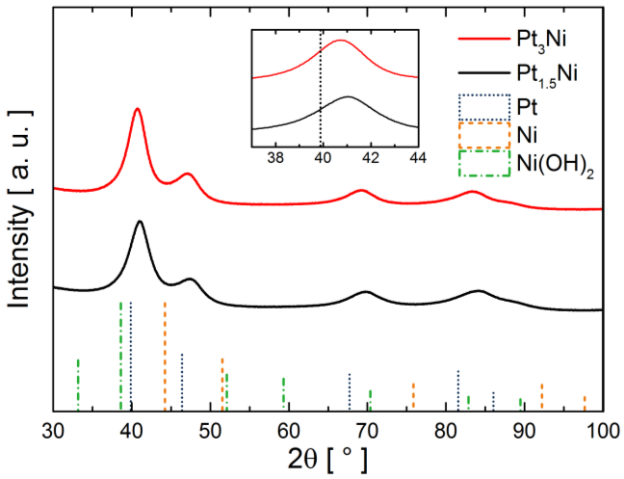

Figure 4.10 XRD spectra for Pt_3Ni (top) and $Pt_{1.5}Ni$ (bottom) aerogel. Reflections for metallic Pt[154], Ni[155] and $Ni(OH)_2$[156] are shown as a reference bars at the bottom of the chart; the inset shows a magnification of the (111) reflections.

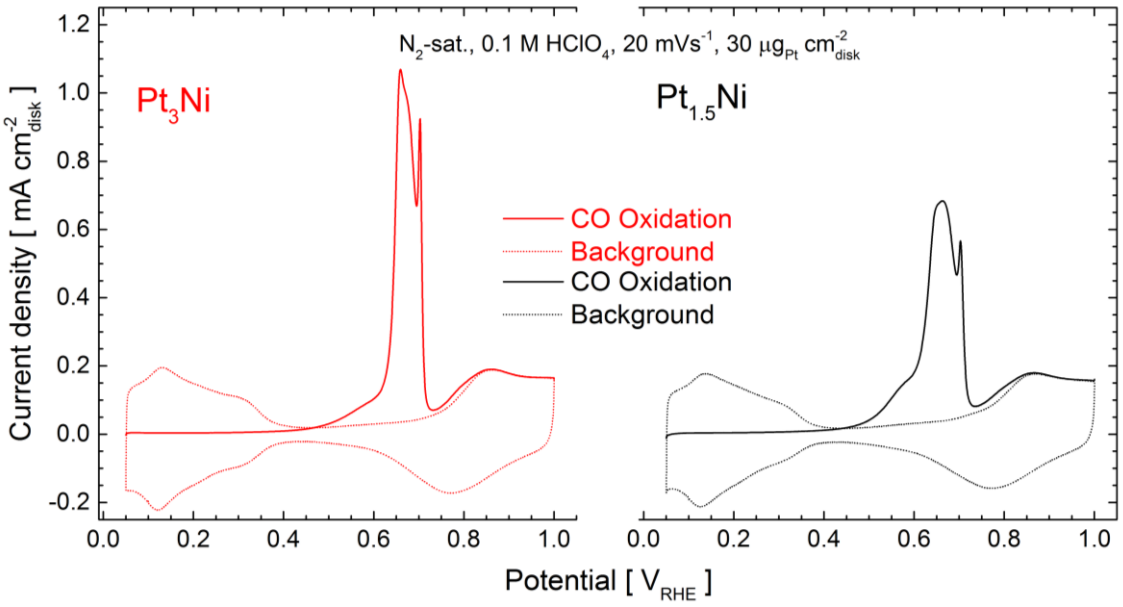

Figure 4.11 Cyclic voltammograms from CO stripping experiments (solid lines) for Pt_3Ni (left) and $Pt_{1.5}Ni$ (right) aerogels. In brief, the electrode was held at a potential of 0.1 V_{RHE} while the 0.1 M $HClO_4$ electrolyte was purged with CO for ~ 5 min. Subsequently the electrolyte was saturated with N_2 for 20 min before the adsorbed CO was oxidized by a positive potential sweep at 20 mVs^{-1} up to 1.0 V_{RHE}. The subsequent, steady-state CVs in N_2-saturated electrolyte that were used to calculate H_{upd} charges are shown in dotted lines as a reference.

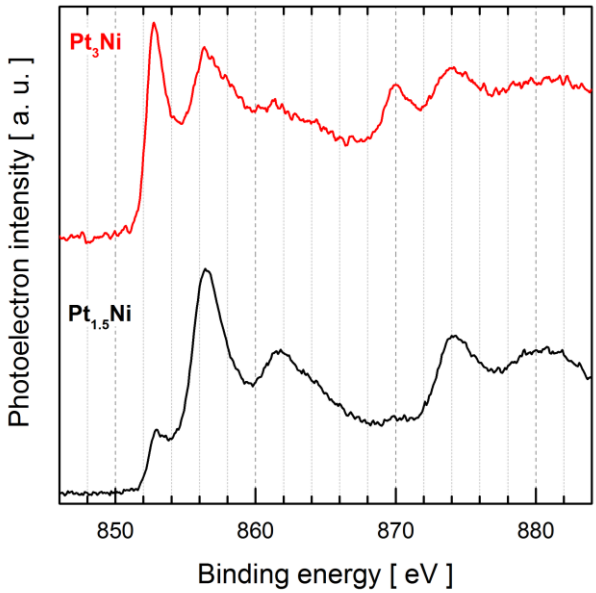

Figure 4.12 Ni 2p X-ray photoelectron spectra of Pt_3Ni (top) and $Pt_{1.5}Ni$ (bottom).

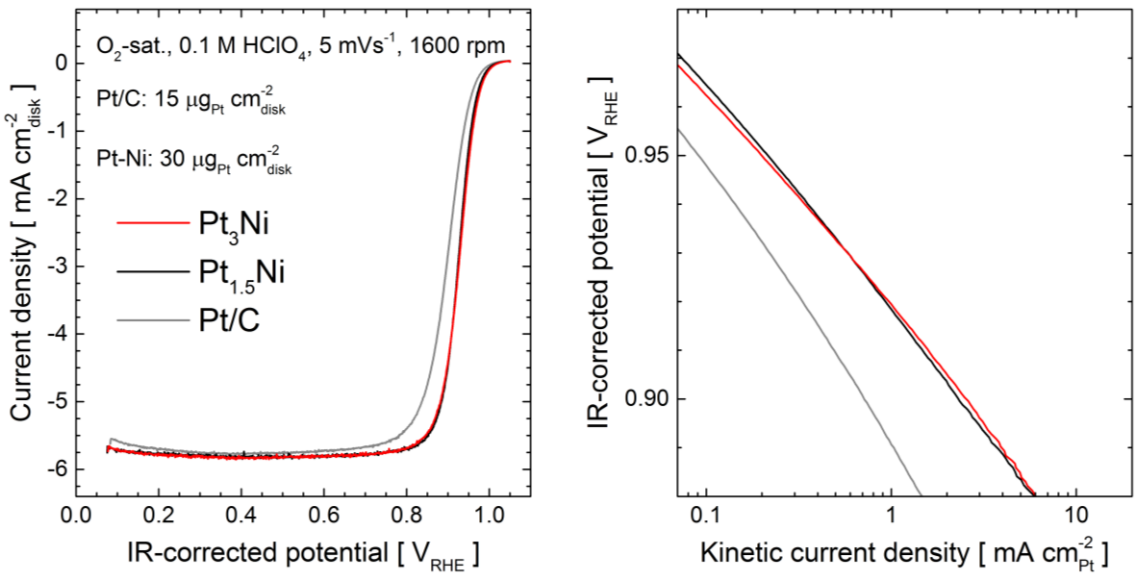

Figure 4.13 Non-capacitively corrected, anodic ORR polarization curves (left) and corresponding Tafel plots (right).

5 Acid Washing Modification of Pt-Cu Aerogel Catalysts

5.1 Effect of Acid Washing on the Oxygen Reduction Reaction Activity of Pt-Cu Aerogel Catalysts

As an intermediary step towards fuel cell implementation, the behavior of aerogels under PEFC relevant conditions (low pH value), simulated by acid washing of the latter, is discussed in this chapter. First, the composition, structure and ORR activity of two different aerogels (Pt_3Cu and PtCu) are characterized by XRD, XPS, XAS, scanning transmission electron microscopy - energy dispersive X-ray spectroscopy (STEM-EDX) and RDE experiments. These experiments are repeated for Pt_3Cu and PtCu aerogels that were subjected to two days of acid washing and results are compared to the ones for the as-synthesized samples. In the last part, the effect of acid washing is discussed and a descriptor that can predict the ORR activity for Pt-Cu aerogels is presented.

Effect of Acid Washing on the Oxygen Reduction Reaction Activity of Pt-Cu Aerogel Catalysts

Sebastian Henning[a,‡], Laura Kühn[b,‡], Juan Herranz[a], Maarten Nachtegaal[c], René Hübner[d], Matthias Werheid[b], Alexander Eychmüller[b] and Thomas J. Schmidt[a,e]

[a]Electrochemistry Laboratory, Paul Scherrer Institut, 5232 Villigen, Switzerland

[b]Physical Chemistry, Technische Universität Dresden, Bergstr. 66b, 01062 Dresden, Germany

[c]Paul Scherrer Institut, 5232 Villigen, Switzerland

[d]Institute of Ion Beam Physics and Materials Research, Helmholtz-Zentrum Dresden - Rossendorf, Bautzner Landstraße 400, 01328 Dresden, Germany

[e]Laboratory of Physical Chemistry, ETH Zurich, 8093 Zurich, Switzerland

[‡]These authors contributed equally

ABSTRACT

Developing highly active and durable oxygen reduction reaction catalysts is crucial to reduce the cost of polymer electrolyte fuel cells. To meet those requirements, unsupported Pt-Cu alloy nanochains (aerogels) were synthesized by a simple co-reduction route in aqueous solution and their structure was characterized by X-ray absorption spectroscopy and scanning transmission electron microscopy coupled with energy-dispersive X-ray spectroscopy. These catalysts exceeded the ORR activity of commercial Pt/C catalysts by more than 100 % in rotating disk electrode experiments and met the corresponding DOE target for automotive PEFC implementation, thereby qualifying as very promising materials. The behavior of Pt-Cu aerogels under PEFC operation conditions was mimicked by acid washing experiments which showed that the Cu content in the alloy phase and ORR activity decrease through this step. Comparing composition, structure and ORR activity for various specimens, the Cu content in the alloy phase was identified as the main descriptor of ORR activity. An almost linear correlation was found between those two parameters and complemented by supporting data from the literature.

Published in *Electrochim. Acta*, **233**, 210 (2017).

5.2 Introduction

Hydrogen powered polymer electrolyte fuel cells are considered a viable power supply for all-electric vehicles.[3] In order to become more competitive with respect to alternative technologies, i.e. batteries, the system cost of PEFCs needs to be reduced. An important fraction of the overall costs is attributed to the use of expensive catalyst materials to accelerate the anodic hydrogen oxidation and the cathodic oxygen reduction reaction in the fuel cell.[32] Due to its slow kinetics, the latter ORR causes more than 50 % of the cell voltage losses during PEFC operation.[35] Thus, the development of O_2-reduction catalysts with enhanced activities that exceed state-of-the-art materials consisting of Pt nanoparticles supported on carbon is of great importance.[32] This improvement is typically achieved by alloying Pt with various transition metals (e.g. Ni, Cu, Co),[6, 157-159] thereby tuning (i.e. decreasing) the surface binding energies of adsorbed O-intermediates.

On top of these activity requirements, state-of-the-art Pt-based catalysts undergo significant losses of performance during PEFC operation due to the corrosion of their carbon support.[7, 41, 160, 161] As a result, research effort increasingly focuses on materials with C-free supports, or even fully unsupported catalysts.[24, 33, 125] Among the latter, aerogels consisting of tridimensionally interconnected metal nanoparticles provide the large electrochemical surface areas and porosities required for PEFC implementation, and can additionally be prepared in the bimetallic compositions required for an enhanced ORR activity.[51, 53] Our previous work on non-supported Pt-Ni aerogels[53] showed that these materials yield a Pt_3Ni alloy upon contact to acid, reaching the ORR activity target for automotive PEFCs set by the U.S. Department of Energy (i.e. 440 A/g_{Pt} at 0.9 V_{RHE}). Looking for a further improvement, we have extended this approach to the preparation of Pt-Cu aerogels for which higher ORR activities can be excepted on the basis of the larger decrease of the oxygen binding energies on these alloy surfaces.[162]

An important, yet often overlooked aspect for PEFC implementation of such Pt alloy catalysts is the leaching of their non-noble metal component, triggered by the acidic reaction environment concomitant to the perfluorosulfonic acid groups in the ionomer and membrane.[35, 144] Such exposure to acid can change the composition and corresponding catalytic properties of the Pt alloy catalyst. Additionally, the leached metal ions have a greater affinity for sulfonic acid groups than H^+, therefore poisoning the ionomer and negatively impacting PEFC performance.[97, 98, 100] In some works dealing with Pt-Ni and Pt-Cu alloys with an initially large non-noble metal content (i.e. prone to severe Ni or Cu

leaching), this poisoning effect was circumvented by acid washing the membrane electrode assembly after Ni/Cu dissolution and prior to PEFC operation, as to restore the ionomer's initial H^+-inventory.[153, 163, 164] Thus, in this work we focus on two Pt-Cu aerogels with different initial copper contents, and mimic the dealloying effects related to MEA fabrication / PEFC operation by acid washing these materials. The relations established between the composition, structure and ORR activity of the resulting catalysts provide valuable insight on the key parameters that determine their reactivity.

5.3 Experimental

5.3.1 Synthesis

Pt-Cu hydrogels were prepared by a simple co-reduction route in aqueous solution under ambient conditions (room temperature, air). Briefly, Pt and Cu precursors were dissolved in water (18.2 MΩ cm, Millipore) and reduced by $NaBH_4$. For the synthesis of Pt_3Cu hydrogel, 585µL of a 0.205 M H_2PtCl_6 solution (8 wt. % in H_2O, Sigma Aldrich) [final reactant concentration 0.15 mM] and 4 ml of a freshly prepared 10 mM $CuCl_2$ solution ($CuCl_2$*$2H_2O$ 99.999 %, Sigma Aldrich) [final reactant concentration 0.05 mM] were dissolved in 790 mL water and stirred until mixing was complete. Subsequently, 8.4 mL of freshly prepared 0.1 M $NaBH_4$ solution (granular, 99.99 %, Sigma Aldrich) [$c(Pt^{4+} + Cu^{2+}):c(NaBH_4)=1:1.5$] were added under vigorous stirring. In order to obtain PtCu hydrogel, 8 mL of a freshly prepared 10 mM K_2PtCl_4 solution (K_2PtCl_4 99.99 %, Sigma-Aldrich) [final reactant concentration 0.10 mM] and 8 ml of a 10 mM $CuCl_2$ solution [final reactant concentration 0.10 mM] were mixed in 780 mL water. 4.0 ml of freshly prepared 0.1 M $NaBH_4$ solution [$c(Pt^{4+} + Cu^{2+}):c(NaBH_4)=1:1.25$] were added to reduce the metal salts. Upon addition of $NaBH_4$, the color of the solutions turned immediately from light yellow to dark brown. The solutions were kept stirring for another 30 min. Afterwards, the reaction solutions were divided and transferred to 100 mL vials. After about four (PtCu) to six (Pt_3Cu) days, black hydrogel was formed at the bottom of the containers. The hydrogel parts obtained from the same synthesis were collected in a small vial and washed with water. For this, half of the supernatant was removed and replaced cautiously with fresh water. This step was repeated six times. Afterwards, the solvent was exchanged stepwise with acetone. Again, half of the supernatant was removed and replaced by acetone. This step was repeated 11 times. The resulting anhydrous gels were transferred to a critical point dryer (Critical Point Dryer 13200J-AB, SPI Supplies) operating with CO_2.

5.3.2 XAS Spectroscopy

XAS spectra at the Pt L_3 and Cu K edges were recorded at the SuperXAS beamline of the Swiss Light Source (Paul Scherrer Institut, Villigen, Switzerland), whereby the beam current and the energy of the SLS storage ring were 400 mA and 2.4 GeV, respectively. All spectra were recorded in transmission mode using N_2-filled ionization chambers at different gas pressures. A reference foil was measured simultaneously between the transmitted X-ray intensity and a third ionization chamber. The polychromatic beam was collimated by a Rh (at the Pt L_3 edge) or Si coated (at the Cu K edge) collimating mirror, respectively. The mirror was followed by a channel-cut crystal Si (111) monochromator. Focusing of the beam to a spot of 100 x 100 micrometer was achieved by a Rh coated toroidal mirror, located after the channel-cut monochromator. Measurements were performed ex-situ on pellets made of aerogel powder and cellulose. The quick-EXAFS method was used to increase time resolution;[132] 100 and 600 quick-XAS spectra were recorded at the Pt L_3 and Cu K edges, respectively, and were averaged into a single spectrum. Subsequently, normalization and background subtraction was performed using the Demeter software package.[110] The energy units (eV) were then converted to photoelectron wave vector k units ($Å^{-1}$) by assigning the photoelectron energy origin, E_0, corresponding to $k = 0$, to the first inflection point of the absorption edge. The resulting $\chi(k)$ functions for the Pt and Cu edge spectra were weighted with k^3 and then Fourier-transformed to obtain pseudo radial structure functions (RSFs). The fit of the EXAFS spectra was performed with the Demeter Software[110] for the R-range 1.5 - 3.5 Å by using a face centered cubic Pt-Cu structure for the paths description. In case of the hetero-metallic pairs (Pt-Cu and Cu-Pt) in the nearest neighboring of the absorbing atoms, atoms of one type were substituted with atoms of the opposite type. Amplitude reduction terms (S_0) were calculated from EXAFS fits of Pt and Cu reference foils assuming a coordination number of 12 and amounted to $S_{0,Cu}^2 = 0.87$ and $S_{0,Pt}^2 = 0.81$, respectively.

5.3.3 Electrochemical Measurements

Electrolyte solutions were prepared from 60% $HClO_4$ (Kanto Chemical Co., Inc.) diluted in ultrapure water (18.2 MΩ cm, Elga Purelab Ultra). High purity N_2 (5.0), O_2 (5.0) and CO (4.7) were purchased from Messer AG, Switzerland. The benchmark catalyst for this study is a Pt/Vulcan XC-72 electrocatalyst with a Pt weight fraction of 30 % (E-TEK Inc., Lot# C0160311). The electrochemical setup used has been described in detail in a previous work;[53] in brief it consists of a three electrode glass cell, equipped with a gold

mesh counter electrode, a reversible hydrogen reference electrode and PTFE-made rotating ring-disk electrode (Pine Research Instrumentation) as working electrode. Thin-film electrodes were prepared by dispersing catalyst materials in mixtures of ultrapure water (18.2 MΩ cm, Elga Purelab Ultra) and isopropanol (99.9 %, Chromasolv Plus® for HPLC, Sigma Aldrich), followed by 10 min sonication in an ultrasonic bath (USC100T, 45 kHz, VWR).[111] Fractions of the inks were pipetted onto the glassy carbon inset of the RRDE to obtain catalyst loadings of 15 $\mu g_{Pt}/cm^2_{electrode}$. Subsequently, coatings were dried under a gentle N_2-flux.

The resulting electrode was immersed in the N_2-saturated, 0.1 M $HClO_4$ electrolyte, and conditioned by recording 15 voltammetric cycles between 0.05 and 1.2 V_{RHE} at 50 mVs^{-1}, followed by electrolyte saturation with O_2. ORR-polarization curves were recorded between 0.05 and 1.05 V_{RHE} at 5 mVs^{-1} and electrode rotation speeds of 400, 900 and 1600 rpm. The electrolyte was then re-saturated with N_2, and carbon monoxide was dosed for 5 min while holding the electrode at 0.1 V_{RHE}. Following bubbling with N_2 for 20 min, this adsorbed CO was oxidized by scanning the potential at 20 mVs^{-1} up to 1.0 V_{RHE}, and three more cyclic voltammograms were recorded.

5.4 Results and Discussion

Pt-Cu aerogels with two different metal precursor ratios were synthesized by co-reduction as specified in section 5.3.1, and inductively coupled plasma - optical emission spectrometry analysis of the products yielded the expected Pt:Cu atomic ratios of 3:1 and 1:1, respectively; the samples will therefore be denoted Pt_3Cu and PtCu in the following. In parallel, fractions of Pt_3Cu and PtCu hydrogels (cf. section 5.3.1) were suspended in 0.1 M $HClO_4$ solution for 2 days before washing with water, acetone exchange and final supercritical drying step. The resulting acid-washed (AW) materials (Pt_3Cu AW and PtCu AW) showed lower Cu contents than their as-synthesized counterparts, namely 20 and 26 at. % for Pt_3Cu AW and PtCu AW, respectively (as opposed to 25 and 50 at. % for Pt_3Cu and PtCu; see Table 5.2).

Figure 5.1 shows representative transmission electron microscopy images for Pt_3Cu, PtCu and their acid-washed derivatives that all exhibit the typical 3D nanochain structure observed in previous works on similar materials.[51, 53] Size distributions were determined by measuring the nanochain diameter at different positions along the chains and amounted to 3.8 ± 1.0, 3.9 ± 1.1, 4.0 ± 1.0 and 3.7 ± 0.9 nm for Pt_3Cu, Pt_3Cu AW, PtCu and PtCu AW, respectively (see Figure 5.6 in section 5.6.2 for TEM images at enhanced magnification).

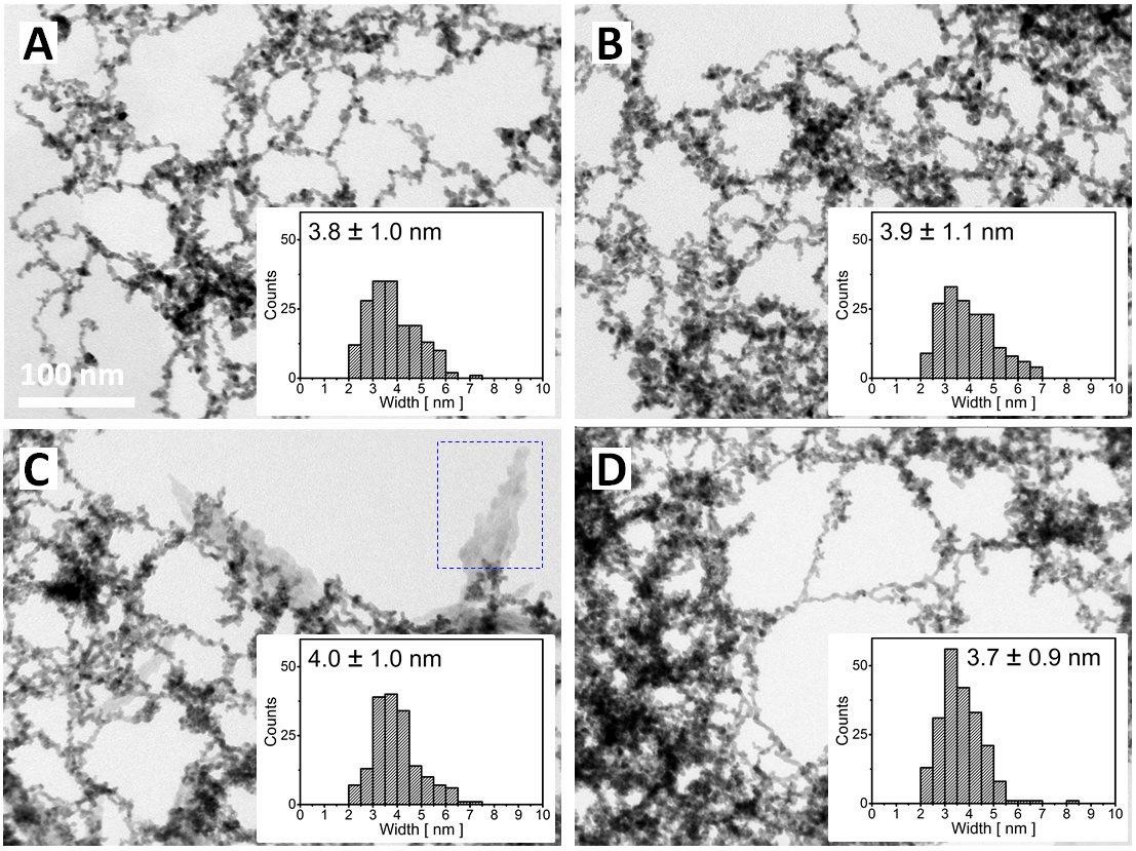

Figure 5.1 TEM images of Pt_3Cu (A: as-synthesized, B: acid-washed) and PtCu (C: as-synthesized, D: acid-washed) aerogels; the insets show the corresponding distributions of nanochain diameters and the copper oxide side phase for PtCu (C) is highlighted by a blue frame.

Besides the nanochain network, large needle-like structures were observed in the PtCu sample (Figure 5.1) which can be attributed to the presence of copper oxide that precipitates during the synthesis. This hypothesis is supported by XPS spectra at Cu 2p binding energies (see Figure 5.7, section 5.6.2), in which the peaks at ≈ 962 eV and ≈ 942 eV in the PtCu spectrum indicate the presence of copper oxides.[165] For the same specimen after acid washing, PtCu AW, those needle-like structures could not be observed anymore when TEM images were taken at different locations (not shown here) in agreement with the disappearance of Cu oxides features in the XPS spectrum (cf. Figure 5.7D). As for Pt_3Cu, no effect of the acid washing on its morphology and composition was discernible from TEM and XPS.

Next, the ORR activities of the as-synthesized and acid-washed Pt-Cu aerogels were determined using rotating disk electrode voltammetry[111] in 0.1 M $HClO_4$ electrolyte. The mass-specific ORR activities at 0.95 V_{RHE} in Figure 5.2A were extracted from anodic

sweeps at 5 mVs^{-1} and 1600 rpm in O_2-satured electrolyte after correcting for cell resistance and mass transport limitations applying the Koutecky-Levich equation [147]. Both Pt_3Cu and PtCu show ≈ 1.5-2 fold higher mass-specific ORR activities than the benchmark Pt/C catalyst, whereby the latter aerogel (PtCu) exceeds by ≈ 30 % the DOE ORR activity target for 2017, extrapolated from the reported value[3] of 440 A/g_{Pt} at 0.9 V_{RHE} to the 0.95 V_{RHE} used herein by assuming a Tafel slope of 60 mV dec^{-1}.[151] Interestingly, mass-specific ORR activities were lower for Pt_3Cu AW (- 10 % vs. Pt_3Cu) and PtCu AW (- 25 % vs. PtCu), indicating that the loss of copper upon exposure to acid is detrimental to the aerogels' catalytic activity. A similar trend was observed for surface-specific activities (cf. Figure 5.2B) that were calculated by normalizing ORR currents with the average electrochemical surface area obtained from hydrogen underpotential deposition[35] and CO stripping charges (assuming conversion factors of 210 and 420 $\mu C/cm^2_{Pt}$, respectively)[119, 136] (cf. Figure 5.8, section 5.6.2). The corresponding ECSAs used for normalization differed by less than 5 % among techniques (i.e., H_{upd} vs. CO-stripping), and are written vertically across the bars in Figure 5.2B. Additionally, these values did not change significantly upon acid washing, therefore excluding the formation of distinct Pt-skeleton core−shell structures that would lead to an increase in ECSA following Cu-dealloying.[158, 159, 166-168]

As discussed in our previous work,[53] the ≈ 3-fold increase of ECSA-specific activity for Pt-Cu aerogels vs. Pt/C is mainly related to a weaker adsorption of oxygen containing intermediates, in terms caused by a downshift of the d-band center[150] induced by the alloying with Cu.[162] To be more precise, two effects are triggered when Pt is alloyed with other metals. First, alloying induces a long-range lattice strain which affects the Pt-Pt bond length and that is referred to as 'geometric effect'. Second, short-range electronic transfer between the different metals in the alloy is referred to as 'ligand effect'.[169, 170] For multi-metallic alloy catalysts like the aerogel structures investigated in this study, both effects simultaneously influence the d-band center position and corresponding ORR activity, making it impossible to determine their relative contributions to the reactivity enhancement.[170]

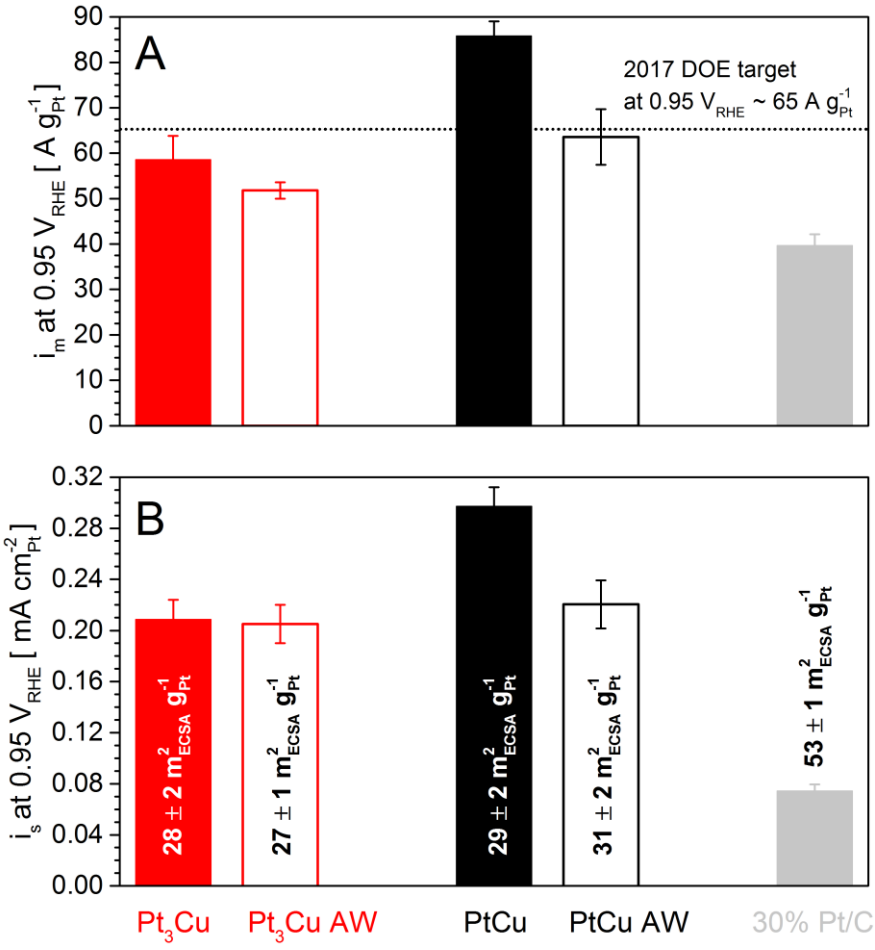

Figure 5.2 Mass-specific (A) and Pt-ECSA-specific (B) ORR activity values at 0.95 V_{RHE} for Pt-Cu aerogels as-synthesized (solid) and acid-washed (hollow), plus a 30 % Pt/C benchmark (averaged from 3 independent measurements). The dotted line represents the DOE ORR activity target at 0.95 V_{RHE}, extrapolated from the benchmark value of 440 A/g_{Pt} at 0.9 V_{RHE}[3] assuming a Tafel slope of 60 mV dec^{-1}.[151] Vertical column labels are ECSA values averaged from H_{upd} and CO stripping charges.

Since the decrease of ORR activity observed for the Pt-Cu aerogels upon acid washing is expected to be reproduced during MEA preparation / PEFC operation, it is fundamental to unravel the reasons for this behavior in order to assess the material's PEFC applicability. Comparing the ORR activity for all four specimens, the trend PtCu > PtCu AW ≥ Pt_3Cu ≥ Pt_3Cu AW qualitatively matches the Cu content in the as-synthesized and acid-washed aerogels, determined by ICP-OES, thus agreeing with reports by the Strasser group correlating ORR activity and Cu concentration.[164, 171] However, those studies included catalysts with initial copper contents ≥ 50 at. % that experienced significant Cu leaching during the initial voltammetric conditioning step.[171]

Analogously, considering the existence of a copper oxide side phase in PtCu, the initial Cu content (derived by ICP-OES) in these aerogel catalysts can be a misleading property to relate to their ORR activity.

With this motivation, the four samples of the present study were investigated by X-ray diffraction to determine their degree of alloying and corresponding composition. As discernible from the inset in Figure 5.3, the (111) reflection for PtCu is at larger 2θ values than for Pt_3Cu, indicating a higher Cu content in the alloy phase and coinciding with the ~ 50 % greater surface-specific ORR activity.

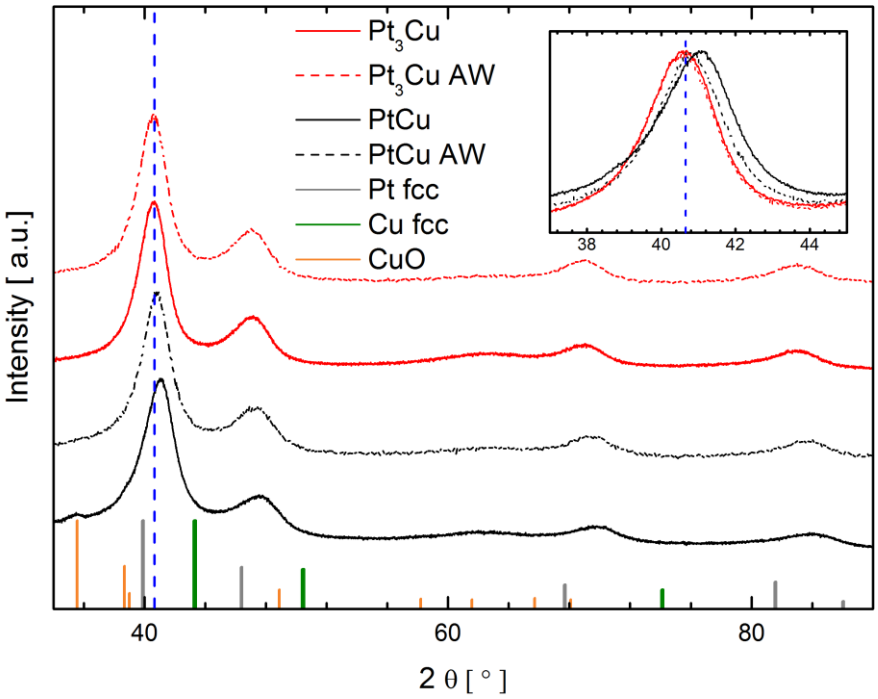

Figure 5.3 XRD patterns for Pt_3Cu (solid red), PtCu (solid black) and respective acid-washed samples (dotted). Reflections for metallic Pt[154], Cu[172] and CuO[173] are shown as reference bars at the bottom of the chart; the inset shows a magnification of the (111) reflections.

Additionally, the small reflection at ≈ 35° for the PtCu diffraction pattern can be assigned to the copper oxide side phase that was also observed in the TEM images (cf. Figure 5.1) and the XPS spectrum (cf. Figure 5.7, section 5.6.2). Furthermore, upon acid washing (i.e. sample PtCu AW) the (111) reflection shifts to lower angles and almost coincides with the peaks of Pt_3Cu and Pt_3Cu AW, thereby indicating Cu loss from the alloy phase. This in turn can explain the significant decrease in ORR activity for PtCu upon acid washing and the similar activities for PtCu AW, Pt_3Cu and Pt_3Cu AW. In parallel, the diffraction peak corresponding to copper oxide disappears in the PtCu AW diffraction pattern, in agreement

with observations from both TEM and XPS. Applying Vegard's law[174] the stoichiometric compositions were determined as $Pt_{65}Cu_{35}$ (PtCu), $Pt_{71}Cu_{29}$ (PtCu AW), $Pt_{75}Cu_{25}$ (Pt_3Cu) and $Pt_{76}Cu_{24}$ (Pt_3Cu AW); besides for PtCu, containing a copper oxide side phase, these figures are similar to the initial ICP-OES values (cf. Table 5.2).

Next, the aerogels' structure was studied further to potentially unravel additional reasons for the apparent relation between ORR activity and Cu content. First, extended X-ray absorption fine structure spectroscopy was performed at the Pt L_3 (11564 eV) and Cu K (8979 eV) edges to get insights into the local structure of the Pt-Cu aerogels. Figure 5.9 in section 5.6.2 displays the Fourier-transformed EXAFS at the Cu K edge for all samples; similar spectral shapes are observed with the only exception of the PtCu aerogel, which features a peak at ≈ 1.5 Å that can be assigned to Cu-O scattering contributions from the copper oxide side-phase observed in TEM images and XPS spectra (cf. Figure 5.1 and Figure 5.7). As expected, those contributions disappear for PtCu AW suggesting that the side phase is removed upon acid washing, which is consistent with the corresponding TEM, XRD and XPS results (cf. Figure 5.1, Figure 5.3 and Figure 5.7).

As a result of the compositional heterogeneity caused by the presence of a Cu oxide phase, the fitting of the first shell EXAFS for PtCu was not successful. For all three other samples, the result of the simultaneous first shell fit at both edges is summarized in Table 5.1 and the Fourier transformed EXAFS spectra and corresponding fits are shown in Figure 5.10 in section 5.6.2. As summarized in Table 5.1, coordination numbers and bond lengths (CNs, Rs) for Pt_3Cu and Pt_3Cu AW are similar, in agreement with their alike XRD profiles and ORR activities. What is more, almost identical CN- and R-values have been reported previously for carbon-supported Pt_3Cu nanoparticles with a comparable particle size,[175] endorsing the observation from TEM images that the aerogels consist of individual nanoparticles connected to nanochains. Additionally, on the basis of the coordination numbers in Table 5.1, the atomic ratio of Pt:Cu (n_{Pt}:n_{cu}) and Pt- and Cu-contents, x_{Pt} and x_{cu} (in at. %), were determined as follows[54, 142]

$$\frac{n_{Pt}}{n_{Cu}} = \frac{CN_{Cu-Pt}}{CN_{Pt-Cu}} \tag{5.1}$$

$$x_{Cu} = \frac{1}{\frac{n_{Pt}}{n_{Cu}} + 1} \cdot 100 \tag{5.2}$$

whereby CN_{Cu-Pt} and CN_{Pt-Cu} refer to number of nearest Pt and Cu neighbours surrounding Cu and Pt atoms, respectively. As discernible from Table 5.2, there is a close agreement between the molar ratios inferred from EXAFS and XRD, thus providing another indication that Pt_3Cu and Pt_3Cu AW are homogeneous bimetallic alloys at all spatial scales.[54] A more quantitative descriptor of the local homogeneity (up to ~ 6 Å) of bimetallic nanoparticles is the Cowley short range order parameter (α_{Pt-Cu}), given by: [142, 143]

$$\alpha_{Pt-Cu} = 1 - \frac{CN_{Pt-Cu}/(CN_{Pt-Pt} + CN_{Pt-Cu})}{x_{Cu}/100} \quad (5.3)$$

whereby CN_{Pt-Pt} refer to number of nearest Pt neighbours surrounding Pt atoms, and x_{Cu} is derived from equation (5.2).[54] A complementing parameter (α_{Cu-Pt}) can additionally be estimated on the basis of CN_{Cu-Pt}, CN_{Cu-Cu} and $x_{Pt} = 100 - x_{Cu}$ (which substitute CN_{Pt-Cu}, CN_{Pt-Pt} and x_{Cu} in equation (5.2)). Regardless of the approach, both calculations yield values of ~ +0.1 for both samples, which is again indicative of a homogeneously random alloy[142] and similar to the results for Pt-Ni[53] and Pt-Pd aerogels.[54]

Table 5.1 Coordination number (CN), atomic bond length (R), mean square bond length disorder (σ^2) and shift of energy (ΔE_0) derived from the simultaneous fitting of the EXAFS (Pt L_3 and Cu K edges) for Pt_3Cu, Pt_3Cu AW and PtCu AW aerogels, along with the corresponding R-factors (fit quality parameter,[2] whereby R-values ≤ 0.02 are regarded as indicative of high quality fits).

Aerogel	Bond	CN	R [Å]	σ^2 [10^{-3} Å^2]	ΔE_0 [eV]	R-factor
Pt_3Cu	Pt-Pt	7.8 ± 0.7	2.717 ± 0.004	7 ± 1	5.3 ± 0.5	0.017
	Pt-Cu	2.1 ± 0.5	2.661 ± 0.010	10 ± 2		
	Cu-Pt	6.7 ± 0.9	2.661 ± 0.010	10 ± 2		
	Cu-Cu	3.2 ± 1.4	2.633 ± 0.014	10 ± 4	2.4 ± 0.6	
Pt_3Cu AW	Pt-Pt	7.6 ± 0.8	2.716 ± 0.004	7 ± 1	5.4 ± 0.7	0.016
	Pt-Cu	2.1 ± 0.7	2.660 ± 0.013	10 ± 3		
	Cu-Pt	6.9 ± 2.1	2.660 ± 0.013	10 ± 3		
	Cu-Cu	3.3 ± 2.6	2.623 ± 0.030	10 ± 8	1.4 ± 1.6	
PtCu AW	Pt-Pt	7.0 ± 0.9	2.698 ± 0.005	7 ± 1	4.1 ± 0.8	0.025
	Pt-Cu	2.8 ± 0.9	2.647 ± 0.013	12 ± 3		
	Cu-Pt	6.8 ± 1.8	2.647 ± 0.013	12 ± 3		
	Cu-Cu	3.1 ± 2.0	2.618 ± 0.023	10 ± 6	1.4 ± 1.3	

On the other hand, the EXAFS fit for PtCu AW yielded an R-factor that was slightly larger than 0.02, indicating a lower quality fit.[2] In this case the local bimetallic composition deviated only slightly from the ICP-OES result ($x_{Cu} \approx 26$ at. % for the latter, vs. 29 at. % from EXAFS) and Cowley's short range order parameter amounted to ≈ 0. These results point towards a homogeneous alloy[142] with a shorter Pt-Pt bond length than the Pt_3Cu samples (2.698 vs. 2.717 Å) that may explain the slightly higher ORR activity of PtCu AW. Indeed, this well-documented impact of the Pt-Pt bond length on the ORR activity[170, 175-177] ties directly with the 'geometric effect' discussed above, whereby alloy-induced compressive lattice strain leads to a weaker adsorption of O-intermediates.[178] As an example of this, Kaito et al.[175] have recently presented a linear correlation between Pt-Pt bond length and ORR activity for alloys of Pt with other transition metals (i.e., Ni, Co, Cu) in which shorter bond lengths are directly related with a higher ORR activity, which is in line with our own trend (PtCu AW ≥ Pt_3Cu ≥ Pt_3Cu AW).

Table 5.2 Copper contents (x_{Cu}, at. %) obtained from ICP-OES, XRD, STEM-EDX and EXAFS data and Cowley short range order parameter (α) for various aerogel samples.

Aerogel	x_{Cu} (ICP-OES)	x_{Cu} (XRD)	x_{Cu} (EDX)	x_{Cu} (EXAFS)	α (Pt-Cu)	α (Cu-Pt)
Pt_3Cu	25	25 ± 3	22 ± 7	24 ± 7	+0.11	+0.11
Pt_3Cu AW	20	24 ± 1	20 ± 5	23 ± 11	+0.07	+0.11
PtCu	50	35 ± 5	39 ± 2	n/a	n/a	n/a
PtCu AW	26	29 ± 4	29 ± 3	29 ± 12	+0.02	+0.03

In a last step, scanning transmission electron microscopy in combination with energy-dispersive X-ray spectroscopy was used to locally investigate the alloy homogeneity and structure (e.g. formation of core-shell-type structures[169]) for selected regions, in contrast to the integral techniques discussed above (XRD and XAS). Representative combined Cu (red)/Pt (blue) element maps for all four specimens are shown in Figure 5.4. Their respective chemical compositions, calculated by averaging the corresponding values obtained from EDX maps of at least ten regions (~ 150 nm^2 each) for each sample, are summarized in Table 5.2. Visually comparing the Cu/Pt element maps obtained for each of the four specimens, no inhomogeneities can be observed. For Pt_3Cu and Pt_3Cu AW (Figure 5.4A and Figure 5.4B), however, we sporadically found regions with Cu contents of up to ~ 30 at. % upon quantitative analysis of EDX maps, which explains

the rather large error bars in Table 5.2. Nonetheless, in sight of the Cowley short range order parameters (α) of ~ +0.1 derived from bulk-sensitive EXAFS (cf. Table 5.2), these regions are not representative of the overall samples' homogeneity. Even so, sporadic variations in the chemical composition along the nanochains could explain the slightly positive value of α.[54] Moreover, no indication was found for the formation of a core-shell-type structure after acid washing, i.e., a Cu deficient shell and a Pt rich core.

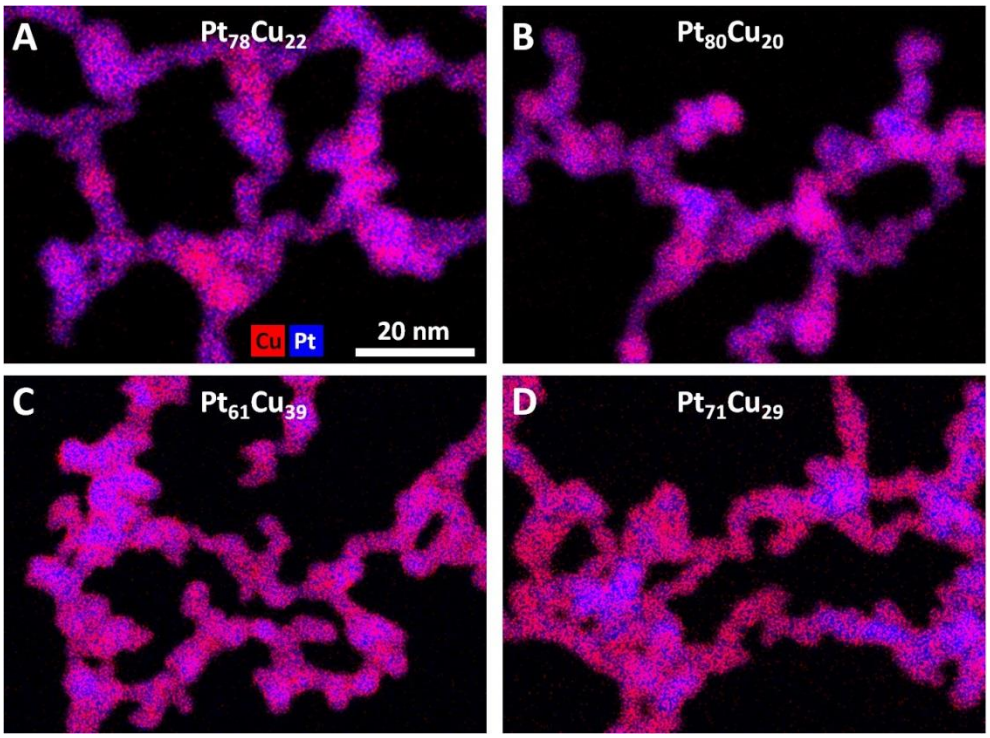

Figure 5.4 Combined Cu (red)/Pt (blue) element maps obtained by STEM-EDX measurements of Pt_3Cu (A: as-synthesized, B: acid-washed) and PtCu (C: as-synthesized, D: acid-washed) aerogels; the stoichiometric compositions are included at the top of the maps.

Similarly to the Pt_3Cu specimens, PtCu (Figure 5.4C) shows a homogeneous distribution of Pt and Cu atoms in the EDX map, whereby the average x_{Cu} was determined to be 39 at. %; this is slightly lower than the value 50 at. % derived from ICP-OES, probably due to the presence of Cu oxides in parts of the sample, while remaining in good agreement with XRD data (cf. Table 2). After acid washing (Figure 5.4D) the homogeneity of PtCu AW is retained but x_{Cu} decreases to 29 at. %, again in good agreement with values from ICP-OES, XRD and EXAFS.

Based on the combined findings from XRD, STEM-EDX and EXAFS, the main reason for the difference in ORR activities for the investigated samples appears to be the Cu content

in the Pt-Cu alloy phase. Thus, in Figure 5.5 the ORR surface-specific activities were plotted vs. the initial alloy phase Cu contents derived through Vegard's law on the basis of the XRD data (cf. Table 5.2). To extend this analysis to a wider range of Cu contents, we included in Figure 5.5 ORR activity values reported for several Pt-Cu/C catalysts (cf. references 166, 171, 174, 175, 179, 180), adapted from the customary value of 0.9 V_{RHE} to the 0.95 V_{RHE} used herein by assuming a Tafel slope of 60 mV dec^{-1}. Those references were selected carefully following three criteria to increase comparability. First, the ORR activities were recorded under similar conditions [181], i.e. in O_2-saturated 0.1 M $HClO_4$ and using scan rates between 5 and 10 mVs^{-1}. Second, the alloy compositions were determined by either XRD or EDX (which in our case yielded similar results, cf. Table 5.2) and, for alloys with an initially high Cu-content, they were assessed after voltammetric conditioning. And third, only materials with ECSAs below 50 m^2/g_{Pt} were considered to minimize the influence of particle size effects on the ORR activity.[35]

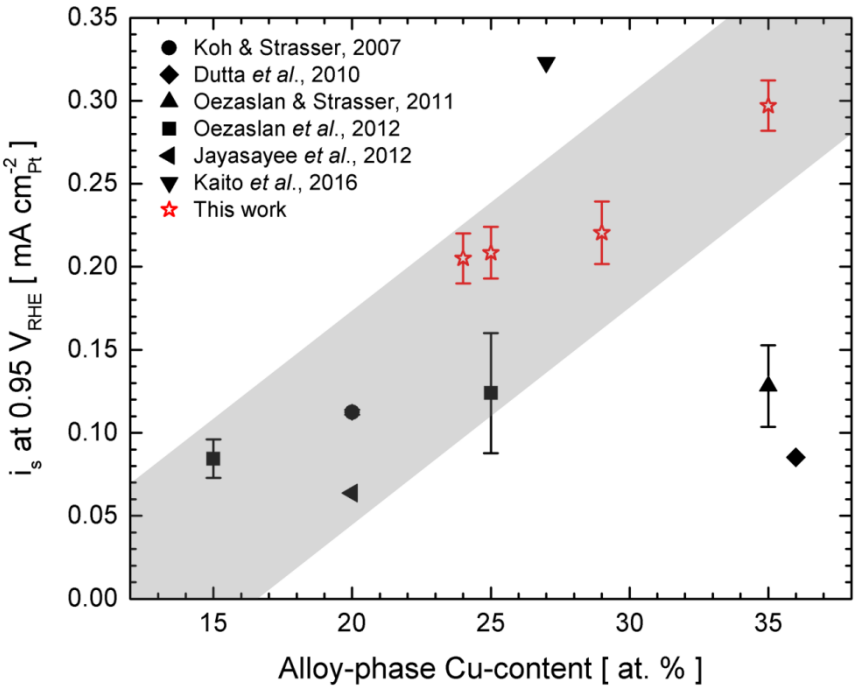

Figure 5.5 Surface-specific ORR activities at 0.95 V_{RHE} (from Figure 5.2 or various literature sources) vs. Cu content in the alloy phase (from XRD or EDX). The activity values for Pt-Cu/C catalysts (black symbols) are deduced from references 166, 171, 174, 175, 179, 180, assuming a Tafel slope of 60 mV dec^{-1} and the grey area serves as guide for the eye of the linear correlation.

Interestingly, when the Cu range covered by the as-synthesized and acid-washed aerogels in this work is considered (24 - 35 at. %), an almost linear correlation between ORR activity and alloy phase Cu content can be found. When considering additional values from

the literature, this correlation still holds true for the majority of data points, as illustrated by a grey area in Figure 5.5.

The strong deviation from the general trend of the Pt-Cu/C catalysts with Cu-contents ≥ 35 at. % can be explained by the fact that these correspond to alloys with initial copper contents ≥ 50 at. % Cu, which were either electrochemically dealloyed[174] or acid-washed[166] before their composition and ORR activity were determined, possibly leading to non-uniformity of the samples and / or unreliability in the determination of their composition. Keeping in mind these differences in starting materials and preparation methods, the general trend points at the alloy phase Cu content as the critical parameter determining the catalytic activity of this sort of materials. The observed correlation can in terms be explained by the d-band center theory, since an increase in the Cu content leads to a downshift of the d-band center (with undetermined contributions from geometric and ligand effects), thereby increasing the number of free sites for O_2 adsorption and thus leading to the observed enhancement of the ORR activity.[150]

Beyond these mechanistic considerations, the apparent absence in these alloys of a protecting Pt-layer (i.e., of a core-shell structure, cf. above) that could prevent Cu-dissolution may have negative implications for their stability and PEFC-applicability. To verify this possibility, voltammetrically-conditioned electrodes of both alloy compositions were submitted to 100 more potential cycles between 0.5 and 1.0 V_{RHE} (at 50 mVs^{-1}, in 0.1 M $HClO_4$). Figure 5.11 in section 5.6.2 displays the effect of this added step on the aerogels' surface-specific ORR-activity, which barely changed for Pt_3Cu but decreased by ≈ 10 % for PtCu – a greater extent of activity loss that is likely related to the initially larger Cu-content (and corresponding ORR-activity) of this alloy, unfortunately liable to dissolution and that will lead to an increase of the overpotential contributions related to ORR-kinetics and proton transfer along the catalyst layer upon PEFC-implementation.

5.5 Conclusion

In summary, we have presented the synthesis of bimetallic Pt-Cu aerogels with different Cu contents and studied the effect of acid washing (a mimic of the low pH in the PEFC) on the composition, structure and catalytic activity of these materials. The as-synthesized samples consist of Pt-Cu alloys, along with a copper oxide side phase for the aerogel with a higher Cu content. Upon acid washing, this oxide was removed and the Cu content in the alloy phase decreased but the overall aerogel structure was not altered. Additionally, as-synthesized Pt-Cu aerogels were tested for ORR activity in RDE experiments, whereby

they met or even exceeded the DOE ORR mass-specific activity target by up to 30 %. Acid-washed specimens showed lower ORR activity which could be related to the reduced Cu content in the alloy phase which, in agreement with previous reports in the literature, is linearly related to the ORR activity due to the upshift of the d-band center induced by a decrease of the alloy Cu content. Most importantly, since the loss of copper upon acid washing reported here will likely be reproduced during PEFC operation, affecting catalyst activity and cell performance, aerogels should be submitted to resembling acid-washing or equivalent voltammetric conditioning steps (seemingly detrimental to their reactivity) prior to MEA implementation. Thus, in order to retain the outstanding initial ORR activity of the PtCu aerogel, future work will focus on minimizing Cu leaching for these materials.

5.6 Appendix – Supplementary Information

5.6.1 Materials and Methods

Electron microscopy

Transmission electron microscopy was performed using a Tecnai T20 from FEI equipped with a LaB_6 cathode at an accelerating voltage of 200 kV. TEM specimens were prepared by drop casting a dispersion of aerogel in acetone on a copper grid with a thin Formvar-carbon film. For determination of the aerogel nanochain diameter histogramms, the nanochain diameter was measured at least in 200 different spots.

HAADF-STEM imaging and element mapping based on energy dispersive X-ray spectroscopy (EDX) of the as-synthesized and acid-washed Pt-Cu aerogels were performed at 200 kV with a Talos F200X analytical microscope equipped with X-FEG electron source and Super-X detector system (FEI). Prior to STEM analysis, the specimen mounted in a high-visibility low-background holder was placed for 2 s into a Model 1020 Plasma Cleaner (Fischione) to remove possible organic contamination. Quantification of the EDXS data including Bremsstrahlung background correction based on the physical TEM model, series fit peak deconvolution, and application of tabulated theoretical Cliff-Lorimer factors was done for the elements Pt and Cu using the ESPRIT software version 1.9 (Bruker). For at least 10 specimen regions (~ 150 nm^2 each) per sample, integrated EDX spectra were analyzed and the obtained composition values were averaged.

X-ray photoelectron spectroscopy

X-ray photoelectron spectroscopy measurements were performed using a VG ESCALAB 220iXL spectrometer (Thermo Fischer Scientific) with an Al Kα monochromatic source (1486.7 eV) and a magnetic lens system. Binding energies of the acquired spectra were referenced to the C 1s line at 284.9 eV.

X-ray diffraction measurements

XRD measurements were performed in reflection mode with a Bruker D2 PHASER operated at a voltage of 30 kV and a current of 10 mA with Cu Kα radiation (λ = 0.15406 nm).

5.6.2 Supplementary Figures

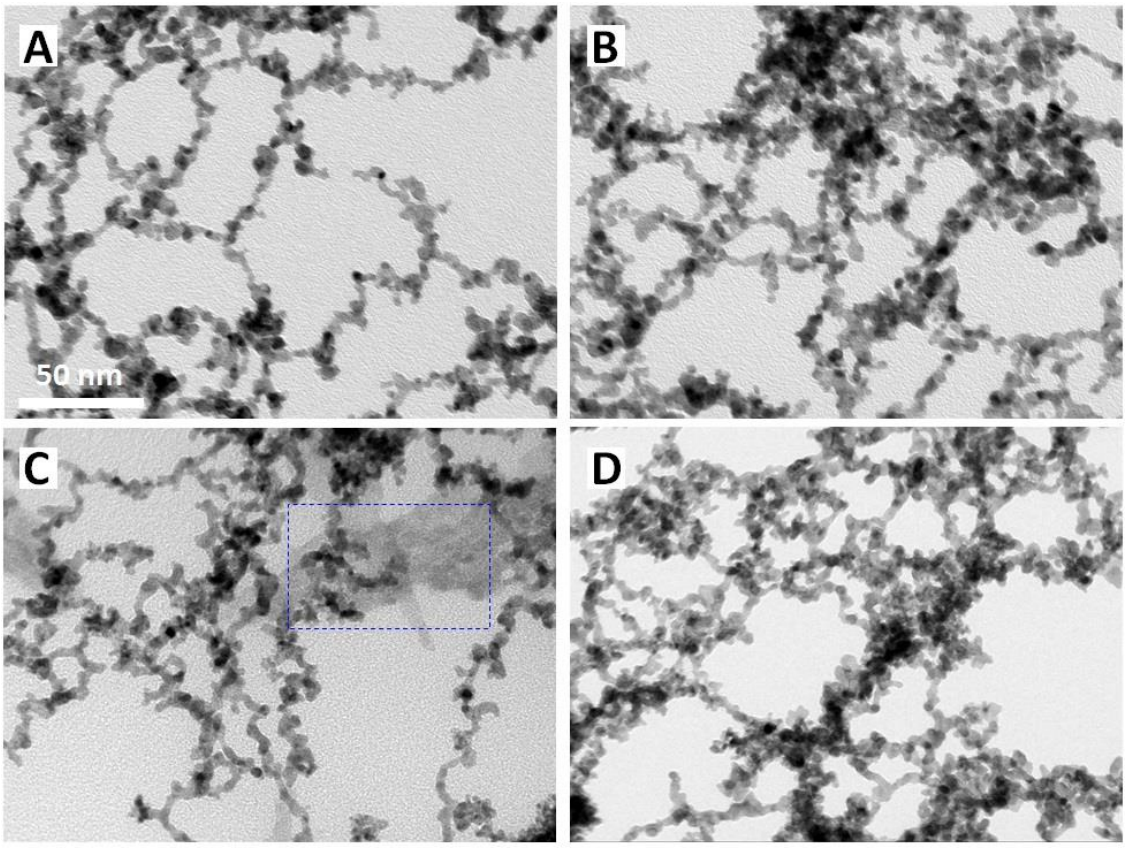

Figure 5.6 TEM images of Pt_3Cu (A: as-synthesized, B: acid-washed) and PtCu (C: as-synthesized, D: acid-washed) aerogels; the copper oxide side phase for PtCu is highlighted by a blue frame.

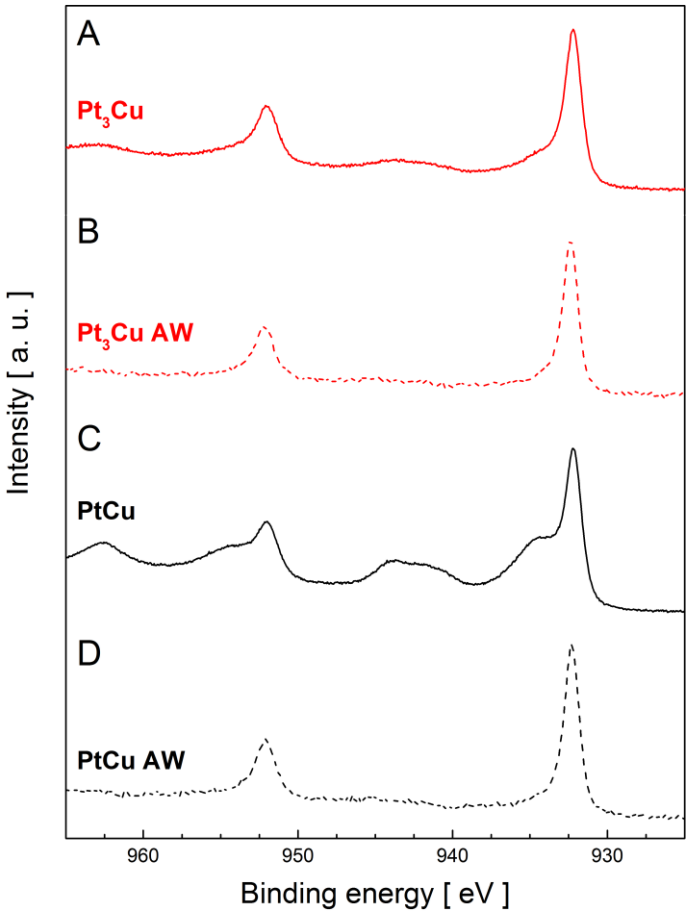

Figure 5.7 Cu 2p X-ray photoelectron spectra of Pt_3Cu (A), Pt_3Cu AW (B), PtCu (C) and PtCu AW (D).

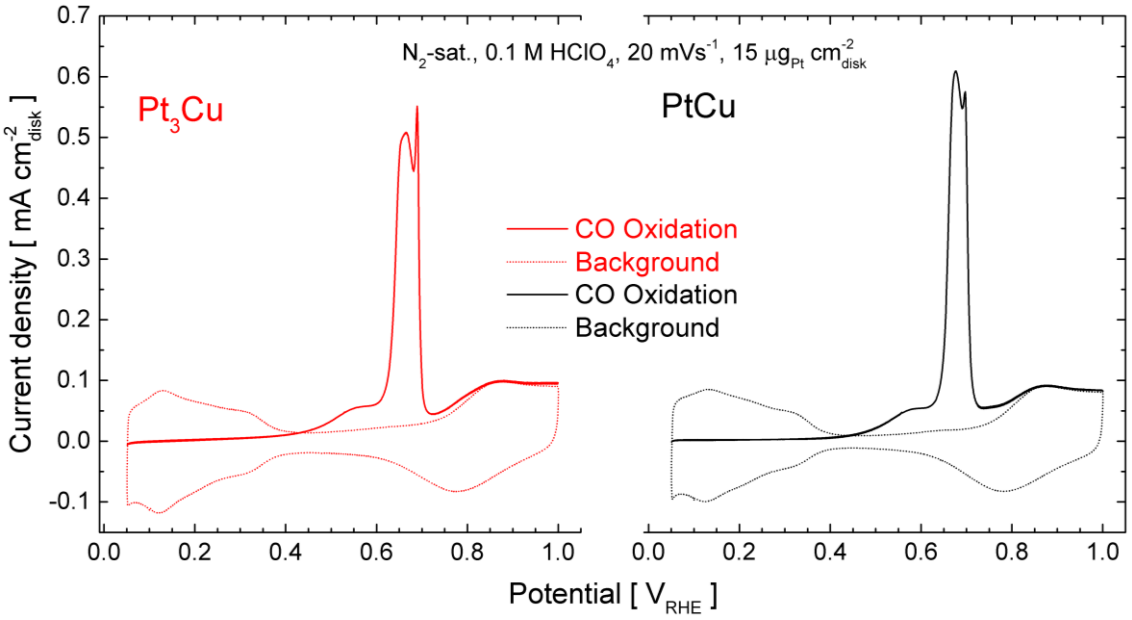

Figure 5.8 Cyclic voltammograms from CO stripping experiments (solid lines) for Pt_3Cu (left) and PtCu (right) aerogels. In brief, the electrode was held at a potential of 0.1 V_{RHE} while the 0.1 M $HClO_4$ electrolyte was purged with CO for 5 min. Subsequently the electrolyte was saturated with N_2 for 20 min before the adsorbed CO was oxidized by a positive potential sweep at 20 mVs^{-1} up to 1.0 V_{RHE}. The subsequent, steady-state CVs in N_2-saturated electrolyte that were used to calculate H_{upd} charges are shown in dotted lines as a reference.

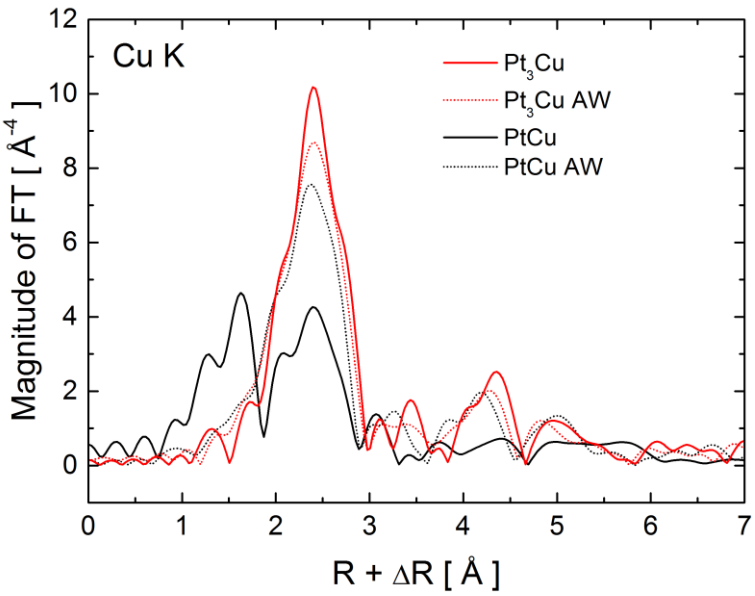

Figure 5.9 Cu K edge Fourier-transformed EXAFS (k^3-weighted) in R-space (uncorrected for phase shifts) for Pt-Cu aerogels.

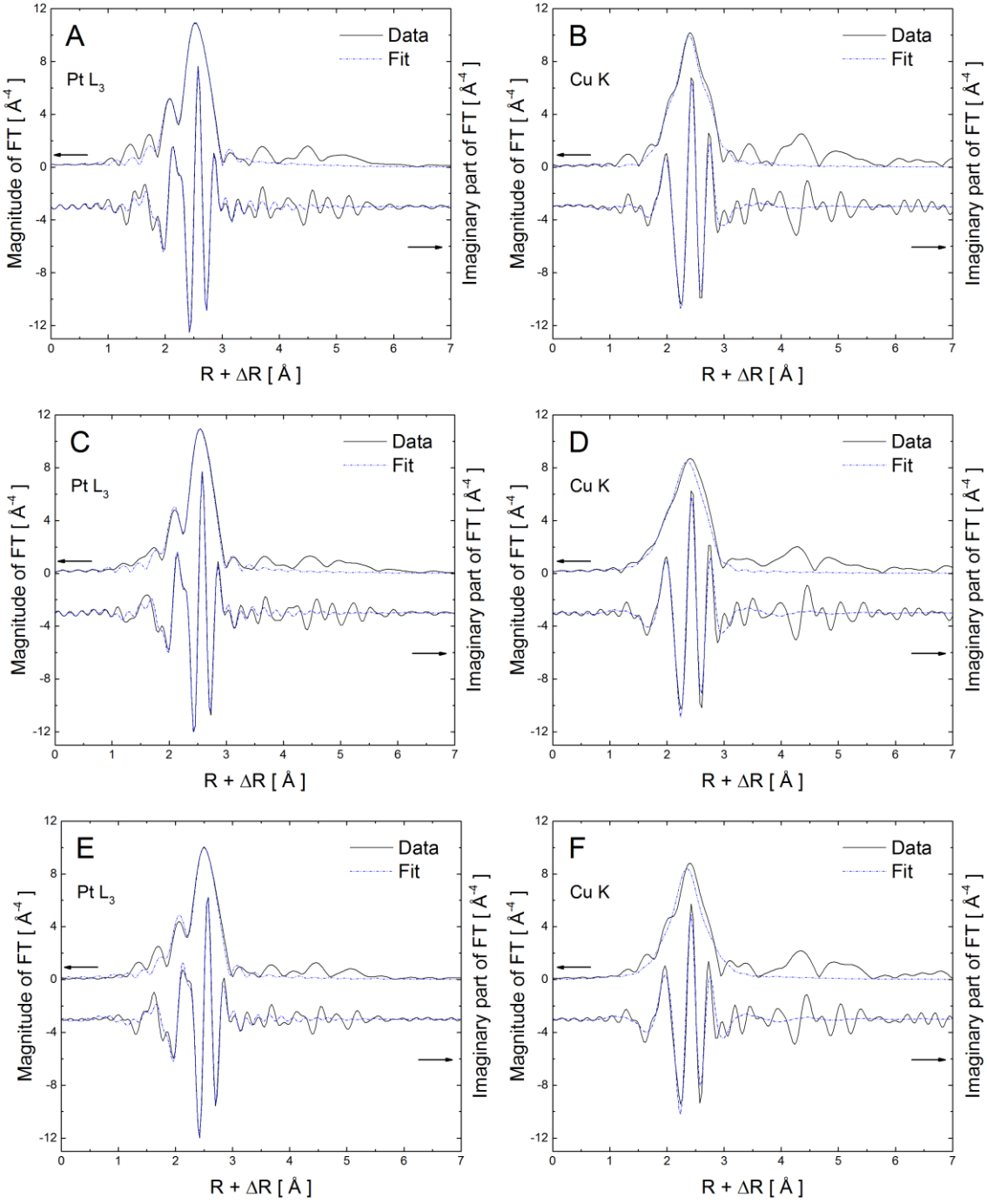

Figure 5.10 EXAFS fit and experimental data (k^3-weighted) in R-space (uncorrected for phase shifts) for Pt_3Cu (A, B), Pt_3Cu AW (C, D) and PtCu AW (E, F) at the Pt L_3 and Cu K edge.

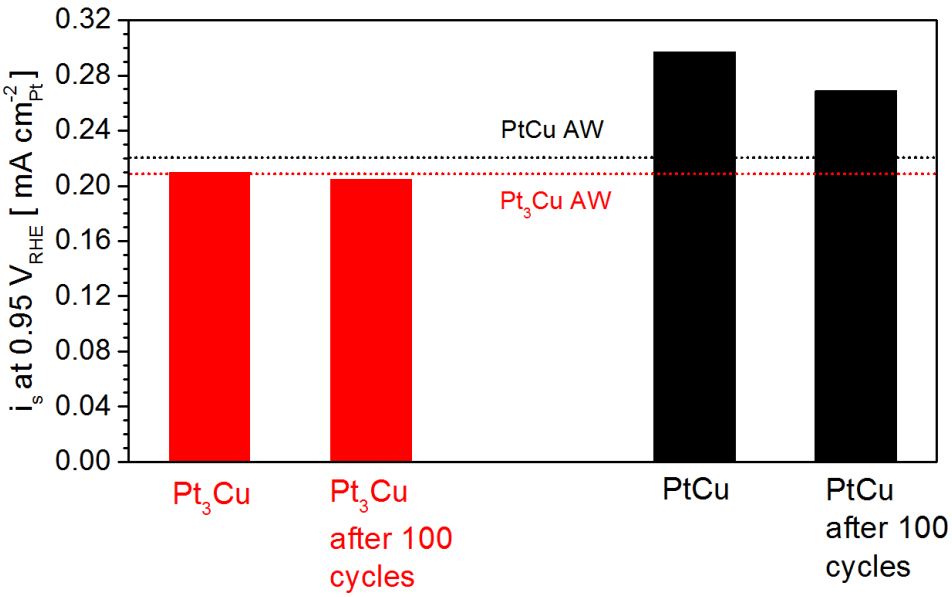

Figure 5.11 Surface-specific ORR-activities of Pt_3Cu and PtCu aerogels at 0.95 V_{RHE}, derived from RDE voltammetry measurements in O_2-saturated 0.1 M $HClO_4$ performed just after the standard voltammetric pre-conditioning, or following the recording of 100 additional cycles (at 50 mVs^{-1}) between 0.5 and 1.0 V_{RHE}.

6 Optimization of Pt-Ni Aerogel Catalyst Layer for PEFC Application

6.1 Unsupported Pt-Ni Aerogels with Enhanced High Current Performance and Durability in Fuel Cell Cathodes

As discussed in section 2.3, switching from supported to unsupported catalysts can entail significant changes of the catalyst layer properties, stressing the importance of real PEFC tests to assess a catalyst's application potential. What is more, in recent years, the adequacy of ORR activity values (i.e. current at 0.9 V_{RHE} in RDE experiments) as predictors of the performance at the high current densities relevant for high power fuel cell operation has been questioned.[32, 182] Thus in this chapter, a thorough study of the high current density performances and the respective CLs for unsupported Pt_3Ni aerogel and a supported commercial Pt/C catalyst is presented. At first, the mass transport efficiencies in the former catalyst layers are compared by I/E curve experiments under H_2/air and H_2/O_2 conditions. Next, the observed differences are related to different CL porosities and pore size distributions, both obtained from FIB-SEM experiments. Lastly, a method to optimize the CL of unsupported Pt_3Ni aerogel to reach a performance commensurate with the one of a supported Pt/C catalyst is introduced and an outlook on the durability of Pt_3Ni aerogel is given.

Unsupported Pt-Ni Aerogels with Enhanced High Current Performance and Durability in Fuel Cell Cathodes

Sebastian Henning[a], Hiroshi Ishikawa[b], Laura Kühn[c], Juan Herranz[a], Elisabeth Müller[d], Alexander Eychmüller[b] and Thomas J. Schmidt[a,e]

[a]Electrochemistry Laboratory, Paul Scherrer Institut, 5232 Villigen, Switzerland

[b]Interdisciplinary Graduate School of Medicine and Engineering, University of Yamanashi, 4 Takeda, Kofu, 400-8511, Japan

[c]Physical Chemistry, Technische Universität Dresden, Bergstr. 66b, 01062 Dresden, Germany

[d]Paul Scherrer Institut, 5232 Villigen, Switzerland

[e]Laboratory of Physical Chemistry, ETH Zurich, 8093 Zurich, Switzerland

ABSTRACT

Highly active and durable oxygen reduction catalysts are needed to reduce the costs and enhance the service life of polymer electrolyte fuel cells. This can be accomplished by alloying Pt with a transition metal (e.g. Ni) and by eliminating the corrodible, carbon-based catalyst support – however, materials combining both approaches have seldom been implemented in PEFC cathodes. In this work, an unsupported Pt-Ni alloy nanochain ensemble (aerogel) demonstrates high current PEFC performance commensurate with that of a carbon-supported benchmark (Pt/C) following optimization of the aerogel's catalyst layer structure. The latter is accomplished using a soluble filler to shift the CL's pore size distribution towards larger pores which improves reactant and product transport. Chiefly, the optimized PEFC aerogel cathodes display ≈ 2.5-fold larger surface-specific ORR activity than Pt/C and maintain 90 % of the initial activity after an accelerated stress test (vs. 40 % for Pt/C).

Published in *Angew. Chem. Int. Ed.*, **56**, 10707 (2017).

6.2 Introduction

Polymer electrolyte fuel cells are a promising, environmentally friendly alternative to combustion engines for automotive application, yet further cost reductions and durability improvements are necessary to foster their widespread use.[3] To reach cost targets, the amount of Pt required for catalyzing the reactions inside the PEFC needs to be reduced ≈ 4-fold, down to 0.1 g_{Pt}/kW.[3] Thereby, efforts focus on the catalytically more demanding oxygen reduction reaction, for which improved activity is commonly achieved by alloying Pt with non-noble metals.[51] Complementarily, the excessive loss of performance observed during PEFC operation is caused by the corrosion of the carbon support used in state-of-the-art platinum catalysts (Pt/C) upon high potential excursions,[35] and has intensified research on non C-supported and unsupported catalysts over the last years.[31, 89, 128] Aiming to tackle both challenges, our previous work on an unsupported Pt_3Ni aerogel (cf. transmission electron microscopy images in Figure 6.6, section 6.5.4) showed that this material reaches the ORR activity target for automotive PEFCs set by the U.S. Department of Energy (i.e. 440 A/g_{Pt} at 0.9 V_{RHE}) when tested in liquid electrolyte half cells using the rotating disk electrode technique.[53] Considering the need to translate these advances to the technical system and the lack of fuel cell studies dealing with unsupported systems,[32, 182] this study reports on the successful optimization of the Pt_3Ni aerogel PEFC performance, also demonstrating the material's remarkable stability under accelerated stress test conditions.

6.3 Results and Discussion

The first PEFC tests in H_2/air conditions revealed the poor performance of Pt_3Ni vs. Pt/C cathodes (Figure 6.1A), which is attributed to inefficient gas transport discernible from the large mass transport losses that arise when switching from O_2 to air ($\eta_{tx}(O_2\text{-air})$ in Figure 6.1B; cf. sections 6.5.2 and 6.5.3 for calculation details and a more detailed breakdown of the different overpotential contributions discussed along Figure 6.4 and Figure 6.5). Moreover, the ≈ 30 % smaller electrochemical surface area values obtained in PEFC vs. RDE experiments for Pt_3Ni aerogel (see Table 6.1, section 6.5.4) imply that the electrode suffers from low utilization, i.e. not all the Pt surface area is available for the electrochemical reaction (in contrast to the parity among ECSA values for Pt/C).[35] This condition makes the activity determination less reliable and causes the relatively low surface-specific ORR activity (SA) for Pt_3Ni in the PEFC, which is comparable to the one of

Pt/C (cf. Figure 6.1C and Figure 6.7B, section 6.5.4),[35] whereas from RDE experiments a 3-fold activity enhancement would have been expected (see Figure 6.7A).

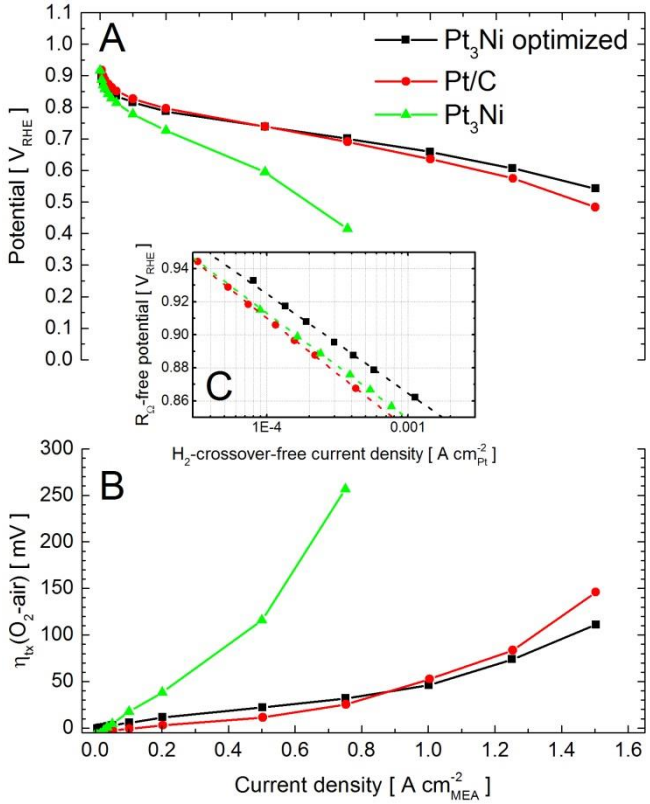

Figure 6.1 (A) I/E curves at 80°C, 100 % RH in H_2/air at 1.5 bar_{abs}, (B) air vs. O_2 mass transport losses at the cathode (see section 6.5.1 for details) and (C) Tafel plots in H_2/O_2 for Pt_3Ni optimized, Pt_3Ni and Pt/C MEAs (≈ 0.31 mg_{Pt}/cm^2_{geom} for all cathodes).

To understand the reason for this poor mass transport, we prepared catalyst layers of Pt_3Ni and Pt/C on conductive metal foil substrates (see section 6.5.1) and analyzed their cross section by scanning electron microscopy. The CL thicknesses for comparable electrode loadings of ≈ 0.5 mg_{Pt}/cm^2_{geom} at the electrode centers amount to ≈ 1.6 µm and ≈ 20 µm for Pt_3Ni and Pt/C, respectively (see Figure 6.2A and Figure 6.8, section 6.5.4), whereby the latter value is in agreement with the literature.[31] Moreover, despite its surface roughness, the average thickness of the Pt_3Ni CL is fairly constant along various locations between the electrode's center and edge, as shown in Figure 6.2C. Additionally, based on the measured thicknesses and assuming densities of 19 g/cm^3 for Pt_3Ni and 2 g/cm^3 for carbon and ionomer,[35] significantly different porosities of ≈ 64 % for Pt_3Ni (see Figure 6.9, section 6.5.4) and ≈ 78 % for Pt/C were estimated (disregarding the electrode's edge at ≥ 4.0 mm from its center).

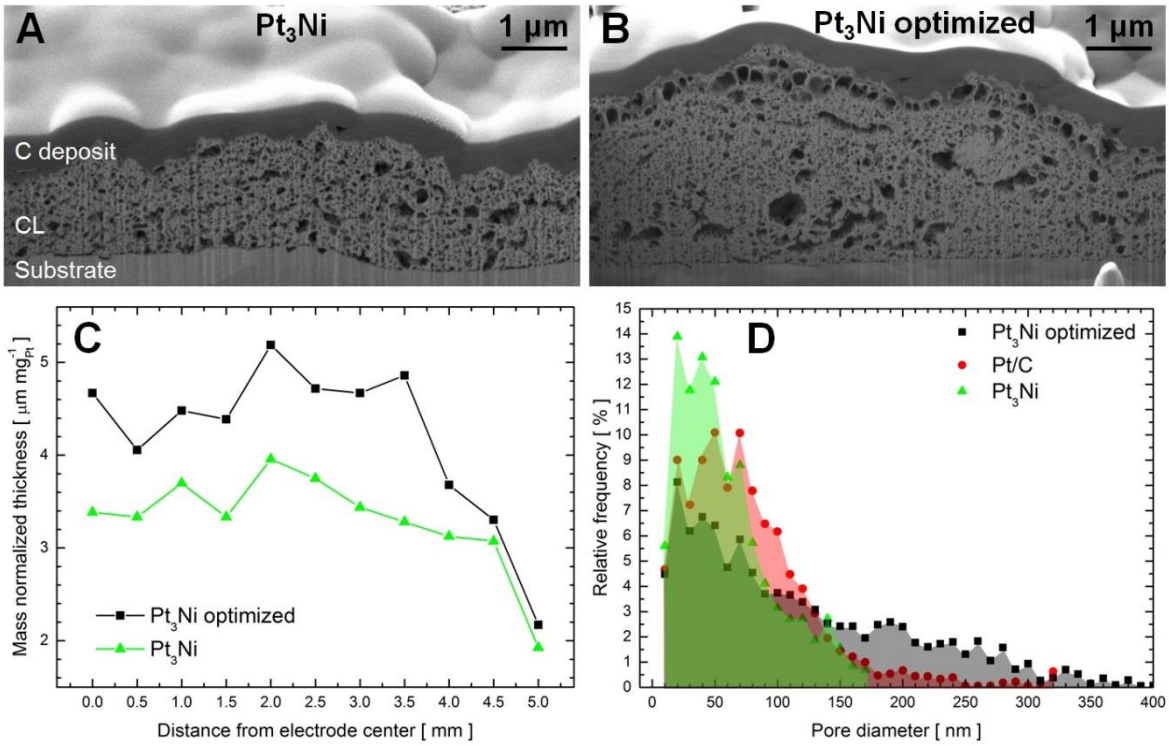

Figure 6.2 (A, B) Representative cross section SEM images and (C) thickness as a function of the distance from the electrode center for catalyst layers of Pt_3Ni (0.48 mg_{Pt}/cm^2_{geom}) and Pt_3Ni optimized (0.53 mg_{Pt}/cm^2_{geom}). (D) Pore size distributions derived from FIB SEM tomography for Pt_3Ni, Pt_3Ni optimized and Pt/C CLs.

The impact of the CL structure on the PEFC performance was further clarified by analyzing the corresponding pore size distributions (PSDs) using focused ion beam SEM tomography (see Figure 6.10 in section 6.5.4 for representative cross section SEM images). As summarized in Figure 6.2D, the pores in the Pt_3Ni CL are concentrated in the mesoporous range (diameter < 50 nm) in which Knudsen diffusion prevails under PEFC operation conditions.[20, 29, 183] This mechanism is considered less efficient than the molecular diffusion in macropores of diameters > 50 nm and likely explains the poorer mass transport in Pt_3Ni vs. Pt/C CLs. However, the PSDs and porosities to reach optimal PEFC performance are expected to be different for unsupported Pt_3Ni aerogel and Pt/C CLs due to the dissimilar electrode thickness and catalyst hydrophilicity.

To address the issue of poor mass transport, a filler material was added to the aerogel ink in an attempt to provide a template for pore formation during the initial spray coating step of the catalyst layer onto the membrane (see section 6.5.1 for details). Looking for a salt with high solubility in water that could be easily removed from the resulting catalyst coated

membrane by a simple washing step, K_2CO_3 was selected due to its additional ability to evolve CO_2 gas (and potentially further increase the CL's porosity) if the washing step were to be performed in an acidic solution. Thus, CCMs were prepared according to this approach and the amounts of K_2CO_3 and Nafion ionomer (Na^+-exchanged to avoid acidic conditions) were optimized via a series of screening experiments with an abbreviated break-in protocol. First, the volume ratio of salt vs. aerogel and ionomer ($V_{K2CO3}/V_{Pt3Ni+Naf}$, for details see section 6.5.1) was varied between 0 and 1.5, and subsequently the Nafion-to-catalyst ratio (NCR) was optimized for the best $V_{K2CO3}/V_{Pt3Ni+Naf}$ value. Figure 6.11A in section 6.5.4 displays the effect of the initial K_2CO_3 content on the mass-specific ORR activities (MAs) at 0.9 V_{RHE}, which increase by ≈ 90 % before reaching a plateau for $V_{K2CO3}/V_{Pt3Ni+Naf}$ values ≥ 0.5; similarly, the mass of Pt per kW at 0.65 V_{RHE} (in H_2/air) reaches a constant minimum in the same $V_{K2CO3}/V_{Pt3Ni+Naf}$ range (cf. Figure 6.11C). Fixing the $V_{K2CO3}/V_{Pt3Ni+Naf}$ ratio to 0.5, analogous screening experiments (cf. Figure 6.11B/D) yielded an optimized NCR-value of 0.12.

Such best-performing CLs (referred to as 'Pt_3Ni optimized' in the following) show greatly improved PEFC performance (Figure 6.1A) and mass transport properties comparable to those of Pt/C electrodes as displayed in Figure 6.1B, and the CL optimization displays good reproducibility (Figure 6.12, section 6.5.4). Moreover, the SA of the Pt_3Ni optimized membrane electrode assembly is ≈ 2.5-fold larger than that of Pt/C and Pt_3Ni, as discernable from Figure 6.1C and Figure 6.7B, thereby almost matching the ≈ 3-fold improvement factor observed in RDE experiments (cf. Figure 6.7A) and slightly exceeding the performance of a commercial Pt_3Ni/C catalyst (see Figure 6.13 and Table 6.2 in section 6.5.4). This SA increase coincides with an improved electrode utilization following CL optimization (from ≈ 75 % to ≈ 95 %, cf. Table 6.1), which also becomes apparent when comparing mass-normalized cyclic voltammogramms of these two electrodes (see Figure 6.14, section 6.5.4).

Analysis of Pt_3Ni optimized CLs by FIB-SEM reveals significant increases in thickness (Figure 6.2B) and porosity (Figure 6.9) when compared to Pt_3Ni CLs, whereby the latter increased from ≈ 64 % to ≈ 74 % and almost matches the value for Pt/C (≈ 78 %). Moreover, the PSDs in Figure 6.2D reveal a positive shift in the average pore sizes for Pt_3Ni optimized vs. Pt_3Ni CLs, leading to fewer pores in the mesoporous range and emphasizing the determining role of mesopore vs. macropore diffusion mechanisms on the improved mass transport and PEFC performance of Pt_3Ni optimized CLs.[20, 29, 183]

To understand how K_2CO_3 alters the CL's porosity and PSD, cross sections of the Pt_3Ni optimized CL before and after acid washing (AW) were studied by SEM and energy dispersive X-ray spectroscopy elemental mapping. Pt, Ni and K are homogeneously distributed (cf. Figure 6.15, section 6.5.4) and there are no indications of large K_2CO_3 precipitates. The K_2CO_3 is completely dissolved upon acid washing, since the unambiguous potassium Kα-line peak at ≈ 3.3 keV present in the EDX spectra of the as-prepared CL disappeared after AW (cf. Figure 6.16C/D, section 6.5.4). Moreover, identical location SEM images recorded before and after AW (cf. Figure 6.16A/B) did not reveal any discernable structural changes of the CL cross section. Together, these observations suggest that K_2CO_3 is incorporated in the CLs as precipitates of sizes below 300 nm (cf. Figure 6.2D) which dissolve upon AW and thereby shift the CL′s porosity and PSD.

Lastly, Pt_3Ni optimized MEAs were subjected to an AST consisting of 10000 cycles between 1.0 and 1.5 V_{RHE} at 500 mVs^{-1} (cf. Figure 6.3) proposed by the DOE to investigate catalyst support stability,[4, 33] and to an even more extended protocol of 1000 cycles at 20 mVs^{-1} (see Figure 6.17, section 6.5.4). The beginning- and end-of-life (BOL, EOL) I/E curves in H_2/air in Figure 6.3A illustrate that the performance of the Pt_3Ni optimized MEAs is sustained throughout the stress test, whereas Pt/C suffers from severe degradation. More precisely, the MA at 0.9 V_{RHE} decreases by ≈ 10 % for Pt_3Ni optimized, as compared to a ≈ 60 % decrease for Pt/C, as shown in Figure 6.3B and Figure 6.17B, highlighting the stability of the Pt_3Ni aerogel in the investigated potential range.

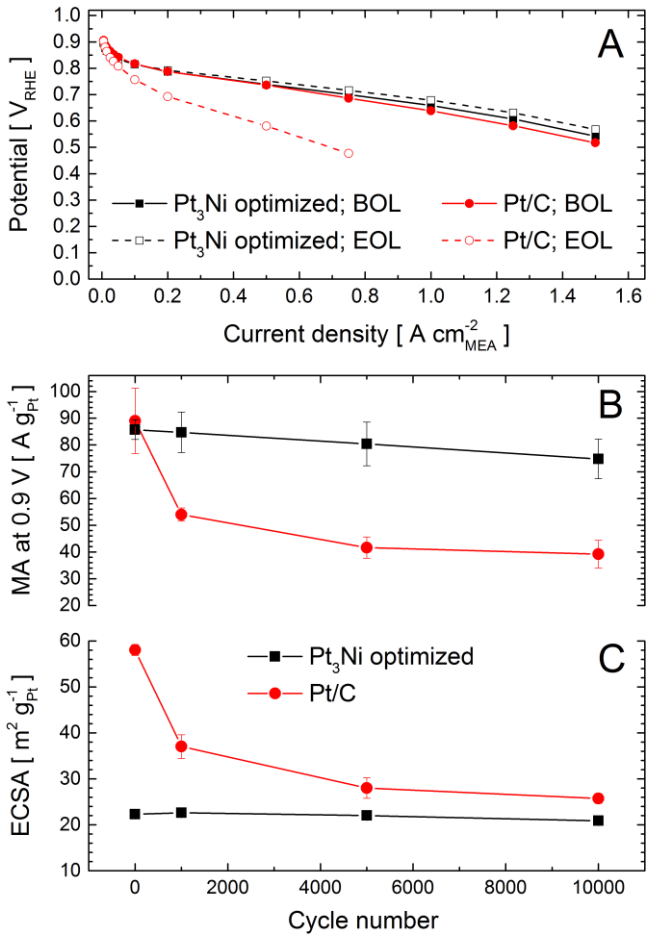

Figure 6.3 (A) Beginning- and end-of-life I/E curves at 80°C, 100 % RH, in H_2/air at 1.5 bar_{abs} for the accelerated stress test of Pt_3Ni optimized and Pt/C MEAs (cathode loadings of 0.3 - 0.4 mg_{Pt}/cm^2_{geom}). (B, C) Average (three repetitions) MA at 0.9 V_{RHE} and ECSA (at 80°C) as a function of the potential cycles between 1.0 and 1.5 V_{RHE}.

Interestingly, the evolution of the ECSA values measured at 80°C in Figure 6.3C matches that of the mass activities, showing a minor decrease for Pt_3Ni optimized and a ≈ 60 % loss for Pt/C (see Figure 6.18 in section 6.5.4 for CVs at different stages of the AST). Consequently, surface-specific activities (cf. Figure 6.19, section 6.5.4) remain almost constant for Pt/C and Pt_3Ni optimized, indirectly suggesting a lack of change in the catalysts' particle size that should have led to SA changes (on the basis of the well-known particle size effect on SA, cf. references 24, 35, 184). Thus, mechanisms like Ostwald ripening and particle coalescence that lead to an increase in particle size do not constitute the dominant degradation cause.[7] Instead, in agreement with previous literature,[7, 33, 160, 185] the performance loss for Pt/C is mainly attributed to particle detachment due to carbon corrosion. This additionally leads to a decrease in porosity and average pore size that in

terms cause the large EOL mass transport losses in Figure 6.3A.[48] Albeit minor, the degradation observed for the Pt_3Ni aerogel is tentatively attributed to metal dissolution, whereby non-noble Ni is expected to be leached out of the alloy preferentially. This event can lead to a positive shift of the catalyst's d-band center, thereby decreasing the number of free sites for O_2 adsorption and the ORR activity.[150] The details of the degradation mechanism will be studied separately in a forthcoming work.

6.4 Conclusion

In summary, we have for the first time presented the successful implementation of an unsupported aerogel as the ORR catalyst in a PEFC cathode. To achieve the same high current density performance as a Pt/C benchmark, Pt_3Ni aerogel CLs were optimized by adding K_2CO_3 to the catalyst ink, which was later removed by acid washing the CCM. The performance improvement caused by the addition of K_2CO_3 is explained by an increase in porosity and average pore size that were calculated from cross section SEM images and FIB-SEM tomography data. Additionally, optimized Pt_3Ni MEAs showed a ≈ 2.5-fold increased surface-specific ORR activity with respect to Pt/C, which is in good agreement with the results from RDE experiments. Finally, the Pt_3Ni aerogel displayed excellent stability during an AST of 10000 potential cycles between 1.0 and 1.5 V_{RHE}, making this material a very promising cathode catalyst for PEFCs.

6.5 Appendix – Supplementary Information

6.5.1 Materials and Methods

Catalyst synthesis

Pt_3Ni aerogel was synthesized according to the procedure described in reference 53. In brief, 0.585 ml of a 0.205 M H_2PtCl_6 solution (8 wt. % in H_2O, Sigma Aldrich) and 4 ml of a freshly prepared 10 mM $NiCl_2$ solution ($NiCl_2$*$6H_2O$ 99 %, Sigma Aldrich) were dissolved in 790 ml of ultrapure water (18.2 MΩ cm, Millipore) and stirred until the mixing was complete. Subsequently, 7.0 ml of freshly prepared 0.1 M $NaBH_4$ solution (granular, 99.99 %, Sigma Aldrich) were added while stirring vigorously. A brown solution was obtained that was kept stirring for another 30 min. Afterwards, the reaction solution was distributed among several 100 ml vials. After about four days, black Pt_3Ni hydrogel was formed at the bottom of the containers. The hydrogel was washed with water and the solvent was exchanged with acetone afterwards. The resulting anhydrous gels were subjected to critical point drying in CO_2 (Critical Point Dryer 13200J-AB, SPI Supplies).

Rotating disk electrode measurements

Electrolyte solutions were prepared from 60% $HClO_4$ (Kanto Chemical Co., Inc.) diluted in ultrapure water (18.2 MΩ cm, Elga Purelab Ultra). High purity N_2 (5.0) and O_2 (5.0) were purchased from Messer AG, Switzerland. The electrochemical measurements were performed in a home-made three electrode glass cell. A reversible hydrogen electrode was connected to the main cell compartment through a Luggin capillary, and a gold mesh (99.99 % metals basis, Alfa Aesar) held in a separate tube in contact with the main cell served as counter electrode. The working electrode was a PTFE-made, interchangeable rotating ring-disk electrode (Pine Research Instrumentation) equipped with a Pt-ring and a mirror-polished, glassy carbon disk insert (5 mm diameter, HTW Hochtemperatur-Werkstoffe GmbH). Before the measurements, the WE was mounted to a polyetheretherketone shaft that was attached to a modulated speed rotator (both Pine Research Instrumentation). A Biologic VSP-300 was used as potentiostat, in combination with the EC-Lab® V11.01 software package. The ohmic drop was determined by electrochemical impedance spectroscopy, applying a 5 mV perturbation (100 kHz to 1 Hz) at 0.45 V_{RHE}. Thin-film electrodes were prepared by dispersing Pt/C (47 wt%, Tanaka Kikinzoku Kogyo K.K. (TKK), TEC10E50E) in mixtures of ultrapure water (18.2 MΩ cm, Elga Purelab Ultra) and isopropanol (99.9 %, Chromasolv Plus® for HPLC, Sigma Aldrich),

followed by 10 min of sonication in an ultrasonic bath (USC100T, 45 kHz, VWR).[111] Fractions of the ink were pipetted onto the glassy carbon inset of the RRDE to obtain catalyst loadings of 15 $\mu g_{Pt}/cm^2_{electrode}$. Subsequently, coatings were dried under a gentle N_2-flux.

The mass-specific ORR activity at 0.9 V_{RHE} was extracted from anodic sweeps between 0.05 and 1.05 V_{RHE} at 5 mVs^{-1} and 1600 rpm in O_2-satured electrolyte after correcting for cell resistance and mass transport limitations applying the Koutecky-Levich equation.[147] The electrochemical surface area was obtained from the hydrogen underpotential deposition charge in cyclic voltammogramms in N_2-saturated electrolyte (at 20 mVs^{-1}), assuming a conversion factor of 210 $\mu C/cm^2_{Pt}$.[35] ECSA and ORR activity values for Pt_3Ni aerogel were taken from reference 53 and the latter values (reported at 0.95 V_{RHE}) were extrapolated to 0.9 V_{RHE} assuming a Tafel slope of 60 mV dec^{-1}.[151]

MEA fabrication

Membrane electrode assemblies were fabricated using Pt_3Ni aerogel, Pt/C (47 wt%, TKK, TEC10E50E) or Pt_3Ni/C (27 wt% on high surface area carbon, Umicore AG) as the cathode catalyst (with loadings of 0.3 - 0.4 mg_{Pt}/cm^2_{geom}), Nafion XL-100 (DuPont) as the membrane and commercial gas diffusion electrodes (Johnson Matthey, 0.4 mg_{Pt}/cm^2_{geom} HISPEC 9100 Pt/HAS on Sigracet GDL 25 BC) as the anode.

Catalyst inks for Pt_3Ni electrodes were prepared by mixing 5 mg of catalyst, 12 mg of a 5 wt% Nafion solution (Nafion 1100EW, Sigma Aldrich, equal to a Nafion-to-catalyst-ratio of 0.12) and 1.0 ml of a 8 wt% aqueous isopropanol solution (ultrapure water, 18.2 MΩ cm, Elga Purelab Ultra and isopropanol, 99.9 %, Chromasolv Plus® for HPLC, Sigma Aldrich). After ultrasonication (USC100T, 45 kHz, VWR) for 30 minutes, the ink was applied on the membrane by spray coating, using a frame to confine the coating to the active area of 1 cm^2. For Pt/C (Pt_3Ni/C) cathodes, 50 mg of catalyst was mixed with 500 (660) mg of 5 wt% Nafion solution (equal to a Nafion-to-carbon-ratio of 1.0) and 4.5 ml of a 20 wt% aqueous isopropanol solution, followed by the steps described above. Optimized Pt_3Ni electrodes were prepared by mixing 5 mg of catalyst, 0.7 mg of K_2CO_3 (99.995% trace metals basis, Sigma Aldrich), 18 mg of Na^+-exchanged Nafion solution (prepared from a 1:2 mixture of 0.1 M NaOH and Nafion solution,[186] and equal to a Nafion-to-catalyst-ratio of 0.12) and 1.0 ml of an 8 wt% aqueous isopropanol solution. Na^+-exchanged Nafion was selected to avoid acidic conditions before the acid washing step. After ultrasonication and spray coating, the resulting catalyst coated membranes were immersed into 1 M H_2SO_4

solution (96 %, Suprapur, Merck) overnight (≈ 16 hours), followed by rinsing with ultrapure water and drying under ambient conditions. According to EDX analyses of optimized aerogel catalyst layer cross sections before and after acid washing, this step causes a minor composition change, from $Pt_{75}Ni_{25}$ to $Pt_{77}Ni_{23}$, which is also consistent with the Ni content in the washing solution, quantified by inductively coupled plasma - optical emission spectroscopy. Note also that, in sections 6.3 and 6.5.4, the amount of K_2CO_3 is referred to as $V_{K2CO3}/V_{Pt3Ni+Naf}$, i.e. the volume of K_2CO_3 divided by the combined volume of Pt_3Ni aerogel and Nafion assuming solid materials. For the masses given above, and Pt_3Ni, K_2CO_3 and Nafion densities[35] of 19.0, 2.4 and 2.0 g/cm^3, $V_{K2CO3}/V_{Pt3Ni+Naf}$ amounts to ≈ 0.5 for optimized Pt_3Ni cathodes.

In a last step, the CCMs were hotpressed at 120°C and 1 bar/cm$^2_{geom}$ for 5 minutes with a gas diffusion layer (GDL 25 BC, Sigracet) and a commercial gas diffusion electrode (see above) on the cathode and anode side, respectively.

MEA characterization

The fabricated MEAs were placed in a differential fuel cell that allows studying the MEA under homogeneous, well-defined conditions in the absence of along-the-channel effects such as changing temperature, relative humidity and gas concentration.[121] The cell used for this study was developed inhouse, featuring 5 parallel channels of 1 mm width over an active area of 1 cm^2.[122] Using steel spacers with defined thickness, cell compression was set such that ≈ 25 % compression of the gas diffusion media was obtained.[122, 187] The abbreviated MEA break-in for the screening experiments (cf. Figure 6.11) was done in H_2/O_2 at 1.5 bar_{abs} and a relative humidity of 100 % between 25 and 80° for 2 hours (flow rates anode/cathode: 300/750 ml/min[188], stoichiometries ≥ 30/≥ 30), drawing the maximum current that would yield cell potentials > 0.6 V. The extended MEA break-in used for the I/E curves in Figure 6.1, Figure 6.3 and Figure 6.12 was comprised of the abbreviated break-in, cooling down of the cell, and the abbreviated break-in again. It must be noted here that even as the applied stoichiometry ratios are significantly higher than for technical cells, the gas flow velocities remain in the same order of magnitude due to the reduced size of the device.[121]

CVs were measured after break-in at 25°C and 100% RH, scanning the potential between 0.075 and 1.0 V_{RHE} at 50 mVs^{-1} with a H_2 anode flow rate of 50 ml/min and the N_2 cathode flow halted just prior to the measurement. The corresponding ECSA value was averaged from the H-adsorption and H-desorption charges between 0.09 and 0.4 V_{RHE} after

double-layer correction, assuming a conversion factor of 210 $\mu C/cm^2_{Pt}$.[35] H_2-crossover tests were conducted by a linear potential sweep from 0.6 to 0.1 V_{RHE} with a scan rate of 1 mVs^{-1} at 80°C, 100 % RH, 1.5 bar_{abs}, an anode H_2 flow rate of 300 ml/min and a cathode N_2 flow rate of 750 ml/min, respectively.[19] The H_2-crossover current densities in this study typically amounted to ≈ 2 mA/cm^2_{MEA}.

All I/E curves were recorded at 80°C and 100 % RH with anode/cathode flow rates of 300/750 ml/min (stoichiometries ≥ 30/≥ 30) at 1.5 bar_{abs} for either H_2/O_2 or H_2/air, using a Biologic VSP-300 potentiostat with a 10A/5V current booster. The measurement was done galvanostatically, whereby the cell current was stabilized for 3 minutes at each data point and the data was averaged from the last 2 minutes. Concomitantly, the cell resistance (R_Ω, cf. below) was determined for each data point by galvanostatic electrochemical impedance spectroscopy (1 MHz to 1 Hz). Mass- and surface-specific activites for H_2/O_2 operation were extracted at 0.9 V_{RHE} after correcting potential and current for cell resistance and H_2-crossover, respectively.

The accelerated stress test was performed by cycling the potential 10000 (1000) times between 1.0 and 1.5 V_{RHE} at 500 (20) mVs^{-1} at 80°C, 100 % RH, ambient pressure, anode H_2 flow of 100 ml/min and cathode N_2 flow of 100 ml/min, respectively. At designated times (1000, 5000 cycles), the AST was interrupted to record I/E curves and CVs (cf. above) to determine the ECSA. Since the latter CVs were recorded at 80°C in this test, the ECSA values in Figure 6.3C are lower than the ones reported in Table 6.1 and Figure 6.17 (derived at 25°C).[189]

Electron microscopy

Transmission electron microscopy images were obtained on a TECNAI F30 operated at 300 kV. For tomography and cross section preparation with a focused ion beam/scanning electron microscope, a Zeiss NVision 40 microscope with a Ga^+ beam source and EDX detector was employed. Catalyst layers subjected to electron microscopy analysis were prepared similarly to the CCMs as described in the section ‘MEA fabrication’, albeit on conductive Cu-foil, Au-foil or GDL substrates.

To analyze the catalyst layer thickness at various locations between center and edge of the electrode, two cross sections of 10 µm width and at least 20 µm apart were cut for each data point in Figure 6.2C. Prior to the FIB cutting, the area around the cross section was covered with a smooth carbon layer (thickness ≥ 0.5 µm) to minimize curtaining

effects.[48] Due to the great surface roughness of the catalyst layer, minimum and maximum thicknesses were determined for each cross section image and averaged to yield the values in Figure 6.2C. Elemental mapping of these cross sections by EDX was performed at an accelerating voltage of 7 kV, thereby acquiring 25 line scans (voxel size 8 nm x 8 nm) of an area of ≈ 8 µm x 2 µm.

FIB SEM tomography, i.e. serial sectioning, was performed on cuboid-shaped structures (cf. Figure 6.10) using an acceleration voltage of 30 kV (beam current of 10 pA) for the Ga^+ beam and a slice thickness of ≈ 5 nm. For each section, SEM images at a magnification of ≈ 14000 and an acceleration voltage of 1 kV were recorded with a secondary (SE) and energy selective backscattered electron (ESB) detector in an automated mode, resulting in a voxel size of 4 nm x 4 nm x 5 nm.

Reconstruction of the three-dimensional structure was performed with the ImageJ software package including the Fiji plugin package. First, images were properly aligned using ImageJ's StackReg plugin, thereby applying a rigid body transformation algorithm correcting for both translation and rotation in the image plane.[190, 191] Second, a representative region of interest for further analysis was selected on the images. For Pt_3Ni a region of 1 µm x 1 µm was found adequate, whereas for Pt_3Ni optimized and Pt/C a region of 2 µm x 2 µm was chosen due the larger pore sizes in the latter structures. Previous to segmentation, SE and ESB images were combined linearly to increase contrast between solid and pore and to remove edge effects, followed by application of a median filter to remove noise and outliers. Next, segmentation (i.e. the distinction between solid and pores) was performed manually by defining a global threshold value[48, 190] based on visual inspection of subsequent sections at the beginning, middle and end of the image stack. Prior to calculating the pore size distribution, x- and y-resolution of the images was reduced by applying ImageJ's scale function to obtain cubic voxels of 5 nm x 5 nm x 5 nm. The PSD was calculated using an algorithm which is available from the ImageJ plugin published in reference 192 and that fits the largest possible spheres into the pore system, yielding a continuous pore size distribution.

6.5.2 Calculation of Mass Transfer Losses (η_{tx} O_2-air)

The cell voltage of a PEFC can be expressed as follows[13]

$$E_{cell} = E_{rev} - i R_{\Omega} - \eta_{HOR} - i R_{H+,anode} - \eta_{ORR} - i R_{H+,cathode} - \eta_{tx} \quad (6.1)$$

whereby E_{rev} is the thermodynamic equilibium potential (a function of gas partial pressures and temperature), R_{Ω} is the cell resistance, i is the current density, $R_{H+,\ anode}$ and $R_{H+,\ cathode}$ are the effective proton resistances of the respective catalyst layers, η_{HOR} and η_{ORR} correspond to the anodic and cathodic kinetic overpotentials, and η_{tx} is the gas diffusion overpotential caused by H_2/O_2 concentration gradients.

When switching from O_2 to air on the cathode side, while keeping the H_2 concentration at the anode and the operating relative humidities (i.e., no changes in η_{HOR}, R_{Ω}, $R_{H+,anode}$ or $R_{H+,cathode}$), the difference in E_{cell} at a given current can be described as

$$E_{cell,O2} - E_{cell,air} = E_{rev,O2} - E_{rev,air} - \eta_{ORR,O2} + \eta_{ORR,air} - \eta_{tx,O2} + \eta_{tx,air} \quad (6.2)$$

Thus, $\eta_{tx}(O_2$-air) can be estimated from the cell potential difference by calculating the shift in E_{rev} and the kinetic overpotential

$$\eta_{tx}(O_2 - air) = -\eta_{tx,O2} + \eta_{tx,air} =$$
$$\Delta E_{cell} - E_{rev,O2} + E_{rev,air} + \eta_{ORR,O2} - \eta_{ORR,air} = \Delta E_{cell} - \frac{R\,T}{z\,F} \ln \frac{p_{O2}}{p_{air}} - \gamma \frac{R\,T}{\alpha\,F} \ln \frac{p_{O2}}{p_{air}} \quad (6.3)$$

where $R = 8.314\ J\ K^{-1}\ mol^{-1}$, $T = 353.15\ K$, $z = 4$, $F = 96485\ C\ mol^{-1}$, $p_{O2}/p_{air} = 4.76$, the cathodic transfer coefficient α equals 1 and the kinetic reaction order at constant overpotential γ is 0.5.[11]

6.5.3 Overpotential Contributions to the PEFC Performance

On the basis of the extremely fast kinetics of the hydrogen oxidation reaction on Pt in acid medium,[147] PEFC anodes with relatively large Pt-loadings (like the 0.4 mg_{Pt}/cm^2_{geom} used in this study) lead to negligible kinetic and proton transfer overpotentials for this reaction (i.e., $\eta_{HOR} \approx R_{H+,anode} \approx 0$),[11] and thus equation (6.1) can be simplified into the form:

$$E_{cell} = E_{rev} - i R_{\Omega} - \eta_{ORR} - i R_{H+,cathode} - \eta_{tx} \quad (6.4)$$

To quantify the relative impact of the resistive terms in this equation (R_{Ω}, $R_{H+,cathode}$) on the fuel cell polarization curves in Figure 6.1, these measurements included potentiostatic electrochemical impedance spectroscopy (PEIS) tests at 0.2 V_{RHE} (with a 1 mV perturbation) while operating the PEFC at 80°C and with fully humidified H_2 and N_2 feeds

at the anode and cathode, respectively.[193] In the corresponding Nyquist plots for all three catalysts displayed in Figure 6.4, the intercept with the imaginary axis yields an R_Ω of ≈ 0.05 Ω·cm^2, in excellent agreement with the values estimated through galvanostatic EIS during the recording of the polarization curves (cf. 'MEA characterization' in section 6.5.1).

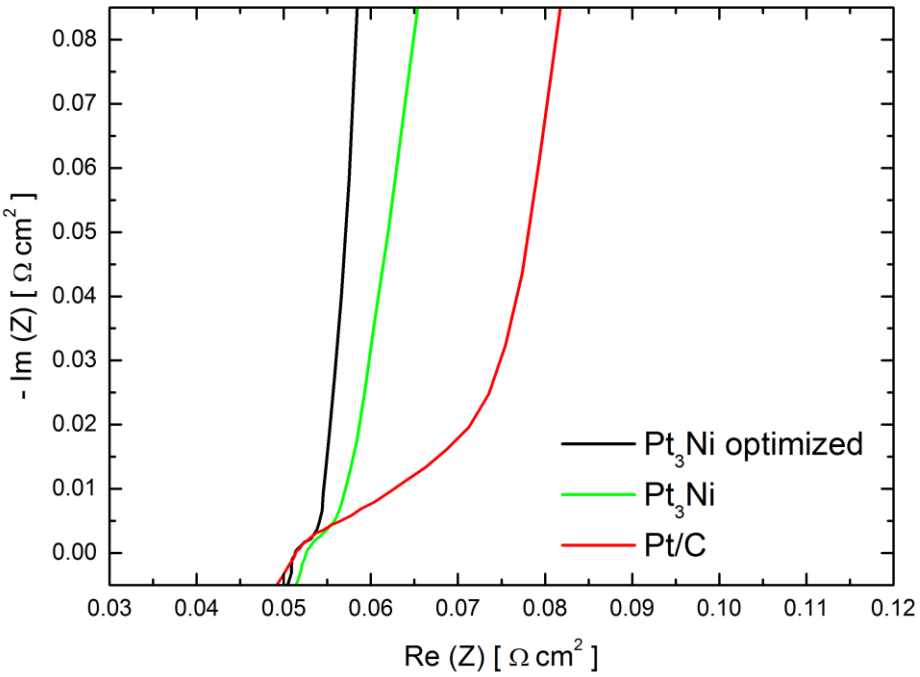

Figure 6.4 Nyquist plots derived from electrochemical impedance spectroscopy measurements at 0.2 V_{RHE} (1 mV perturbation), 80°C, and fully humidified H_2 and N_2 at anode and cathode, respectively.

Additionally, at 0.05 < Re(Z) < 0.07 Ω·cm^2, the Nyquist plot for Pt/C diplays a 45° line from which one can derive $R_{H+,cathode}$ using the equations:[193]

$$R_{H+} = C_{cath} 4\pi f [Re(Z) - R_\Omega]^2 \quad (6.5)$$

$$R_{H+,cathode} \approx R_{H+}/3 \quad (6.6)$$

where R_{H+} is the cathode proton resistance, f is the frequency used in the impedance measurement, and C_{cath} is the capacitance of the cathode catalyst layer, also derivable from the PEIS data with the equation:

$$C_{cath} = \lim_{f \to 0} \left[\frac{-1}{2\pi f \, Im(Z)} \right] \quad (6.7)$$

This approach yielded a C_{cath} value of ≈ 190 mF/cm$^2_{MEA}$, from which we derive R_{H+} ≈ 0.1 Ω·cm^2 and $R_{H+,cathode}$ ≈ 0.03 Ω·cm^2. The former value of R_{H+} is consistent with

literature estimates for CLs prepared using the same catalyst, parameters (0.4 mg_{Pt}/cm^2_{geom}, ionomer-to-carbon weight ratio of 1, 80°C) and PEIS approach, whereby $R_{H+} \approx 0.04$ or $\approx 0.2\ \Omega \cdot cm^2$ at relative humidities of 120 or 75 %, respectively.[194] On the other hand, the Nyquist plots of the aerogel catalyst layers in Figure 6.4 do not feature the characteristic 45° line allowing for this quantification of $R_{H+,cathode}$; a behavior that has been previously reported for impedance measurements on PEFC cathodes catalyzed by unsupported hollow nanospheres,[36] and that we attribute to the negligible proton transfer resistance in those and our ultra-thin CLs.

Following this quantification of R_Ω and (if applicable) $R_{H+,cathode}$, these values can be used to compute the ORR-overpotential (η_{ORR}) at low current densities (≤ 0.1 mA/cm^2_{MEA}) at which mass transport contributions to the measured performance can be considered negligable (i.e., $\eta_{tx} \approx 0$ in equation (6.4)). This data displays the logarthmic relation between potential and current expected from the Butler Volmer equation (i.e., $\eta_{ORR} \propto \log(i)$, with a Tafel slope of ≈ 70 mV/dec), and can therefore be used to compute the value of η_{ORR} at currents beyond this kinetically-controled regime. In Figure 6.5, we have applied this approach to decouple the impact of the different overpotential terms to the overall fuel cell performance for the three catalysts plotted in Figure 6.1 (Pt/C, Pt_3Ni and Pt_3Ni optimized). Chiefly, this analysis illustrates the relative contribution of mass transport losses to the overall performance; as an example, for a current of 0.75 mA/cm^2_{MEA}, η_{tx} accounts for ≈ 300 mV for Pt_3Ni, as compared to ≈ 35 and ≈ 25 mV for Pt/C and Pt_3Ni optimized, respectively − in excellent agreement with the easier-to-estimate values of $\eta_{tx}(O_2\text{-air})$ included in Figure 6.1B (see above section 6.5.2 for details).

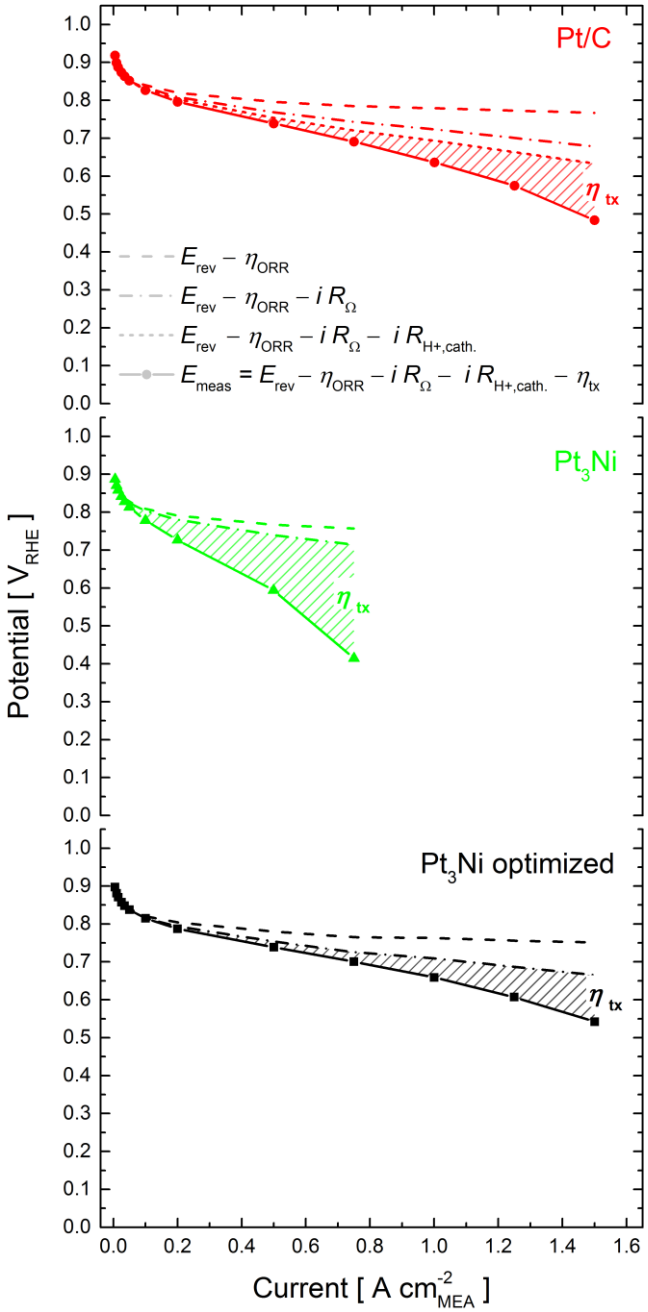

Figure 6.5 I/E curves at 80°C, 100 % RH, 1.5 bar_{abs} in H_2/air (solid lines, cf. Figure 6.1), along with the deconvolution of the overpotential contributions to the overall performance, whereby the patterened area in each pannel corresponds to the mass transport overpotential, η_{tx}.

6.5.4 Supplementary Figures and Tables

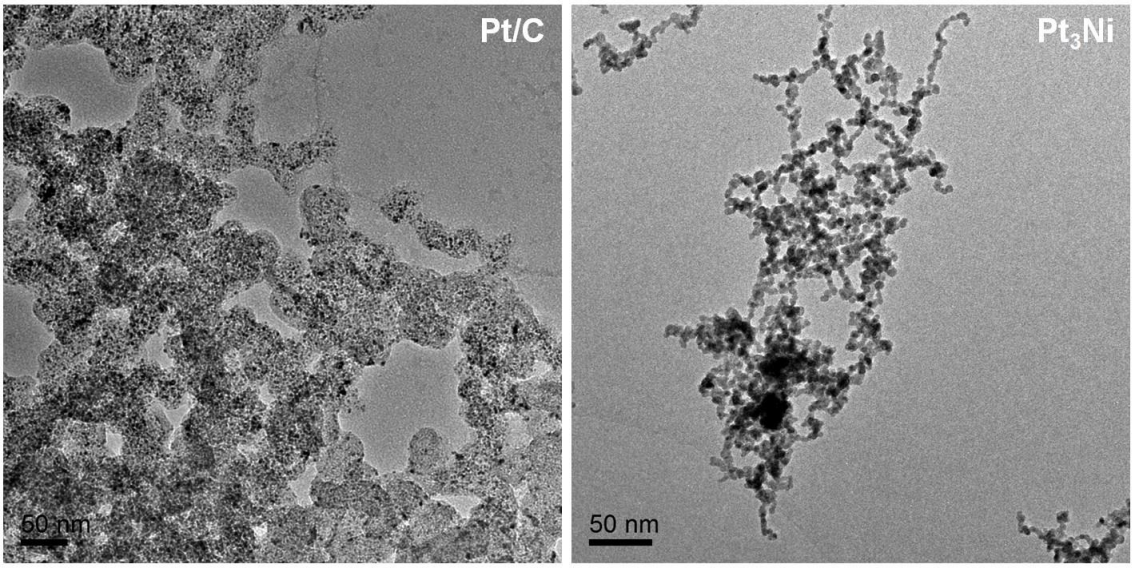

Figure 6.6 TEM images of the Pt/C benchmark catalyst (left) and of the Pt_3Ni aerogel (right).

Table 6.1 ECSA values obtained from cyclic voltammetry at 25°C in RDE and PEFC experiments (see section 6.5.1, averaged on the basis of three measurements); RDE data for Pt_3Ni was taken from reference 53.

ECSA (m^2/g_{Pt}) from	Pt/C	Pt_3Ni	Pt_3Ni optimized
RDE	75 ± 3	31 ± 2	31 ± 2
PEFC	77 ± 2	23 ± 1	30 ± 1

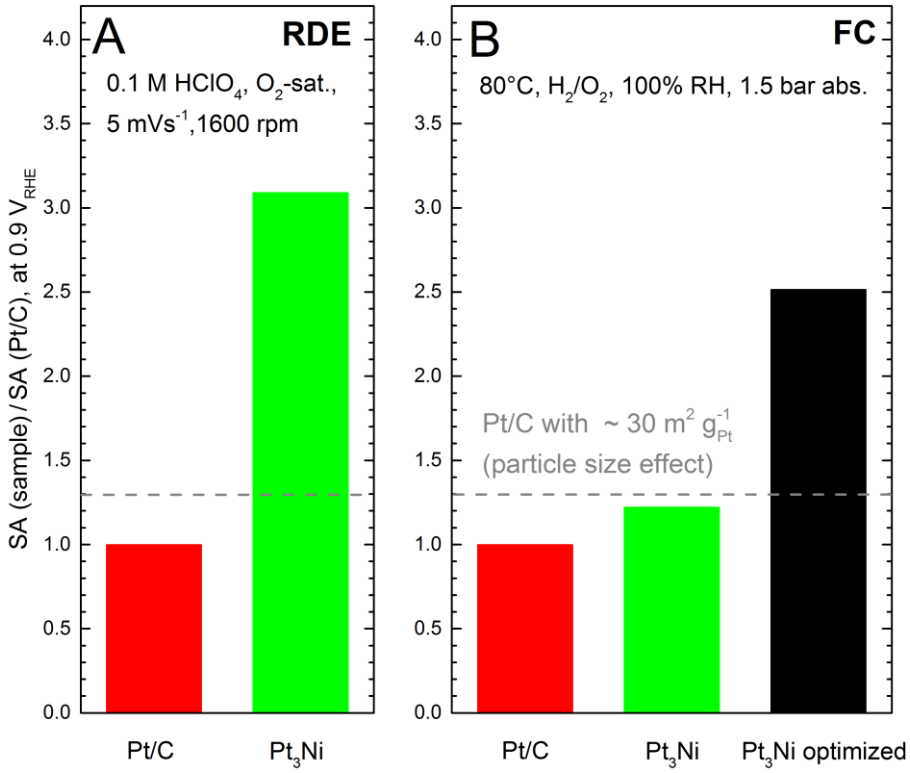

Figure 6.7 Improvement factor for the surface-specific ORR activity (SA) at 0.9 V_{RHE} normalized to the ECSA value derived from (A) RDE or (B) PEFC experiments. The grey dashed line indicates the SA increase that would be expected due to the particle size and ECSA effect on SA[35] upon using a Pt/C benchmark with an ECSA of ≈ 30 m^2/g_{Pt} (equal to the Pt_3Ni aerogel's ESCA, cf. Table 6.1).

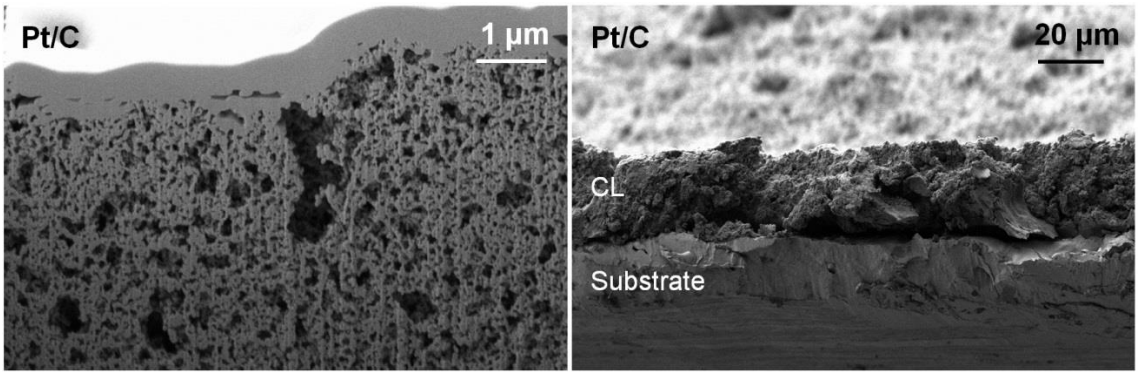

Figure 6.8 Cross section SEM images of the Pt/C benchmark catalyst layer at high (left) and low (right) magnification (0.47 mg_{Pt}/cm^2_{geom}).

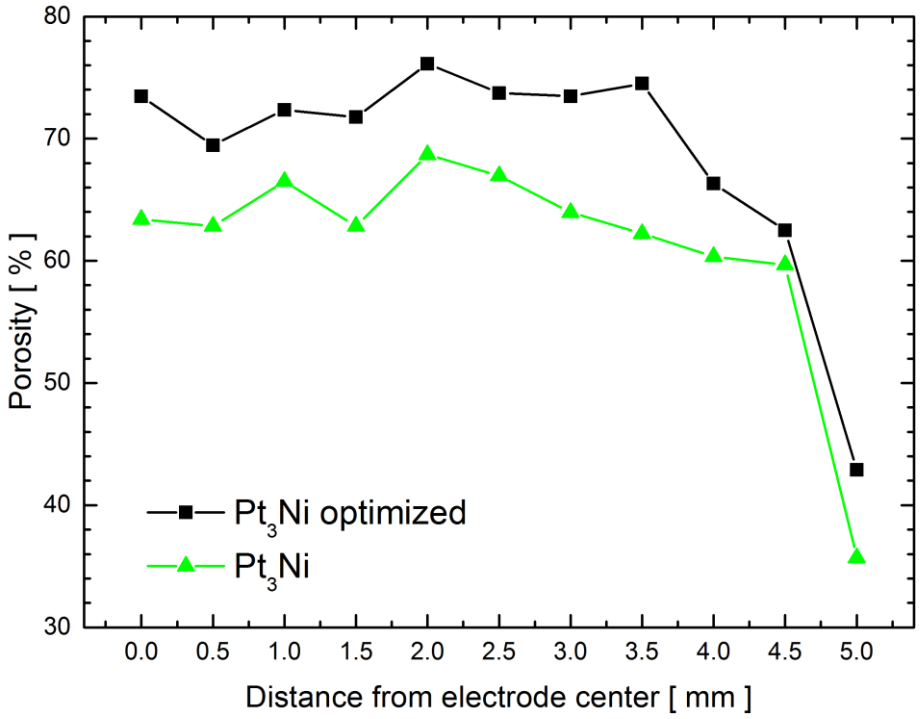

Figure 6.9 Estimated porosity as a function of the distance from the electrode center for catalyst layers of Pt_3Ni and Pt_3Ni optimized.

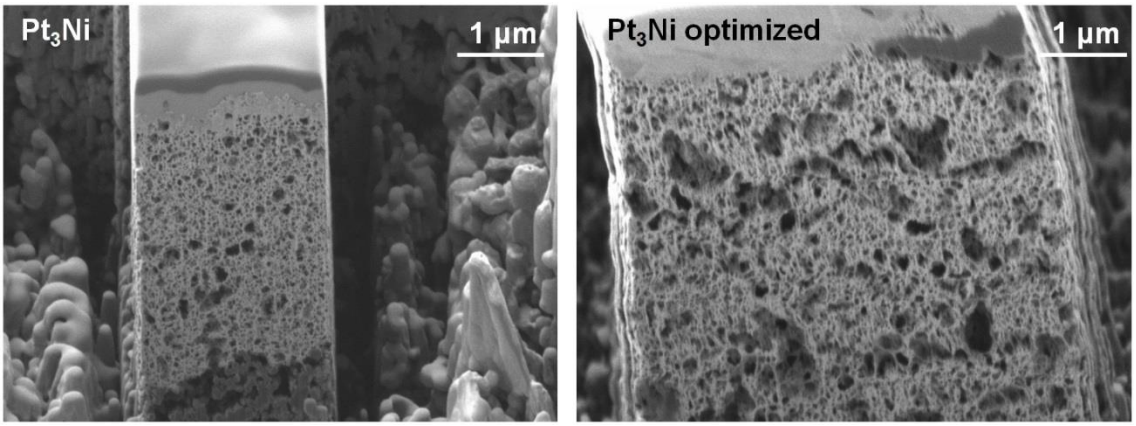

Figure 6.10 Cuboid-shaped structures of Pt_3Ni (left) and Pt_3Ni optimized (right) catalyst layers investigated by FIB-SEM tomography.

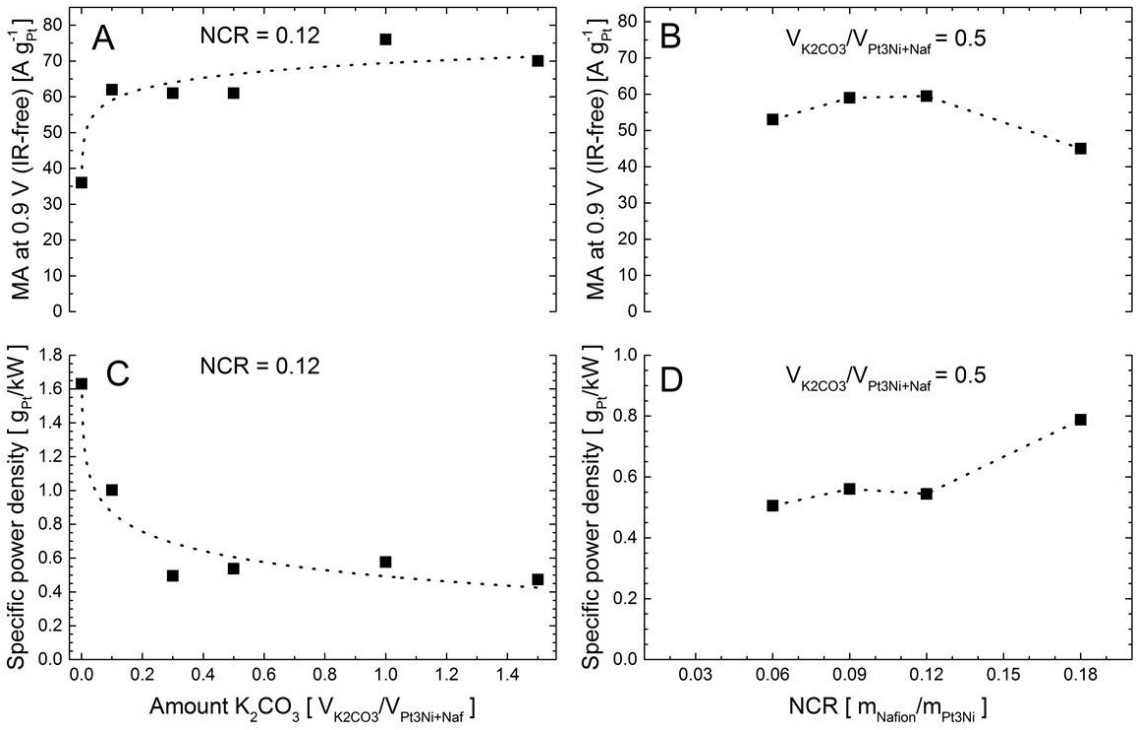

Figure 6.11 Results of Pt_3Ni MEA screening experiments with abbreviated cell break-in. (A) Mass-specific ORR activities (MAs) at 0.9 V_{RHE} from I/E curves at 80°C, 100 % RH, in H_2/O_2 at 1.5 bar_{abs} and (C) platinum-specific power densities at 0.65 V_{RHE} from H_2/air I/E curves vs. the K_2CO_3 amount at a fixed Nafion-to-catalyst ratio of 0.12. (B, D) MAs and specific power densities vs. NCR at a fixed K_2CO_3 amount of $V_{K2CO3}/V_{Pt3Ni+Naf}$ = 0.5.

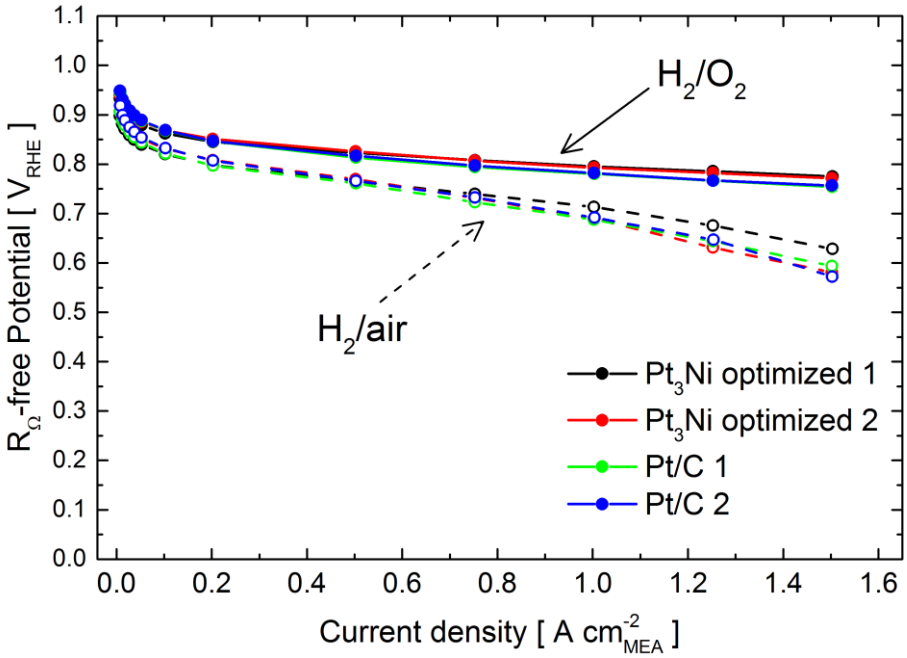

Figure 6.12 I/E curves at 80°C, 100 % RH, 1.5 bar_{abs} in H_2/O_2 (solid) and H_2/air (dotted) condition for two Pt_3Ni optimized and Pt/C MEAs (cathode loadings of 0.3 - 0.4 mg_{Pt}/cm^2_{geom}), respectively.

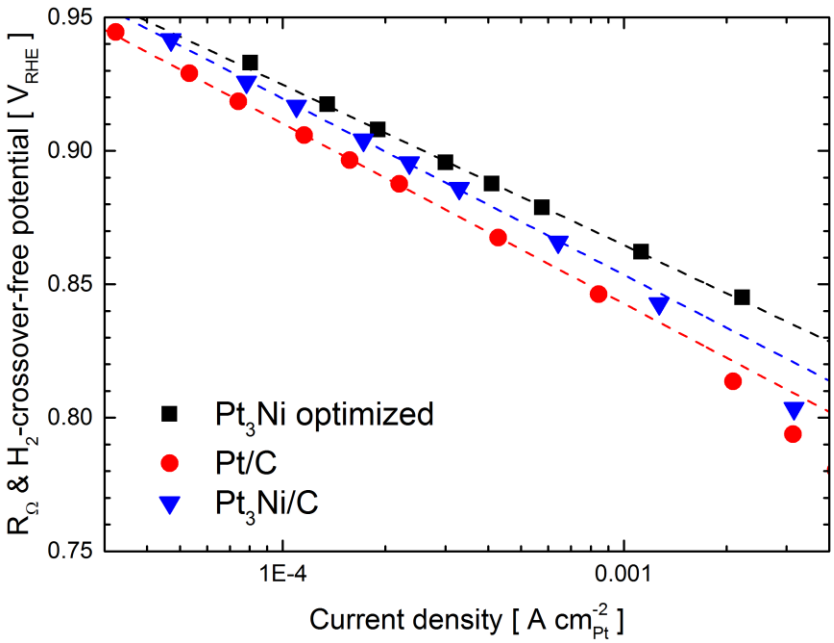

Figure 6.13 Tafel plots at 80°C, 100 % RH, 1.5 bar_{abs} in H_2/O_2 for MEAs of Pt_3Ni optimized, Pt/C and a commercial Pt_3Ni/C (cathode loadings of 0.3 - 0.4 mg_{Pt}/cm^2_{geom}).

Table 6.2 ECSA values obtained from cyclic voltammetry at 25°C in PEFC experiments, along with mass- and surface-specific ORR activities (MA, SA) at 0.9 V derived from PEFC measurements at 80°C, 100 % RH, 1.5 bar_{abs} in H_2/O_2 (cf. Figure 6.13).

	Pt/C	Pt_3Ni/C	Pt_3Ni optimized
ECSA (m^2/g_{Pt})	75	42	30
MA (A/g)	90	91	85
SA ($\mu A/cm^2_{Pt}$)	117	217	283

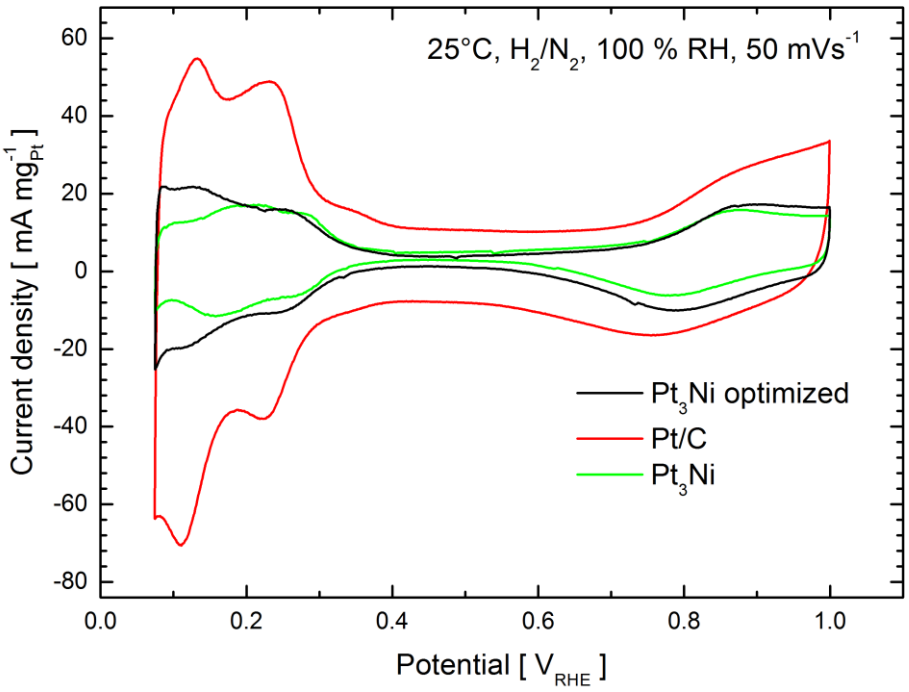

Figure 6.14 Cyclic voltammogramms at 50 mVs^{-1} in the PEFC at 25°C, 100 % RH, H_2/N_2 condition for Pt_3Ni, Pt_3Ni optimized and Pt/C MEAs.

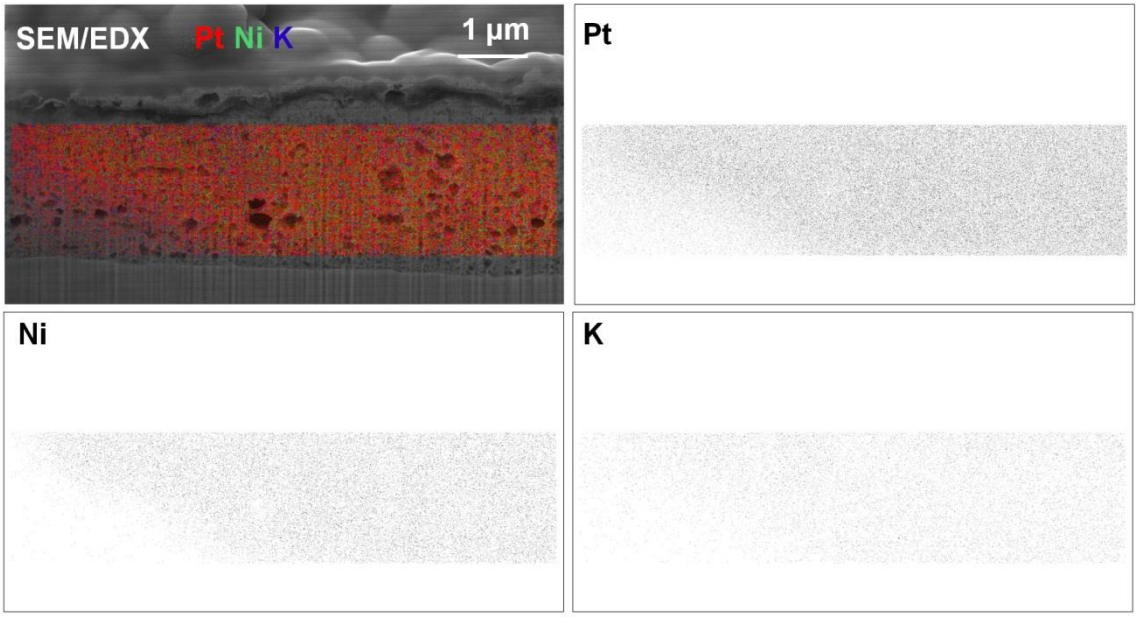

Figure 6.15 EDX elemental mapping of Pt, Ni and K (dark signal on white background) for a Pt_3Ni optimized CL before the acid washing step.

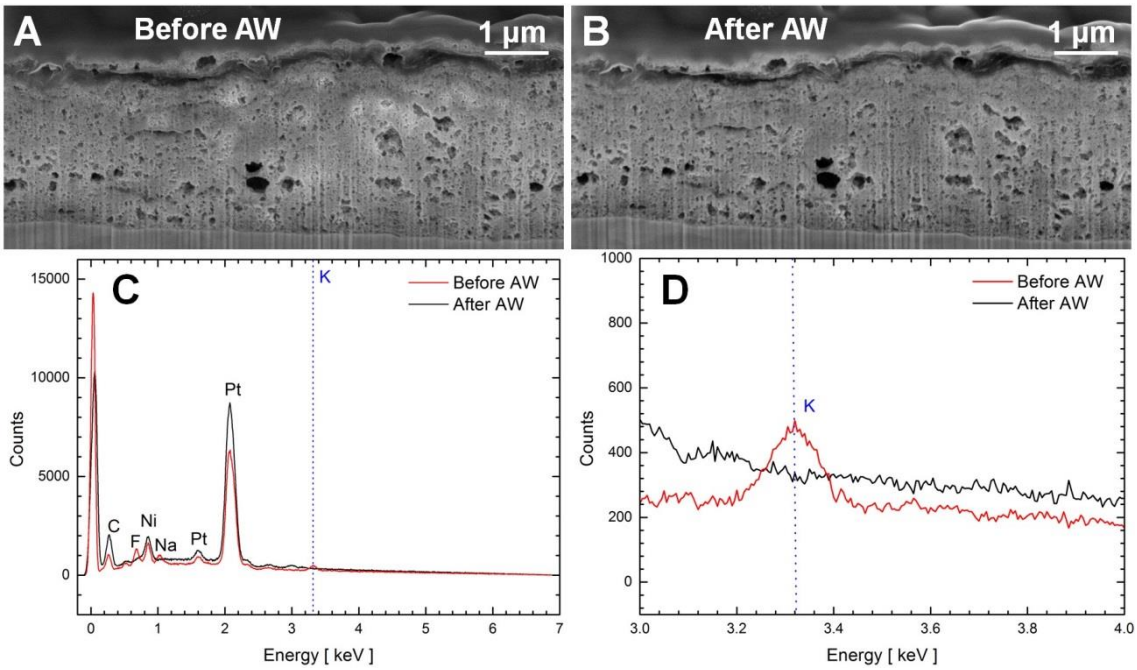

Figure 6.16 Cross section SEM images for a Pt_3Ni optimized CL before (A) and after (B) the acid washing step (0.53 mg_{Pt}/cm^2_{geom}). The disappearance of the potassium Kα-line peak at ≈ 3.3 keV in the corresponding EDX spectra (C, D) indicates complete K_2CO_3 dissolution.

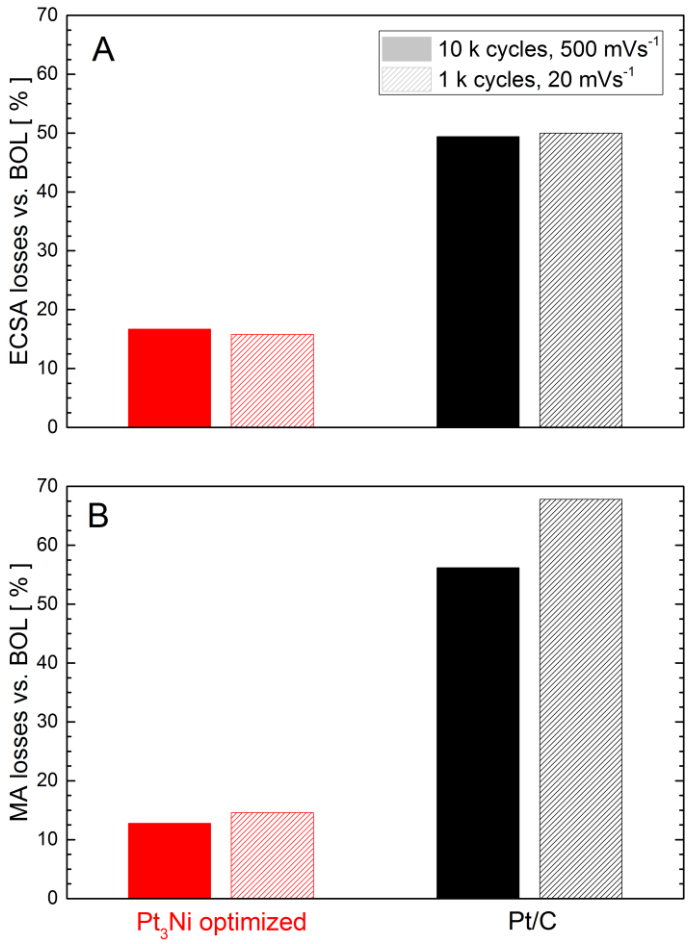

Figure 6.17 Percentual losses (vs. beginning-of-life values) of electrochemical surface area (at 25°C, A) and mass-specific ORR activity (at 80°C and with H_2/O_2 feeds, B) for Pt_3Ni optimized and Pt/C catalyst layers, upon accelerated stress tests consisting of 10000 cycles between 1.0 and 1.5 V_{RHE} at 500 mVs^{-1} or 1000 cycles at 20 mVs^{-1} (filled vs. patterned columns, respectively).

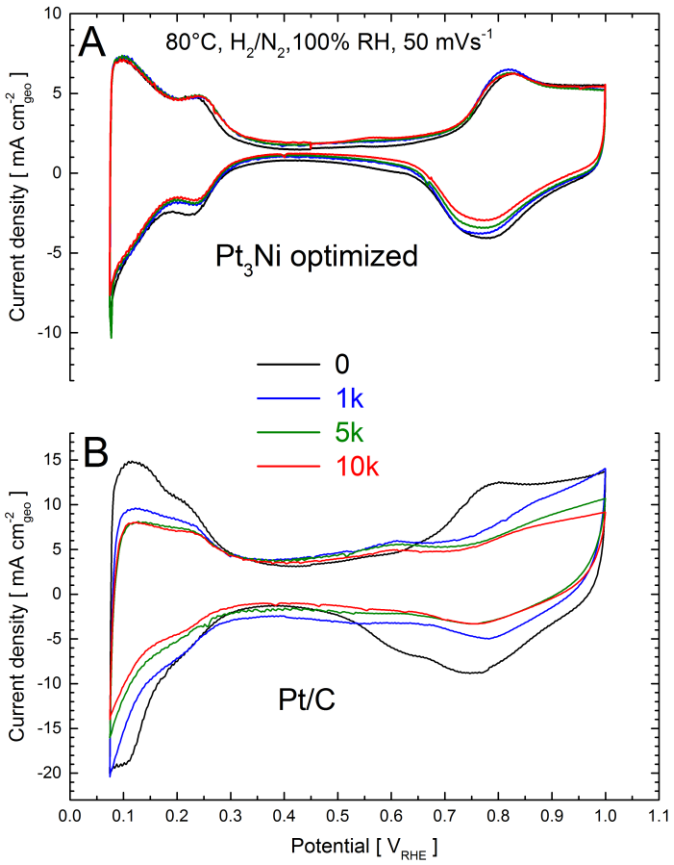

Figure 6.18 Cyclic voltammogramms (at 80°C) for Pt_3Ni optimized (A) and Pt/C (B) MEAs at different stages of the accelerated stress test.

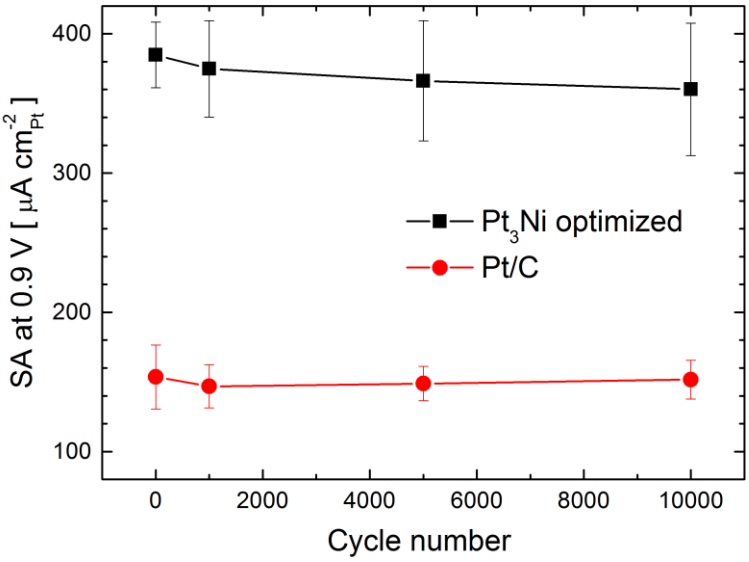

Figure 6.19 Surface-specific activity as a function of accelerated stress test potential cycles between 1.0 and 1.5 V_{RHE}.

7 PEFC Durability of Pt-Ni Aerogel vs. Pt/C Benchmark

7.1 Durability of Unsupported Pt-Ni Aerogels in PEFC Cathodes

Reducing the Pt loading in PEFCs can become feasible by developing ORR catalysts with higher activity and stability (cf. chapter 1). In this chapter the latter stability is investigated in detail for Pt_3Ni aerogel and a commercial Pt/C benchmark by performing two different accelerated stress tests. The applied degradation protocols aim to simulate the conditions in the PEFC while driving or starting/switching off an FCEV, respectively. This study first reports the MEA performances before and after the ASTs, comparing I/E curves in H_2/air, mass-specific ORR activities and ECSAs. In the second part, the observed degradation is related to changes in the CL structure (microscale) and the catalyst material itself (nanoscale), using FIB-SEM, TEM and EDX characterization. The study identifies a key development need to further improve the Pt_3Ni aerogel with respect to durability.

Durability of Unsupported Pt-Ni Aerogels in PEFC Cathodes

Sebastian Henning[a], Juan Herranz[a], Hiroshi Ishikawa[b], Bae Jung Kim[a], Daniel Abbott[a], Laura Kühn[c], Alexander Eychmüller[c] and Thomas J. Schmidt[a,d]

[a]Electrochemistry Laboratory, Paul Scherrer Institut, 5232 Villigen, Switzerland

[b]Interdisciplinary Graduate School of Medicine and Engineering, University of Yamanashi, 4 Takeda, Kofu, 400-8511, Japan

[c]Physical Chemistry, Technische Universität Dresden, Bergstr. 66b, 01062 Dresden, Germany

[d]Laboratory of Physical Chemistry, ETH Zurich, 8093 Zurich, Switzerland

ABSTRACT

The commercial success of polymer electrolyte fuel cells depends on the development of Pt-based oxygen reduction reaction catalysts with greater activity and stability to reduce the amount of expensive noble metal per device. To advance towards this goal, we have tested a novel class of unsupported bimetallic alloy catalysts (aerogels) as cathode material in PEFCs under two accelerated stress test conditions and compared it to a state-of-the-art carbon-supported benchmark (Pt/C). The investigated Pt_3Ni aerogel shows little degradation under high potential conditions (> 1.0 V) which can occur during fuel starvation and start-up/shut-down of the cell. If tested under the same conditions, the Pt/C benchmark displays significant losses of electrochemical surface area and ORR activity due to carbon support corrosion as observed in cross section and transmission electron microscopy analysis. When testing the durability upon extended load cycling (0.6 - 1.0 V), Pt_3Ni aerogel demonstrates less stability than Pt/C which is related to the severe Ni leaching from the alloy under such conditions. These findings highlight the advantages of using unsupported ORR catalysts in PEFCs and point to the reduction of non-noble metal dissolution as the next development step.

Published in *J. Electrochem. Soc.*, **164**, F1136 (2017).

7.2 Introduction

Polymer electrolyte fuel cells currently rely on large amounts of carbon supported platinum catalysts (≈ 0.4 $mg_{Pt}/cm^2_{electrode}$) to reduce the voltage losses due to the sluggish kinetics of the cathodic oxygen reduction reaction.[5] Recent advancements in minimizing the Pt loading and associated costs were achieved by alloying platinum with other metals like Ni, Cu and Co which increases the Pt mass-specific ORR activity.[6] On the other hand, these catalysts suffer from significant corrosion of the carbon support and Pt nanoparticles during PEFC operation which compromises their long-term efficiency and reliability.[24] To specifically mitigate the issue of support stability, researchers have developed alternative corrosion-resistant supports (e.g. conductive metal oxides[33, 124-126]), extended metal surfaces (e.g. 3M® nanostructured thin film catalysts[71]) and unsupported materials (e.g. Pt-coated Ni, Co or Cu nanowires[86, 87, 123]). Pursuing this last strategy, unsupported bimetallic Pt-Ni electrocatalysts with high specific surface area (≈ 30 m^2/g_{Pt}) and nanochain network structure, referred to as aerogels, were synthesized in a previous work.[53] These materials reach the U.S. Department of Energy target (i.e. 440 A/g_{Pt} at 0.9 V_{RHE}) for automotive PEFC application when tested as thin films by the rotating disk electrode technique,[3] which is the standard tool employed by the majority of researchers in this field for initial assessment of catalyst activities. Considering that performance figures derived from such RDE experiments often do not translate fully to the technical system, it is fundamental to also assess activity and durability in PEFCs to evaluate the real application potential of new catalysts.[182, 195]

At present, few groups have reported promising durability in PEFCs for spray-coated membrane electrode assemblies prepared from unsupported catalysts. Studies by Tamaki et al.[89] (on hollow Pt-Fe nanocapsules) and Lee et al.[31] (on FePt nanotubes) showed outstanding retention of electrochemical surface area and performance in H_2/O_2 polarization (I/E) curves for 10000 potential cycles between 1.0 and 1.5 V_{RHE}, and upon constant exposure to a high potential of 1.4 V_{RHE} for three hours, respectively. However, none of those studies focused on the PEFC-performance of these materials under application-relevant conditions, i.e., using H_2 and air at the anode and cathode inlet feeds, respectively. With this motivation, in a recent report we have demonstrated how the increase of porosity in the catalyst layer of Pt_3Ni aerogel MEAs caused by the addition of a removable filler material greatly improves the performance in H_2/air I/E curves.[196]

Following this recent study, in this work the durability of Pt_3Ni aerogels in the PEFC is investigated for two different accelerated stress tests proposed by the DOE and compared to a commercial Pt/C benchmark. The first AST exposes the catalyst to the potential regime of 1.0 to 1.5 V_{RHE}, which can occur in an operating PEFC during fuel starvation and start-up/shut-down of the cell and triggers C-support corrosion,[7, 8, 33, 41, 185] and that will be referred to as 'start-stop degradation' in the following.[4] The second AST which has not been investigated in the studies cited above simulates the variation in power output present during automotive application that results in potential fluctuations between ≈ 0.6 and ≈ 1.0 V_{RHE} causing Pt dissolution (and re-deposition);[7, 161, 197, 198] it will be denoted 'load-cycle degradation'. As we will demonstrate in this article, Pt_3Ni electrodes show superior durability for start-stop degradation compared to Pt/C due to the absence of a corrodible carbon-support. Additionally, severe Ni-leaching from the Pt_3Ni aerogel in load-cycle degradation experiments is identified as the major cause for their activity loss and inferior stability when compared to Pt/C under these conditions.

7.3 Experimental

Pt_3Ni aerogel was synthesized according to the procedure described in reference 53. In brief, 0.585 ml of a 0.205 M H_2PtCl_6 solution (8 wt. % in H_2O, Sigma Aldrich) and 4 ml of a freshly prepared 10 mM $NiCl_2$ solution ($NiCl_2$*$6H_2O$, 99 %, Sigma Aldrich) were dissolved in 790 ml of ultrapure water (18.2 MΩ cm, Millipore) and stirred until the mixing was complete. Subsequently, 7.0 ml of freshly prepared 0.1 M $NaBH_4$ solution (granular, 99.99 %, Sigma Aldrich) were added while stirring vigorously. A brown solution was obtained that was kept stirring for another 30 min. Afterwards, the reaction solution was distributed among several 100 ml vials. After about four days, black Pt_3Ni hydrogel was formed at the bottom of the containers. The hydrogel was washed with water and the solvent was exchanged with acetone afterwards. The resulting anhydrous gels were subjected to critical point drying in CO_2 (Critical Point Dryer 13200J-AB, SPI Supplies).

Membrane electrode assemblies were fabricated using Pt_3Ni aerogel, Pt/C (47 wt%, TKK, TEC10E50E) or $Pt/C_{graphitized}$ (30 wt%, TKK, TEC10EA30E) as the cathode catalyst (with loadings of 0.3 - 0.4 mg_{Pt}/cm^2_{geom}), Nafion XL-100 (DuPont) as the membrane and commercial gas diffusion electrodes (Johnson Matthey, 0.4 mg_{Pt}/cm^2_{geom} HISPEC 9100 Pt/HAS on Sigracet GDL 25 BC) as the anode. Catalyst inks for Pt_3Ni electrodes were prepared as described in reference 196 by mixing 5 mg of catalyst, 0.7 mg of K_2CO_3 (99.995% trace metals basis, Sigma Aldrich), 18 mg of Na^+-exchanged Nafion solution

(prepared from a 1:2 mixture of 0.1 M NaOH and Nafion solution,[186] and equal to a Nafion-to-catalyst-ratio of 0.12) and 1.0 ml of an 8 wt% aqueous isopropanol solution (ultrapure water, 18.2 MΩ cm, Elga Purelab Ultra and isopropanol, 99.9 %, Chromasolv Plus® for HPLC, Sigma Aldrich). After ultrasonication (USC100T, 45 kHz, VWR) for 30 minutes and spray coating (using a frame to confine the coating to the active area of 1 cm^2), the resulting catalyst coated membranes were immersed into 1 M H_2SO_4 solution (96 %, Suprapur, Merck) overnight (≈ 16 hours), followed by rinsing with ultrapure water and drying under ambient conditions. The acid washing step was introduced to remove the filler material K_2CO_3 and thus to create a CL with increased porosity (for details see reference 196). For Pt/C ($Pt/C_{graphitized}$) cathodes, 50 mg of catalyst was mixed with 500 (650) mg of 5 wt% Nafion solution (equal to a Nafion-to-carbon-ratio of 1.0) and 4.5 ml of a 20 wt% aqueous isopropanol solution, followed by the steps described above without the acid washing. In a last step, the CCMs were hotpressed at 120°C and 1 bar/cm^2_{geom} for 5 minutes to a gas diffusion layer (GDL 25 BC, Sigracet) and a commercial gas diffusion electrode (see above) on the cathode and anode side, respectively.

The MEAs were placed in a differential fuel cell that allows studying the MEA under homogeneous, well-defined conditions in the absence of along-the-channel effects such as changing temperature, relative humidity and gas concentration.[121] The fuel cell used for this study was developed inhouse, featuring 5 parallel channels of 1 mm width over an active area of 1 cm^2.[122] Using steel spacers with defined thickness, cell compression was set such that ≈ 25 % compression of the gas diffusion media was obtained.[122, 187] The MEA break-in started by drawing the maximum current that would yield cell potentials > 0.6 V in H_2/O_2 at 1.5 bar_{abs} and a relative humidity (RH) of 100 % between 25 and 80°C for 2 hours (flow rates anode/cathode: 300/750 ml/min[188], stoichiometries ≥ 30/≥ 30), followed by cooling down of the cell, activating potential cycles and a repetition of the first step (at 80°C). It must be noted here that even as the applied stoichiometry ratios are significantly higher than for technical cells, the gas flow velocities remain in the same order of magnitude due to the reduced size of the device.[121]

Cyclic voltammograms were measured after break-in at 25°C and 100 % RH, scanning the potential between 0.075 and 1.0 V_{RHE} at 50 mVs^{-1} with a H_2 anode flow rate of 50 ml/min and the N_2 cathode flow halted just prior to the measurement. The corresponding electrochemical surface area value was averaged from the H-adsorption and H-desorption charges between 0.09 and 0.4 V_{RHE} after double-layer correction, assuming a conversion factor of 210 µC/cm^2_{Pt}.[35] H_2-crossover tests were conducted by a linear potential sweep

from 0.6 to 0.1 V_{RHE} with a scan rate of 1 mVs^{-1} at 80°C, 100 % RH, 1.5 bar_{abs}, an anode H_2 flow rate of 300 ml/min and a cathode N_2 flow rate of 750 ml/min, respectively;[19] the H_2-crossover current densities typically amounted to ≈ 2 mA/cm^2_{MEA}. All I/E curves were recorded at 80°C and 100 % RH with anode/cathode flow rates of 300/750 ml/min (stoichiometries ≥ 30/≥ 30) at 1.5 bar_{abs} for either H_2/O_2 or H_2/air, using a Biologic VSP-300 potentiostat with a 10A/5V current booster. The measurement was done galvanostatically, whereby the cell current was stabilized for 3 minutes at each data point and the data was averaged from the last 2 minutes. Concomitantly, the cell resistance (R_Ω) was determined for each data point by galvanostatic electrochemical impedance spectroscopy (1 MHz to 1 Hz). Mass- and surface-specific activites for H_2/O_2 operation were extracted at 0.9 V_{RHE} after correcting potential and current for cell resistance and H_2-crossover, respectively. The accelerated stress tests were performed at 80°C, 100 % RH, ambient pressure, anode H_2 flow of 100 ml/min and cathode N_2 flow of 100 ml/min following shortened AST protocols established by the DOE for automotive PEFC application.[4] For start-stop and load-cycle degradation, the potential was cycled 10000 times between 1.0 and 1.5 V_{RHE} at 500 mVs^{-1} and 0.6 and 1.0 V_{RHE} at 50 mVs^{-1}, respectively.[4, 33, 89] At designated times (1000, 5000 cycles), the ASTs were interrupted to record I/E curves and CVs (cf. above) to determine the ECSA.

Transmission electron microscopy images and elemental composition of the catalysts were obtained on a TECNAI F30 operated at 300 kV and equipped with an energy dispersive X-ray spectroscopy detector. For tomography and cross section preparation with a focused ion beam/scanning electron microscope, a Zeiss NVision 40 microscope with a Ga^+ beam source and an EDX detector was employed.

7.4 Results and Discussion

Figure 7.1A, Figure 7.1C, and Figure 7.1E (adapted from reference 196) show the evolution of mass-specific activities, surface-specific activities and electrochemical surface areas for the start-stop degradation test of 10000 potential cycles between 1.0 and 1.5 V_{RHE} at 500 mVs^{-1}, normalized to the respective beginning-of-life values. The latter are summarized in Table 7.1, whereby the experimental data for the benchmark catalyst is in good agreement with literature reports for the same material.[35] After the start-stop AST, Pt_3Ni aerogel cathodes show only a minor decrease of the MA, SA and ECSA. The aerogel thus behaves similarly to the unsupported hollow Pt-Fe nanocapsule catalyst that was recently investigated by Tamaki et al. following the same protocol.[89] The Pt/C

benchmark, however, suffers from ≈ 50 % loss of MA and ECSA at the end-of-life, in agreement with observations in reference 33 using the same protocol. Additionally, the Pt/C benchmark displays drastic performance reduction in H_2/air I/E curves, whereas Pt_3Ni again maintains the BOL performance as discernable from Figure 7.2A. Moreover, we conducted the same start-stop AST on a commercial Pt catalyst implementing a graphitized carbon support ($Pt/C_{graphitized}$, see section 7.3 for experimental details). As showcased in Figure 7.7 of section 7.6, in the early stages of the AST, this $Pt/C_{graphitized}$ underwent a less severe decrease of MA and ECSA when compared to Pt/C, but by the end of the 10000 potential cycles both variables reached ≈ 50 % of their BOL-values (as compared to ≈ 40 % for Pt/C, cf. Figure 7.1A and Figure 7.1E). Therefore, this result further highlights the enhanced stability of the Pt_3Ni aerogel, even when compared to a commercial catalyst implementing a graphitized carbon support with a short-term durability better than that of Pt/C. For the rest of this study, though, we limit the comparison among degradation behaviors to the Pt_3Ni aerogel and the standard (i.e. with a non-graphitized support) Pt/C benchmark, which has received much more attention in the existing literature.

Table 7.1 Average values of the beginning-of-life MA, SA (at 0.9 V_{RHE}, 80°C, 100 % RH, H_2/O_2, 1.5 bar_{abs}) and ECSA (at 25°C) of Pt_3Ni aerogel and Pt/C MEAs.

	Pt_3Ni	Pt/C
MA [A/g_{Pt}]	113	120
SA [$\mu A/cm^2_{Pt}$]	526	233
ECSA [m^2/g_{Pt}]	29	69

Upon load-cycle degradation tests of 10000 potential cycles between 0.6 and 1.0 V_{RHE} at 50 mVs^{-1} (see Figure 7.1B, Figure 7.1D, and Figure 7.1F) on the other hand, Pt_3Ni MEAs display a severe MA reduction of ≈ 60 % as opposed to moderate losses of ≈ 30 % for the Pt/C benchmark. Concomitantly, the SA of Pt_3Ni aerogel decreases by ≈ 40 % whereas for Pt/C electrodes the EOL value exceeds the BOL one by 50 %. Moreover, the ECSAs for both catalysts evolve similarly (≈ 50 % reduction, in agreement with literature reports on Pt/C[161]) and the potential in H_2/air I/E curves at high current densities decrease moderately (≈ 50 mV at 1.5 A/cm^2, cf. Figure 7.2B). To explain the observed degradation of Pt_3Ni aerogel vs. Pt/C MEAs during the ASTs, beginning- and end-of-life samples were analyzed at the micro- and nanoscale to complement the electrochemical characterization in Figure 7.1 and Figure 7.2. First, cross sections of the catalyst layers were cut with a

focused-ion beam and captured by scanning electron microscopy. Qualitative comparison of the cross section images for the Pt_3Ni CL at BOL (Figure 7.3A) with the ones at EOL after start-stop (Figure 7.3B) and after load-cycle degradation (Figure 7.3C) does not reveal any significant morphology or porosity changes. To support this observation by a quantitative parameter, the thickness of the CL was measured in at least three different locations and normalized to the Pt loading to allow for a comparison between the different electrodes (BOL, EOL start-stop, EOL load-cycle).

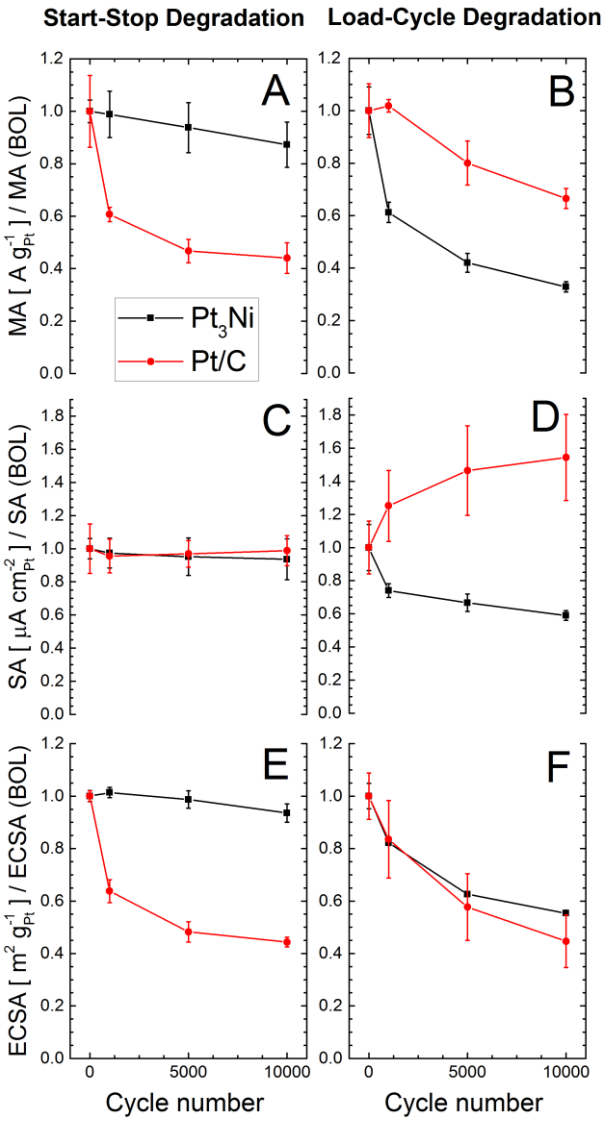

Figure 7.1 Average (three repetitions) MA (A, B), SA (C, D) at 0.9 V_{RHE} and (E, F) ECSA normalized to the respective BOL values of Pt_3Ni and Pt/C MEAs (cathode loadings of 0.3 - 0.4 mg_{Pt}/cm^2_{geom}) for start-stop (left) and load-cycle degradation (right), respectively.

As discernable from Figure 7.4, the EOL CL thicknesses for Pt_3Ni aerogel are comparable to the one at beginning-of-life indicating negligible variations in porosity throughout the ASTs. Changes of the latter porosity can affect the mass transport of reactants by molecular and Knudsen diffusion within the catalyst layer and alter the gas diffusion overpotential caused by O_2 concentration gradients.[20, 29] Variations of this overpotential can e.g. be deduced from the overall cell potential at high current densities (HCDs) in H_2/air I/E curves, i.e. in conditions of strong concentration gradients. Thus, the negligible changes in HCD performance throughout the ASTs of Pt_3Ni aerogel CLs in Figure 7.2 are consistent with a steady gas diffusion overpotential, and support the hypothesis that the porosity regime crucial to reactant and product mass transport remains unmodified.

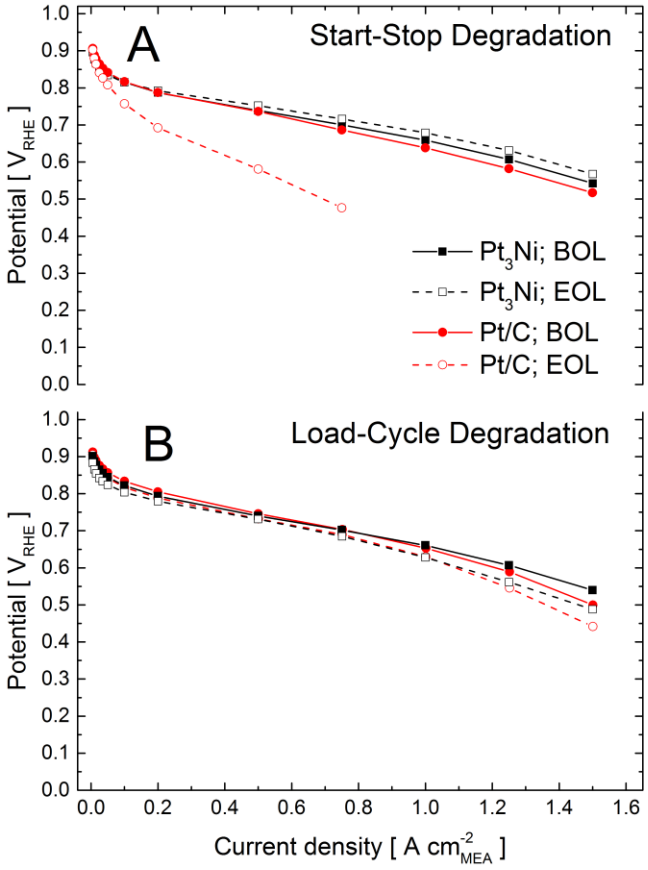

Figure 7.2 Beginning- and end-of-life I/E curves at 80°C, 100 % RH, in H_2/air at 1.5 bar_{abs} for the start-stop (A) and load-cycle degradation (B) of Pt_3Ni and Pt/C MEAs (cathode loadings of 0.3 - 0.4 mg_{Pt}/cm^2_{geom}).

The corresponding SEM cross section images for Pt/C are displayed in Figure 7.3D, Figure 7.3E and Figure 7.3F for BOL and following the start-stop and load cycle ASTs, respectively. At the end of the start-stop degradation test, one can identify domains in the

CL (highlighted by red circles in Figure 7.3E) that appear far less porous than at the BOL. This observation is concomitant with a ≈ 40 % decrease in thickness (cf. Figure 7.4D) from a BOL value of ≈ 38 µm/($mg_{Pt}\,cm^{-2}$) (or ≈ 33 µm/($mg_C\,cm^{-2}$), which agrees with the 28 ± 2 µm/($mg_C\ cm^{-2}$) reported in literature)[30] to ≈ 23 µm/($mg_{Pt}\,cm^{-2}$) and points to a collapse of the CL structure which can inhibit effective mass transport of reactants and that is supported by the drastic performance decline in the H_2/air I/E curves in Figure 7.2A. The CL collapse can be attributed to carbon support corrosion in the applied potential regimes[7, 8, 160, 185, 199] and the resulting CL porosity decrease has been demonstrated by Schulenburg et al.[48] in a FIB-SEM tomography study. On the other hand, representative cross section images before/after the load-cycle AST (Figure 7.3D/Figure 7.3F) do not indicate significant morphology/porosity changes concomitant with the negligible decrease in thickness to ≈ 34 µm/($mg_{Pt}\ cm^{-2}$) discernable from Figure 7.4B. Again, this agrees well with the electrochemical results at the cell level, where only a minor alteration of the HCD performance in H_2/air curves is observed (cf. Figure 7.2B).

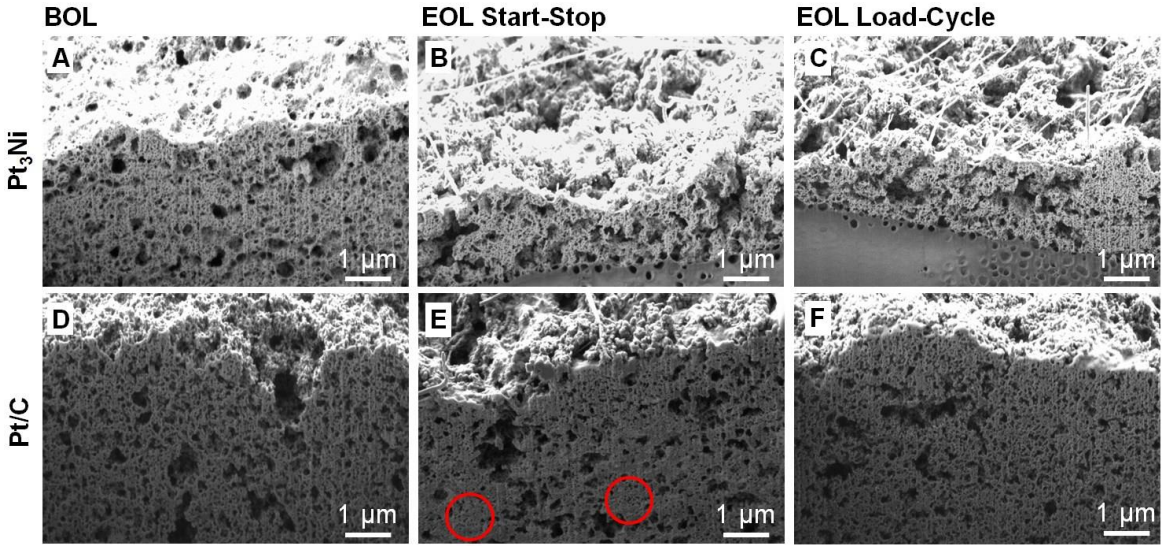

Figure 7.3 Representative cross section SEM images for catalyst layers of Pt_3Ni aerogel (top row) and Pt/C (bottom row) at the beginning-of-life (A, D) and after start-stop (B, E) and load-cycle degradation (C, F). Note that only the top part of the catalyst layer is visible for Pt/C at the shown magnification. The red circles highlight catalyst layer domains in which the porous structure has almost vanished.

To analyze the materials' change on the nanoscale, TEM images of the catalysts at BOL and after ASTs were taken and are summarized in Figure 7.5 (for additional images at other magnifications see Figure 7.8 and Figure 7.9 in section 7.6). At beginning-of-life, Pt_3Ni consists of a well-defined 3D network of interconnected nanoparticles with an

average nanochain diameter of 5 - 6 nm (cf. Figure 7.5A).[53] After the start-stop test (Figure 7.5B), the nanochain diameter seems to be of similar size, yet the nanochains appear somewhat “smoothed”, i.e. individual nanoparticle segments are less distinct. Unfortunately, it was not feasible to determine an accurate average nanochain diameter by measuring the size at multiple locations along the nanochain as in the case of the BOL sample since the catalyst layer was difficult to disperse in the process of TEM grid preparation (cf. 3D nanochain ‘stacks’ in low magnification images of Figure 7.8). Regardless, the finding of comparable nanochain diameters agrees well with the electrochemical results in Figure 7.1E which displays the almost constant ECSA of the Pt_3Ni aerogel after 10000 degradation cycles. On the other hand, after load-cycle degradation, Pt_3Ni aerogel displays a significant increase in the nanochain diameter to a value ≥ 10 nm (see Figure 7.5C), albeit this finding cannot be quantified either due to the issue of poor CL dispersibility discussed above. Assuming $d_{nanochain} \propto 1/ECSA$,[35] the increase in nanochain size by about a factor of two is in good agreement with the halving of the ECSA values in Figure 7.1F at EOL.

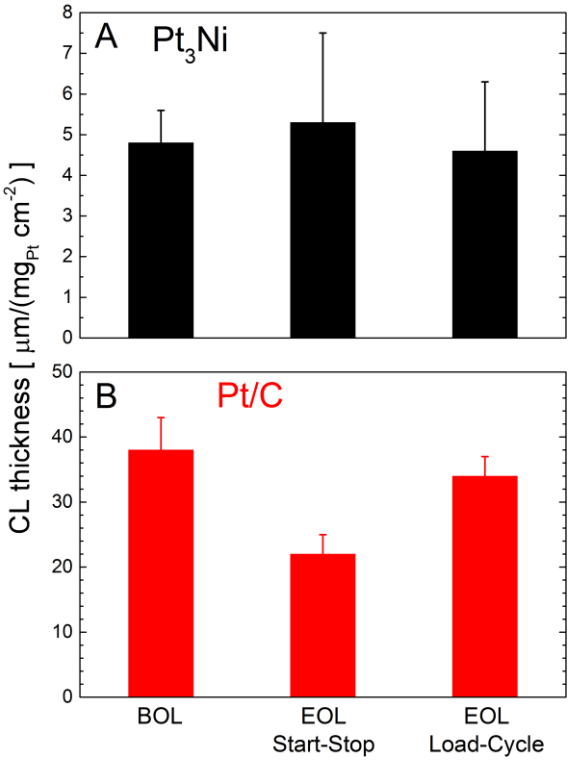

Figure 7.4 Catalyst layer thicknesses normalized to Pt loading for CLs of Pt_3Ni aerogel (A) and Pt/C (B) at the beginning-of-life and after start-stop and load-cycle degradation.

As for the Pt/C benchmark, Figure 7.5D vs. Figure 7.5E illustrate the carbon support corrosion during start-stop degradation that was introduced above to explain the porosity decrease of the CL (Figure 7.3E and Figure 7.4B) and the decline of high current density performance (cf. Figure 7.2A). This corrosion leads to domains which are completely void of Pt nanoparticles (especially at the carbon edges) and to changes in the morphology of the carbon support that, as reported in previous studies,[42, 45] becomes preponderantly amorphous during these start-stop stress tests (see Figure 7.9). The dramatic ECSA reduction for Pt/C in Figure 7.1E (estimated on the basis of the initial mass of Pt in the catalyst layer) is thus related to particle detachment due to carbon corrosion, whereby smaller nanoparticles exhibit an increased probability to detach,[7] and not to other ECSA decreasing mechanisms leading to Pt nanoparticle growth (see below). Specifically, the negligible impact of these nanoparticle-aggregation routes is likely related to the potential regime applied in the start-stop AST (i.e. 1.0 - 1.5 V_{RHE}), which does not include sufficiently low potentials that would lead to the reduction (and dissolution/redeposition)[200-202] of the Pt-(hydr)oxides passivating the nanoparticles' surface.

Complementarily, the loss of ECSA during the load-cycle degradation tests (cf. Figure 7.1F) is most likely caused by Ostwald ripening and particle migration/coalescence,[7, 161, 198] which trigger the formation of larger Pt nanoparticles as discernable by comparison of Figure 7.5D and Figure 7.5F. It has been observed that such an increase in particle size increases the surface-specific ORR activity of Pt-based catalysts, in terms caused by a positive shift of the adsorption energy of ORR impeding, oxygen-containing species (OH_{ads}) and the subsequent presence of more sites available for the catalysis of the reaction on the nanoparticles' surface.[24, 35, 203] Considering the universal ORR activity – ECSA value relationships introduced in references 24, 35, 204 and 205 that express this particle size effect, the ECSA reduction in the load-cycle AST from ≈ 70 m^2/g_{Pt} to ≈ 30 m^2/g_{Pt} should result in a SA increase to ≈ 140 % and a MA reduction to ≈ 60 % of the respective BOL values. These estimates are very close to the actual EOL SA and MA values of ≈ 155 % and ≈ 65 % (vs. BOL), respectively. The remaining difference could arise from the fact that the ORR activity – ECSA value relations in the above references[24, 35, 204, 205] are based on RDE experiments in 0.1 M $HClO_4$ or H_2SO_4 between 20 and 60°C, whereas the activity values reported in this work were obtained in a PEFC at 80°C.

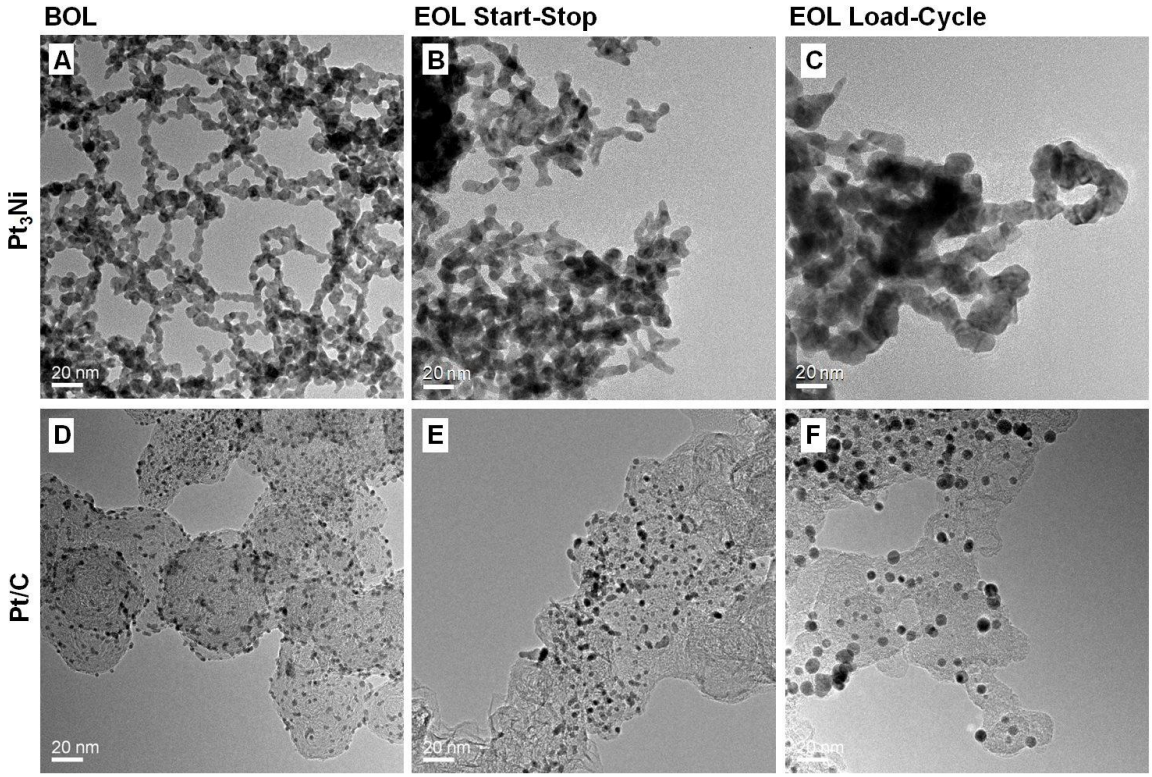

Figure 7.5 Representative TEM images of the Pt_3Ni aerogel (top row) and Pt/C catalyst (bottom row) at the beginning-of-life (A, D) and after start-stop (B, E) and load-cycle degradation (C, F).

While the particle size effect can account for the load-cycle degradation results of the Pt/C benchmark, it falls short to explain the behavior of the Pt_3Ni aerogel. To be precise, the ECSA reduction from ≈ 30 m^2/g_{Pt} to ≈ 15 m^2/g_{Pt} observed in this AST is expected to increase the SA to ≈ 135 % and reduce the MA to ≈ 55 % of the initial values, yet the final SA and MA amount to a mere ≈ 65 % and ≈ 30 % of their BOL counterparts, respectively. Consequently, other factors that can contribute to the evolution of the ORR activity need to be considered. In this respect, the leaching of the non-noble metal from Pt alloy ORR catalysts during ASTs has been reported as a cause for the concomitant activity decrease;[35, 206] as an example, the resembling, ≈ 70 % SA loss reported for a $PtNi_3$/C catalyst cycled between 0.4 and 1.4 V_{RHE} in reference 207 was partially related to the dissolution of ≈ 60 % of its initial Ni content. Moreover, previous works on Pt-Cu aerogels[66] and carbon-supported Pt-Cu and Pt-Ni electrocatalysts[207-209] have unveiled a correlation between the bulk phase non-noble metal content and the ORR activity that could explain this decrease of catalytic activity upon extended potential cycling.

To evaluate the possibility that the loss of Ni during the load-cycle AST may lead to the aerogel's ORR activity decrease, the catalyst layers and individual Pt_3Ni nanochains were

analyzed by SEM-EDX and TEM-EDX (three different locations each) to determine their Ni content (see Figure 7.6). The accuracy of the analysis is supported by the agreement of SEM and TEM data and the good match of the beginning-of-life Ni content values with the one derived from inductively coupled plasma - optical emission spectroscopy analysis in reference 53. As discernable from Figure 7.6, Pt_3Ni aerogel suffers from the loss of ≈ 35 % of its Ni content during start-stop AST vs. ≈ 60 % in the load-cycle degradation test. The lower Ni loss in the start-stop AST is related to the passivation of Pt by the formation of a PtO surface layer that mitigates the dissolution of surface Pt and subsurface Ni when cycling the potential above ≈ 1.0 V_{RHE}.[197, 210] The severe Ni leaching in the load-cycle test is a consequence of the observed Ostwald ripening phenomenon which constantly exposes Ni atoms from the nanochain interior to the corrosive PEFC environment. This effect can explain the mismatch between the ORR activity evolution of the Pt_3Ni aerogel (cf. Figure 7.1D/Figure 7.1F) and the predictions from the particle size effect introduced above.[161, 198] More precisely, Ni dissolution can lead to a positive shift of the catalyst's d-band center, thereby increasing the binding energy of oxygenated species and decreasing the ORR activity.[149, 150] To study other potential degradation effects associated with Ni leaching, such as ionomer poisoning in the membrane and catalyst layer,[35] we performed BOL/EOL impedance measurements in H_2/N_2[211, 212] which showed a constant high frequency resistance with non-measurable proton transfer resistance along the catalyst layer (not shown here),[36, 196] thus preventing the quantification of possible changes in this last variable. Alternatively, Ni loss may also lead to an increase in O_2-transport resistance[213] tentatively derivable from limiting current measurements[214] – a possibility that will be within the focus of our forthcoming works.

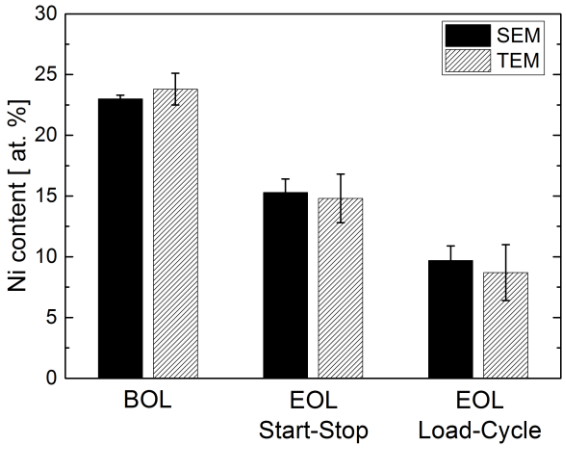

Figure 7.6 Average (from three locations) Ni content in at. % from SEM-EDX (solid) and TEM-EDX analysis (shaded) at the beginning-of-life and after start-stop and load-cycle degradation.

7.5 Conclusion

In summary, we have investigated the behavior of unsupported Pt_3Ni aerogel cathodes under start-stop and load-cycle ASTs in the PEFC. Under start-stop degradation conditions, Pt_3Ni MEAs retain their BOL mass-specific activity, ECSA and high current density performance in H_2/air I/E curves after 10000 cycles, whereas Pt/C shows a ≈ 50 % MA and ECSA loss concomitant with a drastic performance reduction in H_2/air I/E curves. This superior durability of Pt_3Ni aerogel vs. Pt/C is related to the severe corrosion of the carbon support in the latter catalyst that leads to Pt nanoparticle detachment and collapse of the catalyst layer structure. For the load-cycle AST, both Pt_3Ni and Pt/C display a ≈ 50 % reduction of the ECSA which is related to nanochain/nanoparticle size growth due to Ostwald ripening and particle migration/coalescence. The simultaneous decrease of MA and increase of SA for the Pt/C benchmark was found to be in excellent agreement with the well-known particle size effect on the ORR activity of Pt nanoparticles. For the Pt_3Ni aerogel, though, the activity loss does not follow the same trend since, in addition to the increase in particle sizes, the catalyst also undergoes significant Ni dissolution (≈ 60 %) from the alloy phase which further decreases both MA and SA. Nevertheless, based on our results and the overall fuel cell power output in the course of both ASTs, Pt_3Ni aerogel is a promising PEFC catalyst for automotive application that warrants high durability in case of fuel starvation and cell start-up/shut-down events. To further improve its stability under normal PEFC operation, future work will focus on tuning the aerogel nanochain structure and surface vs. bulk composition, as to minimize Ni dissolution from the alloy catalyst.[215]

7.6 Appendix – Supplementary Information

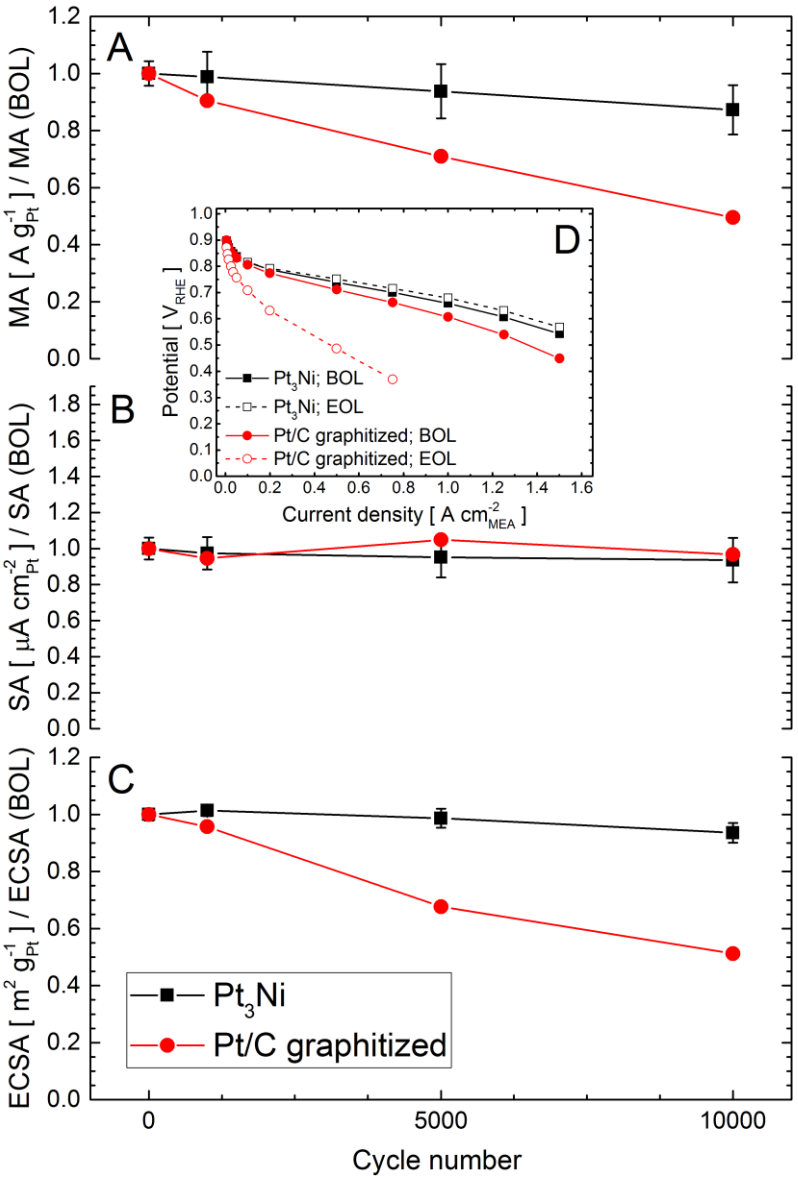

Figure 7.7 MA (A) and SA (B) at 0.9 V_{RHE}, as well as the ECSA (C) normalized to the respective BOL values of Pt_3Ni and $Pt/C_{graphitized}$ MEAs (cathode loadings of 0.3 - 0.4 mg_{Pt}/cm^2_{geom}) for start-stop degradation. The inset (D) shows beginning- and end-of-life I/E curves at 80°C, 100 % RH, in H_2/air at 1.5 bar_{abs}. Note that at the BOL, the $Pt/C_{graphitized}$ catalyst layer displays a MA of 84 A/g_{Pt} and a SA of 227 $\mu A/cm^2_{Pt}$ (both at 0.9 V_{RHE}), along with an ECSA of 49 m^2/g_{Pt}.

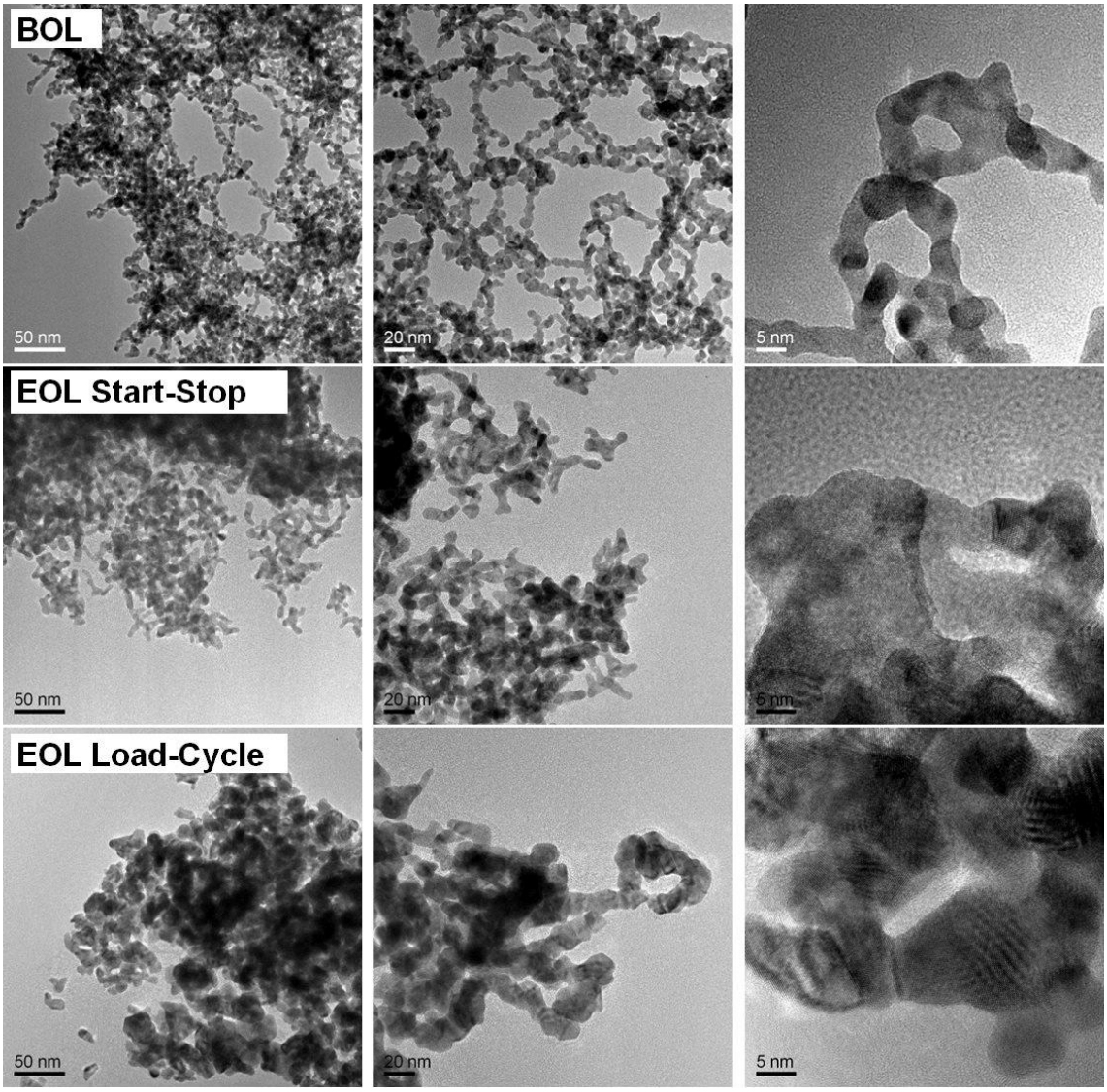

Figure 7.8 TEM images of the Pt_3Ni aerogel catalyst at the beginning-of-life (top row), after start-stop (middle row) and after load-cycle degradation test (bottom row).

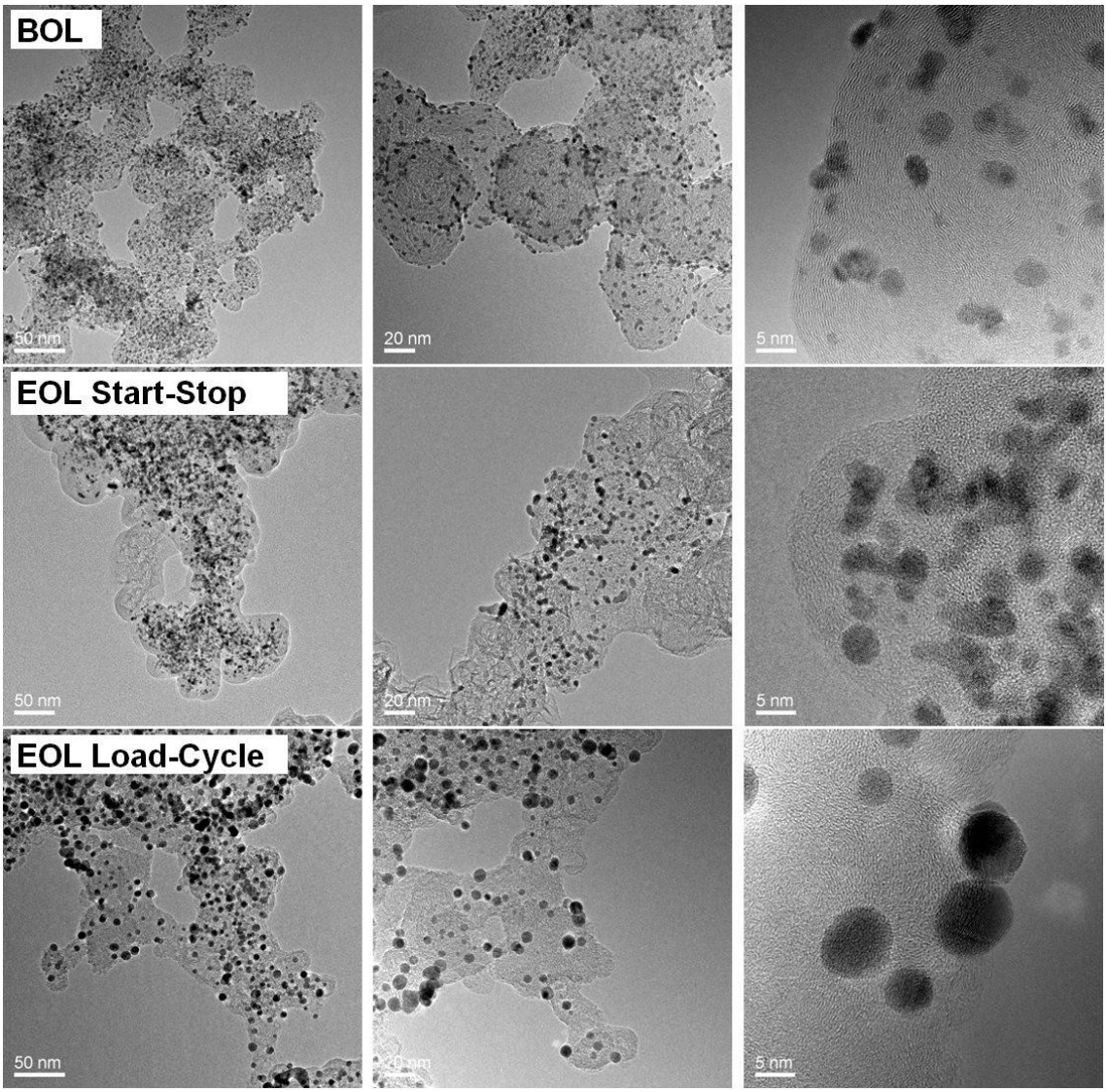

Figure 7.9 TEM images of the Pt/C catalyst at the beginning-of-life (top row), after start-stop (middle row) and after load-cycle degradation test (bottom row).

8 Conclusions and Outlook

In this chapter, the main conclusions of the thesis are presented and an outlook of future research directions is given. For greater clarity, conclusions and outlook sections are divided into three subsections that best account for the areas of focus in this work.

8.1 Conclusions

Synthesis and material characterization

This work presents the first synthesis of Pt-non-noble metal (Pt-M) alloy aerogels with an extended 3D nanochain structure (diameter ≈ 4 - 5.5 nm) by co-reduction of Pt and M-precursors in aqueous solution. For both Pt-Ni and Pt-Cu aerogels it was found that side phases (Ni-(hydr)oxide or Cu-oxide) are formed when the final M-content exceeds about 25 at. %. The former side phases dissolved rapidly in acidic solutions leaving behind a pure bimetallic alloy phase, and EXAFS and STEM-EDX analysis indicated homogeneous elemental distribution within the remaining aerogel's alloy phase. Additionally, these acid washing experiments demonstrated that Pt-M aerogels with M-contents > 25 at. % are prone to significant metal leaching, whereas great M-retention was found for M-content ≤ 25 at. %. These results point at the latter materials as the most promising catalysts for PEFC implementation.

Liquid electrolyte half cell tests

Using the thin film RDE technique, ORR activities of Pt_3Ni and Pt_3Cu aerogel were determined as ≈ 62 ± 5 and ≈ 60 ± 5 A/g_{Pt} at 0.95 V_{RHE} (≈ 422 ± 34 and ≈ 408 ± 34 A/g_{Pt} at 0.9 V_{RHE}), respectively. Thus, within error bars, both materials exceed the DOE activity target of 440 A/g_{Pt} (0.44 A/mg_{Pt}) at 0.9 V_{RHE}[3] and surpass the activity of the commercial Pt/C benchmark used in the same study by ≈ 50 % (≈ 40 ± 2 A/g_{Pt} at 0.95 V_{RHE}). The observed ≈ 3-fold increase of the surface-specific ORR activity vs. Pt/C was in agreement with reports for Pt-M/C catalysts in the literature. What is more, an almost linear correlation between alloy M-content and ORR activity has been found which agrees with the results obtained for supported materials in references 207-209. The ECSA values for all investigated aerogels amounted to ≈ 30 m^2/g_{Pt} irrespective of the employed technique, i.e. hydrogen underpotential deposition or CO stripping method. While these values are certainly lower than those for Pt/C (typically ≈ 60 - 90 m^2/g_{Pt})[35] and Pt-M/C (typically ≈ 40 - 50 m^2/g_{Pt})[153, 216], lower ECSA values are known to coincide with enhanced catalyst

durability.[217] Overall, the liquid electrolyte half cell tests confirmed that a synthesis method to produce highly active aerogel ORR catalysts has been developed.

To compare the performance of the catalysts in this thesis to the other unsupported materials presented in section 2.5.1, electrochemical behavior and ORR activity in RDE configuration of the latter are summarized in Figure 8.1; when multiple alloy compositions were investigated in the same reference, only the most active catalyst was included for greater clarity. Additionally, state-of-the-art carbon-supported catalysts, Pt/C (≈ 50 wt% Pt, Tanaka Kikinzoku Kogyo K. K., TEC1050E)[113, 116] and dealloyed $PtNi_3/C$[152, 153] that are available via scalable synthesis routes were considered as benchmarks. As various literature reports suggest (cf. section 3.5),[112, 113, 181] the obtained activity values are tightly interlinked to the quality of the thin films, measurement conditions (e.g. scan rate) and data treatment (e.g. with/without correction for mass transfer limitations), making it challenging to compare measurements performed in different laboratories. Considering this limitation, results that were extracted at 0.9 V vs. RHE from anodic sweeps at a scan rate of 20 mVs^{-1} and a rotation speed of 1600 rpm in O_2-saturated 0.1 M $HClO_4$ electrolyte at room temperature are predominantly reported here.[116, 181] Activity values reported at different potential, e.g. 0.95 V_{RHE}, were extrapolated to 0.9 V_{RHE} assuming a Tafel slope of 60 mV dec^{-1};[151] results at different scan rates were adapted considering the relation between current and scan rates investigated in reference 181.

Interestingly, almost 50 % of the catalysts in Figure 8.1 meet or exceed the DOE ORR mass activity target like the aerogel catalysts, proving that unsupported structures can go together with high catalytic performance and compete with state-of-the-art Pt alloy/C catalysts. Exemplary for the materials of this thesis, Pt_3Ni and PtCu aerogel were included, whose activity falls into the upper middle range. Considering the difficulties when comparing data from different labs, Figure 8.1B displays the MA as an improvement factor vs. the Pt/C benchmark measured in the same study, which can help to further mitigate artifacts from unlike measuring conditions that cannot be accounted in this estimate (e.g. cleanliness of the electrochemical measurement). Assuming a MA of ≈ 0.3 A/mg_{Pt} for Pt/C (averaged from the results reported in references 113, 116), an improvement factor of ≈ 1.5 indicated by the red dotted line can be considered equal to reaching the 0.44 A/mg_{Pt} defined by the DOE. Applying this new criterion, additional samples from section 2.5.1 meet the activity target.

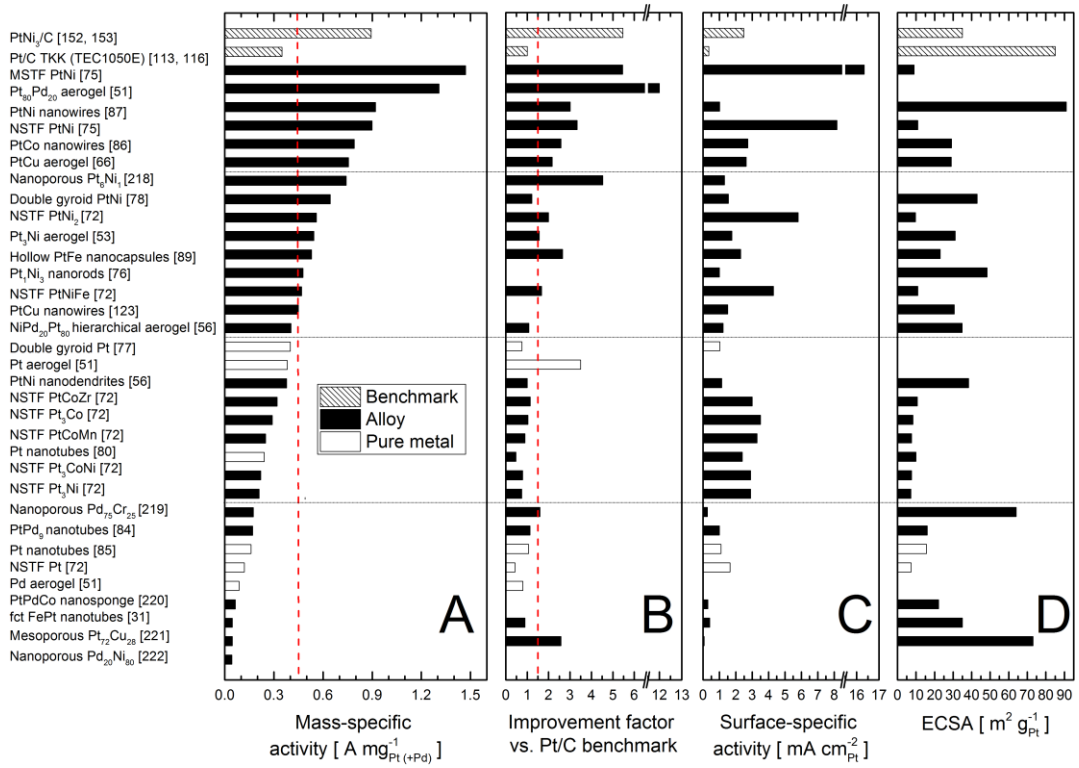

Figure 8.1 (A) Overview of mass-specific ORR activity, (B) corresponding improvement factor vs. Pt/C benchmark used in the same study, (C) surface-specific ORR activity and (D) ECSA for unsupported catalysts derived from liquid electrolyte half cell (RDE) experiments. Activity values are stated at 0.9 V_{RHE} in O_2-saturated 0.1 M $HClO_4$ electrolyte, following adaption of some reported values as specified in the main text and were normalized to Pt or total Pt and Pd contents (where applicable). The red dotted line in A illustrates the DOE MA target of 0.44 A/mg_{Pt}[3]; the line in B corresponds to an ORR activity improvement factor of 1.5. State-of-the art Pt/C and Pt alloy/C catalysts are included as benchmarks at the top of the chart and blank spaces correspond to missing data that was not provided in the references.[218-222] Reproduced with permission.[62] Copyright 2017, Wiley-VCH.

Fuel cell tests

The preparation of Pt_3Ni catalyst layers using the conventional method of spraying an ink on the membrane resulted in MEAs with poor high current density performance (H_2/air). This was related to the lower porosity and less favorable pore size distribution of the CL as compared to Pt/C catalyst layers, resulting in inefficient reactant mass transport. However, the addition of a water-soluble 'pore precursor' material to the Pt_3Ni aerogel catalyst ink (K_2CO_3) that was removed after spraying and drying by simple acid washing led to increased porosity and an increase of the average pore size. The resulting optimized Pt_3Ni aerogel catalyst layers showed a high current density performance (H_2/air) commensurate

to a commercial Pt/C benchmark (and ≈ 2.5-fold larger SA than Pt/C), thereby confirming the positive material evaluation from RDE experiments. To the best of the author's knowledge, this work thus represents the first successful implementation of an unsupported aerogel in the PEFC and one of the rare cases in which promising application-relevant H_2/air performance was demonstrated with unsupported catalysts. Additionally, these findings highlight the particular importance of tailoring the CL pore size distribution when working with unsupported catalysts and emphasize the adequacy of the FIB-SEM technique to support this process.

As anticipated, Pt_3Ni aerogel showed superior durability to Pt/C in an accelerated stress test that simulates start-up and shut-down of an automotive PEFC. Interestingly, this circumstance even held true when a Pt catalyst supported on more durable graphitized carbon was used as a benchmark. Given the fact that only negligible losses in ECSA, mass-specific activity and potential at high current densities were measured for Pt_3Ni aerogel, further endorses the potential of this material and unsupported catalysts in general. The enhanced stability vs. Pt/C could be attributed to severe carbon support corrosion in the latter case that considerably decreased the number of catalytically active Pt nanoparticles and resulted in a collapse of the porous catalyst layer structure. When subjected to an AST mimicking the PEFC voltage fluctuation during FCEV driving operation, Pt_3Ni aerogel displayed ≈ 50 % ECSA and MA loss as well as minor deterioration of the high current density performance. The more pronounced mass-specific ORR activity reduction compared to Pt/C (≈ 30 % loss) was assigned to severe Ni leaching from Pt_3Ni aerogel (≈ 60 % loss) that weakens the positive effect on catalytic activity induced by the alloying of Pt.

8.2 Outlook

Synthesis and material characterization

A serious constraint when researching novel catalyst materials is the small sample amounts that can be prepared per batch (≈ 200 mg for the synthesis presented in this work). While at an early research stage this limits the number of subsequent experiments and characterization options, it can turn out to be a major barrier for a material's large-scale application. Thus, it is crucial to think ahead for possibilities to increase the synthesis output and decrease its cost. For the aerogels, one important lever to obtain more catalyst per batch could be the increase of the reactant concentrations in aqueous solution that currently are set at a very low ≈ 0.1 mM. Additionally, the current synthesis

route involves a time-consuming and costly supercritical drying step to obtain the final product. Preliminary ORR activity tests in liquid electrolyte half cells however indicate similar results for aerogels that have undergone the final drying step and hydrogels, i.e. the water-suspended catalyst after all excess reactants have been removed by washing. If these Pt-M unsupported catalysts can be stored and processed as aqueous suspensions the synthesis would simplify drastically.

What is more, it would be beneficial if the synthesis parameters could be optimized in such a way that Pt-M aerogels with higher M-content in the alloy phase (and without a side phase) and smaller nanochain diameter are obtained. As demonstrated in chapter 5, an increase of the alloy M-content could translate into an ORR activity enhancement and so would the larger reactive surface area of materials with narrower nanochains. Ultimately, it should be investigated if post-synthesis catalysis treatment can enhance the material's robustness with respect to non-noble metal leaching during PEFC operation (cf. section 7.4). In this respect, the recent work of Alia et al.[215] that reports excellent activity and stability for an extended unsupported Pt-Ni system which was exposed to post-synthesis heat treatment in H_2, acid washing, and another heat treatment in O_2, could be an interesting starting point for such an endeavor. Naturally, potential detrimental effects from heat treatment and acid washing like catalyst sintering and too excessive non-noble metal leaching render adaptation of this process to the aerogels necessary and impede accurate prediction of its benefits.

Liquid electrolyte half cell tests

ORR activity tests using the RDE technique have proven a reliable tool to assess the catalytic proficiency of aerogel materials despite a disagreement between RDE and PEFC mass-specific activity values. The latter can be explained considering the differences in measurement parameters such as temperature and potential control (typically scanned vs. held in RDE vs. PEFC experiments).[32] Moreover, this circumstance applied to the commercial Pt/C benchmark as well, so that relative activities were successfully predicted. Overall, RDE tests should remain an integral part of the material characterization during the stage of further synthesis optimization, yet early-on PEFC tests are highly advised to simultaneously address challenges of efficient mass transport in the catalyst layer.

Fuel cell tests

Following synthesis scale-up as noted in the beginning of this section, CCMs should be prepared by using a semi-automated spray coating machine rather than manually operated spraying guns to systematically study the performance reproducibility of multiple samples and demonstrate reliable processability of the aerogel catalyst. Next, PEFC tests of larger CCMs in single cells under non-differential conditions (e.g. following the DOE recommendation of H_2/air stoichiometry 1.5/1.8[4]) are fundamental to showcase the aerogel's potential for real application. Given that the promising activity and durability behavior in differential fuel cells (cf. chapter 7) can also be demonstrated in the single cell, it is worthwhile to ultimately prepare MEAs containing aerogel catalyst on both anode and cathode side. This configuration renders it possible to also take advantage of the material's robustness on the anode side which can e.g. mitigate severe degradation damages from gross fuel starvation events.[47] All in all, assuming that further durability enhancements and material processing are feasible, unsupported Pt-M aerogel catalysts could provide a pathway to reduce the Pt-content in automotive PEFCs.

9 Bibliography

1. O. Z. Sharaf and M. F. Orhan, An overview of fuel cell technology: Fundamentals and applications, *Ren. Sust. En. Rev.*, **32**, 810 (2014).
2. *http://toyotanews.pressroom.toyota.com/releases/toyota-announces-2017-mirai-pricing.htm (accessed 02.10.17)*
3. O. Gröger, H. A. Gasteiger and J. P. Suchsland, Review-Electromobility: Batteries or Fuel Cells?, *J. Electrochem. Soc.*, **162**, A2605 (2015).
4. T. Abdel-Baset, T. Benjamin, R. Borup, K. E. Martin, N. Garland, S. Hirano, J. Kopasz, B. Lakshmanan, D. Masten, M. Mehall, D. Myers, D. Papageorgopoulos, W. Podolski, T. Trabold, B. Vermeersch and J. Waldecker, Fuel Cell Technical Team Roadmap, *http://energy.gov/sites/prod/files/2014/02/f8/fctt_roadmap_june2013.pdf (accessed 02.10.17)*.
5. F. T. Wagner, B. Lakshmanan and M. F. Mathias, Electrochemistry and the Future of the Automobile, *J. Phys. Chem. Lett.*, **1**, 2204 (2010).
6. C. Wang, M. Chi, D. Li, D. Strmcnik, D. van der Vliet, G. Wang, V. Komanicky, K. C. Chang, A. P. Paulikas, D. Tripkovic, J. Pearson, K. L. More, N. M. Markovic and V. R. Stamenkovic, Design and synthesis of bimetallic electrocatalyst with multilayered Pt-skin surfaces, *J. Am. Chem. Soc.*, **133**, 14396 (2011).
7. J. Speder, A. Zana, I. Spanos, J. J. K. Kirkensgaard, K. Mortensen, M. Hanzlik and M. Arenz, Comparative degradation study of carbon supported proton exchange membrane fuel cell electrocatalysts – The influence of the platinum to carbon ratio on the degradation rate, *J. Pow. Sourc.*, **261**, 14 (2014).
8. T. Mittermeier, A. Weiß, F. Hasché, G. Hübner and H. A. Gasteiger, PEM Fuel Cell Start-up/Shut-down Losses vs Temperature for Non-Graphitized and Graphitized Cathode Carbon Supports, *J. Electrochem. Soc.*, **164**, F127 (2017).
9. B. D. James, J. M. Moton and W. G. Colella, Mass Production Cost Estimation of Direct H_2 PEM Fuel Cell Systems for Transportation Applications: 2013 Update, *https://energy.gov/eere/fuelcells/downloads/mass-production-cost-estimation-direct-h2-pem-fuel-cell-systems (accessed 02.10.17)*.
10. H. A. Gasteiger, W. Gu, R. Makharia, M. F. Mathias and B. Sompalli, Beginning-of-life MEA performance — efficiency loss contributions, in *Handbook of Fuel Cells*, W. Vielstich, A. Lamm and H. A. Gasteiger Editors, John Wiley & Sons, Ltd., Chichester (2010).

11. K. C. Neyerlin, W. Gu, J. Jorne and H. A. Gasteiger, Determination of Catalyst Unique Parameters for the Oxygen Reduction Reaction in a PEMFC, *J. Electrochem. Soc.*, **153**, A1955 (2006).

12. K. C. Neyerlin, W. Gu, J. Jorne and H. A. Gasteiger, Study of the Exchange Current Density for the Hydrogen Oxidation and Evolution Reactions, *J. Electrochem. Soc.*, **154**, B631 (2007).

13. K. C. Neyerlin, W. Gu, J. Jorne, A. Clark and H. A. Gasteiger, Cathode Catalyst Utilization for the ORR in a PEMFC, *J. Electrochem. Soc.*, **154**, B279 (2007).

14. M. K. Debe, Electrocatalyst approaches and challenges for automotive fuel cells, *Nature*, **486**, 43 (2012).

15. V. Mehta and J. S. Cooper, Review and analysis of PEM fuel cell design and manufacturing, *J. Pow. Sourc.*, **114**, 32 (2003).

16. A. Forner-Cuenca, J. Biesdorf, L. Gubler, P. M. Kristiansen, T. J. Schmidt and P. Boillat, Engineered Water Highways in Fuel Cells: Radiation Grafting of Gas Diffusion Layers, *Adv. Mater.*, **27**, 6317 (2015).

17. A. El-Kharouf, N. V. Rees and R. Steinberger-Wilckens, Gas Diffusion Layer Materials and their Effect on Polymer Electrolyte Fuel Cell Performance - Ex Situ and In Situ Characterization, *Fuel Cells*, **14**, 735 (2014).

18. S. Holdcroft, Fuel Cell Catalyst Layers: A Polymer Science Perspective, *Chem. Mater.*, **26**, 381 (2014).

19. S. S. Kocha, Principles of MEA preparation, in *Handbook of Fuel Cells*, W. Vielstich, A. Lamm and H. A. Gasteiger Editors, John Wiley & Sons, Ltd., Chichester (2010).

20. B. Andreaus and M. Eikerling, Catalyst Layer Operation in PEM Fuel Cells: From Structural Pictures to Tractable Models, in *Device and Materials Modeling in PEM Fuel Cells*, S. J. Paddison and K. S. Promislow Editors, Springer New York, New York (2009).

21. K. Kojima and K. Fukazawa, Current Status and Future Outlook of Fuel Cell Vehicle Development in Toyota, *ECS Trans.*, **69**, 213 (2015).

22. A. Ohma, T. Mashio, K. Sato, H. Iden, Y. Ono, K. Sakai, K. Akizuki, S. Takaichi and K. Shinohara, Analysis of proton exchange membrane fuel cell catalyst layers for reduction of platinum loading at Nissan, *Electrochim. Acta*, **56**, 10832 (2011).

23. B. Schwanitz, A. Rabis, M. Horisberger, G. G. Scherer and T. J. Schmidt, Sputtered cathodes for polymer electrolyte fuel cells: insights into potentials, challenges and limitations, *Chimia*, **66**, 110 (2012).

24. A. Rabis, P. Rodriguez and T. J. Schmidt, Electrocatalysis for Polymer Electrolyte Fuel Cells: Recent Achievements and Future Challenges, *ACS Catal.*, **2**, 864 (2012).
25. T. Soboleva, X. Zhao, K. Malek, Z. Xie, T. Navessin and S. Holdcroft, On the micro-, meso-, and macroporous structures of polymer electrolyte membrane fuel cell catalyst layers, *ACS Appl. Mater. Interfaces*, **2**, 375 (2010).
26. K. More, R. Borup and K. Reeves, Identifying Contributing Degradation Phenomena in PEM Fuel Cell Membrane Electride Assemblies Via Electron Microscopy, *ECS Trans.*, **3**, 717 (2006).
27. T. Soboleva, K. Malek, Z. Xie, T. Navessin and S. Holdcroft, PEMFC Catalyst Layers: The Role of Micropores and Mesopores on Water Sorption and Fuel Cell Activity, *ACS Appl. Mater. Interfaces*, **3**, 1827 (2011).
28. S. Thiele, T. Fürstenhaupt, D. Banham, T. Hutzenlaub, V. Birss, C. Ziegler and R. Zengerle, Multiscale tomography of nanoporous carbon-supported noble metal catalyst layers, *J. Pow. Sourc.*, **228**, 185 (2013).
29. N. Nonoyama, S. Okazaki, A. Z. Weber, Y. Ikogi and T. Yoshida, Analysis of Oxygen-Transport Diffusion Resistance in Proton-Exchange-Membrane Fuel Cells, *J. Electrochem. Soc.*, **158**, B416 (2011).
30. W. Gu, D. R. Baker, Y. Liu and H. A. Gasteiger, Proton exchange membrane fuel cell (PEMFC) down-the-channel performance model, in *Handbook of Fuel Cells*, W. Vielstich, A. Lamm and H. A. Gasteiger Editors, John Wiley & Sons, Ltd., Chichester (2010).
31. J. Lee, J. M. Yoo, Y. Ye, Y. Mun, S. Lee, O.-H. Kim, H.-W. Rhee, H. I. Lee, Y.-E. Sung and J. Lee, Development of Highly Stable and Mass Transfer-Enhanced Cathode Catalysts: Support-Free Electrospun Intermetallic FePt Nanotubes for Polymer Electrolyte Membrane Fuel Cells, *Adv. Energy Mater.*, **5**, 1402093 (2015).
32. A. Kongkanand and M. F. Mathias, The Priority and Challenge of High-Power Performance of Low-Platinum Proton-Exchange Membrane Fuel Cells, *J. Phys. Chem. Lett.*, **7**, 1127 (2016).
33. A. Pătru, A. Rabis, S. E. Temmel, R. Kotz and T. J. Schmidt, Pt/IrO_2-TiO_2 cathode catalyst for low temperature polymer electrolyte fuel cell - Application in MEAs, performance and stability issues, *Catal. Today*, **262**, 161 (2016).
34. M. H. Eikerling, K. Malek and Q. Wang, Catalyst Layer Modeling: Structure, Properties and Performance, in *PEM Fuel Cell Electrocatalysts and Catalyst Layers: Fundamentals and Applications*, J. Zhang Editor, Springer London, London (2008).

35. H. A. Gasteiger, S. S. Kocha, B. Sompalli and F. T. Wagner, Activity benchmarks and requirements for Pt, Pt-alloy, and non-Pt oxygen reduction catalysts for PEMFCs, *Appl. Catal. B: Environ.*, **56**, 9 (2005).

36. H. Kuroki, T. Tamaki and T. Yamaguchi, Nanostructural Control and Performance Analysis of Carbon-Free Catalyst Layers Using Nanoparticle-Connected Hollow Capsules for PEFCs, *J. Electrochem. Soc.*, **163**, F927 (2016).

37. M. K. Debe, Tutorial on the Fundamental Characteristics and Practical Properties of Nanostructured Thin Film (NSTF) Catalysts, *J. Electrochem. Soc.*, **160**, F522 (2013).

38. U. A. Paulus, Z. Veziridis, B. Schnyder, M. Kuhnke, G. G. Scherer and A. Wokaun, Fundamental investigation of catalyst utilization at the electrode/solid polymer electrolyte interface: Part I. Development of a model system, *J. Electroanal. Chem.*, **541**, 77 (2003).

39. L. Hu, M. Zhang, S. Komini Babu and S. Litster, Investigation of Ion Conductivity and ORR on Metal/Water Interfaces in Proton Exchange Membrane Fuel Cells, *ECS Trans.*, **75**, 339 (2016).

40. P. K. Sinha, W. Gu, A. Kongkanand and E. Thompson, Performance of Nano Structured Thin Film (NSTF) Electrodes under Partially-Humidified Conditions, *J. Electrochem. Soc*, **158**, B831 (2011).

41. X.-Z. Yuan, H. Li, S. Zhang, J. Martin and H. Wang, A review of polymer electrolyte membrane fuel cell durability test protocols, *J. Pow. Sourc.*, **196**, 9107 (2011).

42. L. Castanheira, W. O. Silva, F. H. B. Lima, A. Crisci, L. Dubau and F. Maillard, Carbon Corrosion in Proton-Exchange Membrane Fuel Cells: Effect of the Carbon Structure, the Degradation Protocol, and the Gas Atmosphere, *ACS Catal.*, **5**, 2184 (2015).

43. L. Dubau, L. Castanheira, G. Berthomé and F. Maillard, An identical-location transmission electron microscopy study on the degradation of Pt/C nanoparticles under oxidizing, reducing and neutral atmosphere, *Electrochim. Acta*, **110**, 273 (2013).

44. C. A. Reiser, L. Bregoli, T. W. Patterson, J. S. Yi, J. D. Yang, M. L. Perry and T. D. Jarvi, A Reverse-Current Decay Mechanism for Fuel Cells, *Electrochem. Solid State Lett.*, **8**, A273 (2005).

45. J. Durst, A. Lamibrac, F. Charlot, J. Dillet, L. F. Castanheira, G. Maranzana, L. Dubau, F. Maillard, M. Chatenet and O. Lottin, Degradation heterogeneities induced by repetitive start/stop events in proton exchange membrane fuel cell: Inlet vs. outlet and channel vs. land, *Appl. Catal., B*, **138**, 416 (2013).

46. L. Castanheira, L. Dubau, M. Mermoux, G. Berthomé, N. Caqué, E. Rossinot, M. Chatenet and F. Maillard, Carbon Corrosion in Proton-Exchange Membrane Fuel Cells:

From Model Experiments to Real-Life Operation in Membrane Electrode Assemblies, *ACS Catal.*, **4**, 2258 (2014).

47. P. Rodriguez and T. J. Schmidt, Platinum-Based Anode Catalysts for Polymer Electrolyte Fuel Cells, in *Encyclopedia of Applied Electrochemistry*, G. Kreysa, K.-I. Ota and R. F. Savinell Editors, Springer New York, New York (2014).

48. H. Schulenburg, B. Schwanitz, N. Linse, G. n. G. Scherer, A. Wokaun, J. Krbanjevic, R. Grothausmann and I. Manke, 3D Imaging of Catalyst Support Corrosion in Polymer Electrolyte Fuel Cells, *J. Phys. Chem. C*, **115**, 14236 (2011).

49. W. Liu, A.-K. Herrmann, N. C. Bigall, P. Rodriguez, D. Wen, M. Oezaslan, T. J. Schmidt, N. Gaponik and A. Eychmüller, Noble Metal Aerogels—Synthesis, Characterization, and Application as Electrocatalysts, *Acc. Chem. Res.*, **48**, 154 (2015).

50. W. Liu, A. K. Herrmann, D. Geiger, L. Borchardt, F. Simon, S. Kaskel, N. Gaponik and A. Eychmüller, High-performance electrocatalysis on palladium aerogels, *Angew. Chem. Int. Ed.*, **51**, 5743 (2012).

51. W. Liu, P. Rodriguez, L. Borchardt, A. Foelske, J. Yuan, A. K. Herrmann, D. Geiger, Z. Zheng, S. Kaskel, N. Gaponik, R. Kotz, T. J. Schmidt and A. Eychmüller, Bimetallic aerogels: high-performance electrocatalysts for the oxygen reduction reaction, *Angew. Chem. Int. Ed.*, **52**, 9849 (2013).

52. D. Wen, W. Liu, D. Haubold, C. Zhu, M. Oschatz, M. Holzschuh, A. Wolf, F. Simon, S. Kaskel and A. Eychmüller, Gold Aerogels: Three-Dimensional Assembly of Nanoparticles and Their Use as Electrocatalytic Interfaces, *ACS nano*, **10**, 2559 (2016).

53. S. Henning, L. Kühn, J. Herranz, J. Durst, T. Binninger, M. Nachtegaal, M. Werheid, W. Liu, M. Adam, S. Kaskel, A. Eychmüller and T. J. Schmidt, Pt-Ni Aerogels as Unsupported Electrocatalysts for the Oxygen Reduction Reaction, *J. Electrochem. Soc.*, **163**, F998 (2016).

54. M. Oezaslan, W. Liu, M. Nachtegaal, A. I. Frenkel, B. Rutkowski, M. Werheid, A. K. Herrmann, C. Laugier-Bonnaud, H. C. Yilmaz, N. Gaponik, A. Czyrska-Filemonowicz, A. Eychmüller and T. J. Schmidt, Homogeneity and elemental distribution in self-assembled bimetallic Pd-Pt aerogels prepared by a spontaneous one-step gelation process, *Phys. Chem. Chem. Phys.*, **18**, 20640 (2016).

55. B. Cai, D. Wen, W. Liu, A. K. Herrmann, A. Benad and A. Eychmüller, Function-Led Design of Aerogels: Self-Assembly of Alloyed PdNi Hollow Nanospheres for Efficient Electrocatalysis, *Angew. Chem. Int. Ed.*, **54**, 13101 (2015).

56. B. Cai, A. Dianat, R. Hübner, W. Liu, D. Wen, A. Benad, L. Sonntag, T. Gemming, G. Cuniberti and A. Eychmüller, Multimetallic Hierarchical Aerogels: Shape Engineering of the Building Blocks for Efficient Electrocatalysis, *Adv. Mater.*, **29**, 1605254 (2017).

57. W. Liu, D. Haubold, B. Rutkowski, M. Oschatz, R. Hübner, M. Werheid, C. Ziegler, L. Sonntag, S. Liu, Z. Zheng, A.-K. Herrmann, D. Geiger, B. Terlan, T. Gemming, L. Borchardt, S. Kaskel, A. Czyrska-Filemonowicz and A. Eychmüller, Self-Supporting Hierarchical Porous PtAg Alloy Nanotubular Aerogels as Highly Active and Durable Electrocatalysts, *Chem. Mater.*, **28**, 6477 (2016).

58. N. Gaponik, A.-K. Herrmann and A. Eychmüller, Colloidal Nanocrystal-Based Gels and Aerogels: Material Aspects and Application Perspectives, *J. Phys. Chem. Lett.*, **3**, 8 (2011).

59. A. K. Herrmann, P. Formanek, L. Borchardt, M. Klose, L. Giebeler, J. Eckert, S. Kaskel, N. Gaponik and A. Eychmüller, Multimetallic Aerogels by Template-Free Self-Assembly of Au, Ag, Pt, and Pd Nanoparticles, *Chem. Mater.*, **26**, 1074 (2014).

60. N. C. Bigall, A. K. Herrmann, M. Vogel, M. Rose, P. Simon, W. Carrillo-Cabrera, D. Dorfs, S. Kaskel, N. Gaponik and A. Eychmüller, Hydrogels and aerogels from noble metal nanoparticles, *Angew. Chem. Int. Ed.*, **48**, 9731 (2009).

61. D. Wen, A. K. Herrmann, L. Borchardt, F. Simon, W. Liu, S. Kaskel and A. Eychmüller, Controlling the growth of palladium aerogels with high-performance toward bioelectrocatalytic oxidation of glucose, *J. Am. Chem. Soc.*, **136**, 2727 (2014).

62. B. Cai, S. Henning, J. Herranz, T. J. Schmidt and A. Eychmüller, Nanostructuring Noble Metals as Unsupported Electrocatalysts for Polymer Electrolyte Fuel Cells, *Adv. En. Mater.*, 1700548 (2017).

63. H. You, S. Yang, B. Ding and H. Yang, Synthesis of colloidal metal and metal alloy nanoparticles for electrochemical energy applications, *Chem. Soc. Rev.*, **42**, 2880 (2013).

64. C. Zhu, Q. Shi, S. Fu, J. Song, H. Xia, D. Du and Y. Lin, Efficient Synthesis of MCu (M = Pd, Pt, and Au) Aerogels with Accelerated Gelation Kinetics and their High Electrocatalytic Activity, *Adv. Mater.*, **28**, 8779 (2016).

65. L. Kühn, A. K. Herrmann, B. Rutkowski, M. Oezaslan, M. Nachtegaal, M. Klose, L. Giebeler, N. Gaponik, J. Eckert, T. J. Schmidt, A. Czyrska-Filemonowicz and A. Eychmüller, Alloying Behavior of Self-Assembled Noble Metal Nanoparticles, *Chem. Eur. J*, **22**, 13446 (2016).

66. S. Henning, L. Kühn, J. Herranz, M. Nachtegaal, R. Hübner, M. Werheid, A. Eychmüller and T. J. Schmidt, Effect of Acid Washing on the Oxygen Reduction Reaction Activity of Pt-Cu Aerogel Catalysts, *Electrochim. Acta*, **233**, 210 (2017).

67. D. R. Rolison, Catalytic Nanoarchitectures – the Importance of Nothing and the Unimportance of Periodicity, *Science*, **299**, 1698 (2003).

68. K. G. S. Ranmohotti, X. Gao and I. U. Arachchige, Salt-Mediated Self-Assembly of Metal Nanoshells into Monolithic Aerogel Frameworks, *Chem. Mater.*, **25**, 3528 (2013).

69. X. Gao, R. J. Esteves, T. T. Luong, R. Jaini and I. U. Arachchige, Oxidation-induced self-assembly of Ag nanoshells into transparent and opaque Ag hydrogels and aerogels, *J. Am. Chem. Soc.*, **136**, 7993 (2014).

70. M. K. Debe, R. T. Atanasoski and A. J. Steinbach, Nanostructured Thin Film Electrocatalysts - Current Status and Future Potential, *ECS Trans.*, **41**, 937 (2011).

71. M. K. Debe, Nanostructured Thin Film Electrocatalysts for PEM Fuel Cells - A Tutorial on the Fundamental Characteristics and Practical Properties of NSTF Catalysts, *ECS Trans.*, **45**, 47 (2012).

72. D. van der Vliet, C. Wang, M. Debe, R. Atanasoski, N. M. Markovic and V. R. Stamenkovic, Platinum-alloy nanostructured thin film catalysts for the oxygen reduction reaction, *Electrochim. Acta*, **56**, 8695 (2011).

73. M. Shao, Q. Chang, J. P. Dodelet and R. Chenitz, Recent Advances in Electrocatalysts for Oxygen Reduction Reaction, *Chem. Rev.*, **116**, 3594 (2016).

74. M. K. Debe, A. K. Schmoeckel, G. D. Vernstrom and R. Atanasoski, High voltage stability of nanostructured thin film catalysts for PEM fuel cells, *J. Pow. Sourc.*, **161**, 1002 (2006).

75. D. F. van der Vliet, C. Wang, D. Tripkovic, D. Strmcnik, X. F. Zhang, M. K. Debe, R. T. Atanasoski, N. M. Markovic and V. R. Stamenkovic, Mesostructured thin films as electrocatalysts with tunable composition and surface morphology, *Nat. Mater.*, **11**, 1051 (2012).

76. N. N. Kariuki, W. J. Khudhayer, T. Karabacak and D. J. Myers, GLAD Pt-Ni Alloy Nanorods for Oxygen Reduction Reaction, *ACS Catal.*, **3**, 3123 (2013).

77. J. Kibsgaard, Y. Gorlin, Z. Chen and T. F. Jaramillo, Meso-structured platinum thin films: active and stable electrocatalysts for the oxygen reduction reaction, *J. Am. Chem. Soc.*, **134**, 7758 (2012).

78. J. Kibsgaard, A. Jackson and T. F. Jaramillo, Mesoporous platinum nickel thin films with double gyroid morphology for the oxygen reduction reaction, *Nano Energy*, **29**, 243 (2016).

79. Y. Liu, J. Goebl and Y. Yin, Templated synthesis of nanostructured materials, *Chem. Soc. Rev.*, **42**, 2610 (2013).

80. A. B. Papandrew, R. W. Atkinson, G. A. Goenaga, S. S. Kocha, J. W. Zack, B. S. Pivovar and T. A. Zawodzinski, Oxygen Reduction Activity of Vapor-Grown Platinum Nanotubes, *J. Electrochem. Soc.*, **160**, F848 (2013).

81. S. M. Alia, Y. S. Yan and B. S. Pivovar, Galvanic displacement as a route to highly active and durable extended surface electrocatalysts, *Catal. Sci. Technol.*, **4**, 3589 (2014).

82. Z. Chen, M. Waje, W. Li and Y. Yan, Supportless Pt and PtPd nanotubes as electrocatalysts for oxygen-reduction reactions, *Angew. Chem. Int. Ed.*, **46**, 4060 (2007).

83. S. M. Alia, G. Zhang, D. Kisailus, D. Li, S. Gu, K. Jensen and Y. Yan, Porous Platinum Nanotubes for Oxygen Reduction and Methanol Oxidation Reactions, *Adv. Funct. Mater.*, **20**, 3742 (2010).

84. S. M. Alia, K. O. Jensen, B. S. Pivovar and Y. Yan, Platinum-Coated Palladium Nanotubes as Oxygen Reduction Reaction Electrocatalysts, *ACS Catal.*, **2**, 858 (2012).

85. S. M. Alia, B. S. Pivovar and Y. Yan, Platinum-Coated Copper Nanowires with High Activity for Hydrogen Oxidation Reaction in Base, *J. Am. Chem. Soc.*, **135**, 13473 (2013).

86. S. M. Alia, S. Pylypenko, K. C. Neyerlin, D. A. Cullen, S. S. Kocha and B. S. Pivovar, Platinum-Coated Cobalt Nanowires as Oxygen Reduction Reaction Electrocatalysts, *ACS Catal.*, **4**, 2680 (2014).

87. S. M. Alia, B. A. Larsen, S. Pylypenko, D. A. Cullen, D. R. Diercks, K. C. Neyerlin, S. S. Kocha and B. S. Pivovar, Platinum-Coated Nickel Nanowires as Oxygen-Reducing Electrocatalysts, *ACS Catal.*, **4**, 1114 (2014).

88. S. M. Alia, S. Pylypenko, A. Dameron, K. C. Neyerlin, S. S. Kocha and B. S. Pivovar, Oxidation of Platinum Nickel Nanowires to Improve Durability of Oxygen-Reducing Electrocatalysts, *J. Electrochem. Soc.*, **163**, F296 (2016).

89. T. Tamaki, H. Kuroki, S. Ogura, T. Fuchigami, Y. Kitamoto and T. Yamaguchi, Connected nanoparticle catalysts possessing a porous, hollow capsule structure as carbon-free electrocatalysts for oxygen reduction in polymer electrolyte fuel cells, *Energy Environ. Sci.*, **8**, 3545 (2015).

90. O.-H. Kim, Y.-H. Cho, S. H. Kang, H.-Y. Park, M. Kim, J. W. Lim, D. Y. Chung, M. J. Lee, H. Choe and Y.-E. Sung, Ordered macroporous platinum electrode and enhanced mass transfer in fuel cells using inverse opal structure, *Nat. Commun.*, **4**, 2473 (2013).

91. G. Sievers, S. Mueller, A. Quade, F. Steffen, S. Jakubith, A. Kruth and V. Brueser, Mesoporous Pt–Co oxygen reduction reaction (ORR) catalysts for low temperature proton exchange membrane fuel cell synthesized by alternating sputtering, *J. Pow. Sourc.*, **268**, 255 (2014).

92. A. J. Steinbach, D. van der Vliet, A. E. Hester, J. Erlebacher, C. Duru, I. Davy, M. Kuznia and D. A. Cullen, Recent Progress in Nanostructured Thin Film (NSTF) ORR Electrocatalyst Development for PEM Fuel Cells, *ECS Trans.*, **69**, 291 (2015).

93. A. Kongkanand, J. E. Owejan, S. Moose, M. Dioguardi, M. Biradar and R. Makharia, Development of Dispersed-Catalyst/NSTF Hybrid Electrode, *J. Electrochem. Soc*, **159**, F676 (2012).

94. A. Kongkanand, M. Dioguardi, C. Ji and E. L. Thompson, Improving Operational Robustness of NSTF Electrodes in PEM Fuel Cells, *J. Electrochem. Soc.*, **159**, F405 (2012).

95. D. Papageorgopoulos, Fuel Cells Program – Plenary Presentation, *2015 DOE Annual Merit Review and Peer Evaluation Meeting, http://www.hydrogen.energy.gov/pdfs/review15/fc000_papageorgopoulos_2015_o.pdf (accessed 02.10.17)*.

96. S. A. Mauger, K. C. Neyerlin, S. M. Alia, K. Hurst, S. Shulda, C. Ngo, J. N. Weker, S. Pylypenko and B. S. Pivovar, Performance of Platinum-Nickel Nanowires in a PEMFC, *ECS Prime 2016 – Oral Presentation 2447, https://ecs.confex.com/ecs/230/webprogram/Paper93933.html (accessed 02.10.17)*.

97. T. A. Greszler, T. E. Moylan and H. A. Gasteiger, Modeling the impact of cation contamination in a polymer electrolyte membrane fuel cell, in *Handbook of Fuel Cells*, W. Vielstich, A. Lamm and H. A. Gasteiger Editors, John Wiley & Sons, Ltd, Chichester (2010).

98. B. Kienitz, B. Pivovar, T. Zawodzinski and F. H. Garzon, Cationic Contamination Effects on Polymer Electrolyte Membrane Fuel Cell Performance, *J. Electrochem. Soc.*, **158**, B1175 (2011).

99. B. Pivovar, Extended, Continuous Pt Nanostructures in Thick, Dispersed Electrodes, *2015 DOE Hydrogen and Fuel Cells Program Review, https://www.hydrogen.energy.gov/annual_review15_fuelcells.html?print (accessed 02.10.17)*.

100. T. Okada, Effect of ionic contaminants, in *Handbook of Fuel Cells*, W. Vielstich, A. Lamm and H. A. Gasteiger Editors, John Wiley & Sons, Ltd, Chichester (2010).

101. B. Pivovar, Extended Surface Electrocatalyst Development, *2016 DOE Hydrogen and Fuel Cells Program Review, https://www.hydrogen.energy.gov/annual_review16_fuelcells.html?print (accessed 02.10.17)*.

102. A. A. Bunaciu, E. G. Udriştioiu and H. Y. Aboul-Enein, X-Ray Diffraction: Instrumentation and Applications, *Crit. Rev. Anal. Chem.*, **45**, 289 (2015).

103. P. van der Heide, Introduction, in *X-Ray Photoelectron Spectroscopy*, John Wiley & Sons, Inc. (2011).

104. S. J. Kerber, T. L. Barr, G. P. Mann, W. A. Brantley, E. Papazoglou and J. C. Mitchell, The complementary nature of x-ray photoelectron spectroscopy and angle-resolved x-ray diffraction Part I: Background and theory, *JMEPEG*, **7**, 329 (1998).

105. M. Newville, Fundamentals of X-Ray Absorption Fine Structure, *http://www.xafs.org/Tutorials (accessed 02.10.17)*.

106. A. E. Russell and A. Rose, X-ray Absorption Spectroscopy of Low Temperature Fuel Cell Catalysts, *Chem. Rev.*, **104**, 4613 (2004).

107. D. E. Ramaker and C. Roth, X-ray absorption near edge structure (Δμ XANES) techniques for low temperature fuel cell characterization, in *Polymer Electrolyte Membrane and Direct Methanol Fuel Cell Technology*, C. Hartnig and C. Roth Editors, Woodhead Publishing (2012).

108. N. Becknell, Y. Kang, C. Chen, J. Resasco, N. Kornienko, J. Guo, N. M. Markovic, G. A. Somorjai, V. R. Stamenkovic and P. Yang, Atomic Structure of Pt_3Ni Nanoframe Electrocatalysts by in Situ X-ray Absorption Spectroscopy, *J. Am. Chem. Soc.*, **137**, 15817 (2015).

109. A. N. Mansour, J. W. Cook and D. E. Sayers, Quantitative technique for the determination of the number of unoccupied d-electron states in a platinum catalyst using the L2,3 x-ray absorption edge spectra, *J. Phys. Chem.*, **88**, 2330 (1984).

110. B. Ravel and M. Newville, ATHENA, ARTEMIS, HEPHAESTUS: data analysis for X-ray absorption spectroscopy using IFEFFIT, *J. Synchrotron Rad.*, **12**, 537 (2005).

111. T. J. Schmidt, H. A. Gasteiger, G. D. Stäb, P. M. Urban, D. M. Kolb and R. J. Behm, Characterization of High-Surface-Area Electrocatalysts Using a Rotating Disk Electrode Configuration, *J. Electrochem. Soc.*, **145**, 2354 (1998).

112. K. Shinozaki, J. W. Zack, S. Pylypenko, B. S. Pivovar and S. S. Kocha, Oxygen Reduction Reaction Measurements on Platinum Electrocatalysts Utilizing Rotating Disk Electrode Technique: II. Influence of Ink Formulation, Catalyst Layer Uniformity and Thickness, *J. Electrochem. Soc.*, **162**, F1384 (2015).

113. Y. Garsany, J. Ge, J. St-Pierre, R. Rocheleau and K. E. Swider-Lyons, Analytical Procedure for Accurate Comparison of Rotating Disk Electrode Results for the Oxygen Reduction Activity of Pt/C, *J. Electrochem. Soc.*, **161**, F628 (2014).

114. E. Gileadi, *Electrode Kinetics for Chemists, Chemical Engineers and Materials Scientists*, John Wiley & Sons (1993).
115. A. J. Bard and L. R. Faulkner, *Electrochemical Methods: Fundamentals and Applications*, John Wiley & Sons (2000).
116. S. Kocha, Best Practices and Benchmark Activities for ORR Measurements by the Rotating Disk Electrode Technique, *2014 DOE Hydrogen and Fuel Cells Program Review, https://www.hydrogen.energy.gov/pdfs/progress14/v_m_1_kocha_2014.pdf (accessed 02.10.17)*.
117. S. Trasatti and O. A. Petrii, Real surface area measurements in electrochemistry, *Pure Appl. Chem.*, **63**, 711 (1991).
118. D. F. van der Vliet, C. Wang, D. Li, A. P. Paulikas, J. Greeley, R. B. Rankin, D. Strmcnik, D. Tripkovic, N. M. Markovic and V. R. Stamenkovic, Unique electrochemical adsorption properties of Pt-skin surfaces, *Angew. Chem. Int. Ed.*, **51**, 3139 (2012).
119. F. Maillard, M. Eikerling, O. V. Cherstiouk, S. Schreier, E. Savinova and U. Stimming, Size effects on reactivity of Pt nanoparticles in CO monolayer oxidation: The role of surface mobility, *Faraday Discuss.*, **125**, 357 (2004).
120. F. N. Büchi and P. Boillat, Polymer Electrolyte Fuel Cells, Mass Transport, in *Encyclopedia of Applied Electrochemistry*, G. Kreysa, K.-i. Ota and R. F. Savinell Editors, Springer New York, New York (2014).
121. P. Oberholzer and P. Boillat, Local Characterization of PEFCs by Differential Cells: Systematic Variations of Current and Asymmetric Relative Humidity, *J. Electrochem. Soc.*, **161**, F139 (2014).
122. P. Oberholzer, P. Boillat, A. Kaestner, E. H. Lehmann, G. G. Scherer, T. J. Schmidt and A. Wokaun, Characterizing Local O_2 Diffusive Losses in GDLs of PEFCs Using Simplified Flow Field Patterns ("2D","1D","0D"), *J. Electrochem. Soc.*, **160**, F659 (2013).
123. S. M. Alia, K. Jensen, C. Contreras, F. Garzon, B. Pivovar and Y. S. Yan, Platinum Coated Copper Nanowires and Platinum Nanotubes as Oxygen Reduction Electrocatalysts, *ACS Catal.*, **3**, 358 (2013).
124. G. Ozouf, G. Cognard, F. Maillard, L. Guetaz, M. Heitzmann and C. Beauger, SnO_2 Aerogels: Towards Performant and Stable PEFC Catalyst Supports, *ECS Trans.*, **69**, 1207 (2015).
125. E. Fabbri, A. Rabis, R. Kotz and T. J. Schmidt, Pt nanoparticles supported on Sb-doped SnO_2 porous structures: developments and issues, *Phys. Chem. Chem. Phys.*, **16**, 13672 (2014).

126. E. Fabbri, A. Pătru, A. Rabis, R. Kötz and T. J. Schmidt, Advanced Cathode Materials for Polymer Electrolyte Fuel Cells Based on Pt/ Metal Oxides: From Model Electrodes to Catalyst Systems, *Chimia*, **68**, 217 (2014).
127. A. Bonnefont, P. Ruvinskiy, M. Rouhet, A. Orfanidi, S. Neophytides and E. Savinova, Advanced catalytic layer architectures for polymer electrolyte membrane fuel cells, *WIREs Energy Environ.*, **3**, 505 (2014).
128. C. Zhu, D. Du, A. Eychmüller and Y. Lin, Engineering Ordered and Nonordered Porous Noble Metal Nanostructures: Synthesis, Assembly, and Their Applications in Electrochemistry, *Chem. Rev.*, **115**, 8896 (2015).
129. X. Yu, D. Wang, Q. Peng and Y. Li, Pt-M (M = Cu, Co, Ni, Fe) nanocrystals: from small nanoparticles to wormlike nanowires by oriented attachment, *Chem. Eur. J.*, **19**, 233 (2013).
130. J. Lai, L. Zhang, W. Qi, J. Zhao, M. Xu, W. Gao and G. Xu, Facile Synthesis of Porous PtM (M=Cu, Ni) Nanowires and Their Application as Efficient Electrocatalysts for Methanol Electrooxidation, *ChemCatChem*, **6**, 2253 (2014).
131. M. Xiao, S. Li, X. Zhao, J. Zhu, M. Yin, C. Liu and W. Xing, Enhanced Catalytic Performance of Composition-Tunable PtCu Nanowire Networks for Methanol Electrooxidation, *ChemCatChem*, **6**, 2825 (2014).
132. O. Müller, M. Nachtegaal, J. Just, D. Lützenkirchen-Hecht and R. Frahm, Quick-EXAFS setup at the SuperXAS beamline for in situ X-ray absorption spectroscopy with 10 ms time resolution, *J. Synchrotron Rad.*, **23**, 260 (2016).
133. S. Henning, J. Herranz and H. A. Gasteiger, Bulk-Palladium and Palladium-on-Gold Electrocatalysts for the Oxidation of Hydrogen in Alkaline Electrolyte, *J. Electrochem. Soc.*, **162**, F178 (2015).
134. K. S. W. Sing, D. H. Everett, R. A. W. Haul, L. Moscou, R. A. Pierotti, J. Rouquerol and T. Siemieniewska, Reporting Physisorption Data for Gas Solid Systems with Special Reference to the Determination of Surface-Area and Porosity (Recommendations 1984), *Pure Appl. Chem.*, **57**, 603 (1985).
135. K.-W. Park, J.-H. Choi, B.-K. Kwon, S.-A. Lee, Y.-E. Sung, H.-Y. Ha, S.-A. Hong, H. Kim and A. Wieckowski, Chemical and Electronic Effects of Ni in Pt/Ni and Pt/Ru/Ni Alloy Nanoparticles in Methanol Electrooxidation, *J. Phys. Chem. B*, **106**, 1869 (2002).
136. K. J. J. Mayrhofer, D. Strmcnik, B. B. Blizanac, V. Stamenkovic, M. Arenz and N. M. Markovic, Measurement of oxygen reduction activities via the rotating disc electrode method: From Pt model surfaces to carbon-supported high surface area catalysts, *Electrochim. Acta*, **53**, 3181 (2008).

137. D. H. McNear Jr, R. L. Chaney and D. L. Sparks, The effects of soil type and chemical treatment on nickel speciation in refinery enriched soils: A multi-technique investigation, *Geochim. et Cosmochim. Acta*, **71**, 2190 (2007).

138. M. C. Biesinger, B. P. Payne, L. W. M. Lau, A. Gerson and R. S. C. Smart, X-ray photoelectron spectroscopic chemical state quantification of mixed nickel metal, oxide and hydroxide systems, *Surf. Interface Anal.*, **41**, 324 (2009).

139. A. P. Grosvenor, M. C. Biesinger, R. S. Smart and N. S. McIntyre, New interpretations of XPS spectra of nickel metal and oxides, *Surf. Sci.*, **600**, 1771 (2006).

140. C. Chen, Y. Kang, Z. Huo, Z. Zhu, W. Huang, H. L. Xin, J. D. Snyder, D. Li, J. A. Herron, M. Mavrikakis, M. Chi, K. L. More, Y. Li, N. M. Markovic, G. A. Somorjai, P. Yang and V. R. Stamenkovic, Highly Crystalline Multimetallic Nanoframes with Three-Dimensional Electrocatalytic Surfaces, *Science*, **343**, 1339 (2014).

141. F. H. B. Lima, J. R. C. Salgado, E. R. Gonzalez and E. A. Ticianelli, Electrocatalytic Properties of PtCo/C and PtNi/C alloys for the Oxygen Reduction Reaction in Alkaline Solution, *J. Electrochem. Soc.*, **154**, A369 (2007).

142. A. I. Frenkel, Q. Wang, S. I. Sanchez, M. W. Small and R. G. Nuzzo, Short range order in bimetallic nanoalloys: an extended X-ray absorption fine structure study, *J. Chem. Phys.*, **138**, 064202 (2013).

143. A. I. Frenkel, A. Yevick, C. Cooper and R. Vasic, Modeling the structure and composition of nanoparticles by extended X-ray absorption fine-structure spectroscopy, *Annu. Rev. Anal. Chem.*, **4**, 23 (2011).

144. M. Pourbaix, *Atlas of Electrochemical Equilibria in Aueous Solutions*, Pergamon Press, Oxford (1966).

145. P. J. Rheinländer, J. Herranz, J. Durst and H. A. Gasteiger, Kinetics of the Hydrogen Oxidation/Evolution Reaction on Polycrystalline Platinum in Alkaline Electrolyte Reaction Order with Respect to Hydrogen Pressure, *J. Electrochem. Soc.*, **161**, F1448 (2014).

146. D. S. Hall, C. Bock and B. R. MacDougall, An Oxalate Method for Measuring the Surface Area of Nickel Electrodes, *J. Electrochem. Soc.*, **161**, H787 (2014).

147. W. Sheng, H. A. Gasteiger and Y. Shao-Horn, Hydrogen Oxidation and Evolution Reaction Kinetics on Platinum: Acid vs Alkaline Electrolytes, *J. Electrochem. Soc.*, **157**, B1529 (2010).

148. F. Maillard, M. Martin, F. Gloaguen and J. M. Léger, Oxygen electroreduction on carbon-supported platinum catalysts. Particle-size effect on the tolerance to methanol competition, *Electrochim. Acta*, **47**, 3431 (2002).

149. V. R. Stamenkovic, B. Fowler, B. S. Mun, G. Wang, P. N. Ross, C. A. Lucas and N. M. Markovic, Improved oxygen reduction activity on $Pt_3Ni(111)$ via increased surface site availability, *Science*, **315**, 493 (2007).

150. V. R. Stamenkovic, B. S. Mun, M. Arenz, K. J. Mayrhofer, C. A. Lucas, G. Wang, P. N. Ross and N. M. Markovic, Trends in electrocatalysis on extended and nanoscale Pt-bimetallic alloy surfaces, *Nat. Mater.*, **6**, 241 (2007).

151. U. A. Paulus, T. J. Schmidt, H. A. Gasteiger and R. J. Behm, Oxygen reduction on a high-surface area Pt/Vulcan carbon catalyst: a thin-film rotating ring-disk electrode study, *J. Electroanal. Chem.*, **495**, 134 (2001).

152. L. Gan, M. Heggen, S. Rudi and P. Strasser, Core-shell compositional fine structures of dealloyed Pt(x)Ni(1-x) nanoparticles and their impact on oxygen reduction catalysis, *Nano Lett.*, **12**, 5423 (2012).

153. B. H. Han, C. E. Carlton, A. Kongkanand, R. S. Kukreja, B. R. Theobald, L. Gan, R. O'Malley, P. Strasser, F. T. Wagner and Y. Shao-Horn, Record activity and stability of dealloyed bimetallic catalysts for proton exchange membrane fuel cells, *Energ. Environ. Sci.*, **8**, 258 (2015).

154. T. Barth and G. Linde, Die Gitterkonstanten des Platinmetalle, Silber und Gold, *Zeitschrift für Physikalische Chemie* **121**, 78 (1926).

155. J.-E. Jorgensen and R. I. Smith, On the compression mechanism of FeF_3, *Acta. Crystallogr. B*, **62**, 987 (2006).

156. R. W. Cairns and E. Ott, X-Ray Studies of the System Nickel-Oxygen-Water. I. Nickelous Oxide and Hydroxide, *J. Am. Chem. Soc.*, **55**, 527 (1933).

157. P. Strasser, Dealloyed core-shell fuel cell electrocatalysts, *Rev. Chem. Eng.*, **25**, 255 (2009).

158. F. Hasché, M. Oezaslan and P. Strasser, Activity, Stability, and Degradation Mechanisms of Dealloyed $PtCu_3$ and $PtCo_3$ Nanoparticle Fuel Cell Catalysts, *ChemCatChem*, **3**, 1805 (2011).

159. F. Hasché, M. Oezaslan and P. Strasser, Activity, Structure and Degradation of Dealloyed $PtNi_3$ Nanoparticle Electrocatalyst for the Oxygen Reduction Reaction in PEMFC, *J. Electrochem. Soc.*, **159**, B24 (2011).

160. S. J. Ashton and M. Arenz, Comparative DEMS study on the electrochemical oxidation of carbon blacks, *J. Pow. Sourc.*, **217**, 392 (2012).

161. P. J. Ferreira, G. J. la O', Y. Shao-Horn, D. Morgan, R. Makharia, S. Kocha and H. A. Gasteiger, Instability of Pt/C Electrocatalysts in Proton Exchange Membrane Fuel Cells: A Mechanistic Investigation, *J. Electrochem. Soc.*, **152**, A2256 (2005).

162. J. Greeley, I. E. L. Stephens, A. S. Bondarenko, T. P. Johansson, H. A. Hansen, T. F. Jaramillo, J. Rossmeisl, I. Chorkendorff and J. K. Nørskov, Alloys of platinum and early transition metals as oxygen reduction electrocatalysts, *Nat. Chem.*, **1**, 552 (2009).
163. L. Dubau, M. Lopez-Haro, J. Durst, L. Guétaz, P. Bayle-Guillemaud, M. Chatenet and F. Maillard, Beyond conventional electrocatalysts: hollow nanoparticles for improved and sustainable oxygen reduction reaction activity, *J. Mater. Chem. A*, **2**, 18497 (2014).
164. P. Mani, R. Srivastava and P. Strasser, Dealloyed Pt−Cu Core−Shell Nanoparticle Electrocatalysts for Use in PEM Fuel Cell Cathodes, *J. Phys. Chem. C*, **112**, 2770 (2008).
165. C. D. Wagner and G. E. Muilenberg, *Handbook of X-ray Photoelectron Spectroscopy : A Reference Book of Standard Data for use in X-ray Photoelectron Spectroscopy*, Physical Electronics Division, Perkin-Elmer Corp., Eden Prairie, Minn. (1979).
166. I. Dutta, M. K. Carpenter, M. P. Balogh, J. M. Ziegelbauer, T. E. Moylan, M. H. Atwan and N. P. Irish, Electrochemical and Structural Study of a Chemically Dealloyed PtCu Oxygen Reduction Catalyst, *J. Phys. Chem. C*, **114**, 16309 (2010).
167. R. Yang, J. Leisch, P. Strasser and M. F. Toney, Structure of Dealloyed $PtCu_3$ Thin Films and Catalytic Activity for Oxygen Reduction, *Chem. Mater.*, **22**, 4712 (2010).
168. J. Erlebacher, M. J. Aziz, A. Karma, N. Dimitrov and K. Sieradzki, Evolution of nanoporosity in dealloying, *Nature*, **410**, 450 (2001).
169. M. Oezaslan, F. Hasché and P. Strasser, Pt-Based Core–Shell Catalyst Architectures for Oxygen Fuel Cell Electrodes, *J. Am. Chem. Soc.*, **4**, 3273 (2013).
170. H. Wang, S. Xu, C. Tsai, Y. Li, C. Liu, J. Zhao, Y. Liu, H. Yuan, F. Abild-Pedersen, F. B. Prinz, J. K. Norskov and Y. Cui, Direct and continuous strain control of catalysts with tunable battery electrode materials, *Science*, **354**, 1031 (2016).
171. M. Oezaslan, F. Hasché and P. Strasser, $PtCu_3$, PtCu and Pt_3Cu Alloy Nanoparticle Electrocatalysts for Oxygen Reduction Reaction in Alkaline and Acidic Media, *J. Electrochem. Soc.*, **159**, B444 (2012).
172. H. M. Otte, Lattice Parameter Determinations with an X-Ray Spectrogoniometer by the Debye-Scherrer Method and the Effect of Specimen Condition, *J. Appl. Phys.*, **32**, 1536 (1961).
173. O. García-Martínez, R. M. Rojas, E. Vila and J. L. M. de Vidales, Microstructural characterization of nanocrystals of ZnO and CuO obtained from basic salts, *Solid State Ionics*, **63**, 442 (1993).

174. M. Oezaslan and P. Strasser, Activity of dealloyed $PtCo_3$ and $PtCu_3$ nanoparticle electrocatalyst for oxygen reduction reaction in polymer electrolyte membrane fuel cell, *J. Pow. Sourc.*, **196**, 5240 (2011).

175. T. Kaito, H. Tanaka, H. Mitsumoto, S. Sugawara, K. Shinohara, H. Ariga, H. Uehara, S. Takakusagi and K. Asakura, In Situ X-ray Absorption Fine Structure Analysis of PtCo, PtCu, and PtNi Alloy Electrocatalysts: The Correlation of Enhanced Oxygen Reduction Reaction Activity and Structure, *J. Phys. Chem. C*, **120**, 11519 (2016).

176. S. Mukerjee, S. Srinivasan, M. P. Soriaga and J. Mcbreen, Role of Structural and Electronic-Properties of Pt and Pt Alloys on Electrocatalysis of Oxygen Reduction - an in-Situ Xanes and Exafs Investigation, *J. Electrochem. Soc.*, **142**, 1409 (1995).

177. S. E. Temmel, E. Fabbri, D. Pergolesi, T. Lippert and T. J. Schmidt, Investigating the Role of Strain toward the Oxygen Reduction Activity on Model Thin Film Pt Catalysts, *ACS Catal.*, **6**, 7566 (2016).

178. P. Strasser, S. Koh, T. Anniyev, J. Greeley, K. More, C. Yu, Z. Liu, S. Kaya, D. Nordlund, H. Ogasawara, M. F. Toney and A. Nilsson, Lattice-strain control of the activity in dealloyed core–shell fuel cell catalysts, *Nat. Chem.*, **2**, 454 (2010).

179. S. Koh and P. Strasser, Electrocatalysis on Bimetallic Surfaces: Modifying Catalytic Reactivity for Oxygen Reduction by Voltammetric Surface Dealloying, *J. Am. Chem. Soc.*, **129**, 12624 (2007).

180. K. Jayasayee, J. A. R. V. Veen, T. G. Manivasagam, S. Celebi, E. J. M. Hensen and F. A. de Bruijn, Oxygen reduction reaction (ORR) activity and durability of carbon supported PtM (Co, Ni, Cu) alloys: Influence of particle size and non-noble metals, *Appl. Catal. B*, **111-112**, 515 (2012).

181. K. Shinozaki, J. W. Zack, R. M. Richards, B. S. Pivovar and S. S. Kocha, Oxygen Reduction Reaction Measurements on Platinum Electrocatalysts Utilizing Rotating Disk Electrode Technique, *J. Electrochem. Soc.*, **162**, F1144 (2015).

182. I. E. L. Stephens, J. Rossmeisl and I. Chorkendorff, Toward sustainable fuel cells, *Science*, **354**, 1378 (2016).

183. G. A. Schuler, Untersuchung der lokalen Gasphase in Polymer-Elektrolyt-Brennstoffzellen, *ETH Dissertation No. 18883*, 29 (2010).

184. K. Shinozaki, Y. Morimoto, B. S. Pivovar and S. S. Kocha, Re-examination of the Pt Particle Size Effect on the Oxygen Reduction Reaction for Ultrathin Uniform Pt/C Catalyst Layers without Influence from Nafion, *Electrochim. Acta*, **213**, 783 (2016).

185. C. Hartnig and T. J. Schmidt, Simulated start–stop as a rapid aging tool for polymer electrolyte fuel cell electrodes, *J. Pow. Sourc.*, **196**, 5564 (2011).

186. J. Suntivich, H. A. Gasteiger, N. Yabuuchi and Y. Shao-Horn, Electrocatalytic Measurement Methodology of Oxide Catalysts Using a Thin-Film Rotating Disk Electrode, *J. Electrochem. Soc.*, **157**, B1263 (2010).

187. P. Oberholzer, P. Boillat, R. Siegrist, A. Kästner, E. H. Lehmann, G. G. Scherer and A. Wokaun, Simultaneous neutron imaging of six operating PEFCs: Experimental set-up and study of the MPL effect, *Electrochem. Comm.*, **20**, 67 (2012).

188. J. Biesdorf, A. Forner-Cuenca, T. J. Schmidt and P. Boillat, Impact of Hydrophobic Coating on Mass Transport Losses in PEFCs, *J. Electrochem. Soc.*, **162**, F1243 (2015).

189. M. Lee, M. Uchida, H. Yano, D. A. Tryk, H. Uchida and M. Watanabe, New evaluation method for the effectiveness of platinum/carbon electrocatalysts under operating conditions, *Electrochim. Acta*, **55**, 8504 (2010).

190. S. Thiele, R. Zengerle and C. Ziegler, Nano-morphology of a polymer electrolyte fuel cell catalyst layer—imaging, reconstruction and analysis, *Nano Res.*, **4**, 849 (2011).

191. A. G. Star and T. F. Fuller, FIB+SEM Tomography and Numerical Simulation of Corroded PEM Fuel Cell Cathodes, *ECS Trans.*, **69**, 431 (2015).

192. B. Münch and L. Holzer, Contradicting Geometrical Concepts in Pore Size Analysis Attained with Electron Microscopy and Mercury Intrusion, *J. Am. Cer. Soc.*, **91**, 4059 (2008).

193. Y. Liu, M. W. Murphy, D. R. Baker, W. Gu, C. Ji, J. Jorne and H. A. Gasteiger, Proton Conduction and Oxygen Reduction Kinetics in PEM Fuel Cell Cathodes: Effects of Ionomer-to-Carbon Ratio and Relative Humidity, *J. Electrochem. Soc.*, **156**, B970 (2009).

194. Y. Liu, C. Ji, W. Gu, J. Jorne and H. A. Gasteiger, Effects of Catalyst Carbon Support on Proton Conduction and Cathode Performance in PEM Fuel Cells, *J. Electrochem. Soc.*, **158**, B614 (2011).

195. A. Kongkanand, N. P. Subramanian, Y. Yu, Z. Liu, H. Igarashi and D. A. Muller, Achieving High-Power PEM Fuel Cell Performance with an Ultralow-Pt-Content Core–Shell Catalyst, *ACS Catal.*, **6**, 1578 (2016).

196. S. Henning, H. Ishikawa, L. Kühn, J. Herranz, E. Muller, A. Eychmüller and T. J. Schmidt, Unsupported Pt-Ni Aerogels with Enhanced High Current Performance and Durability in Fuel Cell Cathodes, *Angew. Chem. Int. Ed.*, **56**, 10707 (2017).

197. M. Uchimura and S. S. Kocha, The Impact of Cycle Profile on PEMFC Durability, *ECS Trans.*, **11**, 1215 (2007).

198. Y. Shao-Horn, W. C. Sheng, S. Chen, P. J. Ferreira, E. F. Holby and D. Morgan, Instability of Supported Platinum Nanoparticles in Low-Temperature Fuel Cells, *Topics Catal.*, **46**, 285 (2007).

199. E. Guilminot, A. Corcella, F. Charlot, F. Maillard and M. Chatenet, Detection of Pt z+ Ions and Pt Nanoparticles Inside the Membrane of a Used PEMFC, *J. Electrochem. Soc.*, **154**, B96 (2007).

200. L. Castanheira, L. Dubau and F. Maillard, Accelerated Stress Tests of Pt/HSAC Electrocatalysts: an Identical-Location Transmission Electron Microscopy Study on the Influence of Intermediate Characterizations, *Electrocatal.*, **5**, 125 (2014).

201. S. Cherevko, G. P. Keeley, S. Geiger, A. R. Zeradjanin, N. Hodnik, N. Kulyk and K. J. J. Mayrhofer, Dissolution of Platinum in the Operational Range of Fuel Cells, *ChemElectroChem*, **2**, 1471 (2015).

202. P. Jovanovič, A. Pavlišič, V. S. Šelih, M. Šala, N. Hodnik, M. Bele, S. Hočevar and M. Gaberšček, New Insight into Platinum Dissolution from Nanoparticulate Platinum-Based Electrocatalysts Using Highly Sensitive In Situ Concentration Measurements, *ChemCatChem*, **6**, 449 (2014).

203. K. Kinoshita, Particle Size Effects for Oxygen Reduction on Highly Dispersed Platinum in Acid Electrolytes, *J. Electrochem. Soc.*, **137**, 845 (1990).

204. E. Fabbri, S. Taylor, A. Rabis, P. Levecque, O. Conrad, R. Kötz and T. J. Schmidt, The Effect of Platinum Nanoparticle Distribution on Oxygen Electroreduction Activity and Selectivity, *ChemCatChem*, **6**, 1410 (2014).

205. S. Taylor, E. Fabbri, P. Levecque, T. J. Schmidt and O. Conrad, The Effect of Platinum Loading and Surface Morphology on Oxygen Reduction Activity, *Electrocatal.*, **7**, 287 (2016).

206. Q. Jia, J. Li, K. Caldwell, D. E. Ramaker, J. M. Ziegelbauer, R. S. Kukreja, A. Kongkanand and S. Mukerjee, Circumventing Metal Dissolution Induced Degradation of Pt-Alloy Catalysts in Proton Exchange Membrane Fuel Cells: Revealing the Asymmetric Volcano Nature of Redox Catalysis, *ACS Catal.*, **6**, 928 (2016).

207. C. Baldizzone, L. Gan, N. Hodnik, G. P. Keeley, A. Kostka, M. Heggen, P. Strasser and K. J. J. Mayrhofer, Stability of Dealloyed Porous Pt/Ni Nanoparticles, *ACS Catal.*, **5**, 5000 (2015).

208. S. Mezzavilla, C. Baldizzone, A.-C. Swertz, N. Hodnik, E. Pizzutilo, G. Polymeros, G. P. Keeley, J. Knossalla, M. Heggen, K. J. J. Mayrhofer and F. Schüth, Structure–Activity–Stability Relationships for Space-Confined Pt_xNi_y Nanoparticles in the Oxygen Reduction Reaction, *ACS Catal.*, **6**, 8058 (2016).

209. N. Hodnik, C. Jeyabharathi, J. C. Meier, A. Kostka, K. L. Phani, A. Recnik, M. Bele, S. Hocevar, M. Gaberscek and K. J. Mayrhofer, Effect of ordering of $PtCu_3$ nanoparticle

structure on the activity and stability for the oxygen reduction reaction, *Phys. Chem. Chem. Phys.*, **16**, 13610 (2014).

210. A. A. Topalov, S. Cherevko, A. R. Zeradjanin, J. C. Meier, I. Katsounaros and K. J. J. Mayrhofer, Towards a comprehensive understanding of platinum dissolution in acidic media, *Chem. Sci.*, **5**, 631 (2014).

211. R. Makharia, M. F. Mathias and D. R. Baker, Measurement of Catalyst Layer Electrolyte Resistance in PEFCs Using Electrochemical Impedance Spectroscopy, *J. Electrochem. Soc.*, **152**, A970 (2005).

212. J. Gazzarri, M. Eikerling, Q. Wang and Z.-S. Liu, Estimation of Local Relative Humidity in Cathode Catalyst Layers of PEFC, *Electrochem. Solid State Lett.*, **13**, B58 (2010).

213. J. Durst, M. Chatenet and F. Maillard, Impact of metal cations on the electrocatalytic properties of Pt/C nanoparticles at multiple phase interfaces, *Phys. Chem. Chem. Phys.*, **14**, 13000 (2012).

214. D. R. Baker, D. A. Caulk, K. C. Neyerlin and M. W. Murphy, Measurement of Oxygen Transport Resistance in PEM Fuel Cells by Limiting Current Methods, *J. Electrochem. Soc.*, **156**, B991 (2009).

215. S. M. Alia, C. Ngo, S. Shulda, M.-A. Ha, A. A. Dameron, J. N. Weker, K. C. Neyerlin, S. S. Kocha, S. Pylypenko and B. S. Pivovar, Exceptional Oxygen Reduction Reaction Activity and Durability of Platinum–Nickel Nanowires through Synthesis and Post-Treatment Optimization, *ACS Omega*, **2**, 1408 (2017).

216. L. Gan, M. Heggen, R. O'Malley, B. Theobald and P. Strasser, Understanding and Controlling Nanoporosity Formation for Improving the Stability of Bimetallic Fuel Cell Catalysts, *J. Am. Chem. Soc.*, **13**, 1131 (2013).

217. K. Matsutani, K. Hayakawa and T. Tada, Effect of Particle Size of Platinum and Platinum-Cobalt Catalysts on Stability Against Load Cycling, *Plat. Met. Rev.*, **54**, 223 (2010).

218. R. Wang, C. Xu, X. Bi and Y. Ding, Nanoporous surface alloys as highly active and durable oxygen reduction reaction electrocatalysts, *Energy Environ. Sci.*, **5**, 5281 (2012).

219. H. Duan and C. Xu, Nanoporous PdCr alloys as highly active electrocatalysts for oxygen reduction reaction, *Phys. Chem. Chem. Phys.*, **18**, 4166 (2016).

220. X. Liu, G. Fu, Y. Chen, Y. Tang, P. She and T. Lu, Pt-Pd-Co trimetallic alloy network nanostructures with superior electrocatalytic activity towards the oxygen reduction reaction, *Chemistry*, **20**, 585 (2014).

221. S. Fu, C. Zhu, J. Song, M. H. Engelhard, H. Xia, D. Du and Y. Lin, Kinetically Controlled Synthesis of Pt-Based One-Dimensional Hierarchically Porous Nanostructures with Large Mesopores as Highly Efficient ORR Catalysts, *ACS Appl. Mater. Interfaces*, **8**, 35213 (2016).
222. L. Chen, H. Guo, T. Fujita, A. Hirata, W. Zhang, A. Inoue and M. Chen, Nanoporous PdNi Bimetallic Catalyst with Enhanced Electrocatalytic Performances for Electro-oxidation and Oxygen Reduction Reactions, *Adv. Funct. Mater.*, **21**, 4364 (2011).

List of Acronyms

AST ..... accelerated stress test
AW ..... acid-washed / acid washing
BET ..... Brunauer−Emmett−Teller
BEV ..... battery electric vehicle
BOL ..... beginning-of-life
CCM ..... catalyst coated membrane
CL ..... catalyst layer
CN ..... coordination number
CO ..... carbon monoxide
CV ..... cyclic voltammogramm
DG ..... double gyroid
DOE ..... U.S. Department of Energy
ECSA ..... electrochemical surface area
EDX ..... energy dispersive X-ray spectroscopy
EOL ..... end-of-life
ESB ..... energy selective backscattered electron detector
EXAFS ..... extended X-ray absorption fine structure
FCEV ..... fuel cell electric vehicle
fct ..... face-centered tetragonal
FIB-SEM ..... focused ion beam - scanning electron microscopy
FT ..... fourier transformation
GDE ..... gas diffusion electrode
GDL ..... gas diffusion layer
HCD ..... high current density
HNS ..... hollow nanosphere
HOR ..... hydrogen oxidation reaction
H_{upd} ..... hydrogen underpotential deposition
I/C ..... ionomer-to-carbon-ratio
ICP-OES ..... inductively coupled plasma - optical emission spectrometry
IEC ..... ion-exchange capacity
M ..... non-noble metal
MA ..... mass-specific ORR activity

MEA ..... membrance electrode assembly
MSTF ..... meso-structured thin film
NBB ..... nano-sized building block
NCR ..... Nafion-to-catalyst ratio
NP ..... nanoparticle
NSTF ..... nanostructured thin film
OCV ..... open circuit voltage
ORR ..... oxygen reduction reaction
PEFC ..... polymer electrolyte fuel cell
PEIS ..... potentiostatic electrochemical impedance spectroscopy
PFSA ..... perfluorosulfonic acid
PSD ..... pore size distribution
Pt/C ..... carbon supported platinum nanoparticle catalyst
PTFE ..... polytetrafluoroethylene
Pt-M ..... alloy of platinum and non-noble metal
Pt-M/C ..... carbon supported alloy of platinum and non-noble metal catalyst
QEXAFS ..... quick-EXAFS
R ..... bond length
RDE ..... rotating disk electrode
RH ..... relative humidity
rpm ..... rounds per minute
RRDE ..... rotating ring-disk electrode
SA ..... surface-specific ORR activity
SE ..... secondary electron detector
SEM ..... scanning electron microscopy
STEM-EDX ..... scanning transmission electron microscopy - energy dispersive X-ray spectroscopy
TEM ..... transmission electron microscopy
V_{RHE} ..... potential vs. reversible hydrogen electrode
WE ..... working electrode
XANES ..... X-ray absorption near-edge spectroscopy
XAS ..... X-ray absorption spectroscopy
XPS ..... X-ray photoelectron spectroscopy
XRD ..... X-ray diffraction

List of Publications

Peer-reviewed Publications

S. Henning, R. Shimizu, J. Herranz, L. Kühn, A. Eychmüller, M. Uchida, K. Kakinuma and T. J. Schmidt, Unsupported Pt_3Ni Aerogels as Corrosion Resistant PEFC Anode Catalysts under Gross Fuel Starvation Conditions, *J. Electrochem. Soc.*, **165**, F3001 (2018).

H. Ishikawa, S. Henning, J. Herranz, A. Eychmüller, M. Uchida and T. J. Schmidt, Tomographic Analysis and Modeling of Polymer Electrolyte Fuel Cell Unsupported Catalyst Layers, *J. Electrochem. Soc.,* **165**, F7 (2018).

S. Henning, J. Herranz, H. Ishikawa, B. Kim, D. Abbott, L. Kühn, A. Eychmüller and T. J. Schmidt, Durability of Unsupported Pt-Ni Aerogels in PEFC Cathodes, *J. Electrochem. Soc.*, **164**, F1136 (2017).

S. Henning, H. Ishikawa, L. Kühn, J. Herranz, E. Müller, A. Eychmüller and T. J. Schmidt, Unsupported Pt-Ni Aerogels with Enhanced High Current Performance and Durability in Fuel Cell Cathodes, *Angew. Chem. Int. Ed.*, **56**, 10707 (2017).

B. Cai, S. Henning, J. Herranz, T. J. Schmidt and A. Eychmüller, Nanostructuring Noble Metals as Unsupported Electrocatalysts for Polymer Electrolyte Fuel Cells, *Adv. Energy Mater.*, 1700548 (2017).

S. Henning, L. Kühn, J. Herranz, M. Nachtegaal, R. Hübner, M. Werheid, A. Eychmüller and T. J. Schmidt, Effect of Acid Washing on the Oxygen Reduction Reaction Activity of Pt-Cu Aerogel Catalysts, *Electrochim. Acta*, **233**, 210 (2017).

S. Henning, L. Kühn, J. Herranz, J. Durst, T. Binninger, M. Nachtegaal, M. Werheid, W. Liu, M. Adam, S. Kaskel, A. Eychmüller and T. J. Schmidt, Pt-Ni Aerogels as Unsupported Electrocatalysts for the Oxygen Reduction Reaction, *J. Electrochem. Soc.*, **163**, F998 (2016).

S. Henning, J. Herranz and H. A. Gasteiger, Bulk-Palladium and Palladium-on-Gold Electrocatalysts for the Oxidation of Hydrogen in Alkaline Electrolyte, *J. Electrochem. Soc.*, **162**, F178 (2015).

P. Rheinländer, S. Henning, J. Herranz and H. A. Gasteiger, Comparing Hydrogen Oxidation and Evolution Reaction Kinetics on Polycrystalline Platinum in 0.1 M and 1 M KOH, *ECS Trans.*, **50**, 2163 (2013).

PSI Electrochemistry Laboratory Annual Reports

S. Henning, R. Shimizu, J. Herranz and T. J. Schmidt, Investigating PEFC anode durability under fuel starvation conditions, *PSI Electrochemistry Laboratory Annual Report 2017*, doi: 10.3929/ethz-a-007047464.

S. Henning, H. Ishikawa, J. Herranz and T. J. Schmidt, Performance of Pt-Ni aerogel as cathode catalyst in differential fuel cells, *PSI Electrochemistry Laboratory Annual Report 2016*, doi: 10.3929/ethz-a-007047464.

H. Ishikawa, S. Henning, J. Herranz and T.J. Schmidt, Modeling and structural analysis of Pt-based catalyst layers in PEFCs, *PSI Electrochemistry Laboratory Annual Report 2016*, doi: 10.3929/ethz-a-007047464.

S. Henning, J. Herranz, L. Kühn, A. Eychmüller and T. J. Schmidt, Bimetallic Pt-Ni aerogels for electrocatalysis of the oxygen reduction, *PSI Electrochemistry Laboratory Annual Report 2015*, doi: 10.3929/ethz-a-007047464.

Contributed Talks

S. Henning, H. Ishikawa, L. Kühn, J. Herranz, A. Eychmüller and T. J. Schmidt, Durability of unsupported Pt-Ni Aerogel Cathodes in Polymer Electrolyte Fuel Cells, *68th Annual Meeting of the International Society of Electrochemistry, Providence (United States of America)*, 2017.

S. Henning, H. Ishikawa, L. Kühn, J. Herranz, A. Eychmüller and T. J. Schmidt, Pt-Ni Aerogels as Cathode Catalysts in Polymer Electrolyte Fuel Cells, *6th European PEFC and Electrolyser Forum, Lucerne (Switzerland)*, 2017.

S. Henning, J. Herranz, L. Kühn, W. Liu, A. Eychmüller and T. J. Schmidt, *Unsupported Bimetallic Aerogels as ORR Catalysts for PEFCs, PRiME 2016, Honolulu (United States of America)*, 2016.

Posters

S. Henning, J. Herranz, L. Kühn, A.-K. Herrmann, W. Liu, A. Eychmüller and T. J. Schmidt, Bimetallic Pt-Ni Aerogels for Electrocatalysis of the Oxygen Reduction, *ECS Conference on Electrochemical Energy Conversion & Storage with SOFC-XIV, Glasgow (United Kingdom)*, 2015.